# Towards a Plasma-Physical Understanding of Cosmic Ray Streaming and Diffusion

# Rouven Gideon Lemmerz

Univ.-Diss.

zur Erlangung des akademischen Grades "doctor rerum naturalium" (Dr. rer. nat.) in der Wissenschaftsdisziplin "Theoretische Astrophysik"

eingereicht an der
Mathematisch-Naturwissenschaftlichen Fakultät
Institut für Physik und Astronomie
der Universität Potsdam
und dem
Leibniz-Institut für Astrophysik Potsdam

Ort und Tag der Disputation:

Hauptbetreuer: Christoph Pfrommer

Betreuer: Martin Pohl

Mentor: Mohamad Shalaby

Gutachter: Martin Lemoine, Christoph Pfrommer, Anatoly Spitkovsky

# **Abstract**

Cosmic rays (CRs) constitute a significant fraction of the energy density in the interstellar medium despite their negligible number density. Their coupling to the ambient plasma through microphysical plasma instabilities makes them an important cornerstone in studies of galaxy formation and large-scale astrophysical phenomena. However, the development of large-scale models incorporating accurate CR feedback remains challenging due to the vast scale separation between microscopic plasma processes and macroscopic transport phenomena. Effective large-scale descriptions of CR feedback must therefore be informed by a detailed understanding of the underlying microphysical processes.

In this thesis, I develop a comprehensive theoretical and numerical framework for studying how CRs generate and interact with electromagnetic waves in astrophysical environments, focusing on the microscopic plasma processes that regulate CR transport. My primary methodological contribution is the development of the novel fluid-particle-in-cell (fluid-PIC) numerical method that bridges the substantial computational challenges inherent in simulating the multi-scale nature of the CR streaming instabilities. This approach treats the dense thermal background plasma as a fluid while maintaining a fully kinetic description of the sparse CR population, enabling the investigation of CR-driven instabilities across previously inaccessible temporal and spatial scales. The method successfully captures essential kinetic effects such as Landau damping through appropriate fluid closures while significantly reducing computational costs compared to traditional particle-in-cell simulations. I implement an efficient, parallelizable and accurate algorithm to calculate the Landau closure that is informed by the global wave spectrum. Various test problems establish the accuracy of the employed algorithm.

Applying the fluid-PIC method to gyroresonant CR-driven streaming instabilities, I uncover the fundamental mechanism of wave growth and saturation. I demonstrate that these processes are governed by a lopsided bunching of CR gyrophases with respect to the wave magnetic field. This gyrophase bunching provides a unified explanation for the growth of all gyroresonant streaming instabilities, including forward- and backward-moving Alfvén waves, whistler waves and electron cyclotron waves. I show that CRs significantly modify the wave velocity with implications for the resonance condition. These findings are contrasted with the assumptions conventional in quasi-linear theory, calling into question the pitch-angle diffusion coefficients derived by assuming a single wave frame and especially the random phase approximation of the CR distribution function. I advance our understanding of the intermediate-scale instability, revealing its similarities and differences to the larger-scale Alfvén waves. I emphasize the differences in growth rates and saturation levels, and explore a resonance gap at pitch angles close to 90° that is distinct from the nonphysical resonance gap in quasi-linear theory. The theoretical framework and numerical methods developed in this dissertation provide tools for investigating CR transport in realistic astrophysical environments. These advances offer new perspectives on fundamental plasma physics processes, such as wave-particle interactions and instability mechanisms in collisionless plasmas, that influence galaxy formation and evolution.

# Zusammenfassung

Kosmische Strahlung (CR) trägt trotz ihrer geringen Teilchendichte einen bedeutenden Anteil der Energiedichte im interstellaren Medium in sich. Ihre Kopplung an das umgebende Plasma durch mikroskopische Plasmainstabilitäten macht sie zu einem wichtigen Grundpfeiler bei der Untersuchung von Galaxienbildung und großskaligen astrophysikalischen Phänomenen. Die Entwicklung makroskopischer Modelle mit präziser CR-Rückkopplung erfordert aufgrund der enormen Skalentrennung zwischen mikroskopischen Plasmaprozessen und makroskopischen Transportphänomenen ein detailliertes Verständnis der zugrundeliegenden Prozesse.

In dieser Dissertation entwickle ich einen umfassenden theoretischen und numerischen Rahmen zur Untersuchung der Erzeugung und Wechselwirkung elektromagnetischer Wellen durch CR in astrophysikalischen Umgebungen, wobei der Fokus auf den mikroskopischen Plasmaprozessen liegt, die den Transport von CR regulieren. Mein primärer methodischer Beitrag ist die Entwicklung der neuen Fluid-Particle-in-Cell (Fluid-PIC) Methode, zur Überbrückung der rechnerischen Herausforderung von skalenübergreifenden CR-getriebenen Instabilitäten. Dieser Ansatz behandelt das dichte thermische Hintergrundplasma als Fluid, während eine vollständig kinetische Beschreibung der weniger dichten CR-Population beibehalten wird, was die Untersuchung von CR-getriebenen Instabilitäten über bisher unzugängliche zeitliche und räumliche Skalen ermöglicht. Die Methode erfasst erfolgreich wesentliche kinetische Effekte wie Landau-Dämpfung durch eine geeignete Fluid-Abschlussrelation, während sie den Rechenaufwand im Vergleich zu traditionellen PIC-Simulationen erheblich reduziert. Ich implementiere einen effizienten parallelen Algorithmus zur Berechnung der Landau-Abschlussrelation basierend auf dem globalen Wellenspektrum und validiere die Methode in Testproblemen.

Durch Anwendung der Fluid-PIC-Methode auf gyroresonante Instabilitäten zeige ich, dass eine asymmetrische Bündelung der CR-Gyrophasen bezüglich des Wellenmagnetfeldes den fundamentalen Mechanismus des Wellenwachstums und der Sättigung darstellt. Dies erklärt einheitlich das Wachstum aller gyroresonanten CR-Instabilitäten, einschließlich vorwärts- und rückwärts propagierender Alfvén-Wellen, Whistler-Wellen und Elektronen-Zyklotron-Wellen. Ich zeige, dass CR die Wellengeschwindigkeit signifikant modifizieren, mit Auswirkungen auf die Resonanzbedingung. Diese Erkenntnisse werden mit der klassischen quasilinearen Theorie verglichen, wobei die Neigungswinkel-Diffusionskoeffizienten in Frage gestellt werden, welche auf den Annahmen einer einzelnen Wellengeschwindigkeit und zufälliger Gyrophasen der CR beruhen. Ich erweitere unser Verständnis der Instabilitäten auf Zwischenskalen und zeige ihre Ähnlichkeiten und Unterschiede zu den Alfvén-Wellen-Instabilitäten auf. Dabei vergleiche ich die Wachstumsraten und Sättigungsniveaus, und untersuche eine Resonanzlücke bei Neigungswinkeln nahe 90°, die sich von der unphysikalischen Resonanzlücke in der quasilinearen Theorie unterscheidet. Der in dieser Dissertation entwickelte theoretische Rahmen und die numerischen Methoden stellen Werkzeuge zur Untersuchung des CR-Transports in realistischen astrophysikalischen Umgebungen bereit. Diese Fortschritte bieten neue Einblicke auf fundamentale plasmaphysikalische Prozesse, wie Wellen-Teilchen-Wechselwirkungen und Instabilitätsmechanismen in kollisionsfreien Plasmen, die Einfluss auf Galaxienentstehung und -entwicklung haben.

# **Contents**

1.	intro	duction		1
	1.1.	Cosmic Ra	ays: Basic Properties	1
	1.2.	Cosmic Ra	ay Transport and Streaming Instabilities	4
2.	Des	criptions of	Astrophysical Plasmas	9
	2.1.	The Kinet	ic Description	9
		2.1.1. Th	e Vlasov-Maxwell System	9
		2.1.2. Lin	ear Waves	11
	2.2.	The Multi-	-Fluid Equations	13
		2.2.1. Th	e Moment Hierarchy	13
		2.2.2. Ad	iabatic Closures	15
		2.2.3. Lai	ndau Closures	16
		2.2.4. Lin	near Waves	19
	2.3.	Quasi-neut	tral fluids and MHD	21
		2.3.1. De	rivation of Generalized Ohm's Law	21
		2.3.2. Sin	applifying Generalized Ohm's Law	22
		2.3.3. Th	e MHD Approximation	22
		2.3.4. Lin	near Waves in Ideal MHD	24
3.	Nun	nerical met	hods 2	27
	3.1.	Kinetic So	lvers: Vlasov Solvers	27
	3.2.	Kinetic So	lvers: Particle-in-Cell (PIC)	28
		3.2.1. Par	rticle Pusher	29
		3.2.2. Int	erpolation	30
		3.2.3. Ele	ectromagnetic Field Solver: Yee Grid and Magnetic Monopoles 3	31
		3.2.4. Nu	merical Stability	32
		3.2.5. Min	nimizing Numerical Heating	33
	3.3.	Fluid Solv	ers	35
		3.3.1. Fin	aite Difference Methods (FD)	36
		3.3.2. Fin	ite Volume Methods (FV)	37
		3.3.3. Otl	her methods	38
	3.4.	Compound	l techniques	40
		3.4.1. Rec	quirements	40
		3.4.2. Ele	ectron Fluids and Kinetic Ions (Hybrid-PIC)	40
		3.4.3. The	ermal Fluids and Kinetic Cosmic Rays	11

# Contents

4.	The	fluid-P	PIC method	47
	4.1.	Introd	uction	48
	4.2.	Numer	rical Method	51
		4.2.1.	Kinetic description of a plasma	52
		4.2.2.	The particle-in-cell method	52
		4.2.3.	Fluid description of plasma	53
		4.2.4.	Finite volume scheme	55
		4.2.5.	Electromagnetic interaction with charged fluids	59
		4.2.6.	Landau closure for fluid species	61
		4.2.7.	Current-coupled fluid-PIC algorithm	68
	4.3.	Code	validation tests	71
		4.3.1.	Shock tube	72
		4.3.2.	Two-fluid dispersion relation	73
		4.3.3.	Langmuir wave damping	76
		4.3.4.	Interacting Alfvén waves	76
		4.3.5.	Gyrotropic CR streaming instability	79
		4.3.6.	Computational scaling	82
	4.4.	Conclu	usion	83
	App	endix		85
		4.A.	C-WENO coefficients	85
		4.B.	Convergence order	86
		4.C.	$R_{31}$ closure and adiabatic coefficients	87
<b>5</b> .	Qua	silinear	Theory of Cosmic Ray Streaming	89
	5.1.	The Fe	okker-Planck Equation	89
	5.2.	Pitch .	Angle Diffusion in the Presence of Random Alfvén Waves	91
	5.3.	Linear	Stability Analysis	94
6.	Grov	wth and	d Saturation Mechanism of the Gyroresonant Instabilities	99
	6.1.	Introd	uction	100
		6.1.1.	Astrophysical motivation	100
		6.1.2.	CR transport and CR-driven instabilities	100
		6.1.3.	Idea to elucidate the physics of CR-driven instabilities	103
	6.2.	Numer	rical Method and Setup	104
		6.2.1.	Method	104
		6.2.2.	Setup	105
	6.3.	Partic	le motions and wave growth	108
		6.3.1.	Momentum balance	108
		6.3.2.	Evolution of the instability without CR back-reaction: the pendulum	
			equation	
		633	Discussing the pendulum picture of CR motions	115

		6.4.3.	Simulated family of particle orbits	123
	6.5.		ation of a single wave mode	
		6.5.1.	Saturation of wave growth due to CR scattering	126
		6.5.2.	Saturation of wave growth due to particle trapping	128
		6.5.3.	Impact of CRs on the wave velocity	130
		6.5.4.	Evolving CR distribution	130
	6.6.	Conclu	usions	
	App	endix		134
		6.A.	Conventions	134
		6.B.	Comparison of fluid-PIC and PIC methods	134
		6.C.	Robustness of initial setup	136
		6.D.	Dispersion Relation	138
7.	Diffe	erences	Between the Gyroresonant Streaming Instabilities	141
	7.1.	Const	raints on Resonance with Forward Moving Waves	141
		7.1.1.	Electron-scale Effects	141
		7.1.2.	Grid-Scale Limitations on Resonant CRs in MHD Simulations	143
		7.1.3.	Comparison and Implications of Resonance Bounds	144
	7.2.	Instab	ility Growth Rates	145
		7.2.1.	Derivation of the Intermediate-scale Instability Growth Rate	145
		7.2.2.	Alfvén Wave Growth Rates	147
		7.2.3.	Comparison of Pitch Angle-dependent Growth Rates	149
8	Con	clusion	S	153

# 1. Introduction

# 1.1. Cosmic Rays: Basic Properties

The field of cosmic ray physics emerged from an observation at the beginning of the 20th century. Electroscopes, instruments designed to measure ionizing radiation, detected radiation even when heavily shielded. While this "penetrating radiation" was initially thought to originate from radioactive material, Pacini et al. (1910) challenged this hypothesis by demonstrating that radiation levels decreased under water. This prompted Hess (1912) to conduct multiple balloon experiments, finding that this radiation intensity increased with altitude rather than decreased, a clear indication of the radiation's extraterrestrial origin.

In light of these observations, the term "penetrating radiation" was later renamed to "cosmic rays" (CR), coined by Millikan (1925) who initially proposed that these particles were gamma rays. However, shortly thereafter, the discovery of the latitude effect by Clay (1927) challenged this interpretation. By demonstrating that the radiation intensity varied with geomagnetic latitude and the corresponding deviations in Earth's magnetic field, Clay provided compelling evidence that CRs were primarily charged particles interacting with magnetic fields. This understanding was further solidified by Bothe and Kolhörster (1929) through their coincidence counting technique, which utilized adjacent Geiger-Müller counters to track individual charged particles and record their path. This technique is still used today to observe and identify CRs in experiments like IceCube (IceCube Collaboration\*, 2013) and the Alpha Magnetic Spectrometer (Aguilar et al., 2013).

Freier et al. (1948) established, that CRs consist predominantly of fully ionized atomic nuclei and about 1% electrons. The composition of the atomic nuclei is made up of approximately 89% protons, 10% helium, and 1% heavier nuclei. This composition varies with energy and continues to be studied in greater detail by experiments like CREAM (Yoon et al., 2011) and PAMELA (Adriani et al., 2011). This composition refers to primary CRs, originating outside of the Earth's atmosphere. As they enter the atmosphere, they also produce a host of secondary CRs as a result of collisions with atmospheric matter (Auger et al., 1939). These secondary particles are free to collide again, leading to a cascade of particles raining down on Earth as a "shower". This has surprisingly practical implications; for example, these showers provide a continuous supply of the radioactive carbon isotope <sup>14</sup>C through spallation. This isotope is used for the radiocarbon dating method, which allows approximately identifying the time when an organism stopped assimilating carbon, and has become an invaluable method for dating archaeological artifacts (Anderson et al., 1947). In the broader context of astrobiology, understanding the intensity of CRs on a planet's surface and its variation over geological timescales is essential in assessing the

#### 1. Introduction

habitability of exoplanets and the potential for life beyond Earth (Lammer et al., 2009).

These showers have also opened the gateways for particle physics research beginning in the 1930s. Antimatter, the muon, the pion, the kaon, and the  $\Lambda$ -baryon were first identified under CR interactions (Anderson, 1933; Rochester and Butler, 1947; Nakamura, 2010). As a comparison of scale, CRs reach energies up to 320 EeV, surpassing the Large Hadron Collider's 7 TeV capability by seven orders of magnitude (albeit the discrepancy in combined energy of collisions is only three orders of magnitude).

Only few candidates can potentially accelerate CRs to these extreme energies. Supernova remnants are considered the primary source of galactic CRs up to approximately 0.1 - -1 PeV energies (Baade and Zwicky, 1934; Ginzburg and Syrovatskii, 1964; Lagage and Cesarsky, 1983; Bell et al., 2013). More energetic particles likely originate from extragalactic sources such as Active Galactic Nuclei (AGN) (Protheroe and Szabo, 1992; Rieger, 2022), pulsar wind nebulae (PWN)(Sironi et al., 2013; Lemoine et al., 2015; The LHAASO Collaboration et al., 2021), and Gamma-Ray Bursts (GRBs) (Waxman, 1995; Zhang et al., 2021). Observations by the Pierre Auger Observatory have strengthened the connection between ultra-high-energy CRs and AGN (Pierre Auger Collaboration et al., 2007).

At these acceleration sites, the CRs undergo the process of diffusive shock acceleration (Axford et al., 1977; Bell, 1978a,b; Blandford and Ostriker, 1978). Particles become trapped between magnetic mirrors, which confine particles between the upstream and downstream of a shock through frequent particle scattering. As these mirrors apparently close in on the particles, they accelerate the particles over successive impacts. While specifics of this process are actively investigated (Caprioli and Spitkovsky, 2014a; Sironi and Spitkovsky, 2011; Lemoine, 2019; Marcowith et al., 2020) – particularly its application to electron acceleration is not obvious (Amano and Hoshino, 2010; Shalaby et al., 2022; Gupta et al., 2024) – the process of diffusive shock acceleration explains both the extreme energies achieved as well as the power-law form of the energy spectrum.

Indeed, the observed CR energy spectrum follows a remarkably smooth power-law spanning ten orders of magnitude, with the peak energy density at 300 MeV. This was first systematically studied by Blackett and Occhialini (1933) using cloud chamber photographs. Even though the energy spectrum is surprisingly smooth, where the density generally falls off with increasing energy as  $dn/dE \propto E^{-2.7}$ , the spectrum exhibits two notable features: the "knee" at approximately 4 PeV where the spectrum steepens to  $\propto E^{-3.1}$ , and the "ankle" at around 4 EeV, where it returns to  $\propto E^{-2.7}$  (Kulikov and Khristiansen, 1959; Amenomori et al., 2008; Anchordoqui, 2019). The ankle's flattening likely results from dominant extragalactic CRs dominating these energies (Aloisio et al., 2012), while the knee may reflect either the maximum acceleration capability of supernova remnants in the Milky Way or an increased galactic escape probability due to transition from pitch angle scattering to Hall diffusion (Ptuskin et al., 1993).

The velocity diffusion mechanism of CRs below the knee (pitch angle scattering) can be quickly summarized as follows: CRs spiral along magnetic field lines, where the angle between their direction of motion and the magnetic field line is called the pitch angle. Small magnetic perturbations scatter CRs without significantly changing their energy, constantly redirecting

their velocity vector. Because the CRs undergo a random walk process in their pitch angle (velocity direction), their average velocity along the magnetic field line is only a fraction of their intrinsic particle velocity. This significantly increases the galactic escape time given the presence of these magnetic perturbations, but the confinement of CRs in the galaxy by pitch angle scattering is not only a coincidence. Kulsrud and Pearce (1969) proposed the concept of CR self-confinement in galaxies, where CRs generate the magnetic turbulence necessary for their own confinement via the CR streaming instabilities. This self-confinement concept fundamentally shaped modern CR transport theories. As such, it lays the foundation for this thesis and we will discuss it in detail in later chapters. In general, CR propagation through the galaxy is a complex process including not only diffusion through self-generated turbulence, but it also encompasses convective processes and various energy loss mechanisms. The development of phenomenological propagation models has evolved significantly since the inception of the simple leaky-box model (Davis Jr, 1960; Ginzburg and Syrovatskii, 1964). Modern numerical codes, like GALPROP (Strong and Moskalenko, 1998), offer more sophisticated approaches, but they do not account for the dynamic interaction between CRs and their environment.

Even though higher-energy CRs (> GeV) are mostly collisionless, the CR streaming instabilities provide an effective mechanism to transfer momentum and energy to the thermal plasma. Despite the low density of CRs—approximately nine orders of magnitude below that of the ambient gas - they contribute significantly to the pressure and energy density in the interstellar medium (ISM) (Boulares and Cox, 1990; Draine, 2011), which makes them dynamically important for galaxy formation. Nevertheless, their importance is not limited to the ISM. They drive galactic winds from the galactic disk as shown in one-dimensional analytical models (Ipavich, 1975; Breitschwerdt et al., 1991; Recchia, 2020) and numerical studies of wind launching from the ISM (Simpson et al., 2016, 2023; Girichidis et al., 2016, 2018; Farber et al., 2018; Sike et al., 2024), thereby accelerating outflows in global galactic disk simulations (Uhlig et al., 2012; Salem and Bryan, 2014; Pakmor et al., 2016; Wiener et al., 2017; Thomas et al., 2023; Thomas et al., 2024) that influence the circumgalactic medium (Buck et al., 2020; Ji et al., 2020). CRs also carry energy from active galactic nuclei into the intracluster medium of cool core clusters, thereby heating it to counteract the cooling losses (Pfrommer, 2013; Ruszkowski et al., 2017a; Jacob and Pfrommer, 2017b). Through their interactions with magnetic fields, CRs can contribute to the dynamo processes that maintain galactic magnetic fields, creating a complex feedback loop that influences galaxy evolution on multiple scales (Parker, 1992; Hanasz et al., 2009).

On the other hand, collisional low-energy CRs (with particle energies  $E \ll \text{GeV}$ ) are key players in the chemical evolution of molecular clouds, where they drive ion-neutral chemistry and influence star formation processes (Dalgarno, 2006b,a; Padovani et al., 2020; Gabici, 2022). Furthermore, they create isotopes like beryllium-10 in the ISM through spallation, which serve as CR chronometers (Simpson and Garcia-Munoz, 1988). The impact of CRs on galaxy formation has become an active area of research recently (Grenier et al., 2015; Ruszkowski and Pfrommer, 2023). However, the galactic scales inherent to the problem prohibit self-consistent modeling of the CRs' microphysical interactions at scales of approximately AUs. Thus, these problems

#### 1. Introduction

depend crucially on our understanding of the underlying plasma processes – specifically the CR streaming instabilities, which allow GeV CRs to couple to the thermal plasma in the first place.

CR transport is on its own already a fascinating problem, but there is also a link to another active area of research in heliophysics. Particles in the solar wind can drive the same streaming instabilities as CRs, thereby sharing a methodological framework. This link can also serve as a viable test bed for investigating the impact of these instabilities in observations (Gary et al., 2016).

# 1.2. Cosmic Ray Transport and Streaming Instabilities

Early observations revealed CRs to be remarkably isotropic in their arrival directions at Earth (Strong et al., 2007; Abbasi et al., 2012, with variations in the relative flux of order  $4 \times 10^{-4}$ ), a fact that demands explanation given their presumed origin in discrete sources such as supernova remnants. Furthermore, the short-lived radioactive spallation products – which must be produced in the local galactic disk to be observed – are present in surprisingly high numbers compared with the primary CRs producing them. This indicates, that the CRs remain confined in the galactic disc for a long time, estimated to be roughly ~  $10^7$  years (Simpson and Garcia-Munoz, 1988; Evoli et al., 2020). Therefore, the time-averaged mean velocity of CRs must be significantly smaller than their absolute velocity, which is close to c, indicating frequent scattering of the mostly collisionless CRs. These observational challenges led to the development of various theoretical frameworks attempting to explain CR confinement and transport within galaxies. Among these frameworks, the self-confinement paradigm emerged as particularly successful in resolving these apparent conflicts.

The self-confinement paradigm (Kulsrud and Pearce, 1969; Wentzel, 1969; Skilling, 1971) posits that CRs generate magnetic fluctuations responsible for their own scattering and confinement. The mechanism operates through the gyroresonant streaming instability, whereby CRs excite Alfvén waves that subsequently scatter the particles. These waves are believed to be regulated through various damping mechanisms, most notably non-linear Landau damping and ion-neutral damping. In this picture, saturation occurs when the instability growth rate balances the damping rate. Thus, the efficiency of the self-confinement process depends not only on the CR distribution but also on the environment. The self-confinement theory has provided the foundation for much of our understanding of CR transport. It naturally explains how CRs transition from an initially anisotropic distribution near their sources to the observed isotropic state, while also providing mechanisms for momentum and energy transfer between CRs and the thermal plasma as mentioned previously.

Streaming instabilities manifest in two distinct categories: resonant and non-resonant instabilities. The self-confinement theory is mainly concerned with the gyroresonant instabilities (Shapiro and Shevchenko, 1964; Lerche, 1967; Shalaby et al., 2021, 2023), as these instabilities are driven at relatively small anisotropies in the CR configurations, with drift velocities of  $v_{\rm dr} \gtrsim v_{\rm A}$ . If the Alfvén speed  $v_{\rm A}$  in the ISM is assumed to be a fraction of the speed of light, e.g.,  $v_{\rm A} \approx 10^{-4} c$ , this naturally limits CR anisotropies to similar, small orders, which agrees with the

observed, almost isotropic CR distribution at Earth. The gyroresonant instabilities drive waves, for which the Doppler shifted gyrofrequency of a CR approximately matches the frequency of the waves carried by the thermal plasma  $\omega(k)$ ,

$$\Omega_{\rm cr} - \boldsymbol{k} \cdot \boldsymbol{v}_{\parallel} = -\omega(k), \tag{1.1}$$

where  $\Omega_{\rm cr}$  is the CR gyrofrequency and  $v_{\parallel}$  is the CR velocity parallel to the magnetic field at wave vector  $\mathbf{k}$ . This gyroresonance *condition* is not particularly restrictive, because a CR with a given gyrofrequency and parallel velocity may resonate with a wave at any scale k. The waves in the background might be Alfvén, whistler or electron cyclotron waves, spanning a large range of different values for k and  $\omega$ , but traditionally only Alfvén waves are taken into account. The resulting gyroresonant coupling resembles a clutch mechanism, where a rotating disc driven by an engine is pressed against a flywheel (representing the background waves). Just as a clutch requires similar rotational velocities of both surfaces for efficient torque transfer, the CRs must approximately fulfill the gyroresonance condition. Nevertheless, the CRs (acting as the rotating disc) must rotate slightly faster (including their Doppler-shifted motion) than the wave frequency such that they can systematically transfer energy to the waves. During this process, the CRs develop a current perpendicular to the background magnetic field,  $J_{\perp}$ , that assumes a coherent wave-like structure adapted to the frequency and wavelength of the electromagnetic waves. Therefore, it is the perpendicular CR current that interacts with the perpendicular magnetic field,  $J_{\perp} \times B_{\perp}$ . The entire process is more complex than sketched out here, we dedicate chapter 6 to understanding the physical mechanism of its growth and saturation mechanism. Even though gyroresonant instabilities are not able to significantly intensify the total magnetic field, the small magnetic perturbations are of similar wavelength as the CRs' gyro radii. This enables efficient scattering provided that waves at this scale are not inhibited by strong wave damping.

As a side note, pressure-anisotropy-driven instabilities represent another class of gyroresonant phenomena in CR transport. These instabilities arise from anisotropy in the CR pressure and can lead to the generation of magnetic fluctuations through mechanisms distinct from the classical streaming instability, able to occur even without a drifting CR distribution (Lebiga et al., 2018; Sun and Bai, 2023). However, its mechanism is presumably orders of magnitude less efficient than CR streaming under general ISM conditions and thus its relevancy is confined to specific circumstances. Here, we are not concerned with these instabilities and use the term gyroresonant instabilities to solely refer to the streaming instabilities.

Among the non-resonant CR-driven instabilities, the Bell instability (Bell, 2004) is the most prominent example. It can generate large magnetic field amplifications, far exceeding the initial magnetic field strength. It becomes only active if large unmitigated CR currents are present, that is if the CR to background density ratio times the square of the CR drift to Alfvén velocity ratio exceed unity,  $n_{\rm cr}/n_{\rm bg} \times (v_{\rm dr}/v_{\rm A})^2 > 1$ . This strong CR current generates a compensating return current in the background plasma, primarily consisting of the more mobile electrons. These large currents parallel to the background magnetic field are perturbed by perpendicular

#### 1. Introduction

magnetic fluctuations, interacting with them according to the Lorentz-force  $J_{\parallel} \times B_{\perp}$ , and thereby driving transverse waves (Zirakashvili et al., 2008). This mechanism has attracted considerable attention for its potential role in magnetic field amplification around supernova remnant shocks and CR acceleration (Niemiec et al., 2008; Riquelme and Spitkovsky, 2009), but in the regime of very large currents other instabilities, like a filamentation instability, start taking precedence (Bret, 2009; Reville and Bell, 2012). While the Bell instability is important to understand the acceleration and escape of CRs at their sources, where the CR current is strong, this instability is negligible for typical ISM conditions. As such, Bell's instability is not relevant for self-confinement in galaxies, and we focus on the gyroresonant interactions.

Although self-confinement has been the predominant theoretical framework for propagating GeV-TeV CRs, its applicability to high-energy CRs (TeV-PeV energys) has been debated (Yan and Lazarian, 2002, 2004). The CR power-law spectrum indicates, that these high-energy CRs have a significantly smaller number and energy density than the CRs at GeV energies. As the high-energy CRs would have to drive coherent waves at larger scales compared to CRs of lower energy, they may not be able to drive instabilities fast enough to overcome turbulent damping (Farmer and Goldreich, 2004). A notable candidate among the alternative theories is external turbulent confinement, where CRs scatter off pre-existing magnetohydrodynamic (MHD) turbulence (Jokipii and Parker, 1969; Giacalone and Jokipii, 1999), which is expected to begin dominating CR transport at energies upwards of around 200 GeV-1 TeV (Blasi et al., 2012; Evoli et al., 2018; Recchia and Gabici, 2024). Recent work suggests that bends in the field line structures can provide efficient CR scattering, potentially rivaling self-generated waves as the primary confinement mechanism (Lemoine, 2023; Kempski et al., 2023). A limitation of external turbulent confinement is its requirement for ubiquitous, nearly isotropically distributed pre-existing scattering centers around Earth because otherwise, it could not explain the almost isotropic arrival directions of CRs. This would then pose a constraint on the injection rate of strong turbulence, which would have to be distributed across the ISM and locally follow a turbulent energy cascade. This requirement of volume-filling turbulence at the AU scale weakens for higher-energy CRs (≥ TeV), which sample larger volumes because of their larger gyro radii, which increases the likelihood of being scattered by externally driven MHD fluctuations on their mean free path.

CR transport is traditionally modeled using quasi-linear theory (QLT) as its analytical framework (Jokipii, 1966), which we discuss in detail in Chapter 5. QLT is a perturbation method, which evolves a slowly changing ground state being impacted by small, first-order fluctuations. Using QLT, the evolution equation of the CR distribution is transformed into a Fokker-Planck equation. This models the CRs as undergoing a random walk in momentum and pitch angle, where they randomly scatter off of (self-generated or pre-existing) resonant magnetic perturbations.

Even though this framework has been quite successful in modeling CR transport, there are some assumptions inherent to or commonly applied together with QLT. These include, for example, the neglect of wave-wave interactions, which emerge as a second-order fluctuation and which might play a role during saturation. It also predicts unphysical singularities leading to

the 90° problem, relevant for CRs moving only perpendicular to the magnetic background field (corresponding to a pitch angle of 90°). These CRs theoretically would encounter a static wave magnetic field and thus would never scatter, which is a consequence of infinitely thin resonance widths and assuming static waves (Völk, 1975; Tautz et al., 2008). As we will show later on, the physical resonance conditions are broader than assumed in QLT, thereby resolving this theoretical problem. The CR distribution is typically assumed to be initially isotropic in some frame, further simplifying the diffusion coefficient to depend only on the CR's energy instead of taking their pitch angle into account as well. This is an observationally motivated assumption, but fails to model how the CRs escaping in a narrow loss cone close to their sources start to isotropize. The transport of freshly injected CRs is not just diffusive, but superdiffusive (Ptuskin et al., 2008) and non-linear. Furthermore, the CRs are assumed to have random phase angles with regard to their resonant waves, neglecting naturally occuring wave steepening and bunching of the CR gyrophases, which is essential for driving the instabilities. Nevertheless, QLT has shaped our understanding of the growth, saturation and diffusion of CRs and likely captures the most important transport processes (Engelbrecht et al., 2022).

While analytical methods have mostly revolved around QLT, the complexity of CR streaming processes and the limitations of analytical approaches have necessitated the development of diverse numerical methods. These computational approaches span multiple scales and physical regimes, ranging from microphysical scales to large scales, including the particle-in-cell (PIC) method (Holcomb and Spitkovsky, 2019; Shalaby et al., 2021), hybrid-PIC (Weidl et al., 2019b; Amano, 2018; Schroer et al., 2024), MHD-PIC (Lucek and Bell, 2000; Bai et al., 2015), CR hydrodynamics (Pfrommer et al., 2017; Zweibel, 2017; Jiang and Oh, 2018; Thomas and Pfrommer, 2019), test particle approaches (Giacalone and Jokipii, 1999). The development of another method, the fluid-PIC method (Lemmerz et al., 2024b), is part of this thesis and we later lay out the reasons for its development as well as its implementation in chapters 3 and 4, respectively.

Despite significant advances in our understanding of CR streaming, several fundamental questions remain unresolved in the field.

- The complex interplay between various wave damping mechanisms presents a critical area of investigation. Multiple damping channels including nonlinear Landau damping, ion-neutral friction, and turbulent cascade operate simultaneously in the interstellar medium (Plotnikov et al., 2021; Schroer et al., 2024; Cerri, 2024). Understanding their relative efficiencies and mutual interactions is essential for accurately predicting CR transport properties.
- A fundamental theoretical challenge lies in bridging the gap between kinetic and fluid descriptions of CR transport (Zweibel, 2013; Thomas and Pfrommer, 2019). While fluid approximations offer computational advantages for large-scale simulations, their ability to capture essential kinetic effects remains uncertain. The development of robust methods for implementing kinetic phenomena in fluid models continues to be an active area of research.
- Finally, the interaction between self-generated and pre-existing turbulence presents a com-

#### 1. Introduction

plex problem that spans multiple scales. Understanding how different scattering mechanisms compete and coexist, how wave spectra evolve under their combined influence, and how these processes ultimately affect CR transport coefficients remains crucial. This understanding is particularly relevant for accurately modeling CR propagation in realistic astrophysical environments, where both self-generated and ambient turbulence play important roles (Reichherzer et al., 2020; Kempski and Quataert, 2022).

The thesis is structured as follows. We review various descriptions of plasmas in Chapter 2, which are needed to understand the differences in numerical methods and analytical models used to study CR streaming. In Chapter 3 we compare numerical methods, before introducing the novel fluid-PIC method in Chapter 4. We summarize quasilinear theory in the context of CR streaming in Chapter 5 before describing a competing description of CR streaming as a gyrophase bunching process in Chapter 6. We further concentrate on growth rates and resonance criteria in Chapter 7. We conclude our findings in Chapter 8. Throughout this thesis we employ SI units.

The description of plasma phenomena spans multiple scales, from microscopic particle dynamics to macroscopic fluid behavior. The most fundamental description is given by kinetic theory, which tracks the evolution of particle distribution functions in phase space. However, for many applications, this level of detail is unnecessary and can be reduced to fluid descriptions through appropriate averaging of the velocity distribution function. If electron scales can be neglected, even further approximations are possible resulting in the magnetohydrodynamic (MHD) description of a plasma. This section presents a derivation of the different fluid models from kinetic theory, carefully examining all assumptions and approximations involved in this process. One important property of each description is the set of linear waves supported by the system of equations, which we will derive for parallel waves that are important for CR streaming.

Throughout this thesis, we will not just frequently employ these different approximations analytically but we also assess the validity of numerical methods using these descriptions. More general overviews are given by (in descending order of use in this chapter) Wolfgang Baumjohann (2012), Treumann and Baumjohann (1997), Stix (1992), Chen (2016), Landau et al. (1990), and Boyd and Sanderson (2003).

# 2.1. The Kinetic Description

**Phase Space and Distribution Functions.** Consider a plasma consisting of particles of different species s (typically electrons and ions). The state of each particle is described by its position x and velocity v in six-dimensional phase space. Rather than tracking individual particles, we describe the plasma through distribution functions  $f_s(x, v, t)$  for each constituent of the plasma, defined such that:

$$f_s(\boldsymbol{x}, \boldsymbol{v}, t) \mathrm{d}^3 x \, \mathrm{d}^3 v$$

represents the number of particles in the phase space volume element  $d^3x d^3v$  centered at (x, v) at time t.

#### 2.1.1. The Vlasov-Maxwell System

The Vlasov-Maxwell system of equations provides a complete description of the collisionless plasma dynamics, including collective effects and the self-consistent evolution of the electromagnetic fields.

The evolution of  $f_s$  in a collisionless plasma is governed by the Vlasov equation,

$$\frac{\mathrm{d}f_s}{\mathrm{d}t} = \frac{\partial f_s}{\partial t} + \boldsymbol{v} \cdot \boldsymbol{\nabla} f_s + \frac{q_s}{m_s} \left( \boldsymbol{E} + \boldsymbol{v} \times \boldsymbol{B} \right) \cdot \boldsymbol{\nabla}_{\boldsymbol{u}} f_s = 0, \tag{2.1}$$

where the proper velocity is denoted as  $\boldsymbol{u} = \gamma \boldsymbol{v}$  using  $\gamma = [1 - (v/c)^2]^{-1/2}$  with the speed of light c; the electric and magnetic field vectors are given by  $\boldsymbol{E}$  and  $\boldsymbol{B}$ , respectively, and  $q_s$  and  $m_s$  represent the charge and mass of the particle species, respectively. This equation expresses the conservation of phase space density along particle trajectories. The electromagnetic fields satisfy Maxwell's equations, which reads as follows in the SI unit system (which we use throughout this thesis),

$$\nabla \cdot \boldsymbol{E} = \frac{\rho}{\epsilon_0}, \qquad \nabla \cdot \boldsymbol{B} = 0, \tag{2.2}$$

$$\nabla \times E = -\frac{\partial \mathbf{B}}{\partial t}, \qquad \nabla \times \mathbf{B} = \mu_0 \mathbf{J} + \frac{1}{c^2} \frac{\partial \mathbf{E}}{\partial t}, \qquad (2.3)$$

denoting vacuum permittivity and susceptibility as  $\epsilon_0$  and  $\mu_0$ , respectively, which are related via  $c = (\epsilon_0 \mu_0)^{-1/2}$ . The electromagnetic fields do not directly depend on the position of any single particle, but rather on velocity-averages of the distribution function, also called velocity moments or just moments. The charge and current density are sums over all the species s for these moments:

$$\rho(\mathbf{x},t) = \sum_{s} q_{s} \int f_{s}(\mathbf{x},\mathbf{v},t) d^{3}u = \sum_{s} q_{s} n_{s}, \qquad (2.4)$$

$$\boldsymbol{J}(\boldsymbol{x},t) = \sum_{s} q_{s} \int \boldsymbol{v} f_{s}(\boldsymbol{x},\boldsymbol{v},t) \, \mathrm{d}^{3} u = \sum_{s} q_{s} n_{s} \boldsymbol{w}_{s}. \tag{2.5}$$

We introduce 4 moments, which correspond to physically meaningful quantities. The zeroth moment, the number density

$$n_s(\mathbf{x}, t) = \int f_s(\mathbf{x}, \mathbf{v}, t) \,\mathrm{d}^3 u \tag{2.6}$$

represents the number of particles per unit volume. The first moment, the bulk velocity,

$$\boldsymbol{w}_{s}(\boldsymbol{x},t) = \frac{1}{n_{s}} \int \boldsymbol{v} f_{s}(\boldsymbol{x},\boldsymbol{v},t) \,\mathrm{d}^{3} u \tag{2.7}$$

represents the average velocity of particles at a spatial location. The second moment, the pressure tensor

$$\mathbf{P}_s = \int (\mathbf{v} - \mathbf{w}_s)(\mathbf{v} - \mathbf{w}_s) f_s \, \mathrm{d}^3 u$$
 (2.8)

represents the momentum flux and thermal motion. The notation vv indicates the dyadic product of two vectors. Another common definition of the pressure tensor includes an additional factor of  $m_s$ . Finally, the third moment, the heat flux tensor

$$\mathbf{Q}_s = \int (\mathbf{v} - \mathbf{w}_s)(\mathbf{v} - \mathbf{w}_s)(\mathbf{v} - \mathbf{w}_s) f_s \, \mathrm{d}^3 u, \qquad (2.9)$$

represents the flow of thermal energy. Of course, even higher order moments can be formed, but those are less important.

#### 2.1.2. Linear Waves

The dispersion relation of the Vlasov-Maxwell system is derived by manipulating Maxwell's equations (2.3),

$$c^{2} \frac{\partial}{\partial t} (\nabla \times \mathbf{B}) = \frac{\partial}{\partial t} \left( \epsilon_{0} \mathbf{J} + \frac{\partial \mathbf{E}}{\partial t} \right).$$

$$\Leftrightarrow -c^{2} \nabla \times (\nabla \times \mathbf{E}) = \frac{\partial}{\partial t^{2}} \left( \epsilon_{0} \int_{t_{0}}^{t} dt' \underline{\sigma} + \mathbf{1} \right) \cdot \mathbf{E}, \tag{2.10}$$

where **1** is the unit tensor and J depends linearly on E with the proportionality factors encoded in the conductivity tensor  $\underline{\sigma}$ ,  $J = \underline{\sigma}E$ . Just like J is the sum of the current of each species  $J_s$ , the total conductivity is just the sum of conductivities of each species,  $\underline{\sigma} = \sum_s \underline{\sigma}_s$ . To further shorten the notation, we use the susceptibility tensor  $\chi = \underline{\sigma}/\mathrm{i}\omega\epsilon_0$ , as it absorbs the prefactors.

We make an ansatz for a plane-parallel, homogeneous wave by varying each quantity U as

$$U = A_U \exp\left[i(-\mathbf{k} \cdot \mathbf{x} + \omega t + \varphi_U)\right]$$
 (2.11)

with some quantity specific amplitude  $A_U$  and phase  $\varphi_U$ . The wave vector k and wave frequency  $\omega$  are common to each quantity. With this ansatz, we further reformulate equation (2.10)

$$c^{2}\mathbf{k} \times (\mathbf{k} \times \mathbf{E}) = -\omega^{2} \left( \mathbf{1} + \underline{\chi} \right) \cdot \mathbf{E}$$

$$\Leftrightarrow \left[ \mathbf{k}\mathbf{k} - k^{2}\mathbf{1} + \frac{\omega^{2}}{c^{2}} \underline{\epsilon} \right] \cdot \mathbf{E} = \mathbf{0}$$
(2.12)

The dielectricity tensor

$$\underline{\epsilon} = \mathbf{1} + \underline{\chi} = \mathbf{1} + \frac{\underline{\sigma}}{\mathrm{i}\omega\epsilon_0} \tag{2.13}$$

has been introduced in the last step.  $\epsilon$ ,  $\chi$  and  $\sigma$  are determined by the Vlasov equation, as we will discuss shortly. The linear waves supported by the Vlasov-Maxwell system of equations are simply those, for which the determinant of the tensor in equation (2.12) vanishes for a given  $\omega$  and k.

For waves propagating parallel to the magnetic field  $\mathbf{B}$ , it is useful to split the dielectricity tensor in two parts: a two-dimensional transverse part (T) and a one-dimensional longitudinal part (L). The transverse part describes the response in the plane perpendicular to  $\mathbf{B}$ , while the longitudinal part describes the response along  $\mathbf{B}$ . The dispersion relation for these wave types

are then given by

Transverse waves: 
$$\det \left\{ -k^2 \mathbf{1} + \frac{\omega^2}{c^2} \left( \mathbf{1} + \sum_s \underline{\chi}_{s,T} \right) \right\} = \mathbf{0},$$
 (2.14)

Longitudinal waves: 
$$\frac{\omega^2}{c^2} \left( 1 + \sum_s \chi_{s,L} \right) = 0.$$
 (2.15)

(2.16)

The exact analytical derivation of all possible linear waves is not feasible in the kinetic picture. Instead, numerical dispersion relation solvers are employed, such as WHAMP (Roennmark, 1982), ALPS (Verscharen et al., 2018) or Bo (Xie, 2019).

Equations (2.14) and (2.15) are useful, because they are general solutions extending beyond kinetic plasma physics.  $\chi_s$  can also be a susceptibility tensor of a fluid or MHD species, which we will introduce later. It also correctly predicts the electromagnetic waves in absence of any plasma species, given by setting  $\chi = \mathbf{0}$ . This yields the dispersion relation  $\omega = \pm ck$  for transverse waves, corresponding to light waves in vacuum.

## Kinetic Contributions to the Conductivity

We search for the linear susceptibility tensor by using the Vlasov equation (2.3), where we are concerned with a small perturbation around a constant ground state,  $f(\mathbf{x}, \mathbf{v}, t) \to f_0(\mathbf{v}) + f_1(\mathbf{x}, \mathbf{v}, t)$ , which generates a current perturbation  $\mathbf{J} \to \mathbf{J}_1$  and electric perturbation  $\mathbf{E}_1$ . We assume a background magnetic field,  $\mathbf{B} \to \mathbf{B}_0 + \mathbf{B}_1$ .

The Vlasov equation for these perturbations yields to first order

$$\underbrace{\left(\partial_t + \boldsymbol{v} \cdot \boldsymbol{\nabla} + \frac{q_s}{m_s} \boldsymbol{v} \times \boldsymbol{B}_0 \cdot \boldsymbol{\nabla}_{\boldsymbol{u}}\right)}_{-f} f_1 = -\frac{q_s}{m_s} \left[\boldsymbol{E}_1 + \boldsymbol{v} \times \boldsymbol{B}_1\right] \cdot \boldsymbol{\nabla}_{\boldsymbol{u}} f_0. \tag{2.17}$$

Solving for  $f_1$  and substituting it into the definition of the current,  $J_1 = q_s \int v f_1 d^3 u$ , yields

$$\boldsymbol{J}_{1} = \frac{q_{s}^{2}}{m_{s}} \int \boldsymbol{v} \mathcal{L}^{-1} \left[ \boldsymbol{E}_{1} + \boldsymbol{v} \times \boldsymbol{B}_{1} \right] \cdot \frac{\partial f_{0}}{\partial \boldsymbol{u}} d^{3} \boldsymbol{u}, \tag{2.18}$$

where  $\mathcal{L}^{-1}$  is the inverse operation of  $\mathcal{L}$ . In the electrostatic case, where  $\mathbf{B} = \mathbf{0}$ , we simplify  $\mathcal{L} = \mathrm{i}(-\omega + \mathbf{v} \cdot \mathbf{k})$  using the plane wave ansatz (2.11). With these assumptions,  $\mathbf{J}_1$  is directly proportional to  $\mathbf{E}_1$ , allowing us to quickly identify  $\underline{\sigma}$  as

$$\underline{\sigma}_{s}(f_{0},\omega,k) = \frac{q_{s}^{2}}{m_{s}} \int \mathbf{v} \frac{\partial f_{0}/\partial(\mathbf{u})}{\mathrm{i}(-\omega + \mathbf{v} \cdot \mathbf{k})} \,\mathrm{d}^{3}\mathbf{u}$$
(2.19)

The conductivity tensor of the electrostatic case is not just valid for  $\mathbf{B}_0 = \mathbf{0}$ , but also accurately describes the longitudinal response along the magnetic background field  $\mathbf{B}_0$  since the corresponding wave modes are independent of magnetic perturbations.

**Resonances.** One important property of equation (2.19) is, that the denominator vanishes for

$$\omega(k) = \mathbf{v} \cdot \mathbf{k},\tag{2.20}$$

where  $\omega(k)$  is a solution of the dispersion relation (2.15). The plasma quickly develops a density current in response to the applied electric field, or it is said to be in *resonance*. This specific resonance is called the Landau resonance. For transverse waves, cyclotron resonances of the form

$$\omega(k) = \mathbf{v}_{\parallel} \cdot \mathbf{k} \pm n\Omega_{s} \tag{2.21}$$

appear, where  $\omega(k)$  is a solution of the dispersion relation (2.14), and the integer n denotes the harmonics of the gyrofrequency. The subscripts parallel and perpendicular denote the relation of the velocity components to the background magnetic field, and  $\Omega_s = q_s B_0/(\gamma m_s)$  is the cyclotron frequency. While in general, a superposition of infinitely many harmonics is considered (see, e.g. chapter 8.3 and 11.2 of Schlickeiser, 2002), we are interested in transverse waves propagating parallel to  $B_0$ . This case is of importance for CR streaming and exhibits the first harmonics of the cyclotron resonance in the linear regime. For these, the susceptibility tensor is of the form

$$\underline{\chi}_{s} = \frac{1}{2\omega^{2}} \frac{q_{s}^{2}}{\epsilon m_{s}} \int v_{\perp}^{2} \left\{ \frac{\left[ (\omega - kv_{\parallel})/v_{\perp} \right] \partial_{u_{\perp}} f_{0} + k_{\parallel} \partial_{u_{\parallel}} f_{0}}{k_{\parallel} v_{\parallel} - \omega - \Omega_{s}} \right\} d^{3}u, \tag{2.22}$$

where the term in the denominator represents the cyclotron resonance.

# 2.2. The Multi-Fluid Equations

Directly solving the Vlasov-Maxwell system can be challenging as phase-space is 6-dimensional, composed of three spatial and three velocity dimensions. The fluid approach reduces this complexity by eliminating velocity dimensions while retaining spatial dimensions. Theoretically, this can be achieved without loss of accuracy, but at the cost of an ever-expanding set of equations. Thus, additional assumptions have to be made to close the fluid hierarchy and to retrieve a solvable set of equations, which we will cover in this section. We focus on non-relativistic fluids and assume  $\gamma = 1$ .

## 2.2.1. The Moment Hierarchy

The derivation of fluid equations proceeds by taking velocity moments of the Vlasov equation, recovering equations for each of the moments presented in Section 2.1.1.

**Particle Conservation.** For the zeroth moment, we simply integrate the Vlasov equation (2.1) (i.e., we apply  $\int d^3v$ ),

$$\underbrace{\int d^3 v \frac{\partial f_s}{\partial t}}_{=\partial n_s/\partial t} + \underbrace{\int d^3 v \ \boldsymbol{v} \cdot \boldsymbol{\nabla} f_s}_{=\boldsymbol{\nabla} \cdot n_s \boldsymbol{w}_s} + \int d^3 v \ \frac{q_s}{m_s} \left( \boldsymbol{E} + \boldsymbol{v} \times \boldsymbol{B} \right) \cdot \boldsymbol{\nabla}_{\boldsymbol{v}} f_s = 0, \tag{2.23}$$

where the temporal and spatial derivatives commute with the velocity integral, allowing us to directly identify the velocity moments. This leaves the last term

$$\frac{q_s}{m_s} \int (\boldsymbol{E} + \boldsymbol{v} \times \boldsymbol{B}) \cdot \nabla_{\boldsymbol{v}} f_s \, \mathrm{d}^3 v = \frac{q_s}{m_s} \left\{ f_s (\boldsymbol{E} + \boldsymbol{v} \times \boldsymbol{B}) \Big|_{\boldsymbol{v} \to -\infty}^{\boldsymbol{v} \to +\infty} - \int f_s \nabla_{\boldsymbol{v}} \cdot (\boldsymbol{E} + \boldsymbol{v} \times \boldsymbol{B}) \, \mathrm{d}^3 v \right\} = 0, \quad (2.24)$$

which vanishes upon integration by parts, given that  $\nabla_v$  is perpendicular to  $v \times B$  and assuming that  $f_s v \to 0$  vanishes for  $|v| \to \infty$ . We retrieve

$$\frac{\partial n_s}{\partial t} + \nabla \cdot (n_s \boldsymbol{w}_s) = 0. \tag{2.25}$$

We make three observations. First, the particle number is conserved as the density  $n_s(\mathbf{x})$  at position  $\mathbf{x}$  can only change by flowing into or out of a neighboring fluid element, where strength and direction of the flow is determined by the divergence term. Second, if Poisson's equation  $\nabla \cdot \mathbf{E} = \rho/\epsilon_0$  (2.2) is fulfilled at some point in time, the continuity equation (2.25) implies that it is fulfilled at any time as

$$\sum_{s} \frac{\partial q_{s} n_{s}}{\partial t} = \frac{\partial \rho}{\partial t} = \epsilon_{0} \nabla \cdot \frac{\partial \mathbf{E}}{\partial t} = \nabla \cdot \left( -\mathbf{J} + \nabla \times \frac{\mathbf{B}}{\mu_{0}} \right) = -\nabla \cdot \mathbf{J} = -\nabla \cdot \sum_{s} q_{s} n_{s} \mathbf{w}_{s}. \tag{2.26}$$

Finally, equation (2.25) necessitates the next higher-order moment, the bulk velocity, for which we will derive another equation.

**Higher-order Moment Equations.** The momentum equation derives from the first velocity moment of the Vlasov equation (i.e., we apply  $\int \mathbf{v} \, \mathrm{d}^3 \mathbf{v}$ ). The temporal derivative terms is trivial once again and results in  $\partial n_s \mathbf{w}_s / \partial t$ , the spatial derivative is (with omitted subscript s for improved readability)

$$\nabla \cdot \int \boldsymbol{v} \boldsymbol{v} f \, \mathrm{d}^3 v = \nabla \cdot \int \left[ (\boldsymbol{v} - \boldsymbol{w})(\boldsymbol{v} - \boldsymbol{w}) + \boldsymbol{v} \boldsymbol{w} + \boldsymbol{w} \boldsymbol{v} - \boldsymbol{w} \boldsymbol{w} \right] f \, \mathrm{d}^3 v \tag{2.27}$$

$$= \nabla \cdot [\mathbf{P} + (n\mathbf{w})\mathbf{w} + \mathbf{w}(n\mathbf{w}) - (n)\mathbf{w}\mathbf{w}] = \nabla \cdot (n\mathbf{w}\mathbf{w} + \mathbf{P}). \tag{2.28}$$

The spatial derivative of a tensor in this notation acts always on its first component, that is  $\nabla \mathbf{P}|_{j} = \partial_{i} \mathbf{P}_{ij}$  in component notation (where we adopted Einstein's sum convention and sum over two identical indices). The final term is treated similarly as in equation (2.24), but we need to make a stronger assumption of  $f_{s}vv \to 0$  as  $|v| \to \infty$ . This yields

$$\frac{q_s}{m_s} \int d^3 v \boldsymbol{v} \left[ (\boldsymbol{E} + \boldsymbol{v} \times \boldsymbol{B}) \cdot \nabla_{\boldsymbol{v}} f_s \right] = \frac{q_s}{m_s} f_s \boldsymbol{v} (\boldsymbol{E} + \boldsymbol{v} \times \boldsymbol{B}) \Big|_{\boldsymbol{v} = -\infty}^{\boldsymbol{v} = +\infty} - \frac{q_s}{m_s} n_s \left( \boldsymbol{E} + \boldsymbol{w}_s \times \boldsymbol{B} \right). \tag{2.29}$$

Thus, the momentum equation is given by

$$\frac{\partial n_s \boldsymbol{w}_s}{\partial t} + \boldsymbol{\nabla} \cdot (n_s \boldsymbol{w}_s \boldsymbol{w}_s + \boldsymbol{\mathsf{P}}_s) = \frac{q_s}{m_s} n_s (\boldsymbol{E} + \boldsymbol{w}_s \times \boldsymbol{B}). \tag{2.30}$$

The pressure tensor evolution equation can be derived similarly, necessitating an even stronger

assumption of  $f_s vvv \to \mathbf{0}$  as  $|v| \to \infty$ . We omit the derivation and continue to give the resulting equation, where superscript T denotes the transpose (Hunana et al., 2019a)

$$\frac{\partial \mathbf{P}_{s}}{\partial t} + \nabla \cdot (\mathbf{w}_{s} \mathbf{P}_{s} + \mathbf{Q}_{s}) + (\mathbf{P}_{s} \cdot \nabla) \mathbf{w}_{s} + [(\mathbf{P}_{s} \cdot \nabla) \mathbf{w}_{s}]^{\mathrm{T}} = -\frac{q_{s}}{m_{s}} [\mathbf{B} \times \mathbf{P}_{s} - \mathbf{P}_{s} \times \mathbf{B}]. \tag{2.31}$$

The cross product of a vector with a tensor is defined as  $(\mathbf{B} \times \mathbf{P})_{ij} = \epsilon_{ilm} B_l P_{mj}$  in index-notation using the Levi-Civita symbol  $\epsilon_{ilm}$ . We denote the tensor product by  $\mathbf{wP}$ , which results in  $[\nabla \cdot (\mathbf{wP})]_{ij} = \partial_k (w_k P_{ij})$ .

The heat flux tensor can also be self-consistently evolved by finding a new set of equations of even higher orders, but the ever-increasing complexity of the higher-order moment equations urges one to apply appropriate approximations. The highest-order moment can be approximated using only lower-order moments, which allows to close the system of equations. Because of this property, the approximation is usually referred to as a *closure*. In the following, we provide some common closures and discuss their applicability.

#### 2.2.2. Adiabatic Closures

 ${\bf Q}$  is a moment of f, see equation (2.9). More specifically,  ${\bf Q}$  describes the skewness of f. Assuming that f is fully symmetric around its mean, its skewness would vanish and thus  ${\bf Q} = {\bf 0}$ . Conversely, if we start with the assumption  ${\bf Q} = {\bf 0}$ , we imply a vanishing skewness of the distribution function. By doing so, we cut off the fluid equation hierarchy and ignore higher-order contributions, which implicitly sets all higher-order moments to  ${\bf 0}$  as well. Therefore, in such a case, the distribution function is not only without any skewness, but it should also be without any kurtosis (or non-Gaussian tail). This is fulfilled by the Maxwell-Boltzmann distribution, which is well modeled in the fluid picture. As the Maxwell-Boltzmann distribution is an equilibrium distribution for gases undergoing elastic collisions, the fluid equations are particularly useful to model collisional species.

Setting the heat flux  $\mathbf{Q} = \mathbf{0}$  enforces the adiabatic assumption, implying that compression and expansion of the gas are reversible processes. Even with this closure,  $\mathbf{P}$  initially has six degrees of freedom – as it is a symmetric tensor by definition – which can be further reduced by taking physical symmetries into account. We can decompose the tensor along the magnetic unit vector  $\hat{\boldsymbol{b}} = \boldsymbol{B}/B$  via  $\mathbf{P} = p_{\parallel}\hat{\boldsymbol{b}}\hat{\boldsymbol{b}} + p_{\perp}(\mathbf{1} - \hat{\boldsymbol{b}}\hat{\boldsymbol{b}}) + \mathbf{\Pi}$ . The stress tensor  $\mathbf{\Pi}$  is often neglected,  $\mathbf{\Pi} = \mathbf{0}$ , which leads to the double adiabatic description of a plasma with just two degrees of freedom (Oraevskii et al., 1968; Passot and Sulem, 2004).

$$\frac{\partial p_{\parallel}}{\partial t} + \nabla \cdot (p_{\parallel} \boldsymbol{w}) + (\Gamma_{\parallel} - 1) p_{\parallel} \hat{\boldsymbol{b}} \cdot \nabla \boldsymbol{w} \cdot \hat{\boldsymbol{b}} = 0$$
(2.32)

$$\frac{\partial p_{\perp}}{\partial t} + \nabla \cdot (p_{\perp} \boldsymbol{w}) + (\Gamma_{\perp} - 1) \left( -p_{\perp} \hat{\boldsymbol{b}} \cdot \nabla \boldsymbol{w} \cdot \hat{\boldsymbol{b}} + p_{\perp} \nabla \cdot \boldsymbol{w} \right) = 0$$
 (2.33)

The adiabatic index  $\Gamma$  is closely linked to the degrees of freedom of the (decomposed parts of the) pressure tensor,  $2p/(\Gamma-1) = \text{Tr } \mathbf{P}$ . For a fully isotropic tensor we have three degrees of freedom (Tr  $\mathbf{P} = 3p$ ) and thus  $\Gamma = 5/3$ , while the perpendicular pressure component has Tr  $\mathbf{P}_{\perp} = 2p_{\perp}$ 

corresponding to  $\Gamma_{\perp} = 2$ , and the parallel component has one degree of freedom, corresponding to  $\Gamma_{\parallel} = 3$ . The isotropic pressure equation follows as

$$\frac{\partial(p_{\parallel} + 2p_{\perp})}{\partial t} = \frac{\partial p}{\partial t} = -\left[\nabla \cdot (p\boldsymbol{w}) + (\Gamma - 1)p\nabla \cdot \boldsymbol{w}\right]. \tag{2.34}$$

The set of fluid equations with the adiabatic closure fulfills the adiabatic equation of state  $d(pn^{-\Gamma})/dt = 0$ . It is also useful to express the pressure evolution equation (2.34) as the energy evolution equation. We define the fluid energy density as the sum of the inner and kinetic energy density of the fluid,  $\epsilon = (\text{Tr } \mathbf{P} + n\mathbf{w}^2)/2 = p/(\Gamma - 1) + n\mathbf{w}^2/2$ , and obtain

$$\frac{\partial \epsilon}{\partial t} + \nabla \cdot [(p + \epsilon)w] = \frac{qn}{m}w \cdot E. \tag{2.35}$$

Here, the total fluid energy is conserved except for the case of an increase in kinetic energy through acceleration by the electric field. This formulation is useful because its conservative properties can be fulfilled numerically up to machine precision; the numerical solution of the non-conservative pressure equation tends to violate the energy conservation and can lead to numerical instabilities. We will get back to this point when discussing numerical algorithms in Section 3.3.2.

The adiabatic closure also has significant drawbacks, as many kinetic effects, like Landau damping or cyclotron damping, are completely lost. These irreversible effects introduce a perturbation in the heat flux, which has to be modeled using more appropriate closures.

## 2.2.3. Landau Closures

Landau closures for fluid models aim to capture Landau damping effects within the fluid framework. We present the general idea of deriving such closures, roughly following the ideas of the original paper by Hammett and Perkins (1990), while a more systematic approach is given by Hunana et al. (2019b). We examine the one-dimensional case along a magnetic field line, focusing on longitudinal wave modes that are subject to Landau damping. An extension to three dimensions is performed by Snyder et al. (1997), which has been further extended to include non-gyrotropic contributions by Passot and Sulem (2007). Jikei and Amano (2021) developed collisionless closures for cyclotron damping affecting transverse waves by using a similar derivation.

The derivation centers on determining the fluid species' conductivity tensors with variable closure coefficients, which are then matched to the Maxwellian conductivity tensor (even though other distributions are also possible).

**Fluid Conductivity.** Following the kinetic approach in Section 2.1.2, we introduce perturbations  $n_s \to n_0 + n_1$ ,  $w_s \to w_1$ , and  $p_s \to p_0 + p_1$ , employ the plane wave ansatz (2.11), and identify the fluid conductivities  $\sigma_s$  from  $J_s = q_s n_0 w_1 = \sigma \cdot E$ . We propose a scalar heat flux closure

 $q_1 = a_n n_1 + a_p p_1 + a_w w_1$  with variable coefficients a, yielding:

$$\frac{\partial n}{\partial t} = -\frac{\partial nw}{\partial x} \Rightarrow n_1 = \frac{k}{\omega} w_1 n_0, \tag{2.36}$$

$$\frac{\partial p}{\partial t} = -\Gamma p \frac{\partial w}{\partial x} - w \frac{\partial p}{\partial x} - \frac{\partial q}{\partial x} \Rightarrow p_1 = \frac{1}{\omega/k - a_p} \left( \Gamma p_0 + a_w w_1 + a_n n_1 \right), \tag{2.37}$$

$$q_s \frac{\partial nw}{\partial t} + q_s \frac{\partial (p + nww)}{\partial x} = \frac{q_s^2 n}{m_s} E$$

$$\Rightarrow w_1 q_s i \left[ \omega n_0 - \frac{k}{\omega/k - a_p} \left( \Gamma p_0 + a_w + a_n \frac{k}{\omega} n_0 \right) \right] = \frac{q_s^2 n_0}{m_s} E_1.$$
 (2.38)

Before deriving the conductivity tensor  $\underline{\sigma}$ , we establish the fundamental parameters and normalizations. The plasma frequency is defined as  $\omega_s^2 = q_s^2 n_0/m_s \epsilon_0$ , with background pressure  $p_0 = n_0(v_{\rm th}^2/2)$ . The system's characteristic velocity is the thermal velocity  $v_{\rm th}$  aligned with the wave vector direction, given by  $\mathrm{sgn}(k)v_{\rm th}$ . This characteristic velocity enables the introduction of dimensionless coefficients  $b_U$ , which relate to the closure variables  $a_U$  through  $a_p = b_p \, \mathrm{sgn}(k)v_{\rm th}$ ,  $a_n = b_n \, \mathrm{sgn}(k)v_{\rm th}p_0/n_0$  and  $a_w = b_w p_0$  We further normalize the wave phase velocity  $v_{\rm wave} = \omega/k$  using the dimensionless parameter  $\zeta = v_{\rm wave}/(\mathrm{sgn}(k)v_{\rm th}) = \omega/(|k|v_{\rm th})$ . With these normalizations, we rearrange equation (2.38) into the form  $J_s = q_s n_0 w_1 = \underline{\sigma} \cdot E$  to obtain the conductivity tensor

$$(\underline{\sigma}_s)_{\text{Landau fluid}} = 2i \frac{\epsilon_0 \omega_s^2 \zeta}{|k| v_{\text{th}}} \frac{-b_p - \zeta}{b_n + \zeta (b_w + \Gamma) + 2b_p \zeta^2 - 2\zeta^3}.$$
 (2.39)

Comparison to Kinetic Conductivity. The next step requires matching the fluid coefficients  $b_U$  to their kinetic counterparts. For the kinetic description, we model  $f_0$  as a Maxwell-Boltzmann distribution  $f_0(v) = n_0 \exp\left(-v^2/v_{\rm th}^2\right)/(\sqrt{\pi}v_{\rm th})$ , which is well approximated by fluids for the reasons outlined beforehand. With this distribution, the kinetic conductivity tensor from equation (2.19) takes the form

$$(\sigma_s)_{\text{MB}} = \frac{q_s}{m_s i} n_0 \int v \frac{\partial e^{-(v/v_{\text{th}})^2}}{\partial v} \frac{1}{\sqrt{\pi} v_{\text{th}} (-\omega + vk)} dv = [v/v_{\text{th}} \to x]$$

$$= \frac{\epsilon_0 \omega_s^2}{i v_{\text{th}}} \int \frac{-2x^2}{\sqrt{\pi} k} \frac{e^{-x^2}}{x - \omega/(k v_{\text{th}})} dx = 2i \frac{\epsilon_0 \omega_s^2}{|k| v_{\text{th}}} \zeta R(\zeta).$$
(2.40)

The integral can be expressed through the plasma response function  $R(\zeta) = 1 + \zeta i \sqrt{\pi} \exp(-\zeta^2)(1 + \text{erf}(i\zeta))$ , where erf denotes the error function (Fried and Conte, 1961). To determine appropriate closure coefficients, we match the fluid conductivity tensor (2.39) to its kinetic counterpart (2.40), requiring  $\sigma_{\text{MB}} \approx \sigma_{\text{Landau fluid}}$ . Of particular interest is the hot, collisionless limit ( $\zeta \to 0$ ), where

we can compare the Taylor series expansions:

$$R(\zeta) \approx \frac{-b_p - \zeta}{b_n + \zeta(b_w + \Gamma) + 2b_p \zeta^2 - 2\zeta^3}$$

$$\stackrel{\zeta \to 0}{\Rightarrow} 1 + i\sqrt{\pi}\zeta - 2\zeta^2 - i\sqrt{\pi}\zeta^3 + O(\zeta^4) \approx -\frac{b_p}{b_n} + \frac{b_n + b_p b_w + b_p \Gamma}{b_n^2} \zeta$$

$$+ \left[ \frac{-b_w - \Gamma}{b_n^2} - \frac{b_p \left( -2b_n b_p + b_w^2 + 2b_w \Gamma + \Gamma^2 \right)}{b_n^3} \right] \zeta^2 + O(\zeta^3).$$
(2.41)

The Landau fluid model achieves second-order accuracy in  $\zeta$  with the coefficients  $b_n = -b_p = -i\sqrt{\pi}/(\pi-4)$  and  $b_w = 4/(\pi-4) - \Gamma = (8-3\pi)/(\pi-4)$  (for  $\Gamma = 3$ ) (Hunana et al., 2018). For applications where first-order accuracy suffices, Hammett and Perkins (1990) provided a simpler set of coefficients,  $b_n = -b_p = -i(1-\Gamma)/\sqrt{\pi} = i2/\sqrt{\pi}$  and  $b_w = 0$ .

**Physical Meaning.** Both, first and second-order closures, share the relation  $b_n = -b_p$ , yielding a heat flux proportional to the perturbed temperature  $T_1$ 

$$q_1 \sim i \operatorname{sgn}(k) v_{\text{th}} n_0 \frac{k_{\text{B}} T_1}{m_s}, \tag{2.42}$$

where 
$$T_1 = \frac{m_s p_1 - k_B T_0 n_1}{n_0}$$
, (2.43)

and 
$$\frac{k_{\rm B}T_0}{m_s} = \frac{v_{\rm th}^2}{2} = \frac{p_0}{n_0}$$
. (2.44)

The most significant feature is the non-local relationship between heat flux and temperature perturbations, evidenced by the  $i \operatorname{sgn}(k)$  term. This indicates that the maximum heat flux occurs at different spatial locations in comparison to the maximum temperature perturbations. This non-locality emerges from the free streaming of collisionless particles along magnetic field lines, where damping processes occur through spatially coherent waves. This non-locality is challenging to efficiently implement in numerical realizations as will be discussed later in Section 4.2.6.

A limitation of Landau closures lies in their inability to capture the flattening of the velocity distribution function around the resonance. In kinetic theory, the wave-particle resonance leads to selective particle acceleration  $(v_{\parallel} < v_{\rm wave})$  and deceleration  $(v_{\parallel} > v_{\rm wave})$ . If more particles are slower than the wave, the particles gain on average energy over time and give rise to Landau damping. Large-amplitude waves can flatten the distribution function near the resonance over time, thereby saturating the damping effect. By contrast, Landau fluid models maintain exponential damping of longitudinal waves until the wave energy is fully converted to thermal energy.

Finally, we compare the Landau closures with the adiabatic closures (of an ideal fluid), where  $q_1=0$  and thus

$$(\sigma_s)_{\text{ideal fluid}} = 2i \frac{\epsilon_0 \omega_s^2 \omega}{k^2 v_{\text{th}}^2} \frac{2}{\Gamma - 2\zeta^2}.$$
 (2.45)

This conductivity tensor is purely imaginary for all real values of  $\zeta$ , which precludes any damping

effects while the plasma is at rest. However, in the limit of a cold plasma or for large wave velocities, i.e.,  $\zeta \to \infty$ , all models converge.

#### 2.2.4. Linear Waves

## Longitudinal Waves (ideal fluid)

For the longitudinal waves, we will only derive equations for the adiabatic closure, as the Landau fluids yield more complicated expressions. We substitute equation (2.45) and insert it into the dispersion relation (2.15). For a two-fluid plasma with immobile ions, the dispersion relation yields

$$\omega^2 = \omega_e^2 + c_{s,e}^2 k^2, \tag{2.46}$$

where the electron sound speed is  $c_{s,e}^2 = \Gamma v_{\mathrm{th},e}^2/2$ . For an electron-ion fluid, two longitudinal wave modes emerge

$$\omega^{2} = \omega_{p}^{2} + c_{s}^{2}k^{2} \pm \sqrt{\left(\omega_{p}^{2} + c_{s}^{2}k^{2}\right)^{2} - 4k^{2}\left(c_{s,e}^{2}c_{s,i}^{2}k^{2} + c_{s,i}^{2}\omega_{e}^{2} + c_{s,e}^{2}\omega_{i}^{2}\right)},\tag{2.47}$$

where the total sound speed is  $c_s^2 = c_{s,e}^2 + c_{s,i}^2$ . These acoustic waves, which experience Landau damping in kinetic theory, exhibit different behaviors in fluid models. In Landau fluid models, the dispersion relation includes an imaginary component  $\text{Im}(\omega) < 0$ , causing wave damping over time.

In the case of CR streaming, the primary interest lies not in direct Landau damping of longitudinal waves because CRs interact with transverse waves. Transverse waves generate these longitudinal modes via wave-wave interactions. The longitudinal modes then experience damping in the Landau fluid model, leading to indirect damping of the transverse waves, which is called non-linear Landau damping. By contrast, the ideal fluid model preserves these longitudinal waves without damping, which results in their saturation and which terminates the transverse wave energy transfer.

#### **Transverse Waves**

We turn our attention to transverse modes with  $p_1 = 0$  and  $n_1 = 0$ . We set  $\mathbf{B}_0 = B_0 \hat{\mathbf{e}}_x$  along the x-axis,  $E_x = 0$  and linearly perturb the remaining quantities to find two equations for the transverse velocity,

$$i\omega v_y = \frac{q}{m}(E_y + v_z B_0), \qquad i\omega v_z = \frac{q}{m}(E_z - v_y B_0)$$
 (2.48)

$$i\omega v_{y} = \frac{q}{m}(E_{y} + v_{z}B_{0}), \qquad i\omega v_{z} = \frac{q}{m}(E_{z} - v_{y}B_{0})$$

$$\Rightarrow J_{y} = q_{s}n_{0}v_{y} = \epsilon_{0}\omega_{s}^{2} \frac{-i\omega E_{y} - \Omega_{s}E_{z}}{\omega^{2} - \Omega_{s}^{2}}, \qquad J_{z} = q_{s}n_{0}v_{z} = \epsilon_{0}\omega_{s}^{2} \frac{-i\omega E_{z} + \Omega_{s}E_{y}}{\omega^{2} - \Omega_{s}^{2}}.$$

$$(2.48)$$

From these equations the conductivity tensor is readily identified with its (anti-)symmetries  $\sigma_{yz} = -\sigma_{zy}$  and  $\sigma_{zz} = \sigma_{yy}$ . These symmetries carry over to the dielectricity tensor  $\epsilon = \sigma/(i\omega\epsilon_0)$ and help to solve the dispersion relation (2.14) for the transverse wave modes. If we split the dielectricity tensor as  $1 + \epsilon_{yy} = (P_+ + P_-)/2$  and  $\epsilon_{yz} = (P_+ - P_-)/2$ , the dispersion relation splits

into a left-hand and right-hand polarized solution as

$$\left(\frac{c^2k^2}{\omega^2} - P_+\right) \left(\frac{c^2k^2}{\omega^2} - P_-\right) = 0$$

$$\Leftrightarrow \left(\frac{c^2k^2}{\omega^2} - P_+\right) = 0 \quad \text{or} \quad \left(\frac{c^2k^2}{\omega^2} - P_-\right) = 0,$$
(2.50)

where 
$$P_{\pm} = 1 - \sum_{s} \frac{\omega_s^2}{\omega(\omega \pm \Omega_s)}$$
. (2.51)

This dispersion relation is important, as its solutions enter into the resonance condition (2.14). Among the solutions for  $\omega(k)$ , we can quickly identify modified light waves  $\omega^2 = c^2 k^2 + \omega_p^2$  for  $|\omega| \gg \max_s |\Omega|_s$ , where the plasma frequency  $\omega_p = \sum_s \omega_s$ . Their phase velocity  $\omega/k$  is larger than c so that they cannot resonate with particles.

Thus, we turn our attention to waves with  $|\omega| \leq \max_s |\Omega|_s$ , as these potentially allow for cyclotron resonances. At very small scales, corresponding to  $k \to \infty$ , waves correspond to the individual particle rotations,  $\omega = \Omega_s$ , with phase velocities of 0. In the low frequency limit,  $\omega^2 \ll \max_s \Omega_s^2$ , we find

$$P_{\pm} - 1 = -\sum_{s} \frac{\omega_s^2(\omega \mp \Omega_s)}{\omega(\omega^2 - \Omega_s^2)} = +\sum_{s} \frac{\omega_s^2(\omega \mp \Omega_s)}{\omega\Omega_s^2} = \sum_{s} \left[ \frac{m_s n_s}{\epsilon_0 B_0^2} \mp \frac{q_s n_s}{\epsilon_0 \omega B_0} \right]. \tag{2.52}$$

Under the assumption of quasi-neutrality,  $\sum_s q_s n_s = 0$ , we identify the Alfvén velocity of a multi-species plasma as

$$v_{\rm A} = \frac{B_0}{\sqrt{\mu_0 \sum_s m_s n_s}},\tag{2.53}$$

The wave frequency is

$$\omega^2 = k^2 \frac{v_{\rm A}^2}{1 + v_{\rm A}^2/c^2},\tag{2.54}$$

which is valid for large scale waves  $k \to 0$ . Only in the limit of non-relativistic Alfvén velocities, the wave (phase) velocity  $v_{\text{wave}}$  converges to  $v_{\text{A}}$ :

$$v_{\text{wave}} = \frac{\omega}{k} = \frac{v_{\text{A}}}{\sqrt{1 + v_{\text{A}}^2/c^2}}.$$
 (2.55)

To estimate the waves between the shortest and largest scales, we need to know about the composition of plasma. One important wave mode are the whistler waves, which we obtain from  $P_+$  for wave lengths smaller than the ion skin depth,  $k \gg d_i = c/\omega_i$ :

$$\omega(k) = \Omega_e \frac{k^2 d_e^2}{2\left(1 + k^2 d_e^2\right)} \left(\sqrt{1 + \frac{4}{k^2 d_i^2}} + 1\right). \tag{2.56}$$

At spatial scales smaller than the electron skin depth  $(kd_e > 1)$ , the wave characteristics transition to electron-cyclotron waves that asymptotically approach  $\Omega_e$  as  $k \to \infty$ .

Instead of finding another solution for  $P_{-}$ , we use the symmetry relation  $P_{+}(\omega) = P_{-}(-\omega)$ .

The choice between solving  $P_+$  or  $P_-$  remains arbitrary, provided that we are clear about the convention that is implied, i.e., whether  $\omega > 0$  is right- or left-hand polarized. Under the  $P_-$  convention, electron-cyclotron waves converge towards  $-\Omega_e$  as  $k \to \infty$ ; it is common to refer to waves co-rotating with the electrons as right-hand polarized ( $P_+$  with  $\omega < 0$ ,  $P_-$  with  $\omega > 0$ ), while waves co-rotating with the ions are left-hand polarized.

# 2.3. Quasi-neutral fluids and MHD

The multi-fluid and Vlasov equations can incorporate multiple particle species, but practical applications typically focus on electron-ion plasmas. We can significantly simplify these equations by invoking the quasi-neutral and inertialess electron assumptions, eliminating the fast electron timescale  $(\omega_e^{-1} \ll \omega_i^{-1})$  from the system of equations. This simplification allows numerical simulations to use larger time steps governed by ion dynamics rather than electron motion, substantially improving computational efficiency. Here, we give an overview of the quasi-neutral two-fluid system.

## 2.3.1. Derivation of Generalized Ohm's Law

The derivation of Ohm's law begins with the fluid momentum equations (2.30) for electrons and ions:

$$m_e \left( \frac{\partial n_e \mathbf{w}_e}{\partial t} + \nabla \cdot n_e \mathbf{w}_e \mathbf{w}_e + \nabla \cdot \mathbf{P}_e \right) = q_e n_e (\mathbf{E} + \mathbf{w}_e \times \mathbf{B}), \tag{2.57}$$

$$m_i \left( \frac{\partial n_i \boldsymbol{w}_i}{\partial t} + \boldsymbol{\nabla} \cdot n_i \boldsymbol{w}_i \boldsymbol{w}_i + \boldsymbol{\nabla} \cdot \boldsymbol{P}_i \right) = q_i n_i (\boldsymbol{E} + \boldsymbol{w}_i \times \boldsymbol{B}). \tag{2.58}$$

Using the assumption of quasi-neutrality,  $n_i = n_e = n$  with  $q_i = -q_e$ , we define the current density,  $\mathbf{J} = q_i n(\mathbf{w}_i - \mathbf{w}_e)$ , and the center-of-mass bulk velocity,  $\mathbf{w} = (m_i \mathbf{w}_i + m_e \mathbf{w}_e)/m_t$  with the total mass  $m_t = m_i + m_e$ .

Thus, the bulk velocities of the different species is expressed in terms of J and w:

$$w_i = w + \frac{m_e}{m_i + m_e} \frac{J}{q_i n}$$
  $w_e = w - \frac{m_i}{m_i + m_e} \frac{J}{q_i n}$ . (2.59)

Next, we replace the electron momentum equation (2.57) with a simpler equation. The generalized Ohm's law emerges as a result of subtracting the electron momentum equation (multiplied by  $m_i$ ) from the ion momentum equation (multiplied by  $m_e$ ). Using  $m_i \gg m_e$  and assuming approximate isothermality,  $m_i \mathbf{P}_i \approx m_e \mathbf{P}_e$  and thus  $\mathbf{P}_i \ll \mathbf{P}_e$ , we obtain:

$$\boldsymbol{E} + \boldsymbol{w} \times \boldsymbol{B} = \frac{\boldsymbol{J} \times \boldsymbol{B}}{q_i n} - \frac{m_e \nabla \cdot \mathbf{P}_e}{q_i n} + \frac{m_e}{n q_i^2} \left[ \frac{\partial \boldsymbol{J}}{\partial t} + \nabla \cdot (\boldsymbol{J} \boldsymbol{w} + \boldsymbol{w} \boldsymbol{J}) \right] + \eta \boldsymbol{J}, \tag{2.60}$$

We have also introduced a resistive term  $\eta J$  to phenomenologically account for collisions, which has been absent in our previous treatment. The resistive term, and sometimes even hyperresistive terms, are often needed to stabilize numerical methods, which is why we include them

here. The terms on the right-hand side of equation (2.60) can be interpreted as follows (from left to right): the Hall electric field, the thermoelectric effect from the electron pressure gradient, the electron inertia and the collisional resistivity. The left-hand side represents the effective electric field experienced by a fluid element moving with velocity w.

## 2.3.2. Simplifying Generalized Ohm's Law

The generalized Ohm's law without additional approximations is not very practical, as it retains the electron time scales. We proceed with two additional assumptions. First, we neglect displacement currents by assuming  $\partial E/\partial t \ll J$  in Maxwell's equations (2.3), yielding  $J = \nabla \times B/\mu_0$ . Second, we consider electrons to have a vanishingly small inertia so that we can set  $m_e \partial J/\partial t = 0$  in the generalized Ohm's law (2.60). Even though any physical species without inertia would be massless, this model retains other effects that result from the electron mass, such as the pressure, so that we prefer to speak of a fluid without inertia. Using these assumptions, Ohm's Law simplifies to

$$\boldsymbol{E} + \boldsymbol{w} \times \boldsymbol{B} = \frac{(\nabla \times \boldsymbol{B}) \times \boldsymbol{B}}{\mu_0 q_i n} - \frac{m_e \nabla \cdot \mathbf{P}_e}{q_i n} + \frac{\eta}{\mu_0} \nabla \times \boldsymbol{B}. \tag{2.61}$$

This simplified form fundamentally changes the nature of the equations: both E and J become derived quantities rather than independent variables with their own evolution equations. These simplifications significantly impact the linear waves supported by the system.

For transverse waves, the removal of  $\frac{\partial E}{\partial t}$  eliminates the  $\mathbf{1}\omega^2/c^2$  term from equation (2.14), reducing it to

$$\det\{k^2\mathbf{1} + \omega^2\chi/c^2\} = 0. \tag{2.62}$$

This modification excludes light waves  $(\omega^2/k^2 = c^2)$  from the solution, effectively removing the fastest time scale from the system. For longitudinal waves the equation (2.15) keeps the  $\omega^2/c^2$  term. However, the assumption of a vanishing electron inertia eliminates Langmuir waves while the ion-acoustic waves, which are coupled with the thermo-electric effect, remain in the system.

## 2.3.3. The MHD Approximation

The MHD model unifies the electron and ion fluids from the quasi-neutral two-fluid description into a single fluid. Ohm's law was retrieved by subtracting the momentum equation for the electrons' (2.57) from the ions' (2.58), but we can also add them together, which yields

$$m_t \left( \frac{\partial n\boldsymbol{w}}{\partial t} + \boldsymbol{\nabla} \cdot n\boldsymbol{w}\boldsymbol{w} + \boldsymbol{\nabla} \cdot \boldsymbol{P}_t \right) = \boldsymbol{J} \times \boldsymbol{B}, \tag{2.63}$$

where  $m_t \mathbf{P}_t = m_e \mathbf{P}_e + m_i \mathbf{P}_i$  defines the total pressure. Similarly, the mass density conservation equation is obtained by summing the ion to the electron contributions ( $m_s$  times equation 2.25)

$$\frac{\partial \rho_m}{\partial t} + \nabla \cdot n \boldsymbol{w} = 0, \tag{2.64}$$

where the mass density is given by  $\rho_m = m_i n_i + m_e n_e$ . Similarly as before, one can also derive an equation for the conservation of the electrical charges by subtracting the electron contributions from the ion contributions, but the charge density vanishes anyway due to the assumed quasineutrality.

Using the adiabatic assumption for the energy evolution equation (2.35), we can proceed just as before in the case of the zeroth- and first-moment equations by adding the ion and electron contributions

$$\frac{\partial \epsilon_m}{\partial t} + \nabla \cdot [(\epsilon_m + m_t p) \, \boldsymbol{w}] = 0, \tag{2.65}$$

where  $\epsilon_m = m_i \epsilon_i + m_e \epsilon_e$  and the scalar pressure, p, is defined as before. The conservation of magnetic energy follows from the electron-ion difference

$$0 = \mathbf{J} \cdot \mathbf{E} = \frac{1}{\mu_0} (\nabla \times \mathbf{B}) \cdot \mathbf{E} = \frac{1}{\mu_0} [\mathbf{B} \cdot (\nabla \times \mathbf{E}) - \nabla \cdot (\mathbf{E} \times \mathbf{B})]$$

$$\Leftrightarrow 0 = \frac{1}{\mu_0} \left[ \frac{\partial B^2/2}{\partial t} + \nabla \cdot (\mathbf{E} \times \mathbf{B}) \right], \tag{2.66}$$

using Faraday's law

$$\frac{\partial \mathbf{B}}{\partial t} = -\nabla \times \mathbf{E} \tag{2.67}$$

in the last step (as given by Maxwell's equations 2.3). The equations (2.63)–(2.65) and equation (2.67) are the MHD evolution equations, which are supplemented with Ohm's law (2.61) and the constraint equation  $\nabla \cdot \boldsymbol{B} = 0$ . Instead of solving the fluid energy equation (2.65) by itself, it is often combined with the magnetic energy equation (2.66) through addition, thereby resulting in the evolution equation of the total energy. Different variants of MHD exist, which differ in accuracy based on the term modeled in Ohm's law. The least accurate model is ideal MHD, which simplifies Ohm's law to  $\boldsymbol{E} = -\boldsymbol{w} \times \boldsymbol{B}$ . The model of resistive MHD keeps the resistivity term, while Hall-MHD includes the Hall term. Furthermore, as the MHD equations derive from the multi-fluid equations, they may also employ different closures in order to more accurately model the pressure tensor.

We summarize the approximations for ideal MHD as follows,

- The plasma is quasi-neutral  $(q_i n_i + q_e n_e = 0)$  and the electron inertia is negligible on the scale of interest.
- The ion gyroradius and ion skin depth  $d_i = c/\omega_i$  are much smaller than the length scale of interest.
- The plasma quickly relaxes to a Maxwellian and the ion and electron temperatures are in equilibrium,  $T_i = T_e$ , for example if the collision frequency is much higher than the time scale of interest.
- Adiabatic equation of state, no viscosity, electrical resistivity and thermal conductivity (although numerical implementations introduce additional dissipative terms for stability).

Despite these significant approximations, the MHD framework successfully describes many astrophysical phenomena. The success of MHD in these diverse applications stems from the astrophysical time and length scales: most astrophysical systems operate on scales much larger than the ion gyroradius and plasma oscillation periods. This scale separation validates the fundamental MHD assumptions and explains its utility in astrophysical research.

## 2.3.4. Linear Waves in Ideal MHD

#### Transverse waves

We use the transverse dispersion relation (2.62), which neglects the displacement currents. Aside from that, we proceed as usual by determining the conductivity tensor as a result of equating J with E from a perturbation analysis. Choosing the background magnetic field  $B_0$  to be aligned with the x-axis, the transverse current density perturbation  $J_1$  lies in the (y, z)-plane. To derive its components, we take the cross product of the momentum conservation equation (2.63) with  $B_0$ . Neglecting the pressure gradient term in the longitudinal direction yields

$$(\mathbf{J} \times \mathbf{B}) \times \mathbf{B}_0 = m_t \left( \frac{\partial n\mathbf{w}}{\partial t} + \nabla \cdot n\mathbf{w}\mathbf{w} + \nabla \cdot \mathbf{P}_t \right) \times \mathbf{B}_0, \tag{2.68}$$

$$\rightarrow (\boldsymbol{J} \times \boldsymbol{B}) \times \boldsymbol{B}_0 = \boldsymbol{B} \underbrace{(\boldsymbol{J}_1 \cdot \boldsymbol{B}_0)}^{-0} - \boldsymbol{J}_1 B_0^2 = i\omega m_t n_0 (\boldsymbol{w}_1 \times \boldsymbol{B}_0) = i\omega m_t n_0 \boldsymbol{E}_1$$
 (2.69)

$$\rightarrow \sigma_{yy} = \sigma_{zz} = -i\omega \frac{m_t n}{B_0^2} = -i\omega \frac{1}{v_A^2 \mu_0}.$$
 (2.70)

We identified the Alfvén velocity as  $\mathbf{v}_{A} = \mathbf{B}_{0}/\sqrt{\mu_{0}m_{t}n}$  (cf. equation 2.53) and find the solution of the dispersion relation  $c^{2}k^{2} + \omega^{2}\sigma_{yy}/(i\omega\epsilon_{0}) = 0$ ,

$$\omega^2 = k^2 v_{\mathcal{A}}^2,\tag{2.71}$$

which is approximately the same as in the more accurate multi-fluid picture (equation 2.54). This dispersion relation significantly simplifies the multi-fluid model, as the waves are dispersionless  $(\partial \omega(k)/\partial k = \text{const.})$ .

#### **Longitudinal Waves**

In ideal MHD, the electric field in the longitudinal direction vanishes

$$\mathbf{B} \cdot \mathbf{E} = \mathbf{B} \cdot (-\mathbf{w} \times \mathbf{B}) = 0. \tag{2.72}$$

In the ideal MHD approximation, longitudinal waves manifest as pure fluid waves without affecting the electric field. We can derive their properties by combining the three fluid equations Using the linearized momentum conservation equation along x,  $i\omega m_t n_1 = m_t i k p_1$  and the density conservation equation  $i\omega n_1 = ikn_0w_1$ , together with the adiabatic equation of state,

$$\mathrm{i}\omega p_1 = (\Gamma p_0/n_0)(\mathrm{i}kn_1) \ , \ \mathrm{yields}$$
 
$$\left(\frac{\omega}{k}\right)^2 = \Gamma \frac{p_0}{n_0} = c_s^2, \tag{2.73}$$

where the speed of sound of the unified fluid is  $c_s$ . The longitudinal waves in the adiabatic MHD description do not dissipate energy, similar to the adiabatic multi-fluid description.

#### **Nomenclature**

Our analysis has identified six fundamental wave modes in parallel propagation: four Alfvén modes propagating at  $\pm v_A$  and two acoustic modes at  $\pm c_s$  (additionally, a non-propagating entropy mode with  $\omega = 0$ ,  $(\rho_m)_1 \neq 0$  and  $B_1 \neq 0$  exists, but is of less interest). However, standard MHD nomenclature refers to these waves as Alfvén, fast magnetosonic and slow magnetosonic waves (also termed magnetoacoustic). This nomenclature is useful if waves propagate at arbitrary angles  $\theta$ , where  $\theta$  is the angle between magnetic field vector and propagation direction fulfilling  $\mathbf{k} \cdot \mathbf{B} = |\mathbf{k}| |\mathbf{B}| \cos(\theta)$ . For theses waves, the wave modes are no longer purely transversal or longitudinal. Instead, magnetic and acoustic effects couple, leading to hybrid wave characteristics. The dispersion relations for oblique waves are for Alfvén waves

$$\omega = v_{\rm A} \cos(\theta) |\mathbf{k}|,\tag{2.74}$$

and for magnetosonic waves,

$$\omega^2 = \frac{k^2}{2} \left[ c_{\text{ms}}^2 \pm \sqrt{c_{\text{ms}}^4 - 4v_{\text{A}}^2 c_s^2 \cos^2(\theta)} \right]$$
 (2.75)

where  $c_{\rm ms}^2 = v_{\rm A}^2 + c_s^2$  defines the magnetosonic speed, and the  $\pm$  distinguishes between fast (+) and slow (-) modes. In the parallel case ( $\theta = 0$ ), these relations reduce to our earlier findings, but with an important subtlety. Our acoustic mode corresponds to the fast magnetosonic wave if  $c_s > v_{\rm A}$ , but it changes character and corresponds to the slow magnetosonic wave if  $c_s < v_{\rm A}$ . One of our two Alfvén modes takes on the respective other role, i.e., it is the fast ( $v_{\rm A} > c_s$ ) or slow ( $v_{\rm A} < c_s$ ) magnetosonic mode. The remaining Alfvén mode in our nomenclature is a so-called shear Alfvén mode in the other nomenclature. This difference arises because fast and slow magnetosonic wave modes are coined after their phase speeds depending on the ratio  $v_{\rm A}/c_s$ , while we prefer to classify them as longitudinal or transverse wave modes.

The hierarchy of plasma models presented in Chapter 2 not only serves as an analytical framework but also offers distinct computational advantages and limitations in numerical implementations. This section presents representative numerical methods for solving each of these models, emphasizing their practicability and computational considerations with respect to the CR streaming problem.

The analytical formulation presented thus far employs SI units. However, numerical implementations of Maxwell's equations (2.3) commonly utilize the Heaviside-Lorentz unit system. This choice optimizes computational efficiency by eliminating numerical prefactors in Maxwell's equations

$$\nabla \cdot \boldsymbol{E} = \rho, \qquad \nabla \cdot \boldsymbol{B} = 0, \tag{3.1}$$

$$c\nabla \times \boldsymbol{E} = -\frac{\partial \boldsymbol{B}}{\partial t}, \qquad c\nabla \times \boldsymbol{B} = \boldsymbol{J} + \frac{\partial \boldsymbol{E}}{\partial t}. \tag{3.2}$$

The subsequent normalization c=1 removes all remaining numerical constants. The Heaviside-Lorentz system can be converted to other unit system like the SI and CGS units (Jackson, 1999). We adhere to SI units for theoretical discussions, which are trivially converted to computational units by setting  $c=\epsilon_0=\mu_0=1$ , yielding the normalized Heaviside-Lorentz system.

In the following, we will introduce numerical techniques to solve the kinetic plasma equations in Sections 3.1 and 3.2, before moving to the fluid equations in Section 3.3. Finally, we describe the most appropriate numerical methods for the CR streaming problem in Section 3.4 by combining these different strategies.

# 3.1. Kinetic Solvers: Vlasov Solvers

The Vlasov equation (2.1) governs the temporal evolution of the particle distribution function in a six-dimensional phase space, comprising three spatial and three velocity dimensions. A direct numerical solution requires discretizing the distribution function  $f(\mathbf{x}, \mathbf{v}, t)$  across this six-dimensional domain. To illustrate the fundamental solution strategy, we follow the semi-Lagrangian method proposed by Cheng and Knorr (1975) (see also Sonnendrücker et al., 1999), and present its non-relativistic formulation in one spatial dimension and one velocity dimension. The approach utilizes operator splitting (Strang, 1968), a method that systematically decomposes complex differential equations into more tractable components. Consider a linear partial differential equation of the form

$$\frac{\partial f}{\partial t} = A \frac{\partial f}{\partial x} + B \frac{\partial f}{\partial v},\tag{3.3}$$

where A and B are coefficients. Strang splitting, a second-order accurate operator splitting method, separates this equation into two separate operations (A)  $\partial_t f = A \partial_x f$  and (B)  $\partial_t f = B \partial_v f$ . These operations are solved sequentially in a specific pattern, first (A) for half a time step, then (B) for a full time step, and finally (A) again for half a time step. The result of each operation (A or B) becomes the initial condition for the successive operation. This approach achieves second-order accuracy in time if all operators are also second-order accurate, while higher-order accuracy can be achieved through additional iterations (Yoshida, 1990).

Applying Strang splitting to the Vlasov equation, we only have to find solutions for each operator (A or B) and apply them in succession. In the following, we show how each operator is solved for a full time-step of size  $\Delta t$ . We discretize time using the forward differencing, where  $f^n$  represents the distribution function at time  $t = n\Delta t$ :

(A) 
$$\frac{f^{n+1} - f^n}{\Delta t} = -v \frac{\partial f^n}{\partial x} + O(\Delta t^2)$$
$$\Rightarrow f^{n+1}(x, v) = f^n(x, v) - v \Delta t \frac{\partial f^n(x, v)}{\partial x} = f^n(x - v \Delta t, v) + O\left(v^2 \Delta t^2\right). \tag{3.4}$$

The last step represents the key insight of semi-Lagrangian schemes, it transforms the evaluation of a gradient into a spatial shift of the distribution function. This reformulation converts the differential equation into an interpolation problem, thereby significantly simplifying the numerical implementation. The same idea is applied to (B), where the electric field was determined beforehand by Maxwell's equations,

$$(\mathrm{B}) \quad f^{n+1}(x,v) = f^n(x,v) + E(x,t)\Delta t \frac{\partial f^n(x,v)}{\partial v} = f^n\left(x,v + E(x,t)\Delta t\right) + O\left(E^2\Delta t^2\right). \tag{3.5}$$

Just as before, the gradient is replaced by a spatial shift, and the problem is simplified to an interpolation. The semi-Lagrangian scheme only translates phase space elements without modifying them, which is in accordance with Liouville's theorem stating that phase space volume is conserved. However, numerical conservation of the phase space volume is not guaranteed in this scheme (Qiu and Shu, 2011).

Even though Vlasov solvers provide the most accurate description of plasma dynamics, they face significant computational challenges. The memory requirements and computational complexity scale as  $N^d$ , where N represents the number of grid points per dimension and the number of dimensions d ranges up to 6. This scaling severely limits the practical applicability of Vlasov solvers. Additionally, the complex geometry of phase space structures demands high resolution to capture fine details. These challenges can be addressed through adaptive mesh refinement (Kolobov and Arslanbekov, 2012) or an involved exploitation of the symmetries (Schween et al., 2024).

# 3.2. Kinetic Solvers: Particle-in-Cell (PIC)

The particle-in-cell (PIC) method provides a powerful approach to simulate kinetic plasma dynamics by tracking discrete particles. Rather than directly solving the Vlasov equation, the distribution function is approximated as a collection of discrete particles:

$$f(\boldsymbol{x}, \boldsymbol{v}, t) \approx \sum_{p=1}^{N_p} w_p S(\boldsymbol{x} - \boldsymbol{x}_p(t)) \delta(\boldsymbol{v} - \boldsymbol{v}_p(t)). \tag{3.6}$$

 $w_p$  represents the particle weight as each computational particle should be understood as a macro-particle that represents multiple physical particles. S is a spatial shape function that describes the spatial extent of the computational particles, which in its simplest form can be represented by Dirac's  $\delta$  function (which is also adopted for the velocity distribution). In practice, we employ higher-order spline functions to minimize our noise properties (Shalaby et al., 2017b, see also the discussion in Sect. 3.2.5). Unlike Vlasov solvers that discretize the entire phase space, the PIC method discretizes only the electromagnetic fields on a spatial grid while maintaining continuous particle positions in phase space. The PIC method is a Monte Carlo method, which requires a substantial number of particles to accurately model the distribution f, with statistical Poisson noise scaling as  $1/\sqrt{N_{\rm pc}}$ , where  $N_{\rm pc}$  represents the number of particles per grid cell. At first glance, this statistical approach appears to be limiting but its strength lies in the grid-less discretization of f, which is an appealing alternative to high-dimensional grids. As a consequence of the discretization, the PIC method automatically concentrates computational effort in densely populated regions in phase space, unlike Vlasov solvers which may use an adaptive grid to achieve the same. Additionally, the particle representation provides direct physical insight and enables trajectory tracking throughout the simulation domain.

In the following, we present some fundamental principles of the PIC method (Hockney, 1988; Birdsall and Langdon, 1991). Nevertheless, some variations of the PIC method deviate from the initial ideas presented here (Fonseca et al., 2002; Markidis and Lapenta, 2011; Hewett and Bruce Langdon, 1987). We first focus on the *particle* dynamics, followed by the "in" aspect, i.e., addressing the interpolation procedures and interaction with the *cell* component responsible for modeling the electromagnetic field, which we detail in the end.

#### 3.2.1. Particle Pusher

The relativistic particle motion is governed by the equations

$$\frac{d\boldsymbol{x}_p}{dt} = \boldsymbol{v}_p, \quad \frac{d\boldsymbol{u}_p}{dt} = \frac{q_p}{m_p} (\boldsymbol{E} + \boldsymbol{v}_p \times \boldsymbol{B}). \tag{3.7}$$

These equations are solved using the leapfrog scheme<sup>1</sup>, where the particle's spatial position  $\boldsymbol{x}_p^n$  and velocity  $\boldsymbol{v}_p^{n+1/2}$  are computed at staggered time points  $t^n$  and  $t^{n+1/2}$ , yielding a simple second-order accurate position update

$$\mathbf{x}_{p}^{n+1} = \mathbf{x}_{p}^{n} + \mathbf{v}_{p}^{n+1/2} \Delta t. \tag{3.8}$$

<sup>&</sup>lt;sup>1</sup>The leapfrog scheme is a Strang splitting scheme. It is common to speak of *leapfrog* in the context of integrating the particle trajectory (x,v) (governed by two separate equations instead of one equation with two operators), and if the algorithm uses two time steps (full-full) instead of three time steps (half-full-half), which is achieved by merging the half-time steps.

The velocity update is performed using the Boris algorithm (Boris et al., 1970), which remains the de-facto standard due to its excellent long-term stability properties (Qin et al., 2013). The algorithm employs Strang splitting to separate electric and magnetic acceleration, executing the following steps for each particle (omitting the subscript p for clarity)

First Electric Push: 
$$\mathbf{u}^{-} = \mathbf{u}^{n-1/2} + \frac{q}{m} \frac{\Delta t}{2} \mathbf{E}^{n}(x), \tag{3.9}$$

Magnetic Rotation: 
$$u' = u^- + u^- \times t'$$
, (3.10)

$$u^{+} = u^{-} + \frac{2}{1 + t'^{2}} (u' \times t'),$$
 (3.11)

Using: 
$$t' = \Delta t \frac{q}{2\gamma^n m} \mathbf{B}^n(x)$$
,

Second Electric Push: 
$$\boldsymbol{u}^{n+1/2} = \boldsymbol{u}^+ + \frac{q}{m} \frac{\Delta t}{2} \boldsymbol{E}^n(x), \qquad (3.12)$$

where  $\gamma^- = \left[1 + (\boldsymbol{u}^-/c)^2\right]^{1/2}$ . The magnetic rotation preserves the four-velocity magnitude if the particle's cyclotron frequency is slow compared to the time step,  $\Omega_p \Delta t \leq 2$ , introducing numerical errors only in the rotational phase. This mirrors the physical reality that magnetic fields can only deflect particles but not increase their velocity, which is vital in eliminating numerical instabilities. Modern variants of the relativistic Boris pusher, such as those developed by Vay (2008) and Higuera and Cary (2017), offer improved predictions of  $\gamma^-$ .

## 3.2.2. Interpolation

We require the electromagnetic fields  $E(x_p)$  and  $B(x_p)$  at the particle locations for equations (3.9)–(3.12). The fields are only defined on their respective discrete grid points  $(x_g)$ , which may differ for each E and E component), so they must be interpolated to the particle locations, accounting for the particle shape function  $S(x-x_p)$ :

$$E_x(\mathbf{x}_p) = \int E_x(\mathbf{x}) S(\mathbf{x} - \mathbf{x}_p) d^3 x \approx \sum_g \frac{E_x(\mathbf{x}_{g+1}) + E_x(\mathbf{x}_g)}{2} W(\mathbf{x}_{g+1/2} - \mathbf{x}_p) + O(\Delta x^2), \quad (3.13)$$

$$W(\boldsymbol{x}_g - \boldsymbol{x}_p) = \int_{\boldsymbol{x}_g - \Delta \boldsymbol{x}/2}^{\boldsymbol{x}_g + \Delta \boldsymbol{x}/2} S(\boldsymbol{x} - \boldsymbol{x}_p) d^3 x, \tag{3.14}$$

with analogous formulae for B and the remaining components of E, although the interpolation method may be adapted for specific purposes. The weight function W represents the fraction of the macro-particle located within each cell volume of extent  $\Delta x$ , satisfying the normalization condition  $\sum_{g} W(x_g - x_p) = \int S(x) d^3x = 1$ .

The current density in equation (2.5) is similarly discretized, and interpolated from the particles to the grid according to

$$\boldsymbol{J}(\boldsymbol{x}_g) = \sum_{p} w_p q_p \boldsymbol{v}_p W(\boldsymbol{x}_p - \boldsymbol{x}_g). \tag{3.15}$$

We have assumed that all interpolated quantities are defined at the same time; sometimes

temporal interpolation is necessary as well using, e.g.,  $\mathbf{x}_p^{n+1/2} \approx (\mathbf{x}_p^{n+1} + \mathbf{x}_p^n)/2$ . Furthermore, the choice of interpolation scheme significantly impacts momentum conservation, with some schemes introducing unphysical self-forces while others preserve momentum exactly (Birdsall and Langdon, 1991; Fehske et al., 2008; Shalaby et al., 2017b).

The charge density  $\rho$ , while not strictly necessary for the PIC algorithm, can be defined analogously to equation (3.15). The interpolation scheme should preferentially conserve charge  $(\partial_t \rho + \nabla \cdot \boldsymbol{J} = 0)$ , which is linked to the constraint  $\nabla \cdot \boldsymbol{E} = \rho/\epsilon_0$ , see the discussion about equation 2.25), which may be achieved using the Esirkepov algorithm that computes currents by tracking particles crossing cell boundaries, numerically enforcing  $\partial_t \rho = -\nabla \cdot \boldsymbol{J}$  and thus charge conservation, see equations (2.25)–(2.26) (Esirkepov 2001, see also Villasenor and Buneman 1992). For one-dimensional simulations, direct integration of  $\nabla \cdot \boldsymbol{E} = \rho/\epsilon_0$  provides a viable alternative to enforce charge conservation.

# 3.2.3. Electromagnetic Field Solver: Yee Grid and Magnetic Monopoles

In continuous electromagnetic theory, a divergence-free magnetic field remains divergence-free, as demonstrated by

$$\frac{\partial \nabla \cdot \mathbf{B}}{\partial t} = -\nabla \cdot (\nabla \times \mathbf{E}) = 0. \tag{3.16}$$

This prohibits the creation of magnetic monopoles, which should also be prohibited in the discrete treatment. We discretize  $\mathbf{B}$  on the three dimensional lattice as  $\mathbf{B}_{i,j,k} = \mathbf{B}(i\Delta x \hat{\mathbf{e}}_x + j\Delta y \hat{\mathbf{e}}_y + k\Delta z \hat{\mathbf{e}}_z)$  with unit vectors  $\hat{\mathbf{e}}$ , integers i, j and k, and spatial steps  $\Delta x$ ,  $\Delta y$  and  $\Delta z$ . We momentarily indicate the components of  $\mathbf{B}$  with superscripts x, y and z, and discretize the divergence as follows

$$0 \stackrel{!}{=} \frac{\partial}{\partial t} \nabla \cdot \boldsymbol{B}_{i,j,k} = \frac{\partial}{\partial t} \left( \frac{B_{i+\frac{1}{2},j,k}^{x} - B_{i-\frac{1}{2},j,k}^{x}}{\Delta x} + \frac{B_{i,j+\frac{1}{2},k}^{y} - B_{i,j-\frac{1}{2},k}^{y}}{\Delta y} + \frac{B_{i,j,k+\frac{1}{2}}^{z} - B_{i,j,k-\frac{1}{2}}^{z}}{\Delta z} \right).$$
(3.17)

The terms on the right-hand side should vanish up to machine precision. Yee (1966) achieved this through strategic staggering of the grid in time and space (Yee grid), his method is also referred to as finite differences in the time domain (FDTD). We reproduce the discretization of  $\partial_t \mathbf{B} = -\nabla \times \mathbf{E}$  for the x component here, while the y and z component are analogous,

$$\frac{\partial B_{i+\frac{1}{2},j,k}^{x}}{\partial t} = -\frac{E_{i+\frac{1}{2},j+\frac{1}{2},k}^{z} - E_{i+\frac{1}{2},j-\frac{1}{2},k}^{z}}{\Delta y} + \frac{E_{i+\frac{1}{2},j,k+\frac{1}{2}}^{y} - E_{i+\frac{1}{2},j,k-\frac{1}{2}}^{y}}{\Delta z}.$$
 (3.18)

When this equation and its counterparts for  $B^y$  and  $B^z$  components are substituted into equation (3.17), all terms cancel exactly. This ensures conservation of magnetic field divergence throughout the simulation, provided the initial condition satisfies  $\nabla \cdot \boldsymbol{B} = 0$ .

The electric field update  $\partial_t E = -J/\epsilon_0 + c^2 \nabla \times B$  (equation 2.3) similarly discretizes the curl,

$$\frac{\partial E_{i,j+\frac{1}{2},k+\frac{1}{2}}^{x}}{\partial t} = -\frac{J_{i,j+\frac{1}{2},k+\frac{1}{2}}^{x}}{\epsilon_{0}} + c^{2} \left( \frac{B_{i,j+1,k+\frac{1}{2}}^{z} - B_{i,j,k+\frac{1}{2}}^{z}}{\Delta y} - \frac{B_{i,j+\frac{1}{2},k+1}^{y} - B_{i,j+\frac{1}{2},k}^{y}}{\Delta z} \right), \tag{3.19}$$

and  $E^y$  and  $E^z$  are obtained analogously.

The above equations are still semi-discrete; temporal discretization is achieved using central differences,  $\partial_t E^{n+1/2} = (E^{n+1} - E^n)/\Delta t$  with analogous expressions for other quantities. The time integration thus follows the leap-frog pattern used in particle integration, achieving second-order accuracy in time as well.

Reviewing the previous update equations, the Yee grid requires tracking electromagnetic quantities at the staggered locations

$$(E_x)_{i,j+\frac{1}{2},k+\frac{1}{2}}^n \qquad (E_y)_{i+\frac{1}{2},j,k+\frac{1}{2}}^n \qquad (E_z)_{i+\frac{1}{2},j+\frac{1}{2},k}^n \\ (B_x)_{i+\frac{1}{2},j,k}^{n+\frac{1}{2}} \qquad (B_y)_{i,j+\frac{1}{2},k}^{n+\frac{1}{2}} \qquad (B_z)_{i,j,k+\frac{1}{2}}^{n+\frac{1}{2}}.$$

**J** is defined at time  $t^{n+1/2}$  but spatially staggered like **E**.

Now that we have gathered all the ingredients, the PIC algorithm simply repeats the four operations:

- 1. Interpolation of the electromagnetic fields to particle positions according to equation (3.14).
- 2. Integration of the particle trajectory (particle push) according to equations (3.8)–(3.12)
- 3. Deposition of particle currents on the grid according to equation (3.15)
- 4. Advancing the electromagnetic fields according to equations (3.18)–(3.19).

## 3.2.4. Numerical Stability

The total computational cost of a PIC simulation scales approximately with

$$C_{\rm tot} \propto \frac{t_{\rm end}}{\Delta t} \times N_p C_{\rm particle}$$
 (3.20)

where  $t_{\rm end}/\Delta t$  represents the number of iterations to reach the simulation time  $t_{\rm end}$ ,  $N_p$  is the number of particles, and  $C_{\rm particle}$  denotes the computational cost per particle for one iteration. While the field solver's cost depends also on the grid resolution  $\Delta x$ , it remains negligible compared to the computational expense of all particle interpolation and pushing operations. Although increasing the time step  $\Delta t$  reduces  $C_{\rm tot}$ , there are limits on how large  $\Delta t$  may be chosen.

The PIC method as laid out here is an explicit scheme, and can become unstable if fundamental frequencies are not resolved. We must consider that propagating waves and particles can move at velocities approaching c, while standing waves oscillating at the plasma and cyclotron frequency must be resolved as well

Courant–Friedrichs–Lewy (CFL) Condition: 
$$c\Delta t \leq \frac{1}{\sqrt{\Delta x^{-2} + \Delta y^{-2} + \Delta z^{-2}}} \sim \Delta x.$$
 (3.21)

Plasma Frequency Resolution: 
$$\Delta t \le 2/\max_{s}(\omega_{s}) \sim 2\omega_{e}^{-1}$$
. (3.22)

Cyclotron Frequency Resolution: 
$$\Delta t \leq 2/\max_{s}(\Omega_s) \sim 2\Omega_e^{-1}$$
. (3.23)

For estimating the order of magnitude, we assumed an equispaced grid for the CFL condition, and that the electron scale is the smallest scale in the simulation. The factor 2 of the oscillation constraints results from a stability analysis of the harmonic oscillator assuming the leapfrog discretization; if a stable time step is taken, the full rotation period  $T = 2\pi\Omega$  is resolved by multiple time steps  $(T/(\Delta t) > \pi)$ , i.e., at least 4). The plasma frequency typically exceeds the cyclotron frequency – unless the plasma is highly magnetized – making equation (3.22) the primary constraint on  $\Delta t$  in case  $\Delta x \gg d_e$ . For numerical accuracy and proper resolution of the frequency constraints (3.22) and (3.23), the simulation time step  $\Delta t$  should be approximately an order of magnitude smaller than the maximum allowable time step derived from stability analysis.

While these restrictions apply to  $\Delta t$ , the grid spacing  $\Delta x$  underlies another constraint. PIC codes are often momentum conserving, but not energy conserving (though variants achieving energy conservation at the expense of momentum conservation have been developed, e.g., Lewis 1970; Markidis and Lapenta 2011). As a consequence of this energy non-conservation combined with aliasing effects of spatially limited grids, the finite-grid instability causes exponential heating in plasmas if the Debye-Length  $\lambda_{\rm D}$  is not resolved

Debye-Length Resolution: 
$$\Delta x < C_{th} \lambda_D \sim C_{th} c_{s,e} / \omega_e$$
. (3.24)

 $C_{\rm th}$  is an implementation dependent constant of roughly on the order of  $C_{\rm th} > 3.4$  (Langdon, 1970; McMillan, 2020). This instability heats the plasma, until the Debye-Length reaches the stability constraint, where the electron sound speed  $c_{s,e}^2 = \Gamma v_{\rm th,e}^2/2$  increases with heating (for definitions of the thermal velocity, see equation 2.44). Preventing the heating to relativistically hot temperatures wherein  $c_{s,e}$  approaches c demands a grid spacing smaller than the electron skin depth  $\Delta x \ll C_{\rm th} d_e$ . A step size of around  $\Delta x \sim d_e/10$  is common in PIC. However, in modern implementations  $C_{\rm th}$  is often large enough to allow for mildly warm plasmas at coarser resolutions of  $\Delta x \sim d_e$  (McMillan, 2020). For grid spacings of this length, the CFL condition (3.21) is not the main limiting factor of  $\Delta t$  (and thus, the computational cost) because the resolution of the plasma frequency necessitates smaller time steps.

## 3.2.5. Minimizing Numerical Heating

Numerical heating occurs not only exponentially fast through the finite-grid instability below the numerical temperature floor, but generally accumulates linearly over time. In terms of equations, this linear numerical heating may be expressed using the particle temperature T(t) that depends approximately on its initial value of  $T_0$  as (Hockney, 1971; Arber et al., 2015)

$$T(t) \approx T_0 \left( 1 + \frac{t}{\tau_H} \right),$$
 (3.25)

where  $\tau_H$  is an implementation and resolution dependent numerical heating time scale. This accumulation limits the maximum simulation time  $t_{\text{end}}$  beyond computational resource constraints set by equation (3.20), as numerical heating degrades the quality of the simulation over time.

For meaningful results, the ratio  $t/\tau_H$  should remain below a few percent throughout the simulation. Simulations of CR streaming can reach millions of time steps, necessitating techniques to maximize  $\tau_H$ . We discuss two approaches to address this challenge.

The most widely adopted approach employs digital filters on the current density prior to interpolation. These filters smooth out small-scale noise while largely preserving large scale components. The binomial filter represents a common implementation, performing a symmetric convolution of the current density with the kernel  $\mathbf{K} = [1/4 \quad 1/2 \quad 1/4]$  spanning three cells. If we interpret the discrete field values as a vector, such as  $\bar{\mathbf{J}}_x = [J_{x,i=0} \quad J_{x,i=1} \quad \dots \quad J_{x,i=N}]$ , the resulting filtered density current is given by  $\bar{\mathbf{J}}_{x,\text{filtered}} = \mathbf{K} * \bar{\mathbf{J}}_x$  using the discrete convolution operator \*.<sup>2</sup> This effectively broadens the particle shape during current deposition, though not during force interpolation. This disparity results in a violation of momentum conservation by introducing nonphysical self-forces (Fehske et al., 2008; Shalaby et al., 2017b). Through successive iterations (or passes) of applying the binomial filter, the particle shape can be further smoothed. The number of iterations p is a tuneable parameter requiring optimization across multiple criteria. p should be small enough to not smear out physically relevant scales, while it should be large enough to lower numerical heating as much as possible by removing small scale noise. Even successive applications of filters are computationally inexpensive, given that they only act on the fields and are not invoked for each particle.

Alternatively, the particle shape can be smoothed self-consistently through higher-order shape functions S, see equation (3.6), which significantly decreases numerical heating by orders of magnitude (Birdsall and Langdon, 1991; Arber et al., 2015). While higher-order shape functions are computationally more expensive per particle, they require fewer particles to achieve the same numerical heating as codes using lower-order shape functions. The hierarchy of spline shape functions begins with the nearest grid point (NGP) interpolation ( $S_0 = \delta$ ). The next level is a cloud-in-cell (CIC) interpolation scheme, which employs linear interpolation using a top-hat function  $S_1(x) = \theta(x + \Delta x/2)\theta(-x + \Delta x/2)/\Delta x$ , where  $\theta$  represents the Heaviside function. Triangular shaped cloud (TSC) extends this to quadratic interpolation. The shape function is never computed in the code, since only the weight function W appears in the interpolation routines. The weight function is always one order higher than the shape function – for instance, the NGP weight function  $W_0 = S_1$  corresponds to the CIC shape function. An example for a code utilizing very high-order shape functions is the SHARP code, which implements fourth-order shape functions corresponding to fifth-order weight functions (Shalaby et al., 2017b).

Figure 3.1 visualizes how filtered interpolation breaks the symmetry of particle self-forces. While the particle's total contribution to the grid remains unity, filtering creates a density current that is asymmetric around the particle's position. Consequently, the particle experiences only half of its deposited field contribution, preventing complete self-force cancellation. However, this apparent deficiency becomes less significant when considering multiple particles, as "missing" self-force contributions are compensated by neighboring particles. In the limit of high particle numbers, filtered and higher-order shape function approaches produce equivalent results. Higher-

<sup>&</sup>lt;sup>2</sup>Filtering of multi-dimensional data is performed successively in each direction, using the property that the binomial filter is separable (App. C of Birdsall and Langdon, 1991).

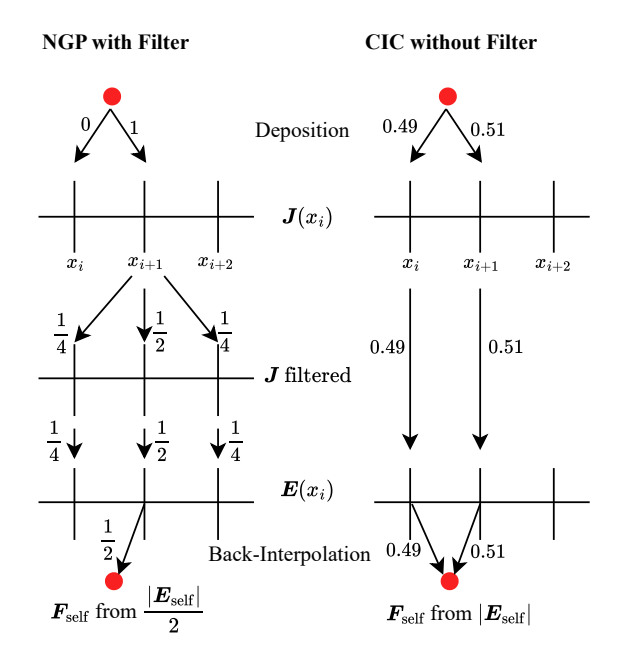


Figure 3.1 Conceptual comparison of particle self-force in electrostatic PIC simulations. Left: Nearest grid point interpolation with binomial filtering spreads particle contributions asymmetrically around the particle location, and the self-force is calculated from half the particle's current contribution. Right: Cloud in cell interpolation maintains consistent particle shape during both current deposition and force calculation, enabling complete self-force cancellation if the electrostatic field solver is properly implemented. Arrow values indicate current contributions at grid points according its weight function W that sums to unity, and how these contributions propagate to calculate the self-force.

order shape functions smooth the particle shape while eliminating self-forces, leading to desired behavior even at low particle numbers.

# 3.3. Fluid Solvers

The multi-fluid and the MHD equations share the basic structure of fluid equations, therefore their numerical solvers share the same fundamentals and we will treat both of them in this section. The structure of these equations resembles

$$\frac{\partial \tilde{\boldsymbol{U}}}{\partial t} + \nabla \cdot \mathbf{F}(\tilde{\boldsymbol{U}}) = S(\tilde{\boldsymbol{U}}),, \tag{3.26}$$

where the fluid quantities are defined in the vector  $\tilde{\boldsymbol{U}}$ ,  $\boldsymbol{\mathsf{F}}$  is the flux tensor and  $\boldsymbol{S}$  are source terms. The multi-fluid equations fit the template of equation (3.26), but only if the pressure evolution equation (2.31) is reformulated into the conservative energy evolution equation (2.35). In ideal MHD, Faraday's law (2.67) is reformulated using the vector triple product expansion and the identity for dyadic and dot products given by  $\boldsymbol{c} \cdot (\boldsymbol{a}\boldsymbol{b}) = (\boldsymbol{c} \cdot \boldsymbol{a}) \boldsymbol{b}$ 

$$\partial_t \mathbf{B} + \nabla \cdot (\mathbf{w}\mathbf{B} - \mathbf{B}\mathbf{w}) = \mathbf{0}. \tag{3.27}$$

The Vlasov equation follows the structure of equation (3.26) as well, thus the methods presented here are also applicable to the Vlasov equation. The solvers presented in this section are called *Eulerian*, while the scheme described in Section 3.1 is *semi-Lagrangian* (for a review see Palmroth et al., 2018) and the PIC method is *Lagrangian*.

Here, we will consider systems with vanishing source terms, S = 0, which is directly applicable to the MHD equations (2.63)–(2.67) and the Vlasov equation. For multi-fluid systems where  $S \neq 0$ , Strang splitting enables decomposition into two sub problems: one with S = 0 and another

with  $\mathbf{F} = \mathbf{0}$ . A detailed treatment of this splitting is given in Section 4.2.4.

For clarity of presentation, we restrict our analysis to one-dimensional geometries ( $\nabla \cdot \mathbf{F} \rightarrow \partial_x \mathbf{F}$ ). An extension to multiple dimensions is easily achievable through dimensional Strang splitting. However, this approach introduces grid-dependent artifacts, particularly in spherical geometries. While dimensionally unsplit schemes exist, they are method-specific and beyond our current scope.

We examine two methods of fluid solvers, finite difference (FD) and finite volume (FV), and briefly introduce two more methods, spectral and discontinuous Galerkin (DG). While spatial discretization varies among these approaches, temporal discretization typically employs finite differences across all schemes, which can be solved using Runge-Kutta or (semi-)implicit methods. Comprehensive treatments of FD and FV methods are provided by LeVeque (2002) and Toro (2009).

## 3.3.1. Finite Difference Methods (FD)

The fundamental principle of finite difference methods lies in approximating derivatives through Taylor series expansions at discrete domain points. The solution is evaluated at these points,, and derivatives are approximated using neighboring point values. The electromagnetic field solver discussed previously in Section 4.2.2 uses FD. The spatial derivative can be approximated in different ways

$$\frac{\partial \mathbf{F}}{\partial x}\Big|_{i} = \frac{\mathbf{F}_{i+1} - \mathbf{F}_{i-1}}{2\Delta x} + O(\Delta x^{3}) \text{ (central difference)}, \tag{3.28}$$

$$\frac{\partial \mathbf{F}}{\partial x}\Big|_{i} \approx \frac{\mathbf{F}_{i} - \mathbf{F}_{i-1}}{\Delta x} + O(\Delta x^{2}) \text{ (backward difference)},$$
 (3.29)

$$\frac{\partial \mathbf{F}}{\partial x}\Big|_{i} \approx \frac{\mathbf{F}_{i+1} - \mathbf{F}_{i}}{\Delta x} + O(\Delta x^{2}) \text{ (forward difference)},$$
 (3.30)

even though the central difference scheme appears well motivated, it results in an unconditionally unstable scheme in conjunction with the temporal discretization  $\frac{\partial U}{\partial t} = \left(U^{n+1} - U^n\right)/\Delta t$ . The instability arises because information propagates along characteristic curves. Physically, these characteristics represent, among other things, shocks or waves. In the following, we will interchange characteristics with waves to to simplify the interpretation, even though the concept applies to characteristics more generally. As the waves carry information, they propagate in a certain direction, and it is important to know where they are coming from to predict where they travel to. Thus, a numerical scheme should be informed by the waves origin, rather than its destination, and stability may be achieved by aligning the differentiation direction with the waves origin. For a scalar conservation law, the characteristic speed  $\lambda$  is given by linearizing F

$$\partial_x F = \frac{\partial F}{\partial \tilde{U}} \partial_x \tilde{U} = \lambda \partial_x \tilde{U}. \tag{3.31}$$

and, more generally, characteristic speeds correspond to eigenvalues of the Jacobian  $\partial F/\partial \tilde{U}$ . The stable upwinding scheme takes the propagation direction into account, where we designate

the directions left referring to lower values of i and right referring to larger values of i

$$\left. \frac{\partial F}{\partial x} \right|_{i} \approx \begin{cases} \frac{F_{i} - F_{i-1}}{\Delta x} & \text{if } \lambda > 0 \text{ (wave moves from left to right, backward difference),} \\ \frac{F_{i+1} - F_{i}}{\Delta x} & \text{if } \lambda < 0 \text{ (wave moves from right to left, forward difference).} \end{cases}$$
(3.32)

FD schemes rarely implement upwinding directly because vector systems feature multiple waves propagating in opposite directions, but the schemes are upwind-biased for each individual wave mode. The unstable central difference scheme (equation 3.28) results from the arithmetic mean of upwind and downwind derivatives assigning equal weights to information propagating from both directions; an upwind-biased scheme applies greater numerical weight to spatial derivatives in the upstream direction. This principle of respecting wave propagation direction is fundamental to all numerical methods in this context.

The FD method is simple to implement and readily extends to higher orders by employing more accurate differencing formulations. However, it does not naturally conserve physical quantities like momentum or energy, but a staggered grid layout might aid in conserving key constraints, e.g., the Yee-grid conserves  $\nabla \cdot \mathbf{B} = 0$  (Section 4.2.2). The FD scheme is well suited for Maxwell's equations, but is not as well suited for fluid equations. FD schemes handle large gradients inadequately, which occur naturally as a consequence of wave steepening in compressible fluids. FD is thus unable to capture shocks correctly, unless the shock width is significantly larger than the cell size or large viscosity is employed to prevent spurious oscillations referred to as Gibbs phenomenon (Pirozzoli, 2011).

# 3.3.2. Finite Volume Methods (FV)

Instead of solving the partial differential equation (3.26) directly, FV methods integrate over the volume and utilize the divergence theorem

$$\int_{\Omega} d\Omega \left[ \frac{\partial}{\partial t} \tilde{\boldsymbol{U}} + \nabla \cdot \mathbf{F}(\tilde{\boldsymbol{U}}) \right] = \mathbf{0}$$
(3.33)

$$\frac{\partial}{\partial t} \int_{\Omega} \tilde{U} d\Omega + \oint_{\partial \Omega} \mathbf{F}(\tilde{U}) \cdot d\mathbf{S}_{\Omega} = \mathbf{0}$$
(3.34)

The domain  $\Omega$  with surfaces  $S_{\Omega}$  is discretized into computational volumes  $\Omega_i$  with surfaces  $S_{\Omega,i\pm1/2}$ . In our one-dimensional, fixed grid treatment each volume has length  $\Delta x$ , and therefore

$$\frac{\partial U_i}{\partial t} = -\frac{1}{\Lambda r} \left[ \boldsymbol{F}_{i+1/2}(\tilde{\boldsymbol{U}}) - \boldsymbol{F}_{i-1/2}(\tilde{\boldsymbol{U}}) \right]$$
(3.35)

where  $U_i$  represents the cell average of  $\tilde{U}$  with boundaries at  $x_{i\pm 1/2}$  and  $F_{i\pm 1/2}$  denotes numerical fluxes through the cell interfaces. The key difference to FD schemes, which solve for nodal points defined at fixed positions  $x_i$ , is that FV schemes solve for cell averages of the physically conserved quantities  $\tilde{U}$ . This allows FV schemes to naturally conserve the volume-averaged physical quantities numerically, as evidenced by the telescoping series  $\sum_i^N \partial_t U_i = -(F_{N+1/2} - F_{-1/2})/\Delta x$  which is determined by the inflows and outflows through the boundaries. This enforced

conservation is a highly desirable numerical property.

Solving equation (3.35) requires determining the numerical fluxes  $F_{i\pm 1/2}$ , which depend on the nodal point values  $\tilde{U}$ . The values at the cell boundaries  $\tilde{U}_{i\pm 1/2}$  are reconstructed using a subgrid description, which is informed by the cell averages  $U_i$  and its neighboring cells. The reconstructed values at the boundaries can be discontinuous, i.e.,  $\tilde{U}_{i-1/2}$  is not equal to  $\tilde{U}_{(i-1)+1/2}$  in FV, requiring the solution of a Riemann problem. The Riemann solver returns wave speeds and propagation directions at cell boundaries, which enables to compute numerically stable fluxes. We keep the description of the reconstruction and Riemann solvers short, but will later return to them in Section 4.2.4, where we apply these concepts concretely.

FV methods captures shocks well, as it does not need to solve for steep gradients, but only has to find the (mass, momentum and energy) fluxes at shock interfaces. This makes this method more robust for compressible flows. It also generalizes to complex geometries or flexible meshes. Brio and Wu (1988) first applied the FV scheme to the MHD equations, an application to the two-fluid (multi-fluid with electrons and ions) equations is given by Shumlak and Loverich (2003). FV methods for MHD automatically conserve mass, momentum, energy and magnetic flux, but the divergence-free constraint remains problematic. This issue becomes apparent when we take the divergence of equation (3.27), resulting in  $\partial_t \nabla \cdot \boldsymbol{B}$  on the left-hand side of the equation while the right-hand side of the equation does not necessarily equal 0 numerically.

Powell et al. (1999) addressed this by deriving the MHD equations without assuming  $\nabla \cdot B = 0$ , introducing a source term S proportional to  $\nabla \cdot B$  in equation (3.26). The inclusion of S sacrifices the strict conservation properties, and it also introduces an additional degree of freedom, corresponding to a new wave mode. Powell's method is also known as the eight-wave formulation, named for adding a divergence wave to the standard seven MHD characteristic waves (four magnetosonic, two Alfvén, and one entropy wave). Alternatively, Dedner et al. (2002) developed a hyperbolic divergence cleaning technique, using an auxiliary scalar field equation. The aim of these methods is not to eliminate the divergence completely, but to quickly transport divergence errors to domain boundaries and damp them. A third approach called constrained transport by Evans and Hawley (1988) employs a staggered grid inspired by the Yee-Grid, defining B exclusively at cell boundaries so that the method maintains vanishing divergence throughout the simulation (see also Gardiner and Stone, 2005).

## 3.3.3. Other methods

#### **Spectral Methods**

Spectral methods approximate solutions through series expansions of global basis functions, offering increased accuracy for smooth problems. The solution representation typically employs either Fourier series for periodic domains or Chebyshev polynomials for non-periodic boundaries

(Boyd, 2013)

$$\tilde{U}(x,t) = \sum_{k=-N}^{N} \tilde{U}_k(t)e^{ikx} \text{ (Fourier)},$$
(3.36)

$$\tilde{U}(x,t) = \sum_{n=0}^{N} \tilde{U}_n(t) P_n(x) \text{ (Chebyshev)},$$
(3.37)

where  $P_n(x)$  is the *n*-th Chebyshev polynomial.

The method transforms differential operations into algebraic manipulations. For instance, the density continuity equation  $\partial n/\partial t = -\nabla \cdot (nw)$  is solved with spectral Fourier methods as follows:

$$\partial_t \sum_{k=-N}^N n_k e^{ikx} = -\sum_{k=-N}^N ik(nw)_k e^{ikx}, \qquad (3.38)$$

where the spatial derivatives reduce to multiplication by wave numbers ik.

This approach yields little numerical dissipation and achieves exponential convergence rates through high-order differentiation. The method naturally accommodates non-local Landau-fluid closures (Section 2.2.3). However, the presence of discontinuities generates Gibbs phenomena, manifesting as oscillatory behavior near sharp gradients. Furthermore, shocks and discontinuities in the solution lead to the Gibbs phenomenon (similar to FD), and non-linear equations are communication-intensive on parallel systems.

#### **Discontinuous Galerkin Methods**

DG methods extends the FV framework (Hesthaven and Warburton, 2008). FV methods construct subgrid models through reconstruction from neighboring cells, which becomes a limiting factor for spatially higher-order codes that rely on information from many neighboring cells. DG methods implement direct subgrid representations through an expansion in basis functions  $\Phi_n(x)$ , given by

$$\tilde{U}(x,t) = \sum_{n=0}^{N} \tilde{U}_n(t)\Phi_n(x). \tag{3.39}$$

 $\Phi_n$  is typically a polynomial function that may be discontinuous at the cell interfaces. Thus, for each basis function of order n and cell i, an evolution equation is given, generalizing the FV evolution equation (3.34):

$$\frac{\partial \tilde{\boldsymbol{U}}_{i,n}}{\partial t} \int_{\Omega_i} \Phi_n dx + \int_{\partial \Omega_i} \Phi_n \boldsymbol{F} \left( \tilde{\boldsymbol{U}}_{i,n} \right) \cdot d\boldsymbol{S}_{\Omega_i} - \boldsymbol{F} (\tilde{\boldsymbol{U}}_{i,n}) \cdot \boldsymbol{\nabla} \int_{\Omega_i} \Phi_n dx = \boldsymbol{0}, \tag{3.40}$$

where, similar to FV schemes, the quantities at the boundaries may be discontinuous, thereby  $\tilde{U}_{i-1/2}$  is not equal to  $\tilde{U}_{(i-1)+1/2}$ . This necessitates the computation of numerical fluxes by solving a Riemann problem, giving DG the same conservative properties as FV. DG methods offer similar advantages as FV methods, but allow even higher-order accurate formulations (though these lead to increased memory and computational requirements).

We attempted incorporating the DG method in our fluid-PIC code (which we will introduce in Chapter 4), but the interpolation of higher-order accurate electromagnetic source terms from the lower-order electromagnetic fields lead to numerical instabilities. Instead, for our fluid-PIC method we settled on an FD scheme for electromagnetic fields (Yee-Grid), a FV scheme for solving the fluid equations while we use a spectral method for the Landau closures.

# 3.4. Compound techniques

So far we have reviewed some fundamental numerical concepts, which we now want to investigate based on their practicability in simulating the CR streaming problem. Reviews on similar topics have been presented previously (Marcowith et al., 2020; Pohl et al., 2020). In our presentation, however, we will set a different focus. We will concentrate on the limitations in reproducing physical effects and present the order-of-magnitude efficiency in comparison to the PIC method.

## 3.4.1. Requirements

First, we lay out multiple requirements, which a code should ideally fulfill to study the CR streaming problem. It should (i) capture all gyroresonant streaming instabilities including the intermediate scale instability (Shalaby et al., 2021, 2023), (ii) capture important damping processes, particularly Landau damping and ion-neutral damping, (iii) support versatile setups with different CR compositions, possibly also CR electrons, (iv) not impose constraints on admissible CR distributions, (v) achieve these goals with reasonable computational costs at high fidelity.

The CR streaming problem is challenging, because of the multiple scales involved. The instabilities develop over the time scale of many inverse ion gyrofrequencies. Furthermore, CRs are very sparse in comparison to the background plasma and require small levels of numerical noise to accurately capture their instabilities. This combination cannot be achieved in kinetic codes without significant compromises of the physical parameters. Nevertheless, CRs exhibit kinetic effects, which makes it necessary to solve the Vlasov equation (2.1). This precludes the use of simplified fluid descriptions for investigating streaming mechanics from first principles, even though fluid-based phenomenological models may emerge as useful approximations by coarse graining the plasma kinetic physics.

Neither kinetic nor fluid solvers can address the streaming problem by themselves, but this problem involves the interaction of multiple species, namely energetic CRs, thermal ions and electrons. A class of numerical techniques, which might be regarded as compound solvers, apply species-specific approximations from the analytical frameworks presented in Chapter 2, thereby combining fluid and kinetic descriptions. This approach eliminates unnecessary detail for the thermal fluids while maintaining detailed velocity space resolution of the CRs.

# 3.4.2. Electron Fluids and Kinetic Ions (Hybrid-PIC)

The Hybrid-PIC method (e.g., Lipatov, 2002) combines PIC modeling for ions with the quasineutral approximation. To start our discussion, we will briefly consider the speed ups obtained with this method. First, the electron particles are replaced by a computationally cheap fluid, which cuts the number of particles in half. This translates in a speed up of a factor  $\sim 2$ . Because electron oscillations are eliminated, the stability conditions (3.21)-(3.23) can be relaxed to ion scales, thus restricting the temporal resolution to the ion plasma frequency  $\Delta t \leq \omega_i^{-1}$ . Hybrid-PIC codes also eliminate light waves as a consequence of neglecting the displacement current, but the CFL condition (3.21) remains constrained by the fastest propagating wave or the maximum particle velocity. As we are interested in CR streaming, the fastest particles move with c and this constraint is not relaxed. Thus, the time step of Hybrid-PIC compared to PIC can be larger by a factor of  $\sim \omega_e/\omega_i = (m_i/m_e)^{1/2} \sim 40$  assuming a realistic mass ratio. While this is achieved by sacrificing the resolution on the electron scales, some implementations incorporate electron inertia effects, allowing them to accurately reproduce some electron physics (Muñoz et al., 2018). This, however, lessens the computational gains especially for relativistic particles. As such, the Hybrid-PIC method is up to  $\sim 80$  times more efficient than the PIC method if electron scales are neglected, which is a substantial speed-up. In the following we will investigate an alternative, which is even better suited for the CR streaming setup.

# 3.4.3. Thermal Fluids and Kinetic Cosmic Rays

Hybrid-PIC treats only electrons as a (typically inertialess) fluid, replacing the Vlasov equation for electrons by a fluid description and solving only the Vlasov equation for ions. However, the full ion distribution function may be split into thermal and CR parts as well,  $f_{\rm all\,ions} \to f_{\rm i} + f_{\rm cr}$ . The linearity of the Vlasov equation in f enables its decomposition into two equations, one for the thermal ions and one for the CRs. The partitioning of ions into thermal species and CRs is thus justified by the system of equations. The coupling between these separate Vlasov equations occurs through Maxwell's equations, which only depend on the total charge density and current. These quantities are readily computed by summing contributions from all species components.

This splitting of f is convenient for two reasons. First, because the (Landau-)fluid approximation is a proper description for thermal species, as established in Section 2.2. While Landau damping is excluded from the fluid descriptions, this damping process can be modeled for Landau fluids. Second, the PIC method concentrates its computational resources on the most densely populated areas in phase space, i.e., the thermal particles. With this splitting, we can concentrate our resources on the lower-density CRs.

In the following, we consider the speed up achieved by codes employing this splitting. The computational cost of PIC simulations scales with the number of particles, which must be sufficient to reduce Poisson noise to an acceptable level. We will provide scaling estimates for the Poisson noise for multiple species in order to show why utilizing the fluid model is so beneficial. The signal-to-noise ratio (SNR) for multiple, statistically independent particle species at a fixed box size scales with (Moschüring, 2020)

$$SNR \propto \frac{\sum_{s} \rho_{s}}{\sqrt{\sum_{s} \rho_{s}^{2}/N_{pc,s}}},$$
(3.41)

where the numerator indicates the signal, and the denominator indicates the Poisson noise. The signal corresponds to the charge density  $\rho_s = q_s n_s$ , but analogous formulations for the current densities are possible. For a single species, the SNR scales as  $\sqrt{N_{\rm pc}}$ , confirming the Poisson noise reduction by  $1/\sqrt{N_{\rm pc}}$ . The number density can be expressed as  $n_s = w_{p,s} N_{\rm pc,s}/\delta V$ , where  $w_{p,s}$  is the macro-particle weight of species s,  $N_s$  is the number of particles (see 3.6) and  $\Delta V$  is the volume of a cell. Given the CR-to-thermal-ion density ratio,  $n_{\rm cr}/n_{\rm i} = \alpha \ll 1$ , we have  $w_{p,\rm cr} N_{\rm pc,cr} = \alpha N_{\rm pc,i} w_{p,i}$ . At first glance, it might seem beneficial to significantly increase the particle weights for CR  $w_{p,\rm cr}$  to achieve an equal number of macro particles for CRs and thermal ions, setting  $N_{\rm pc,cr} = N_{\rm pc,i}$ . This leads to a more accurate representation of the CR distribution in phase space. However, Moschüring (2020) demonstrated that the SNR is maximized if all weights are equal, thus deviations from this actually increase noise. Therefore,  $N_{\rm pc,cr} = \alpha N_{\rm pc,i}$  is the optimal choice to reduce Poisson noise, even for ISM-relevant values as low as  $\alpha = 10^{-9}$ .

Replacing thermal ions with a fluid description eliminates their noise contribution,  $\rho_i^2/N_{\text{pc,i}}$ , while preserving their signal  $\rho_s$ . Neglecting the comparatively small fluid solver noise, we compare the SNR between a pure PIC method and a solver mixing thermal fluids and CR particles

$$SNR_{PIC} \propto \frac{\rho_{\rm i}(1+\alpha)}{\sqrt{\rho_{\rm i}^2 N_{\rm pc,i}^{-1}(1+\alpha)}} = \sqrt{(1+\alpha) N_{\rm pc,i}}, \qquad (3.42)$$

$$SNR_{\text{fluid+PIC}} \propto \frac{\rho_{\text{i}}(1+\alpha)}{\sqrt{\rho_{\text{i}}^{2}N_{\text{pc,i}}^{-1}\alpha}} = \frac{1+\alpha}{\sqrt{\alpha}}\sqrt{N_{\text{pc,i}}},$$
(3.43)

$$\Rightarrow \text{SNR}_{\text{fluid+PIC}} \propto \sqrt{\frac{1+\alpha}{\alpha}} \text{SNR}_{\text{PIC}} \approx \frac{1}{\sqrt{\alpha}} \text{SNR}_{\text{PIC}}.$$
 (3.44)

This demonstrates, that these compound fluid treatments achieve similar SNR with  $\sqrt{\alpha}$  fewer particles per cell. We neglected electrons in this derivation, as this does not affect the scaling. Moreover, the fluid solver replaces  $\alpha^{-1}N_{\rm pc,cr}$  thermal electrons and ions, respectively, which provides an additional speed up factor of  $2\alpha^{-1}$ , resulting in a total speedup of  $2\alpha^{-3/2}$ . Thus, fluidized thermal formulations capturing electron scales are more efficient than Hybrid-PIC codes neglecting electron scales already at artificially high density contrasts of  $\alpha \sim 0.08$  (where  $\alpha^{-3/2} \geq (m_i/m_e)^{1/2}$ ). While this magnitude-of-order estimate neglected fluid noise (which is important for  $\alpha \ll 1$ ) and assumed statistical independence, it demonstrates the effectiveness of utilizing thermal fluids for investigating CR streaming. Additional speed ups can be achieved by neglecting electron scales if necessary. We will now introduce some representatives solvers for these compound methods.

#### MHD-PIC

So far, the MHD-PIC method has emerged as the leading approach for simulating gyroresonant streaming instabilities, with many recent applications (Zachary and Cohen, 1986; Lucek and Bell, 2000; Reville and Bell, 2012; Bai et al., 2015, 2019; Mignone et al., 2018; Lebiga et al., 2018; van Marle et al., 2018; Bambic et al., 2021; Plotnikov et al., 2021; Bai, 2022; Sun and Bai,

2023). This method offers several key advantages beyond simply accelerating computations by representing thermal particles as an MHD fluid.

A primary benefit is the relaxed time step constraint compared to Hybrid-PIC methods. By eliminating plasma oscillations, the gyrofrequency becomes the limiting factor for the time step (see equation 3.23). This allows for larger cell sizes, which is important given that CRs can move with c and the CFL condition,  $c\Delta t \leq \Delta x$ , still has to be fulfilled.

However, the method faces significant challenges. Even with large cell sizes, MHD-PIC codes require thousands of particles per ion skin depth  $d_i$  to mitigate Poisson noise and to observe the streaming instability growth (Bai et al., 2019). As a remedy, the  $\delta f$  method is employed (Dimits and Lee, 1993; Parker and Lee, 1993). Its name stems from the expansion of the distribution function into  $f = f_0 + \delta f$ , where  $f_0$  is assumed to be (almost) static while the PIC particles model the fluctuating part of the distribution function,  $\delta f$ . This approach substantially reduces noise while maintaining the ability to handle non-linear behavior through continuous adjustment of particle weights. Larger deviations in  $\delta f$  increase the respective particle weights, while small deviations decrease it. Therefore, the  $\delta f$  method should not be confused with our prior linear analytic treatments that assumed small perturbations. Nevertheless, large perturbations ( $\delta f \sim$  $f_0$ ) can lead to numerical instabilities or nonphysically, negative quantities because the method does not guarantee conservation of density, momentum or energy (Parker and Lee, 1993; Kunz et al., 2014). The method is thus best suited for small  $\delta f$ , where the Poisson noise is greatly diminished. It also requires defining  $f_0$  throughout phase space, which is straightforward for, e.g., Maxwellian distributions. However, many anisotropic beam setups are sparse in phase space. Thus, the  $\delta f$  method prevents simulations where the CR distribution is initially far from its assumed near isotropic steady state solution. Furthermore, the MHD approximation neglects electron scales, despite the existence of rapidly growing gyroresonant instabilities on these scales (Shalaby et al., 2021, 2023). This makes the MHD-PIC method very efficient, but more accurate alternatives are desirable.

## Including intermediate scales

The quasi-neutral two fluid (QNTF) solver by Amano (2015), extended with PIC capabilities (Amano, 2018), implements a generalized Ohm's law enabling investigation of electron-scale phenomena. This case requires to resolve the electron skin depth, and imposes time step constraints through the CFL condition and the CR particle speed c, severely limiting the time step size in comparison to MHD-scale simulations. A particular strength of the QNTF-PIC code is its ability to adapt to different parameter regimes by including different contributions to generalized Ohm's law. As such, it represents a generalization of the MHD-PIC method by analogy with the relationship between generalized and idealized Ohm's law. However, its fundamental dependence on the two fluid formulation limits its versatility and Landau damping is not contained in the fluid model. Furthermore, relatively large numerical dissipation needs to be applied to achieve numerical stability.

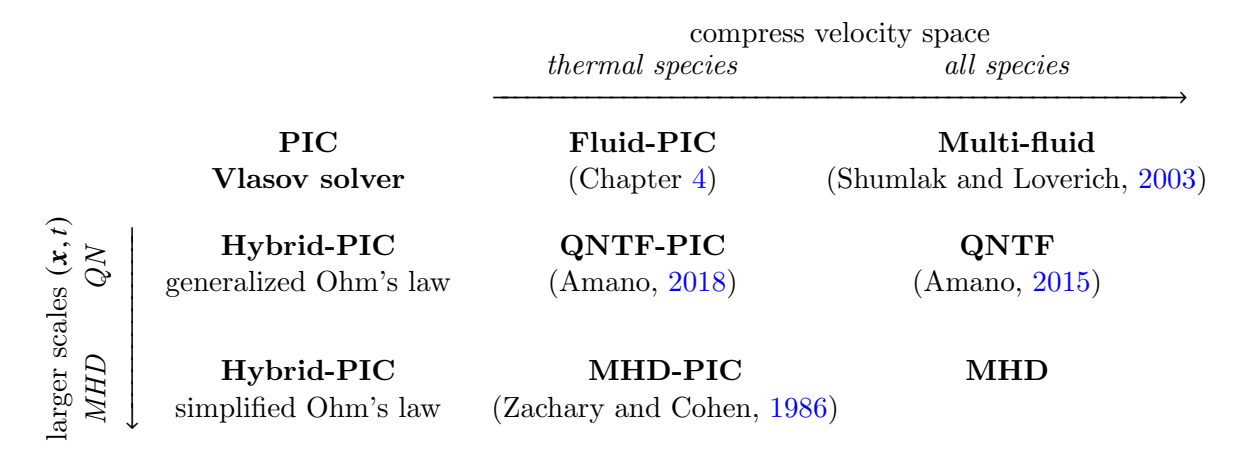


Table 3.1. An overview of numerical solvers. We provide citations for less-frequently applied solvers. Starting from the fully kinetic solvers in the upper-left corner, codes in the lower rows utilizing the quasi-neutral (QN) and MHD approximations are applicable if small spatial and temporal scales can be neglected. Codes to the right are applicable, if some or all species are thermal. Solvers in the central column are generally well-suited for the CR streaming setup in terms of efficiency and accuracy. The solvers by Shumlak and Loverich (2003) and Amano (2015, 2018) presuppose a two-fluid (ion and electron) formulation, the abbreviation QNTF stands for quasi-neutral two-fluid. For multi-fluid solvers we also refer to Shumlak et al. (2011) and Wang et al. (2015). Some compound Vlasov methods exist (Valentini et al., 2007), but we focus on methods employing PIC.

Currently, there is no existing code that meets all the criteria we identified at the beginning of this section; in particular, no fluidized thermal code models Landau damping. To address this gap, we developed a fluid-module extension for the SHARP code (Shalaby et al., 2017b, 2021), which minimizes Poisson noise and numerical heating through high-order shape functions. Since we prioritize capturing electron-scale phenomena (requirement i), we maintain SHARP's original PIC routine unchanged, preserving its excellent conservation properties while adding the fluid component as a supplementary module. The absence of filtering in this code enables the elimination of spurious self-forces even if employing few particles per cell, ensuring an efficient representation of the sparse CRs. We implement a Landau-fluid approximation for thermal species that, while not yet incorporating ion-neutral collisions, provides a theoretical framework for its future implementation (requirement ii). Our approach differs from previous multi-fluid and two-fluid codes (Shumlak and Loverich, 2003; Shumlak et al., 2011; Wang et al., 2015): rather than implicitly coupling electromagnetic sources to the fluid, we employ a fully explicit scheme that preserves the PIC routine's electromagnetic field solver. This enables initialization of arbitrary combinations of fluid and PIC species, allowing to model arbitrary distribution functions (requirement iii and iv), unless excessive noise were to dictate the use of the  $\delta f$  method, which would prohibit arbitrary CR distributions. In the following Chapter 4 we will describe its implementation and perform numerical tests, indicating its high-fidelity and computational efficiency (requirement v) even without the  $\delta f$  method.

Table 3.1 summarizes different numerical approaches. While established kinetic methods (left column) require significant parameter compromises for gyroresonant CR streaming problems

(though they remain applicable to non-resonant Bell instability), pioneering studies using PIC (Holcomb and Spitkovsky, 2019; Shalaby et al., 2021) and Hybrid-PIC codes (Schroer et al., 2024) have been conducted. Pure fluid frameworks (right column) cannot adequately capture CR microphysics, but approaches fluidizing thermal species (central column) offer an optimal balance of efficiency and accuracy. Our proposed fluid-PIC code fills the remaining upper spot of the central column in Table 4.1.

# 4. The fluid-PIC method

This chapter is based on the published paper by Lemmerz, R.; Shalaby, M.; Thomas, T.; Pfrommer, C.:

Journal of Plasma Physics, vol. 90, no. 1, p. 905900104, 2024. doi:10.1017/S0022377823001113

The particle-in-cell (PIC) method is successfully used to study magnetized plasmas. However, this requires large computational costs and limits simulations to short physical run-times and often to setups in less than three spatial dimensions. Traditionally, this is circumvented either via hybrid-PIC methods (adopting massless electrons) or via magneto-hydrodynamic-PIC methods (modelling the background plasma as a single charge-neutral magneto-hydrodynamical fluid). Because both methods preclude modelling important plasma-kinetic effects, we introduce a new fluid-PIC code that couples a fully explicit and charge-conservative multi-fluid solver to the PIC code SHARP through a current-coupling scheme and solve the full set of Maxwell's equations. This avoids simplifications typically adopted for Ohm's Law and enables us to fully resolve the electron temporal and spatial scales while retaining the versatility of initializing any number of ion, electron, or neutral species with arbitrary velocity distributions. The fluid solver includes closures emulating Landau damping so that we can account for this important kinetic process in our fluid species. Our fluid-PIC code is second-order accurate in space and time. The code is successfully validated against several test problems, including the stability and accuracy of shocks and the dispersion relation and damping rates of waves in unmagnetized and magnetized plasmas. It also matches growth rates and saturation levels of the gyro-scale and intermediate-scale instabilities driven by drifting charged particles in magnetized thermal background plasmas in comparison to linear theory and PIC simulations. This new fluid-SHARP code is specially designed for studying high-energy cosmic rays interacting with thermal plasmas over macroscopic timescales.

# 4.1. Introduction

Astrophysical plasmas naturally partition into thermal and non-thermal particle populations. Provided particles collide frequently via (Coulomb) collisions, this eventually leads to a characteristic thermal Maxwellian phase-space distribution. This population can be reliably described with the fluid approximation, which characterizes a vast amount of particles by a few macroscopic fields in space (e.g., number density, mean velocity and temperature). By contrast, the non-thermal cosmic ray (CR) ion population at energies exceeding GeV is mostly collisionless and interacts with the background plasma via wave-particle interactions, thus retaining its initial power-law distribution for much longer times (Blandford and Eichler, 1987; Draine, 2011; Zweibel, 2017). Low-energy CRs ( $\leq$  GeV) more frequently experience Coulomb/ionisation collisions and as such have a direct influence on gas dynamics and molecular chemistry (Dalgarno, 2006a; Padovani et al., 2020). CRs can excite and grow plasma waves via instabilities at which they scatter in pitch angle (i.e., the angle between momentum and magnetic field vector), thereby regulating their macroscopic transport speed and exchanging energy and momentum with the thermal population. Modelling these plasma processes requires to move beyond the classical fluid approximation.

During the process of diffusive shock acceleration, CRs stream ahead of the shock into the precursor region and drive non-resonant Alfvén waves unstable by means of their powerful current (Bell, 2004; Riquelme and Spitkovsky, 2009; Caprioli and Spitkovsky, 2014b), which provides efficient means of increasing their wave-particle scattering and reducing the CR diffusion coefficient (Caprioli and Spitkovsky, 2014c). Upon escaping from the acceleration site into the ambient medium, CRs continue to drive Alfvén-waves through resonant instabilities. Scattering off of these self-induced waves regulates their transport speed (Kulsrud and Pearce, 1969; Marcowith et al., 2021; Shalaby et al., 2021), which is determined by the balancing instability growth and wave damping (Thomas and Pfrommer, 2019; Thomas et al., 2020). In the interstellar medium, CRs provide a comparable if not dominant pressure, despite their negligible number densities in comparison to the thermal population, which makes them dynamically important (Boulares and Cox, 1990; Draine, 2011). Their pressure gradient can drive outflows from the interstellar medium (Simpson et al., 2016; Girichidis et al., 2018; Farber et al., 2018) so that powerful global winds emerge from galaxies (Uhlig et al., 2012; Hanasz et al., 2013; Pakmor et al., 2016; Ruszkowski et al., 2017b) that enrich the circumgalactic medium in galaxy haloes with CRs that can also dominate the pressure support and modify the cosmic accretion of gas onto galaxies (Buck et al., 2020; Ji et al., 2020). The degree to which CRs regulate galaxy formation critically depends on the efficiency of wave-particle interactions, which in turn depends on the amplitude of self-excited plasma waves (Thomas et al., 2023). On even larger scales, CRs energised in jets of active galactic nuclei stream into the surrounding intracluster medium of cool core clusters and heat it via the excitation of Alfvén waves and the successive damping (Guo and Oh, 2008; Pfrommer, 2013; Ruszkowski et al., 2017a; Jacob and Pfrommer, 2017b). Because the plasma physics underlying these processes is highly non-linear, numerical calculations are needed to study these effects.

Due to its ability to resolve kinetic processes, the PIC method (Dawson, 1962; Langdon and Birdsall, 1970; Hockney, 1988; Birdsall and Langdon, 1991) has become one of the most used methods for studying plasmas from laboratory to astrophysical scales. Examples of that include revolutionizing our understanding of the rich physics found in collisionless shocks (Spitkovsky, 2008; Marcowith et al., 2016), magnetic reconnection (Daughton et al., 2006; Daughton et al., 2011; Sironi and Spitkovsky, 2014), instabilities driven by highly relativistic electron-positron beams (Bret et al., 2010; Shalaby et al., 2017a, 2018, 2020), as well as the transport of non-thermal particle populations like CRs (Holcomb and Spitkovsky, 2019; Shalaby et al., 2021). However, the PIC method needs to advance numerous particles per cell each time step, and thus it is quick to reach its computational limit. Even one-dimensional simulations usually only capture dynamics on very short physical times and the extent to which two or three-dimensional simulations can be performed is very limited.

The time interval between the inverse of the electron plasma frequency,  $\omega_e^{-1}$ , (which is necessary to ensure the stability of the PIC algorithm) and that of the ion plasma frequency,  $\omega_i^{-1}$ , depends on the ion-to-electron mass ratio, since  $\omega_i^{-1}/\omega_e^{-1} = (m_i/m_e)^{1/2}$ , assuming charge neutrality, i.e. that the electron and ion densities are equal. Therefore, one frequently used trick to increase the computational efficiency in PIC simulations is to adopt a reduced ion-to-electron mass ratio to bridge the gap between the smallest timescale in the simulation and the larger timescale on which interesting physical processes occur. However, this might lead to artificial suppression of physical effects (Bret and Dieckmann, 2010; Hong et al., 2012; Moreno et al., 2018), including instabilities with excitation conditions that depend on the mass ratio (Shalaby et al., 2021, 2022). This shows the need for a more efficient numerical method to complement the accurate results achieved by PIC simulations in order to enable simulations of realistic physics occurring on longer timescales. One possible method consists in using the less expensive fluid approximation, which works particularly well for collisional systems where frequent particle collisions maintain a thermodynamic temperature but is less well motivated in weakly collisional or even collisionless astrophysical plasmas where it cannot accurately capture some important microphysical plasma processes.

Multiple methods have been devised that combine the computational advantages of a fluid code, while trying to maintain some of the physics accuracy provided by the PIC method. Hybrid-PIC codes (Lipatov, 2002; Gargaté et al., 2007) treat electrons as a massless fluid and ions as particles. With the assumption of charge neutrality and the Darwin approximation (i.e., neglecting the transverse displacement current), these codes are able to overcome some computational barriers while omitting effects on the electron time and length scale. Since this eliminates the need to resolve electron scales, the increase in computational efficiency from pure-PIC to hybrid-PIC methods is roughly a factor of  $(m_i/m_e)^{1/2}$  in timescale and about the same factor in spatial scales. In cases where the electron pressure anisotropy becomes important such as in magnetic reconnection, a hybrid Vlasov-Maxwell system can be coupled to an anisotropic electron fluid with a Landau fluid closure, which captures more kinetic physics (Finelli et al., 2021). On the other hand, an even more efficient method exists, that combines the magneto-hydrodynamic (MHD) description of the thermal background plasma with PIC methods to

#### 4. The fluid-PIC method

model the evolution of energetic particles such as CRs (Bai et al., 2015; van Marle et al., 2018), called MHD-PIC. However, this method inherits the assumptions of MHD, in particular, the use of (simplified) Ohm's law by fully neglecting the displacement current, which precludes physics associated with higher-order terms of Ohm's law as well as the electron dynamics.

In this paper we present a self-consistent algorithm that is suitable for simulating microphysical effects of CR physics by only applying the fluid approximation to thermal particles and solving the full set of Maxwell's equations. Our goal of this novel fluid-PIC method is to sacrifice as little physics accuracy as possible, while at the same time alleviating computational restraints by orders of magnitude for setups involving CRs (or similar, low density non-thermal particle populations interacting with a thermal plasma). The fluid-PIC method, in essence, couples a multi-fluid solver to the PIC method by summing their contributions to the charge and current densities used to solve Maxwell's equations, and the resulting electromagnetic fields. Thus, the subsequent dynamics is dictated by fluid and PIC species. This enables treating any arbitrary number of species in thermal equilibrium by modelling them as separate fluids that interact electromagnetically with each other and with particles of arbitrary momentum distribution (modelled using the PIC method). In contrast to MHD-PIC and hybrid-PIC methods, we do not explicitly assume Ohm's law, and instead, solve Maxwell's equations in a fully selfconsistent manner in our fluid-PIC code. Therefore, displacement currents are included in our model and fast changes in the electric field and electron dynamics are captured. This, in turn, allows studying the interaction of high energy particles with the background plasma, e.g. to investigate CR streaming. Another hybrid approach resolving electron timescales fully, but using pressure coupling, has been used for simulation of pick-up ions in the heliosphere by Burrows et al. (2014).

Often implicit and semi-implicit methods are utilized for stability and resolution reasons to couple the multi-fluid equations to Maxwell's equations (Hakim et al., 2006; Shumlak et al., 2011; Wang et al., 2020). However, this creates an interdependency between all fluids and has limited utility when coupled to explicit particles. We have developed an explicit multi-fluid solver in which each fluid and particle species is agnostic about each other and the coupling is achieved via an indirect current-coupling scheme. Because the PIC part of the code is the most computationally expensive part of the fluid-PIC, hybrid-PIC, and MHD-PIC methods, the computational efficiency is mostly determined by the number of particles required as well as the smallest time and length scales that need to be resolved. Hence, this fluid-PIC approach results in large speed-ups for CR propagation simulations in comparison to traditional hybrid-PIC codes, which treat every ion as a particle and need to initialize a large number of particles according to the density ratio, as well as in comparison to PIC-only simulations. Especially studying comic ray propagation in the interstellar medium, where the typical CR density is of the order 10<sup>-9</sup> times the interstellar medium number density, is challenging. Since the fluid-PIC algorithm is faster by orders of magnitude in comparison to PIC in such a case, we can reach further into the realistic parameter regime without sacrificing some essential microphysics.

One of the most important kinetic effects is arguably Landau damping. The fluid description can emulate this effect using Landau closures (Hammett and Perkins, 1990; Umansky et al.,

2015; Hunana et al., 2019b), which necessitates the computation of the heat flux in Fourier space. While Fourier transforms in 1D are not easily parallelizable, this bottleneck can partially be mitigated by performing global communications of the message-passing interface (MPI) in the background while processing the high computational load (e.g. resulting from evolving orbits of PIC particles) in the foreground. Simulations with periodic boundary conditions are currently handled by convolution with a finite-impulse-response (FIR) filter in our code, but other options are available in the literature (Dimits et al., 2014; Wang et al., 2019). A number of simplifying local approximations exist as well (Wang et al., 2015; Allmann-Rahn et al., 2018; Ng et al., 2020), which scale computationally well but become inaccurate for studying some multiscale plasma physics problems. Our code implements these different approaches so that an appropriate one can be chosen, dependent on the requirements of a simulation. Our implementation is massively parallelized and can be efficiently run on thousands of cores. Furthermore, the fluid-PIC method allows for any multi-fluid setup. As such, this framework allows for some straightforward extensions. Potentially, this involves a setup with actively participating neutrals to incorporate ion-neutral damping into this method. To this end, the coupling between different fluids needs to be extended by a collision term, which is left as a future extension to the code.

The outline of this paper is as follows. In Section 4.2, we introduce the pillars of this method and describe the PIC method, the fluid solver, how we couple both methods by means of electromagnetic fields, and describe various implementations of the Landau closure. In Section 4.3, we show validation tests of the fluid solver (shock tube tests), linear waves in an ion-electron plasma, and the damping rate of Langmuir waves in a single-electron fluid with Landau closures. We then investigate the non-linear effects of two interacting Alfvén waves as well as cosmic-ray-driven instabilities, where fluid-PIC and PIC results are compared. We conclude in Section 4.4. Throughout this work, we use the SI system of units.

## 4.2. Numerical Method

After a review of the kinetic description of a plasma in Section 4.2.1, we briefly introduce our PIC method in Section 4.2.2. The fluid description for plasmas and its assumptions are given in Section 4.2.3. The finite volume scheme we use to numerically solve the compressible Euler equations is described in Section 4.2.4, while the electromagnetic interactions of the fluid are described in Section 4.2.5. In Section 4.2.6, we describe the Landau closure we adopt in order to mimic the Landau damping in kinetic thermal plasmas within the fluid description, and detail its implementation in our code. We close this Section by describing the overall code structure of the fluid-PIC algorithm and finally discuss the interaction between the modules via the current-coupling scheme (Section 4.2.7).

## 4.2.1. Kinetic description of a plasma

The kinetic description of a collisionless relativistic plasma with particles of species s with elementary mass,  $m_s$ , and elementary charge,  $q_s$ , is given by the Vlasov equation,

$$\frac{\partial f_{\rm s}}{\partial t} + \frac{\mathbf{u}}{\gamma} \cdot \nabla f_{\rm s} + \mathbf{a}_{\rm s} \cdot \nabla_{u} f_{\rm s} = 0, \tag{4.1}$$

where  $f_s = f_s(\boldsymbol{x}, \boldsymbol{v}, t)$  is the distribution function,  $\boldsymbol{u} = \gamma \boldsymbol{v}$  is the spatial component of the four-velocity with the Lorentz factor  $\gamma = [1 + (\boldsymbol{v}/c)^2]^{-1/2}$ , and c is the light speed. The acceleration due to the Lorentz force is given by

$$\boldsymbol{a}_{\mathrm{S}} = \frac{q_{\mathrm{S}}}{m_{\mathrm{S}}} \left[ \boldsymbol{E} \left( \boldsymbol{x}, t \right) + \boldsymbol{v} \times \boldsymbol{B} \left( \boldsymbol{x}, t \right) \right], \tag{4.2}$$

where E(x,t) and B(x,t) are the electric and magnetic fields, respectively. The evolution of electric and magnetic fields is governed by Maxwell's equations:

$$\frac{\partial \mathbf{B}}{\partial t} = -\nabla \times \mathbf{E}, \qquad \nabla \cdot \mathbf{B} = 0, \tag{4.3}$$

$$\frac{\partial \mathbf{E}}{\partial t} = c^2 \nabla \times \mathbf{B} - \frac{\mathbf{J}}{\varepsilon_0}, \qquad \nabla \cdot \mathbf{E} = \frac{\rho}{\varepsilon_0}, \tag{4.4}$$

where  $c = 1/\sqrt{\varepsilon_0 \mu_0}$  is the vacuum speed of light, and  $\varepsilon_0$  and  $\mu_0$  are the permittivity and the permeability of free space, respectively. The evolution of the electro-magnetic fields is influenced by the charge density,  $\rho$ , and current density, J. They are given by the charge-weighted sum over all species of the number densities  $n_s$  and bulk velocities  $\boldsymbol{w}_s$  respectively,

$$\rho\left(\boldsymbol{x},t\right) = \sum_{s} q_{s} n_{s}\left(\boldsymbol{x},t\right) \qquad = \sum_{s} q_{s} \int f_{s}\left(\boldsymbol{x},\boldsymbol{v},t\right) d^{3}v, \tag{4.5}$$

$$\boldsymbol{J}(\boldsymbol{x},t) = \sum_{s} q_{s} n_{s}(\boldsymbol{x},t) \boldsymbol{w}_{s}(\boldsymbol{x},t) = \sum_{s} q_{s} \int \boldsymbol{v} f_{s}(\boldsymbol{x},\boldsymbol{v},t) d^{3} v.$$
(4.6)

## 4.2.2. The particle-in-cell method

We use the PIC method to solve for the evolution of plasma species that are modelled with the kinetic description. The PIC method initializes a number of computational macroparticles to approximate the distribution function in a Lagrangian fashion. Each macroparticle represents multiple physical particles and, as such, each macroparticle has a shape in position space which can be represented by a spline function. By depositing the particle motions and positions to the numerical grid (or computational cells), the electromagnetic fields can be computed. This step is followed by a back-interpolation of these fields to the particle positions so that the Lorentz forces on the particles can be computed. In our implementation, these equations are solved using one spatial dimension and three velocity dimensions (1D3V), i.e.  $\nabla = (\partial/\partial x, 0, 0)^{T}$ .

The code quantities are defined as multiples of the fiducial units given for time, fields (electric

and magnetic), charge, current density and length

$$t_0 = \sqrt{m_0 \epsilon_0 / (q_0^2 n_0)}, \quad E_0 = \sqrt{n_0 m_0 c^2 / \epsilon_0},$$

$$\rho_0 = q_0 n_0, \quad J_0 = \rho_0 c, \quad x_0 = c t_0.$$
(4.7)

This enables us to select a fixed time step of

$$\Delta t = C_{\text{cfl}} c \Delta x \tag{4.8}$$

where  $C_{\rm cfl} < 0.5$  to satisfy the Courant-Friedrichs-Lewy (CFL) condition. The value of the reference density  $n_0$  is chosen such that the code timescale,  $t_0$ , obeys  $\omega_{\rm p}^{-2} = t_0^2$ . The total plasma frequency is  $\omega_{\rm p} = (\sum_s \omega_s^2)^{1/2}$ , and related to the plasma frequencies of the individual species,  $\omega_s^2 = q_s^2 n_s/(m_s \epsilon_0)$ . We define the discretized time  $t^k = k\Delta t$ , position  $x_i = i\Delta x$  and quantities at discrete position and times as  $\boldsymbol{E}_i^k = \boldsymbol{E}(t^k, x_i)$ . For details on the PIC code SHARP, the reader is referred to Shalaby et al. (2017b, 2021). Here, we focus on describing how SHARP is extended to include fluid treatment of some plasma species.

## 4.2.3. Fluid description of plasma

A straightforward way of coarse graining the Vlasov equation (4.1) is to reduce its dimensionality. By taking the j-th moment over velocity space, i.e.  $\int \mathbf{v}^j f d^3 v$ , we retrieve the fluid quantities and reduce the dimensionality of the 1D3V kinetic description to 1D. The number density  $n_s$  and the bulk velocity  $\mathbf{w}_s$  are defined through the zeroth and first moment of the distribution function, respectively, while the total energy density per unit mass  $\epsilon_s$  and the scalar pressure per unit mass  $p_s$  are related to the second moment (Wang et al., 2015):

$$n_{\rm s}(\boldsymbol{x},t) = \int f_{\rm s}(\boldsymbol{x},\boldsymbol{v},t) \,\mathrm{d}^3 v, \tag{4.9}$$

$$\boldsymbol{w}_{s}(\boldsymbol{x},t) = \int \frac{1}{n_{s}(\boldsymbol{x},t)} \boldsymbol{v} f_{s}(\boldsymbol{x},\boldsymbol{v},t) d^{3}v, \qquad (4.10)$$

$$\epsilon_{\mathrm{s}}(\boldsymbol{x},t) = \int \frac{1}{2} \boldsymbol{v}^2 f_{\mathrm{s}}(\boldsymbol{x},\boldsymbol{v},t) \,\mathrm{d}^3 v, \tag{4.11}$$

$$p_{\mathrm{s}}(\boldsymbol{x},t) = \int (v_{\mathrm{x}} - w_{\mathrm{s},x})^2 f_{\mathrm{s}}(\boldsymbol{x},\boldsymbol{v},t) \,\mathrm{d}^3 v = \frac{\Gamma - 1}{2} \int (\boldsymbol{v} - \boldsymbol{w}_{\mathrm{s}})^2 f_{\mathrm{s}}(\boldsymbol{x},\boldsymbol{v},t) \,\mathrm{d}^3 v. \tag{4.12}$$

Here, the pressure tensor is under the adiabatic assumption and the degrees of freedom are encoded in the adiabatic index  $\Gamma$ . The following relation is found from the definitions

$$\epsilon_{\rm s} = \frac{p_{\rm s}}{\Gamma - 1} + \frac{1}{2} n_{\rm s} \boldsymbol{w}_{\rm s} \cdot \boldsymbol{w}_{\rm s}. \tag{4.13}$$

The first three moments of the Vlasov equation are called the continuity, momentum, and energy conservation equations. A set of these equations is found for each fluid species, but the

subscript s is neglected here for simplicity:

$$\frac{\partial n}{\partial t} + \nabla \cdot (n\boldsymbol{w}) = 0, \tag{4.14}$$

$$\frac{\partial n\boldsymbol{w}}{\partial t} + \boldsymbol{\nabla} \cdot [p\boldsymbol{1} + n\boldsymbol{w}\boldsymbol{w}] = \frac{q}{m} \boldsymbol{S}_{w} (n, \boldsymbol{w}, \boldsymbol{B}, \boldsymbol{E}), \qquad (4.15)$$

$$\frac{\partial \epsilon}{\partial t} + \nabla \cdot [(p + \epsilon)w] + \frac{1}{\Gamma - 1} \nabla \cdot Q = \frac{q}{m} w \cdot S_w (n, w, B, E). \tag{4.16}$$

We assumed the non-relativistic limit and an isotropic pressure tensor with vanishing non-diagonal components, i.e. the inviscid limit. The notation ww indicates the dyadic product of the two vectors and  $\mathbf{1}$  is the unit matrix. Similar to the definition of the scalar pressure in equation (4.12) we use a definition of the heat flux vector, which is normalized to the degrees of freedom as well

$$\mathbf{Q}(\mathbf{x},t) = \frac{\Gamma - 1}{2} \int (\mathbf{v} - \mathbf{w})^2 (\mathbf{v} - \mathbf{w}) f(\mathbf{x}, \mathbf{v}, t) d^3 v.$$
 (4.17)

The electromagnetic source term is given by

$$S_w(n, \boldsymbol{w}, \boldsymbol{B}, \boldsymbol{E}) = n(\boldsymbol{E} + \boldsymbol{w} \times \boldsymbol{B}). \tag{4.18}$$

The general form of the fluid equations can be written as

$$\frac{\partial \tilde{\boldsymbol{U}}}{\partial t} + \nabla \cdot \mathbf{F}(\tilde{\boldsymbol{U}}) = \boldsymbol{S}(\tilde{\boldsymbol{U}}), \tag{4.19}$$

where  $\tilde{\boldsymbol{U}} = \tilde{\boldsymbol{U}}(\boldsymbol{x},t) = (n,n\boldsymbol{w},\epsilon)^{\mathrm{T}}$  is the fluid state vector at position  $(\boldsymbol{x},t)$ ,  $\boldsymbol{\mathsf{F}}$  is the flux matrix, and  $\boldsymbol{S}$  is the source vector.

Numerically, the complexity of solving equation (4.19) can be reduced by splitting the operator into less complex sub-operators using Strang operator splitting (Strang, 1968; Hakim et al., 2006). This enables us to use the most appropriate solver for each subsystem sequentially. We split the fluid update into three parts; the flux  $\mathbf{F}$  excluding the heat flux (see Section 4.2.4), the electromagnetic source  $\mathbf{S}_{\rm em} = \mathbf{S}_w q/m$  (see Section 4.2.5), and the heat flux  $\mathbf{Q}$  (see Section 4.2.6). For commuting operators  $\exp(\Delta t \mathbf{Q})$  and  $\exp(\Delta t \mathbf{S}_{\rm em})$  a second order accurate Strang splitting is obtained as

$$\boldsymbol{U}^{n+\frac{1}{2}} = e^{\frac{\Delta t}{2}} \mathbf{F} e^{\Delta t} \boldsymbol{Q} e^{\Delta t} \mathbf{S}_{em} e^{\frac{\Delta t}{2}} \mathbf{F} \boldsymbol{U}^{n-\frac{1}{2}} + O(\Delta t^3). \tag{4.20}$$

If Q and  $S_{\rm em}$  act independently on the entries p and w respectively, then the order of applying them can be varied and they need to be evaluated only once. In practice the formulation of Q might partially depend on w. In this case, Strang splitting is performed on this part of the operator Q as well, see equation (4.47). In order to apply  $S_{\rm em}$  (and Q, which depends on the direction of B) one needs to find the electromagnetic quantities at time  $t^n$  first. The components of E along the simulated spatial direction can only be updated from time  $t^{n-1}$  to  $t^n$  after applying  $\exp(\Delta t/2 \times F)$  for the first time (see Section 4.2.5). Therefore, electromagnetic quantities need to be calculated between these updates. This is unproblematic as F is independent of the

electromagnetic field, and we can defer updating E without reducing accuracy.

## 4.2.4. Finite volume scheme

The 1D3V fluid equations are solved using a finite volume method, where the fluid equations are averaged over the cell volume, which is an interval of length  $\Delta x$  in 1D,

$$U_{i}(t) = \frac{1}{\Delta x} \int_{x_{i-\frac{1}{2}}}^{x_{i+\frac{1}{2}}} \tilde{U}(x,t) dx.$$
 (4.21)

This enables us to correctly conserve the overall fluid mass, fluid momentum and fluid energy, even in the presence of large gradients, by utilizing Gauss' theorem:

$$\frac{1}{\Delta x} \int_{x_{i-\frac{1}{2}}}^{x_{i+\frac{1}{2}}} \frac{\partial \boldsymbol{F}(\tilde{\boldsymbol{U}})}{\partial x} dx = \frac{1}{\Delta x} \left[ \boldsymbol{F}_{i+\frac{1}{2}} - \boldsymbol{F}_{i-\frac{1}{2}} \right]$$
(4.22)

where the flux through an interface at  $x_i$  is  $F_i(t) = F[\tilde{U}(x_i, t)]$ , leading to the update equation

$$\frac{\partial \boldsymbol{U}_{i}(t)}{\partial t} = \frac{1}{\Delta x} \left[ -\boldsymbol{F}_{i+\frac{1}{2}} + \boldsymbol{F}_{i-\frac{1}{2}} + \int \boldsymbol{S}(\tilde{\boldsymbol{U}}(x,t)) dx \right]. \tag{4.23}$$

Integrating equation (4.23) in time is achieved by using at least second-order Runge-Kutta methods (Butcher, 2016), which is the limit set by the operator splitting scheme. We could not find examples yet, where higher-order Runge-Kutta methods have performed noticeably different from second-order methods in the fluid-PIC code. In contrast to the finite difference scheme used for electromagnetic fields and particles, where electromagnetic quantities are point values, fluid quantities discretized with the finite volume method are cell averages. This is useful, because the finite difference method does not guarantee the conservation of the conservation equations (4.14) through (4.16), which are governing the fluid; while on the other hand using the finite volume method for the electromagnetic fields needs additional steps to satisfy the constraint  $\nabla \cdot \mathbf{B} = 0$ . Hybridization of both schemes to combine the advantages of each has been used before in other contexts, i.e. Soares Frazao and Zech (2002).

The maximum time step in the 1D3V Euler equations, which allows for stable simulations, is  $\Delta t < C_{\rm cfl} \Delta x/(|w| + c_{\rm s})$ , with the speed of sound  $c_{\rm s} = (\Gamma p/n)^{1/2}$ . For all realistic setups these velocities are limited naturally by the speed of light, |w| < c and  $c_{\rm s} < c$ , and this condition is automatically fulfilled by the time step criterion in equation (4.8). In practice, only equation (4.8) together with a suitable Courant number of  $C_{\rm cfl} \le 0.5$  is used to determine the time step of the simulation.

#### Reconstruction

To approximate the flux at interfaces, we need to reconstruct the fluid state at cell interfaces. The accuracy of the reconstruction has a crucial influence on the diffusivity. A lower-order reconstruction can lead to excessive damping of waves, which might suppress relevant physical

effects on longer timescales.

For reconstructing the point value  $\tilde{\boldsymbol{U}}(x_{i+1/2},t)$ , which is needed to compute  $\boldsymbol{F}_{i+1/2}$ , we employ a central weighted essentially non-oscillatory reconstruction (C-WENO) scheme of spatial order five. The reconstruction computes two point values at each interface  $x_{i+1/2}$ , an interpolation from the left- and right-hand side. We reconstruct the primitive variables  $n, \boldsymbol{w}$ , and p individually.

Our implementation of the C-WENO method is based on the 5th order scheme presented in Capdeville (2008). An introduction to the topic can be found in Cravero et al. (2018a). The C-WENO reconstruction uses a convex combination of multiple low-order reconstruction polynomials to achieve high-order interpolations of the interface values while it employs a non-linear limiter to degrade this high-order interpolation to a lower order if the reconstructed quantity contains discontinuities. The fifth-order C-WENO uses three third-order polynomials  $P_{\rm L}(x), P_{\rm C}(x), P_{\rm R}(x)$  for each cell i to interpolate the four adjacent cells in the following way:

 $P_{\rm L}(x)$  interpolates values at i-2 i-1 i

 $P_{\rm C}(x)$  interpolates values at i-1 i i+1

 $P_{\rm R}(x)$  interpolates values at i = i+1 = i+2

while the optimal fifth-order polynomial interpolates all of them:

 $P_{\text{opt}}(x)$  interpolates values at i-2 i-1 i i+1 i+2.

We define an additional polynomial

$$P_0(x) = \frac{1}{d_0} \left[ P_{\text{opt}}(x) - \sum_{q \in [L, C, R]} d_q P_q(x) \right], \tag{4.24}$$

where  $d_0 + d_L + d_C + d_R = 1$ . The polynomials  $P_0$ ,  $P_L$ ,  $P_C$ , and  $P_R$  are a convex representation of the  $P_{\text{opt}}$  polynomial. We use  $d_0 = 3/4$ ,  $d_C = 2/16$ , and  $d_L = d_R = 1/16$ .

In general, we would like to use the reconstruction provided by the  $P_{\rm opt}$  polynomial as frequently as possible because of its high-order nature. But this high-order reconstruction can cause oscillations similar to the Gibbs phenomenon at discontinuities. Therefore, we need to employ a limiting strategy to avoid such behaviour. In order to accomplish this, we re-weight all of our d-coefficients by taking the smoothness of the associated polynomial into account (Jiang and Shu, 1996). We define

$$\alpha_q = d_q \left[ 1 + \left( \frac{\tau}{\text{IS}[P_q] + 10^{-9} \Delta x} \right)^2 \right] \quad \text{for } q \in [0, L, C, R],$$
 (4.25)

where  $\tau$  is a measure for the overall smoothness of the reconstructed variables, and IS  $[P_q]$  defines a smoothness indicator of the low-order polynomials. Because the formulae for these smoothness indicators are quite cumbersome, we list them in Appendix 4.A. These coefficients define a new set of normalized weights given by

$$w_q = \frac{\alpha_q}{\alpha_0 + \alpha_L + \alpha_C + \alpha_R} \quad \text{for } q \in [0, L, C, R].$$
 (4.26)

The final reconstructed polynomial is then given by the convex combination of the low-order

polynomials using this set of normalized weights:

$$P_{\rm rec}(x) = w_0 P_0(x) + w_{\rm L} P_{\rm L}(x) + w_{\rm C} P_{\rm C}(x) + w_{\rm R} P_{\rm R}(x), \tag{4.27}$$

which we evaluate at the cell interfaces to calculate the required left- and right-handed interface values for the Riemann solver. We detail how these polynomials are evaluated in Appendix 4.A.

The smoothness indicators  $\mathrm{IS}[P_q]$  vanish if the underlying polynomials are smooth. In this case, the re-weighted coefficients reduce to their original value  $\alpha_q \to d_q$  and the reconstructed polynomial reduces to the optimal polynomial  $P_{\mathrm{rec}}(x) \to P_{\mathrm{opt}}(x)$ .

#### Riemann solver

The previous reconstruction step determines two, potentially different, values  $\tilde{\boldsymbol{U}}_{\mathrm{L}}$  and  $\tilde{\boldsymbol{U}}_{\mathrm{R}}$  for each quantity to the left and right of every interface, thereby providing the initial conditions for the Riemann problem:

$$\frac{\partial U}{\partial t} = -\nabla \cdot \mathbf{F}(\tilde{U}) \tag{4.28}$$

$$\tilde{\boldsymbol{U}}(x,0) = \begin{cases} \tilde{\boldsymbol{U}}_{L}, & x < 0\\ \tilde{\boldsymbol{U}}_{R}, & x > 0 \end{cases}$$

$$(4.29)$$

An (approximate) Riemann solver is employed to compute the numerical flux  $\mathbf{F}(\tilde{U})$ . While a number of different families of Riemann solvers have been developed with individual strengths and weaknesses, we have decided to implement multiple solvers which can be changed on demand. Implemented solvers in fluid-SHARP include a Roe solver with entropy fix (Roe, 1981; Harten and Hyman, 1983) and an HLLC solver (Toro et al., 1994). While the Roe solver yields more accurate solutions and fewer overshoots in our tests in comparison to the HLLC solver, it becomes unstable in near vacuum flows and strong expansion shock waves. Even though differences between the solvers are easily visible in some shock setups and artificially extreme conditions, they are typically negligible in most applications common for thermal plasmas. We opt to employ the HLLC solver as our standard for stability purposes and use the Roe solver in cases where stronger shocks with overshoots are expected.

#### Importance of wave characteristics in approximating stable numerical fluxes

The characteristic curves of the Euler equations without sources correspond to the eigensystem of the flux Jacobian  $\partial F/\partial U$ . Approximate Riemann solvers use these characteristics for computing fluxes across small time steps and introduce numerical dissipation to suppress spurious instabilities. For the hydrodynamic Euler equations in 1D3V (without a heat flux), five characteristics emerge with characteristic wave speeds  $\lambda = w_x - c_s, w_x + c_s, w_x$ , where the last eigenvalue  $w_x$  has a multiplicity of 3. In particular, the Roe solver (without the entropy fix) computes the numerical flux at an interface by averaging the physical fluxes as follows (LeVeque,

2002), 
$$\boldsymbol{F}_{\text{num}} = \frac{1}{2} \left[ \boldsymbol{F}(\tilde{\boldsymbol{U}}_{\text{L}}) + \boldsymbol{F}(\tilde{\boldsymbol{U}}_{\text{R}}) - \boldsymbol{D}_{\lambda}(\tilde{\boldsymbol{U}}_{\text{R}}, \tilde{\boldsymbol{U}}_{\text{L}}) \right]. \tag{4.30}$$

The dissipation vector  $\boldsymbol{D}_{\lambda} = \mathbf{R}|\Lambda|\mathbf{R}^{-1}(\tilde{\boldsymbol{U}}_{\mathrm{R}} - \tilde{\boldsymbol{U}}_{\mathrm{L}})$  vanishes for  $\tilde{\boldsymbol{U}}_{\mathrm{R}} = \tilde{\boldsymbol{U}}_{\mathrm{L}}$ . The matrices  $\mathbf{R}(\tilde{\boldsymbol{U}}_{\mathrm{L}}, \tilde{\boldsymbol{U}}_{\mathrm{R}})$ and  $|\Lambda|(\tilde{U}_L, \tilde{U}_R)$  are composed of eigenvectors and a diagonal of the absolute eigenvalues  $|\lambda(\tilde{U}_L, \tilde{U}_R)|$ respectively, where an appropriate averaging of left- and right-hand states at the interface is used to derive these eigenvectors and eigenvalues. That is, the dissipation is directly based on the jump at the interface of each wave multiplied by its characteristic wave velocity. The dissipation vector satisfies the *subcharacteristic condition*, i.e. in characteristic coordinates each eigenvalue is bounded by the dissipation  $-D_{\lambda,i} \leq \lambda_i \leq D_{\lambda,i}$ , and thus stabilizes the scheme without introducing excessive dissipation (LeVeque and Pelanti, 2001; Chen and Liu, 1993; Hsiao, 1997; Whitham, 1974). In multidimensional scenarios, computing the projection of the difference  $(\tilde{U}_{\rm R} - \tilde{U}_{\rm L})$  from a Cartesian grid onto the characteristics can result in violations of this condition or excessive dissipation. In these instances, it can be advantageous to artificially alter the wave speeds entering  $D_{\lambda}$ . Reduced wave speeds can be used to successfully counter excessive dissipation leading to a wrong convergence for low Mach number flows (Dellacherie, 2010), however, this leads to numerical instabilities when applied to high Mach number flows. On the other hand, increased wave speeds have been found to eliminate numerical instabilities at shocks (Peery and Imlay, 1988). While the HLLC solver makes more sophisticated approximations to the wave speeds of the non linear system, the principle of artificially increasing selected wave speed estimates yields the same result (Sangeeth and Mandal, 2019).

To provide an understanding of how these characteristics influence the operator splitting, suppose the following decomposition of the total flux  $F_t = F_A + F_B$  into two fluxes. Hence, we need to compare the numerical estimate of the total flux to that of the individual subsystems, denoted by  $F_A$  and  $F_B$ . The expansion of non-linear systems provided by Strang (1968) yields  $U_i^{n+1} = U_i^n + \Delta t [\Delta F_{i,A}(U^n) + \Delta F_{i,B}(U^n)] + O(\Delta t^2)$ , where we only use terms up to first order for simplicity. The intracell flux  $\Delta F_i = -(F_{\text{num},i+1/2} - F_{\text{num},i-1/2})/\Delta x$  is used for updating U (see equation 4.23). The numerical flux at an interface for one time step is thus

$$\boldsymbol{F}_{\text{num}} = \begin{cases} \frac{1}{2} \left[ \boldsymbol{F}_{\text{t}}(\tilde{\boldsymbol{U}}_{\text{L}}) + \boldsymbol{F}_{\text{t}}(\tilde{\boldsymbol{U}}_{\text{R}}) - \boldsymbol{D}_{\lambda,\text{t}}(\tilde{\boldsymbol{U}}_{\text{R}}, \tilde{\boldsymbol{U}}_{\text{L}}) \right] & \text{if unsplit} \\ \frac{1}{2} \left[ \boldsymbol{F}_{\text{t}}(\tilde{\boldsymbol{U}}_{\text{L}}) + \boldsymbol{F}_{\text{t}}(\tilde{\boldsymbol{U}}_{\text{R}}) - \boldsymbol{D}_{\lambda,A}(\tilde{\boldsymbol{U}}_{\text{R}}, \tilde{\boldsymbol{U}}_{\text{L}}) - \boldsymbol{D}_{\lambda,B}(\tilde{\boldsymbol{U}}_{\text{R}}, \tilde{\boldsymbol{U}}_{\text{L}}) \right] & \text{if split.} \end{cases}$$
(4.31)

Both numerical fluxes converge to the total physical flux; for vanishing dissipation vectors, e.g.  $\tilde{U}_{\rm R} = \tilde{U}_{\rm L}$ , both formulations are equal. Intuitively, the total strength of the dissipation matrix in the unsplit scheme is smaller tr  $|\Lambda_t| \leq {\rm tr} |\Lambda_A| + {\rm tr} |\Lambda_B|$ , while the split scheme is stable provided that the subsolvers are stable (Strang, 1968). As an important consequence, a split Riemann solver only needs to account for the characteristics in the subsystem. This conveniently allows using specific solvers for each subsystem without taking into consideration the other systems of equations. Another possibility is to convert the divergence of a flux into a source term, which eliminates the need for a Riemann solver but results in the loss of guaranteed conservation in the finite volume scheme. We provide two applications, for which this is useful.

First, the heat flux vector  $\mathbf{Q}$ , which is indeed a physical flux, results in a nontrivial change of the wave characteristics. Instead of including this complexity in the Riemann solver here, it is simpler to treat its divergence  $(\nabla \cdot \mathbf{Q})$  as a source term instead (see Section 4.2.6).

Second, in the MHD limit, the evolution equation of the electromagnetic momentum  $\epsilon_0 \partial_t E \times B = -\rho E - J \times B + \nabla \cdot \mathsf{T}_{\rm em}$  collapses to the constraint  $J \times B \sim \nabla \cdot (BB - 1B^2/2)/\mu_0$  (see, e.g., Braginskii, 1965), where the Maxwell stress tensor is given by  $\mathsf{T}_{\rm em} = \epsilon_0 E E + B B/\mu_0 - 0.5(\epsilon_0 E^2 + B^2/\mu_0) \mathbf{1} \approx (BB - 1B^2/2)/\mu_0$ . That is, the electromagnetic source term can be expressed as a divergence of an electromagnetic flux tensor. MHD solvers make use of this constraint, and, by including electromagnetic fluxes into their total flux, the MHD Riemann solvers add dissipation based on the full MHD wave characteristics. Failing to do so leads to numerical instabilities especially for large magnetic field strengths, as in general the fast magnetosonic wave is faster than the characteristic waves treated in our scheme. However, because this source-flux equivalency is invalid without the MHD assumptions, we must include the Lorentz force as a source term (see the following Section 4.2.5) and consequently do not use the MHD characteristic velocities in our Riemann solver. In Section 4.3.2, we demonstrate the accuracy of our implemented algorithm for propagating MHD waves, demonstrating that the numerical dissipation is sufficient to suppress potential numerical instabilities.

## 4.2.5. Electromagnetic interaction with charged fluids

In this section, we first introduce the Lorentz force as a source term in equation (4.15). Furthermore, we describe how the fluid influences the electromagnetic fields. With these two additional parts, the description from an uncharged gas in Section 4.2.4 is expanded here to include plasmas.

## Treatment of electromagnetic source term

Instead of integrating the energy equation (4.16), which would require evaluating the source term on the right-hand side, we convert  $\epsilon$  into p before applying the source update  $\exp(\Delta t S_{\rm em})$  (see equation 4.20). Consequently, we compute the time evolution of the primitive pressure variable, for which the electromagnetic source term conveniently vanishes:

$$\frac{\partial p}{\partial t} + \Gamma p \nabla \cdot \boldsymbol{w} + \boldsymbol{w} \cdot \nabla p + \nabla \cdot \boldsymbol{Q} = 0. \tag{4.32}$$

Then only the computation of the source term for the momentum equation (4.15) is left. Up until now we have only applied the C-WENO method for conservation laws, however, by adding the source term, we are left with a balance law. In C-WENO formulations for balance laws it is customary to approximate the integral of the source term (equation 4.23) numerically to higher orders as well (Cravero et al., 2018b). We use Simpson's formula for approximating equation (4.23)

$$\int_{x_{i-1/2}}^{x_{i+1/2}} S\left(\tilde{U}\right) dx = \frac{1}{6} \left( S(\tilde{U}_{i-\frac{1}{2}}) + 4S(\tilde{U}_i) + S(\tilde{U}_{i+\frac{1}{2}}) \right) + O(\Delta x^5), \tag{4.33}$$

## 4. The fluid-PIC method

where the intracell values  $\tilde{\boldsymbol{U}}_{i\pm1/2}$  are interpolated by the same C-WENO scheme as used for solving the hydrodynamical equations, and the centre-value is computed self-consistently with the numerical integration formula, i.e.  $\tilde{\boldsymbol{U}}_i = (6\boldsymbol{U}_i - \tilde{\boldsymbol{U}}_{i+1/2} - \tilde{\boldsymbol{U}}_{i-1/2})/4$ . We also need to interpolate the electromagnetic field values to a comparable spatial order. This is achieved by performing finite-difference interpolations for each component from the Yee mesh discretized fields, that is

$$\boldsymbol{E}_{i+\frac{1}{2}} = \frac{150(\boldsymbol{E}_i + \boldsymbol{E}_{i+1}) - 25(\boldsymbol{E}_{i-1} + \boldsymbol{E}_{i+2}) + 3(\boldsymbol{E}_{i-2} + \boldsymbol{E}_{i+3})}{256} + O(\Delta x^6), \tag{4.34}$$

and temporal order,  $\mathbf{B}^n = (\mathbf{B}^{n+1/2} + \mathbf{B}^{n-1/2})/2$ , again, for each component necessary. Lower order approximations produce, in our tests, similar results, but converge to slightly lower wave frequencies when compared with the analytical solution of the dispersion relation. We apply  $S(\tilde{U}_i)$  by using an implicit velocity update,

$$\frac{\boldsymbol{w}_{i}^{n+\frac{1}{2}} - \boldsymbol{w}_{i}^{n-\frac{1}{2}}}{\Delta t} = \frac{q}{m} \left[ \boldsymbol{E}_{i}^{n} + \frac{1}{2} \left( \boldsymbol{w}_{i}^{n+\frac{1}{2}} + \boldsymbol{w}_{i}^{n-\frac{1}{2}} \right) \times \boldsymbol{B}_{i}^{n} \right], \tag{4.35}$$

which is solved using the Boris velocity integration (Boris et al., 1970). The splitting of fluid flux update and Lorentz force (equation 4.20) is reminiscent of pushing a particle with the PIC-method, where the Lorentz force for a full-time step is calculated in between half-time step updates of the position vector.

## Deposition of charges

Equations (4.4) govern the electric field evolution, where Faraday's or Gauss' law might be used to compute E. In this section we focus on the one-dimensional setup without particle contributions, which are explained in Section 4.2.7. The perpendicular components' update,  $E_y$  and  $E_z$ , is received straightforwardly by discretizing Faraday's Law

$$(E_y)_{i+\frac{1}{2}}^{n+1} = (E_y)_{i+\frac{1}{2}}^n - \sum_s \frac{\Delta t}{\epsilon_0} q_s \left( n w_y \right)_{i+\frac{1}{2},s}^{n+\frac{1}{2}} - \frac{c^2 \Delta t}{\Delta x} \left[ (B_z)_{i+1}^{n+\frac{1}{2}} - (B_z)_i^{n+\frac{1}{2}} \right]$$
 (4.36)

$$(E_z)_{i+\frac{1}{2}}^{n+1} = (E_z)_{i+\frac{1}{2}}^n - \sum_s \frac{\Delta t}{\epsilon_0} q_s \left( n w_z \right)_{i+\frac{1}{2},s}^{n+\frac{1}{2}} + \frac{c^2 \Delta t}{\Delta x} \left[ \left( B_y \right)_{i+1}^{n+\frac{1}{2}} - \left( B_y \right)_i^{n+\frac{1}{2}} \right], \tag{4.37}$$

where the sum is taken over all fluid species s and  $n\boldsymbol{w}$  are components of the fluid vector  $\boldsymbol{U}$ .

For the  $E_x$  component in spatial direction however, in order to enforce charge-conservation, Gauss' law in discretized form needs to be enforced for all  $i \ge 1$  as well

$$(E_x)_i^n = (E_x)_0^n + \sum_s \frac{q_s}{\epsilon_0} \sum_{i=0}^{i-1} n_{j+\frac{1}{2},s}^n \Delta x = (E_x)_0^n + \sum_s \frac{q_s}{\epsilon_0} \int_{x_0}^{x_i} \tilde{n}_s^n dx, \tag{4.38}$$

where the second equality uses the definition of cell averages in the finite volume scheme (see equation 4.21) and shows, that this numerical formula is exact. Another formula for updating  $(E_x)_0$  to the time step n is still needed. In the analytical case Gauss' law in combination with the density conservation equation (4.14) for the analytical flux (or cell values)  $J_x \propto qnw_x$  can be

shown to be equivalent to Faraday's law; in the numerical case this equivalency is shown using the discretized conservation equation and corresponding numerical flux  $J_x \propto qF_n(\tilde{U}) \simeq qnw_x$  for the current density  $J_x$ . Taking the time derivative of equation (4.38) in conjunction with the discretized density update equation (4.23) leads to the expression

$$\frac{(E_x)_i^{n+1} - (E_x)_i^n}{\Delta t} + \frac{(E_x)_0^{n+1} - (E_x)_0^n}{\Delta t} = \sum_s \frac{q_s}{\epsilon_0 \Delta t} \int_{t_n}^{t_{n+1}} \left[ -(F_{n,s})_i + (F_{n,s})_0 \right] dt.$$
(4.39)

The integration in time using Runge-Kutta methods is the same as used to solve equation (4.23). Faraday's law using fluxes in one spatial dimension is then given by

$$(E_x)_i^{n+1} = (E_x)_i^n - \sum_s \frac{q_s}{\epsilon_0} \int_{t_n}^{t_{n+1}} \left[ F_n \left( \tilde{U} \right) \right]_{i,s} dt, \tag{4.40}$$

and enables us to identify  $J_x$  by comparison to the charge conservation equation (equation 4.14 multiplied by  $q_s$ )

$$(J_x)_i^{n+1/2} = \sum_s \frac{q_s}{\Delta t} \int_{t_n}^{t_{n+1}} \left[ F_n \left( \tilde{\boldsymbol{U}} \right) \right]_{i,s} dt. \tag{4.41}$$

Note, that the numerical flux also includes numerical diffusion and is directly related to changes in  $\rho$ . Due to this, other formulations for  $J_x$  violate the charge conservation equation and can lead to numerical instabilities.

# Magnetic field evolution

Because the fluid evolution influences the magnetic field only indirectly, the finite-difference time-domain (FDTD) update for the magnetic field is unchanged from the previous SHARP code. For completeness we reproduce the formulae here (Shalaby et al., 2021)

$$(B_{y})_{i}^{n+\frac{1}{2}} = (B_{y})_{i}^{n-\frac{1}{2}} + \frac{\Delta t}{\Delta x} \left( (E_{z})_{i+\frac{1}{2}}^{n} - (E_{z})_{i-\frac{1}{2}}^{n} \right), \tag{4.42}$$

$$(B_z)_i^{n+\frac{1}{2}} = (B_z)_i^{n-\frac{1}{2}} - \frac{\Delta t}{\Delta x} \left( (E_z)_{i+\frac{1}{2}}^n - (E_y)_{i-\frac{1}{2}}^n \right). \tag{4.43}$$

 $\boldsymbol{B}_x$  is constant in the 1D3V model because of the requirement  $\boldsymbol{\nabla} \boldsymbol{\cdot} \boldsymbol{B} = 0.$ 

## 4.2.6. Landau closure for fluid species

The highest retained fluid moment, which is in our case the specific heat flux Q, is not evolved in our set of equations. Instead, we need to estimate its value dynamically using an appropriate closure. The simple ideal gas closure sets Q = 0, which, however, prevents the energy dissipation of plasma waves. One important mechanism of such a dissipation is the collisionless damping of electrostatic waves achieved through Landau damping. Landau damping is a microphysical kinetic wave-particle interaction, where particles resonate with the wave to exchange energy as a function of time. In essence, the resonant particles accelerate or decelerate to approach the

## 4. The fluid-PIC method

wave's phase velocity, thereby picking up energy or releasing it, respectively. For Maxwellian phase space distributions, there are more particles at velocities smaller than the phase velocity, which yields a net damping, i.e., energy loss of the wave (Boyd and Sanderson, 2003).

Various attempts, e.g. by Hammett and Perkins (1990), were carried out to approximate the heat flux Q of an almost Maxwellian distributed plasma, such that the kinetic phenomenon of Landau damping is mimicked in the linearized fluid equations. Landau damping is a nonisotropic effect, which can be reflected in the fluid descriptions. Accounting for the gyrotropy of the system around the magnetic field, the double-adiabatic law with two adiabatic coefficients parallel and perpendicular to the magnetic field can be adopted, which might be extended using an appropriate heat flux vector (Snyder et al., 1997; Hunana et al., 2019b,a). This is achieved by first decomposing the pressure tensor in a coordinate system that is aligned with the direction of the magnetic field  $\hat{\boldsymbol{b}} = \boldsymbol{B}/|\boldsymbol{B}|$ , yielding  $\boldsymbol{p} = p_{\parallel}\hat{\boldsymbol{b}}\hat{\boldsymbol{b}} + p_{\perp}(\boldsymbol{1} - \hat{\boldsymbol{b}}\hat{\boldsymbol{b}})$ . The transport of parallel and perpendicular heat along the magnetic field then corresponds to the terms  $Q_{\parallel}\hat{\pmb{b}}$ and  $Q_{\perp}b$ , respectively. In this publication, our algorithm is restricted to pressures with only one common adiabatic coefficient for parallel and perpendicular pressure. We leave the possibility of implementing anisotropic double-adiabatic systems open for future extensions of our algorithm. Hence, we model only the scalar heat flux  $Q = \hat{\boldsymbol{b}} \cdot \boldsymbol{Q}$ , which is a simplification of the doubleadiabatic modelling from the aforementioned literature, i.e.  $2Q/(\Gamma-1)=Q_{\parallel}+2Q_{\perp}$ . In our model, we can assume an isotropized pressure tensor  $\mathbf{p} = p\mathbf{1}$  using the adiabatic coefficient  $\Gamma = 5/3$ . To do this, we set  $p = p_{\parallel} = p_{\perp}$  everywhere without explicitly modelling  $Q_{\perp}$ . Instead, we choose Q such that the linear Landau damping rate of the isotropic system is comparable to that of an anisotropic electrostatic system with the same  $p_{\parallel}$  (for details refer to comments below equation 4.46). This is a simplifying assumption, which does not follow from the kinetic equations. Furthermore, isotropization mainly results from collisions, while collisionless systems are rarely isotropic and Maxwellian as we assume. Nevertheless, this is a convenient choice for damping waves with an isotropic background plasma when particle heating is negligible compared to their thermal energy. A more physically motivated anisotropic pressure tensor  $\mathbf{p} = p\hat{\boldsymbol{e}}_x\hat{\boldsymbol{e}}_x$  is attained for  $\Gamma = 3$ , where  $\hat{\boldsymbol{e}}_x$  is the unit vector in x-direction. This approximates the kinetic equations well when  $p \simeq p_{\parallel}$ . Since we model only components of Q parallel to  $\hat{e}$ , the heat flux enters into the pressure evolution equation (4.32) as

$$\frac{\partial p}{\partial t} \propto -\nabla \cdot \left(\hat{\boldsymbol{b}}Q\right). \tag{4.44}$$

In practice, we make the assumption of locally constant (or slowly varying) magnetic fields on top of the 1D3V geometry, that is  $\nabla \cdot (\hat{\boldsymbol{b}}Q) \simeq \cos(\Theta) \partial_x Q$ , where the angle  $\Theta$  is measured between the background magnetic field  $\boldsymbol{B}_0$  and the x-axis.

Here, we will introduce two different formulae for heat flux closures. The first and most popular collisionless electrostatic closure was proposed by Hammett and Perkins (1990). We refer to it as the  $R_{32}$  closure throughout this paper, and it approximates the heat flux at a fixed

 $\Gamma = 3$ , in Fourier space, by

$$\hat{Q} = -i\operatorname{sign}(k) \frac{2}{\sqrt{\pi}} \sqrt{2\theta_0} c n_0 k_B \frac{\hat{T}}{m} \equiv \hat{Q}_T.$$
(4.45)

Here, hats are used to denote quantities in Fourier space along the magnetic field line, i.e.  $\hat{Q} = \mathcal{F}_{\parallel}(Q)$ , and the subscript 0 refers to simulation box averages, that is  $n_0 = \sum_{i=0}^{N_c} n_i/N_c$  is an average over all  $N_c$  cells. Furthermore  $k_{\rm B}$  is the Boltzmann-constant, and  $k_{\rm B}\hat{T} = (m\hat{p} - k_{\rm B}T_0\hat{n})/n_0$ . Since the plasma average or equilibrium temperature evolves slowly as a function of time, we adjust the background temperature  $T_0$  after every time step to synchronize it with the mean pressure,  $k_{\rm B}T_0(t)/m = p_0(t)/n_0$ , while the density conservation ensures that  $n_0$  stays constant. Note also, that  $Q_0 = 0$ . The dimensionless mass-normalized temperature is  $\theta_0 = k_{\rm B}T_0/(mc^2)$ .

A more recent approximation was proposed by Hunana et al. (2018), who restricts this closure to  $\Gamma=3$  only, for reasons mentioned already. We use an ad hoc formulation of their closure with a variable  $\Gamma$ , thereby allowing our simplified model to be used. They also introduce the nomenclature  $R_{mn}$  adopted here, which is used to denote that the kinetic plasma response function R is mimicked for this closure by a Padé approximant with polynomials  $P_m/Q_n=R_{mn}$  of order m and n. We refer to their closure as  $R_{31}$  and it approximates the heat flux, in Fourier space, by

$$\hat{Q} = \underbrace{\left(\frac{4}{4-\pi} - \Gamma\right) p_0 \hat{w}}_{\hat{Q}_w} + \underbrace{\left(-i \operatorname{sign}(k) \frac{\sqrt{2\pi\theta_0}}{4-\pi} c n_0 \frac{k_B \hat{T}}{m}\right)}_{\hat{Q}_T}.$$
(4.46)

The  $R_{31}$  closure may be seen as a generalization of the  $R_{32}$  closure with an additional degree of freedom in  $\hat{w}$ , which can mimic the kinetic damping more accurately over a broader spectrum. We choose this closure as our fiducial model because it requires only a relatively inexpensive local derivative to compute the additional term dependent on  $\hat{w}$ . This additional term effectively increases the speed of sound obtained from the non-electromagnetic fluid equations and allows retrieving the correct damping rate with our ad-hoc assumption of a specific value of  $\Gamma$ , see Appendix 4.C. This means, that adopting a value of  $\Gamma$ , e.g.,  $\Gamma = 5/3$  in our isotropic model, does not change the linear dispersion relation associated with this closure. For  $\Gamma = 3$ , we retrieve the coefficient for  $\hat{w}$  from the aforementioned literature  $\frac{4}{4-\pi} - 3 = \frac{3\pi-8}{4-\pi}$ .

In only one spatial dimension, as assumed in our code, the global integration along a magnetic field line is approximated to be along the spatial direction, i.e.  $\mathcal{F}_{\parallel} = \mathcal{F}_{x}$ . An extension to multiple spatial dimensions with an anisotropic pressure tensor is not straightforward because in this case, this approach can lead to spurious instabilities (Passot et al., 2014) and the integration would need to be carried out along magnetic field lines.

A kinetic code does not need global communication to accurately reproduce Landau damping, since each particle (or particle bin) tracks its own interaction with each wave mode as a function of time and accumulates this information in the particle velocity. However, after integrating out the individual particle velocities when building the evolution equations for the phase-space distribution function, i.e. equations (4.14)-(4.16), information about the individual particle-

wave interaction is no longer collected. Because some information about this interaction is also contained in the wave, such non-local information can be used to approximate the gradient of the physical heat flux, i.e., a closure of the fluid moments that incorporates such missing information. This non-local information is approximated in equations (4.45) and (4.46), and is manifested by the term  $i \operatorname{sign}(k)$  in Fourier space, which is also referred to as the Hilbert transform.

Numerically, we do not include the heat flux in the Riemann solver used to compute the fluid fluxes. Instead, we compute the spatial derivative of the heat flux  $\nabla_{\parallel} \cdot \mathbf{Q}$  separately. We use Strang splitting for the  $\mathbf{w}$  dependent part  $\mathbf{Q}_w$  and the temperature dependent part  $\mathbf{Q}_T$  to expand equation (4.20) into

$$\boldsymbol{U}^{n+\frac{1}{2}} = e^{\frac{\Delta t}{2}} \mathbf{F} e^{\frac{\Delta t}{2}} \boldsymbol{Q}_{w} e^{\Delta t} \boldsymbol{Q}_{T} e^{\Delta t} \mathbf{S}_{em} e^{\frac{\Delta t}{2}} \boldsymbol{Q}_{w} e^{\frac{\Delta t}{2}} \mathbf{F} \boldsymbol{U}^{n-\frac{1}{2}} + O(\Delta t^{3}), \tag{4.47}$$

such that only one non-global evaluation of  $Q_T$  is needed. Using Heun's method together with the fast Fourier transform (FFT) the update formulae for the pressure w.r.t. operators  $Q_w$  and  $Q_T$  are respectively

$$p^{n+1}|_{O_m} = e^{\Delta t Q_w} p^n = p^n + \Delta t a_w p_0 \nabla_{\parallel} \cdot \boldsymbol{w}, \tag{4.48}$$

$$p^{n+1}|_{Q_T} = e^{\Delta t Q_T} p^n = p^n + \Delta t \mathcal{F}_{\parallel}^{-1} \left[ |k| a_T \left( 1 + \frac{\Delta t}{2} |k| a_T \right) \hat{T}^n \right], \tag{4.49}$$

where the derivative in Fourier space was obtained by multiplying with ik and the inverse FFT is denoted by  $\mathcal{F}^{-1}$ . For the  $R_{31}$  closure the coefficients are given by  $a_w = 4/(4 - \pi)$  and  $a_T = (4 - \pi)^{-1} (2\pi\theta_0)^{1/2} c n_0 k_{\rm B}/m$ , while for the  $R_{32}$  closure these are given by  $a_w = 0$  and  $a_T = 2(2\theta_0/\pi)^{1/2} c n_0 k_{\rm B}/m$ . Both closures compute a term proportional to  $\hat{T}$  (cf. equation 4.49)

$$ik\hat{Q} \propto -i\operatorname{sign}(k)ika_T\hat{T} = |k|a_T\hat{T}.$$
 (4.50)

Computing this term naively using the FFT is expensive. This is why, in the following, we present local, semi-local, and efficient global (Fourier transform-based) numerical approximations of the Landau closures, which we have implemented in the fluid-SHARP code.

## Local approximations of the Hilbert transform

The phase shift between the wanted derivative  $ik\hat{Q}$  and the input of  $\hat{T}$  in equation (4.50) is exactly 0, while the amplitude is proportional to |k|. This is therefore a special case (a = 1) of the fractional Riesz derivative  $\partial^a/\partial |x|^a$  with Fourier representation

$$\mathcal{F}\left(\frac{\partial^a f(x)}{\partial |x|^a}\right) = -|k|^a \hat{f}(k), \qquad (4.51)$$

where  $a \in \mathbb{R}$ . Note, that all approximations mentioned here only introduce errors in the amplitude of |k|, but not in its phase. This makes them easier to integrate into simulations in comparison to approximations which are not designed to prevent phase errors, because large

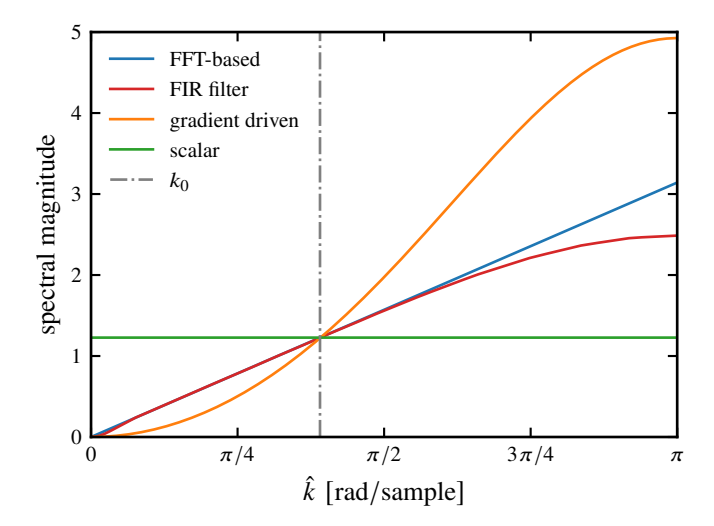


Figure 4.1. The magnitude of the frequency response, which is a quantification of how much the amplitude at a specific frequency is amplified or suppressed, of different approximations of the derivative of the Hilbert transform.  $\hat{k}$  is given in normalized frequencies (with regards to the Nyquist frequency), while the negative frequencies in the interval  $[-\pi, 0]$  are not shown here due to the symmetric dependence of all plotted values on |k|. The FFT-based approach reproduces the correct, linear response. The scalar and gradient driven closures are given by equations (4.52) and (4.53) respectively with the parameter  $k_0$  marked as a grey, vertical line. The FIR filter is described by equation (4.55).

phase errors (between  $\pi/2$  and  $3\pi/2$ ) in any wave mode transform the damping term into an exponentially growing numerical instability. The local approximations make use of the fact, that the fractional Riesz derivative is local and cheap to evaluate for the special case a = 2m with  $m \in \mathbb{N}^0$ , where it reproduces the usual derivative  $\partial^{2m}/\partial |x|^{2m} = (-1)^{m+1} \partial^{2m}/\partial x^{2m}$ . Wang et al. (2015) use a = 0, while Allmann-Rahn et al. (2018) and Ng et al. (2020) approximate the non-isotropic pressure tensors with a = 2. These approximations are scaled to a characteristic wavenumber  $k_0$  at which the damping is expected to occur.

The choice of a = 0 means, that the approximation is a scalar

$$ik\hat{Q} \propto |k_0|\hat{T},$$
 (4.52)

while the gradient-driven closures with a = 2 use

$$ik\hat{Q} \propto \frac{k^2}{|k_0|}\hat{T}.$$
 (4.53)

The gradient-driven closures are equal to the FFT solution at two wavelengths, 0 and  $k_0$ , while the scalar closure is only exact at  $k_0$ , see figure 4.1. Since  $ik\hat{Q}$  is not computed alongside with the conservative fluxes in the Riemann solver, energy conservation is only preserved if the mean energy does not increase. To achieve this, the approximation for the derivative of the heat flux needs to vanish at wavenumber 0, which the scalar approximation does not fulfil.

Because fluid closures are only approximately mimicking kinetic Landau damping anyway, these local approximations to the fluid closures are useful to save computational cost. Further-

more they are easier to implement, especially when the full pressure tensor is computed. However, they may lead to misleading results in multiscale simulations, where multiple characteristic damping lengths are present and depend on the estimate of  $k_0$ . For example, Allmann-Rahn et al. (2022) show a case where ion and electron heating intensities are switched qualitatively.

## Semi-local approximations of the Hilbert transform

While the less accurate local approximations use an arbitrary value of  $k_0$ , the FFT is expensive and depends on periodic boundary conditions. Here, we aim to have a fallback algorithm as a compromise between both approaches.

A digital finite impulse response (FIR) filter can be designed to approximate the non-local effects by convolving the simulation data with adjacent auxiliary data points, where the filter length determines the maximum distance. For example, an asymmetric filter with an even number of entries is applied on an input x using filter coefficients  $b_i$ , producing the output y:

$$y_{i+0.5} = \sum_{j=-(N_f/2-0.5)}^{N_f/2-0.5} b_j x_{i+j+0.5}.$$
 (4.54)

A numerical derivative is then an asymmetrical filter with  $N_f = 2$  and coefficients  $b_{\pm 0.5} =$  $\pm 1/\Delta x$ , such that  $y_{i+0.5} = (x_{i+1} - x_i)/\Delta x$ . Figure 4.1 shows the magnitude of the frequency response. The gradient driven case shows a quadratic  $k^2$  dependence, which is suppressed for larger k. This is due to the relatively small uneven filter length of 7 used here; the filter length is an important parameter, since it influences the accuracy of the approximation. With a filter length corresponding to the simulation box size the results can converge to the FFTbased algorithm (i.e. the  $k^2$  dependence is not suppressed at higher k), if the filter is designed appropriately. As noted previously, the local closures do not converge to  $\partial/\partial |x|$ . A correct convergence for approximating  $\partial/\partial|x|$  is obtained through the high order formulation by Ding et al. (2015). However, this filter violates energy conservation for smaller filter length and is thus, not suitable for our case. Instead, we construct the filter by adopting a convolution of two sub-filters, each of which has an odd amount of asymmetric entries (termed a Type IV filter) similar to the numerical derivative mentioned already. By design, their output has a vanishing mean, thereby guaranteeing energy conservation. A symmetric splitting into the sub-filters  $\partial/\partial|x| = (\partial^{1/2}/\partial|x|^{1/2})^2$  is possible, however its frequency response is not monotonic (and has visible ripples) for small filter lengths. This leads to the nonphysical case that some waves at a particular wavenumber k are damped less than their slightly larger scale waves at  $k - \delta k$ .

Instead, we opt to use the intuitive splitting of  $\partial/\partial|x| = \partial/\partial x\mathcal{H}$  where the Hilbert-transform filter  $\mathcal{H}$  is equivalent to  $-\mathrm{i}\,\mathrm{sign}\,(k)$  in Fourier space. The filter  $\mathcal{H}$  has coefficients  $b_j = 1/(\pi j)$ . We derive an equivalent formulation to equation (4.49), which is first order in time, by applying the derivative and Hilbert-transform filters successively, i.e.

$$p^{n+1} = p^n + \Delta t a_T \frac{\partial}{\partial x} \sum_{j=-(N_f/2-0.5)}^{N_f/2-0.5} \frac{1}{\pi j} T_{i+j+0.5}^n.$$
 (4.55)

Note, that the derivative is also computed by convolution and has a separate filter length corresponding to its spatial order. We opt to use the same spatial order as in the C-WENO reconstruction for the finite volume scheme.

Even for small Hilbert-transform filter lengths in comparison to the number of cells, e.g.,  $N_f/N_c = 0.04$  as shown in figure 4.1, this formulation dramatically improves the accuracy of multiscale problems in comparison to local approximations. Here,  $N_f$  is critical for the accuracy at small wavenumbers k, while the spatial order of the derivative is critical for the accuracy at large k. Most importantly, this semi-local approach does not require setting an arbitrary damping scale  $k_0$  such as the local approximations mentioned before. The only parameter of this approach is the filter length, which should be chosen to be sufficiently large.

#### Efficient FFT-based computation of the Hilbert transform

Provided the plasma background is uniform and periodic, the most accurate while computationally most expensive results are achieved by computing the heat flux of the fluid in Fourier space. While the FFT is easy to compute on a single computer using standard numerical libraries, our code is parallelized using MPI and an efficient one-dimensional FFT is needed. The computation of the Fourier transform is expensive for two reasons:

- 1. globally, each Fourier component needs to be informed about data from every other computational cell (which may be stored on a different processor), and
- 2. the Fourier transform is not easily parallelizable in one dimension, which precludes an efficient scalable Fourier algorithm.

This naturally limits the overall computational scalability of the fluid part of the code. Communication over multiple MPI processes is time consuming because of latency and finite bandwidth. For this reason, parallel FFT algorithms are prone to become a computational bottleneck. However, using non-blocking MPI routines to perform communication in the background can be used while the high computational load of the particles is carried out. Thus, in our case of a combined fluid and PIC algorithm, the communication required for an accurate FFT-based heat flux computation is comparatively computationally cheaper, even with relatively small numbers of PIC particles. Hence, in our case the FFT algorithm does not necessarily become a bottleneck for larger problems.

In order to distribute the computational load of the FFT, we employ a four-step algorithm in the first step of the computation (Bailey, 1990; Takahashi and Kanada, 2000), which extends the Cooley-Tukey algorithm (Cooley and Tukey, 1965) for multiple processors. We shortly describe the algorithm for complex input data as found in the literature and afterwards adapt the parallel FFT for real input data in our implementation. The four-step algorithm interprets the complex data vector  $x_j$  of length N as a two-dimensional vector  $x_j = x_{j_1,j_2}$  with lengths  $n_1$  and  $n_2$  respectively, and volume  $n_1n_2 = N$ . The mapping  $j = j_1 + j_2n_1$  and  $k = k_2 + k_1n_2$  is

inserted into the definition of the discrete Fourier transform, where  $\Psi = \exp\{-2\pi i\}$ 

$$\hat{x}_k = \sum_{j=0}^{N-1} x_j \Psi^{jk/N}, \tag{4.56}$$

$$\hat{x}_{k_2,k_1} = \sum_{j_1=0}^{n_1-1} \sum_{j_2=0}^{n_2-1} x_{j_1,j_2} \Psi^{j_2 k_2/n_2} \Psi^{j_1 k_2/N} \Psi^{j_1 k_1/n_1}. \tag{4.57}$$

This way, a complex-to-complex parallel FFT of length N is distributed to  $n_1$  local FFTs of length  $n_2$ , a multiplication by the twiddle factors  $\Psi^{j_1k_2/N}$  and finally  $n_2$  FFTs of length  $n_1$ , with a communication intensive transpose in between. All-to-all communication takes place two times, in the first step – cyclically distributing j to  $j_1$  and  $j_2$  – and for the transpose. A third all-to-all communication would be needed to properly sort the values in Fourier space. However, a scrambled output suffices for computing the heat flux. Furthermore, since often two FFTs, i.e. electrons and ions, need to be computed simultaneously, they can be computed on different nodes. This has the advantage, that the second all-to-all communication for the transpose is not completely global resulting in reduced communication times.

Adapting this algorithm to a real-to-complex FFT, where due to Hermitian symmetry only values of  $k \leq \lfloor N/2 \rfloor$  need to be computed, a large amount of computational and communicational savings can be realized. A real-to-complex parallel FFT of length N is distributed to  $n_1$  local real-to-complex FFTs of length  $n_2$ , a multiplication by the twiddle factors  $\Psi^{j_1k_2/N}$  and, now only,  $\lfloor n_2/2 \rfloor + 1$  complex-to-complex FFTs of length  $n_1$ . Up to two of the latter FFTs can be replaced by real-to-complex FFTs, along the axes  $k_2 = 0$  and, if  $n_2$  is even,  $k_2 = n_2/2$ . A scrambled output is received, which, due to Hermitian symmetry, needs to be partially complex conjugated.

A key point in ensuring the efficiency of the parallel four-step algorithm consists in choosing large  $n_1$  and  $n_2$ .  $n_1 \simeq n_2 \simeq \sqrt{N}$  is the optimal choice for the distributed complex-to-complex FFT, the real-to-complex FFT should prefer  $n_1 \simeq \lfloor n_2/2 \rfloor + 1 \simeq (\sqrt{2N+1}+1)/2$ . The computational scaling with P processors and roughly optimally distributed  $n_1$  and  $n_2$  is akin to  $O(N/P\log N)$ , but degrades if N is a prime number, or, more generally, if  $n_1$  or  $n_2/2$  is smaller than the number of processors. This easily avoidable because N is a free parameter, and so are  $n_1$  and  $n_2$ . While this does not scale favourably in comparison to the O(N/P) scaling that dominates the rest of the fluid code, still, the FFT is trivially independent of the numbers of particles per cell  $N_{\rm pc}$ . The PIC-module on the other hand scales as  $O(N_{\rm pc}N/P)$  and typical applications have  $N_{\rm pc} \gtrsim 100$ . In many applications the cost of the Fourier transform is, even with worse scaling, subdominant in comparison to the cost of the PIC part. In the remaining cases, local approximations, discussed above, are favourable.

## 4.2.7. Current-coupled fluid-PIC algorithm

The coupling in our code between various fluid and kinetic (PIC) species is achieved through a current-coupling scheme. Namely, both fluid and kinetic species contribute to the charge and current densities. The electromagnetic fields then evolve in response to the total contributions.

$$t^{n}$$
 $t^{n}$ 
 $E_{x}$ 
 $E_{y}, E_{z}, \rho$ 
 $t^{n+\frac{1}{2}}$ 
 $B_{y}, B_{z}, J_{x}$ 
 $(J_{y}, J_{z}), U_{f}$ 

Table 4.1. The grid assignment and time staggering of the fluid-SHARP-1D3V code.  $U_f$  refers to the fluid state vector. Note that it is sufficient to compute either  $\rho$  or  $J_x$ , but not both.

The fields are staggered on a Yee-mesh and are updated with the FDTD scheme. Subsequently, both fluid and kinetic species evolve in response to the new electromagnetic fields. That is our current-coupling scheme does not make any assumption on the velocity distribution of the species modelled using the kinetic description (Park et al., 1992).

The PIC species, using fifth-order spline interpolation, are deposited to specific points on the Yee-grid for which the charge density is defined at full-time steps while the current density is defined at half-time steps as discussed by Shalaby et al. (2017b, 2021). Table 4.1 gives an overview on the staggering of our implementation of the fluid-PIC method. We initialize the staggered quantities directly, with one exception:  $(J_x)_f$ , see equation (4.41), necessitates an integral over the flux from  $t^0$  to  $t^1$ . We approximate the integral between  $t^0$  and  $t^{1/2}$  using an interpolation at  $x_i$  of the cell center values  $J_x \simeq q |nw|_{t^{1/2}}$ , while the remaining part of the integral to  $t^1$  is obtained through the fluxes again. If  $E_x$  is updated using  $J_x$ , then  $\rho$  does not need to be calculated and vice versa. Otherwise, another complication may be seen when obtaining  $\rho$  from equation (4.5), which necessitates U to be defined at full-time steps. While U is formally defined only at half-time steps, we define  $U^{n*} = \exp(\Delta t/2 \times \mathbf{F})U^{n-1/2}$  (i.e. the first part of the splitting in equation 4.20), from which  $\rho$  is obtained. Note, that  $\rho_s = q_s n_s$  stays constant when computing the Lorentz force and heat flux updates and therefore  $\rho^n = \rho^{n*}$  is defined consistently, while bulk velocity and pressure are not well-defined at full time steps.

Our algorithm does not apply any approximations to the electrical field components or to Ohm's law, requiring electron timescales and motions to be fully resolved. Consequently, we apply the same algorithm to fluid electrons and protons. This is accomplished using the modular design of the fluid SHARP code where each fluid species is represented by initializing a fluid code class. Each instance of this code class is initialized using the values of the mass and the charges of their respective particle species. The algorithms which define the evolution of each particle species are implemented as functions of the fluid class. This allows us to set up simulations with multiple species, all of which are evolved with the same numerical algorithms, with little effort.

In figure 4.2 the main loop of the fluid-PIC algorithm is presented schematically. It can be seen that the usual PIC-algorithm loop of electromagnetic update, interpolation to particle position, particle push, and field deposition is retrieved when no fluid species is initialized. On the other hand, without PIC particles, we retrieve a multispecies fluid plasma code. While our fluid-PIC algorithm can simulate an arbitrary mixture of species, it is most efficient if fluids are used for background species and particles for non-thermal particle distributions. Possibilities for task parallelization are shown in figure 4.2 by dashed lines, which allows maximizing computation-communication overlap. The full main loop of our algorithm can be schematically described as

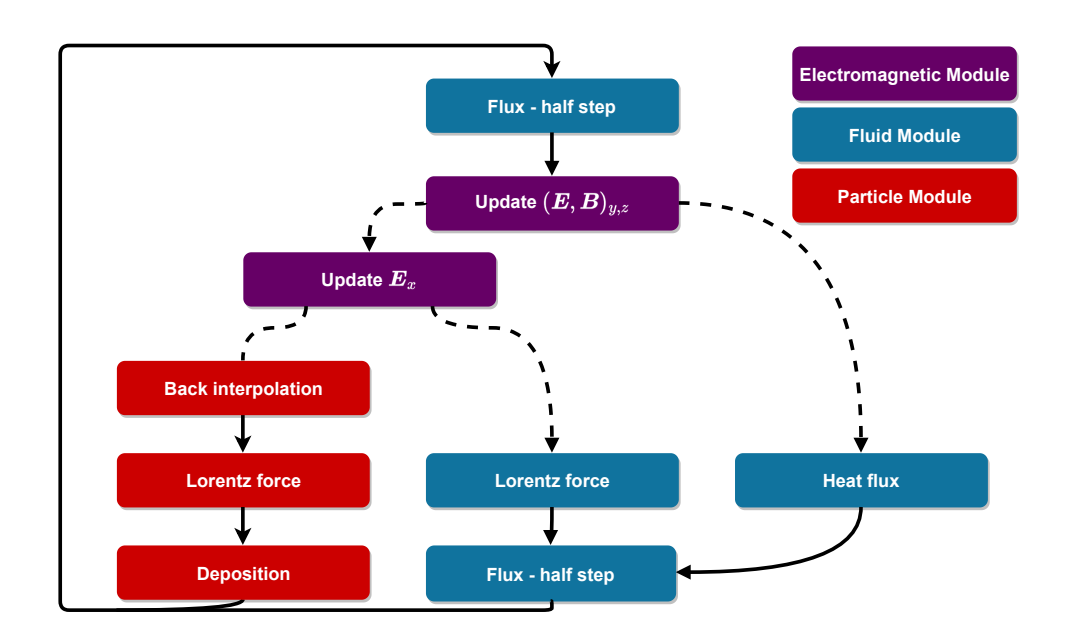


Figure 4.2. Schematic representation of the interaction of the different modules in the fluid-SHARP code. Red boxes belong to the particle class, violet boxes to the electromagnetic class and blue boxes to the fluid class. Dashed lines show branches which are task parallelizable, i.e. where non-blocking MPI communication can be used for overlapping communication and computation. The particle and fluid modules might be instantiated arbitrarily often, where each instance represents a species.

```
follows (referencing the corresponding equations):
```

```
initialize quantities at corresponding grid points(table 4.1)
particle deposition
while t < t_{\text{max}}:
        fluid deposition of J_y, J_z (equations 4.36-4.37)
        fluid flux update by half step (Section 4.2.4)
        fluid deposition of J_x or \rho (equation 4.41)
        electromagnetic update on Yee grid (Sections 4.2.5-4.2.5)
        w-dependent heat flux update by half step (equation 4.48)
        start T-dependent heat flux update (FFT, equation 4.49)
                 fluid electromagnetic source update (Section 4.2.5)
                 particle interpolation
                 particle push
                 particle deposition
        end T-dependent heat flux update (FFT, equation 4.49)
        w-dependent heat flux update by half step (equation 4.48)
        fluid flux update by half step (Section 4.2.4)
        t = t + \Delta t
```

Our fluid implementation is included within the SHARP code, which uses a fifth-order spline function for deposition and back-interpolation for PIC species (Shalaby et al., 2017b, 2021). The

Test	$x_0$	$n_{\mathrm{l}}$	$w_{ m l}$	$p_1$	$n_{ m r}$	$w_{ m r}$	$p_{ m r}$
1	0.3	1	0.75	1	0.125	0	0.1
2	0.8	1	-19.59745	1000	1	-19.59745	0.01

Table 4.2. Parameters adopted for the shock tube tests described in Section 4.3.1.  $x_0$  divides the domain into two halves, where values to the left of  $x_0$  ( $x < x_0$ ) are initialized by the parameters with subscript l. Similarly, subscript r indicates parameters to the right of  $x_0$ .

PIC part of the code does not make use of filtering grid quantities and results in comparatively small numerical heating per time step, which (if present) would affect the reliability of the simulation results on long timescales (see section 5 in Shalaby et al. 2017b). This property is important because we are specifically interested in studying microphysical effects on long timescales with our fluid-PIC code. Noise generated by the PIC particles could influence the fluid through the electromagnetic coupling. The CFL condition keeps the propagation of this noise within a single cell during one time step, and the PIC noise at the next time step will be uncorrelated with this noise so that we do not expect a systematic numerical error emerging from this. Indeed, we have not yet observed a case where this leads to a numerical instability. It has also been observed, that the larger physical dissipation through Landau closures replaces the need for numerical dissipation completely (Passot et al., 2014).

Due to the modularity of our code, each part can be tested individually. These tests, ranging from the uncharged fluid solver to full fluid-PIC simulations, are shown in the next section.

## 4.3. Code validation tests

In this section, we present the results of various code tests. We start with two shock-tube tests in Section 4.3.1, where only the fluid solver presented in Section 4.2.4 without sources (electromagnetic module) is used. Next, we provide tests of the electromagnetic coupling between ion and electron fluids, as described in Section 4.2.5. The two-fluid model consists of an ion and electron fluid described by equations (4.14)-(4.16), coupled via Maxwell's equations (4.3)-(4.4). We show that our code is able to accurately capture all six branches of the two-fluid dispersion relation (Section 4.3.2). The Landau closures tested for Langmuir wave damping of only one electrostatic electron fluid with a fixed ion background (Section 4.3.3) and, using the two-fluid model, for two interacting Alfvén waves generating a new, longitudinal wave along the magnetic field (Section 4.3.4). In Section 4.3.5, we test the entire fluid-PIC code with a simulation of the gyrotropic CR streaming instability, where PIC CRs are streaming in a stationary electron-proton fluid background, utilising two fluid and two PIC species coupled through Maxwell's equations. Finally, we demonstrate the successful parallelization strategy of our code by performing scaling tests in Section 4.3.6.

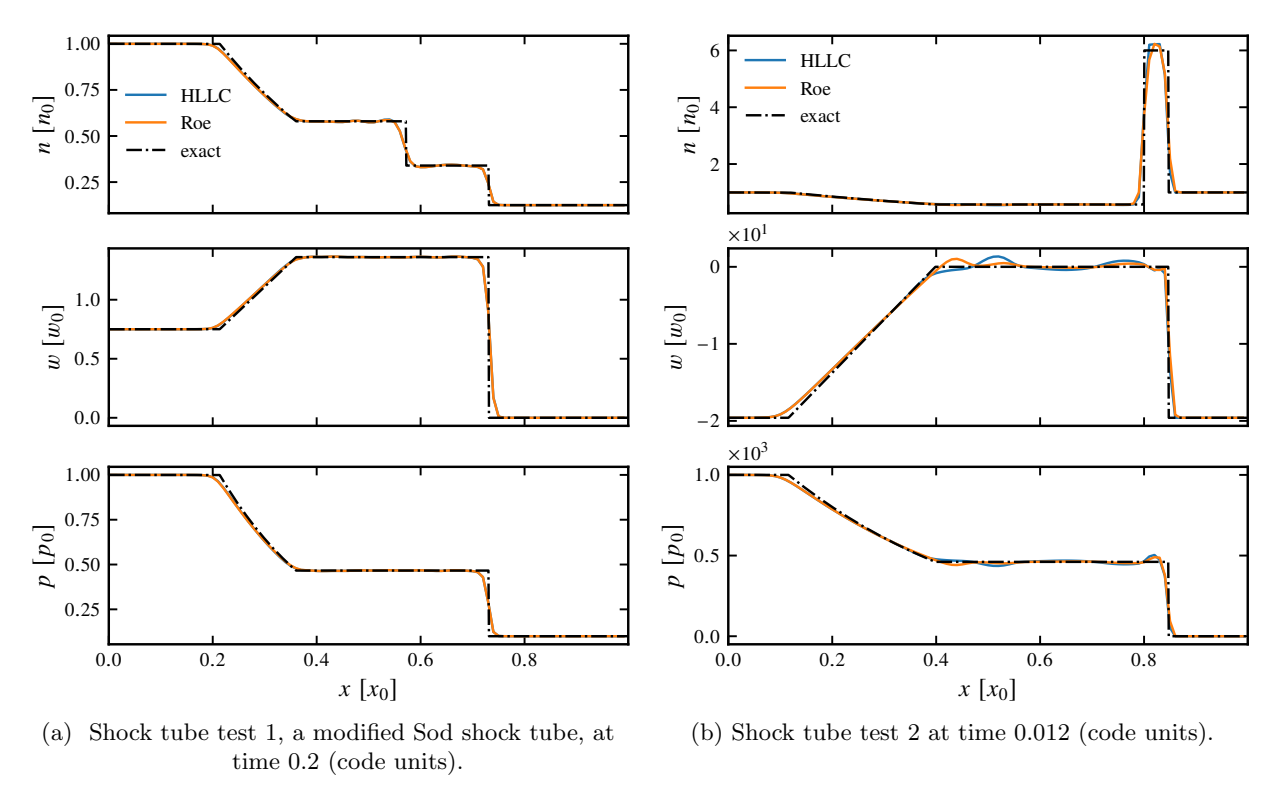


Figure 4.3. 1D1V hydrodynamical shock tube tests with initial conditions given in Table 4.2. The simulations carried out with the HLLC and Roe Riemann solvers are compared to the exact solutions. Density, bulk velocity in x-direction and pressure are plotted for each test.

## 4.3.1. Shock tube

As the fluid approximation will be primarily used for background plasmas without excessive gradients, the accuracy of resolving sharp discontinuities is of secondary importance in practical applications. Still, we stress test our implementation of the fluid equations without electromagnetic coupling to ensure its numerical robustness and to compare the numerical dispersion for different Riemann solvers. For the shock tests a numerical grid of 100 cells is used with a constant CFL number  $C_{\rm cfl} = 0.2$ . The boundary conditions are transmissive and the initial conditions for the tests are given in Table 4.2 with the adiabatic coefficient of  $\Gamma = 1.4$ . These test setups are the same as used by Toro (2009), where, unlike the tests performed here, a CFL number of  $0.2 \times 0.95$  is used only in the first five steps and 0.95 afterwards. The units used for these non-electromagnetic tests are arbitrary units and do not coincide with the usual simulation units.

Test 1, as shown in figure 4.3a, is a modified Sod shock tube test. The sonic rarefaction wave on the left-hand side as well as the shock front on the right are well resolved without noticeable oscillations. The contact discontinuity in the middle introduces small oscillations in the density and is smeared out more than the shock front. While the Roe and HLLC solvers yield almost the same results, the HLLC solver is slightly better at resolving the sonic point at the head (to the left) of the sonic rarefaction wave, which the Roe solver can only resolve because an entropy

fix is applied.

Figure 4.3b shows a test of a stationary contact discontinuity with a shock front of a high Mach number travelling to the right and a rarefaction wave to the left. It can be seen, that while the HLLC method introduces more oscillations, it is also better at resolving the contact discontinuity.

In low-density flows the Roe solver is not suitable because it is not robust without further modifications (Einfeldt et al., 1991), making the HLLC method slightly more robust while the Roe method is slightly less dispersive. We use the HLLC solver as our default, however, for most practical applications, both methods produce similar results.

A natural extension to the hydrodynamic shock tubes are the MHD shock tubes, which also test the evolution of shocks in the electromagnetic variables. A two-fluid model is not expected to exactly replicate the MHD shock tubes used to test MHD codes, because the characteristic waves are different for both system of equations. Finite-volume two-fluid models have been used to replicate the MHD shock tubes with some success, even without informing the Riemann solver about the MHD characteristic wave velocity (Shumlak and Loverich, 2003; Hakim et al., 2006). Because the Maxwell-solver in our implementation uses the finite-difference scheme, the most common choice for PIC codes, it is unable to capture electromagnetic shock tubes properly. Their relevance for two-fluid codes rarely extends beyond testing purposes, as physical shocks stretch over a length scale larger than  $c/\omega_i \gg c/\omega_e$ , which appears smooth in simulations resolving the electron skin depth. However, shock acceleration is not properly captured using the fluid-PIC algorithm at the shock interface. This is because efficient shock acceleration mechanisms are only experienced by the computational particles, but not the fluids. Injection prescriptions for cosmic rays might be used to mitigate this (e.g., Pfrommer et al., 2017). We focus on cases where the electromagnetic quantities are smoothly varying, i.e. wave transport. The choice of the Riemann-solver and its characteristic waves are less important for smooth waves, especially when employing a high-order interpolation routine. This is because different Riemann solvers should converge to the same results when the interface state is unambiguous, for example if  $\dot{U}_{\rm L} = \dot{U}_{\rm R}$  (cf. equation 4.29).

## 4.3.2. Two-fluid dispersion relation

To test the interplay of the fluid solver with the electromagnetic coupling, we perform a test where the linear waves of an ion-electron plasma are reproduced. For an ideal two-fluid plasma the dispersion relation can be solved for six different wave branches (Stix, 1992). We show the solutions to the dispersion relation of a two-fluid plasma in figure 4.4 for a realistic mass ratio of  $m_i = 1836m_e$ ,  $\beta_i = nk_BT_i/[B_0^2/(2\mu_0)] = 0.2$  in an isothermal plasma and  $\Gamma = 3$ .  $B_0$  is oriented along the x-axis and the Alfvén velocity is  $v_A = B_0/(\mu_0 n_i m_i)^{1/2} = 5.83 \times 10^{-3} c$ . Multiple simulations at different wavenumbers have been initialized that have all six wave modes simultaneously present and were run for a total time of  $14 \times 2\pi/\min(\omega)$  ( $20 \times 2\pi/\min(\omega)$ ) for the smallest scale), where  $\omega$  denotes the wave frequencies, which are always completely real for an ideal fluid. Consequently, the waves should be undamped in the linear regime. Initial

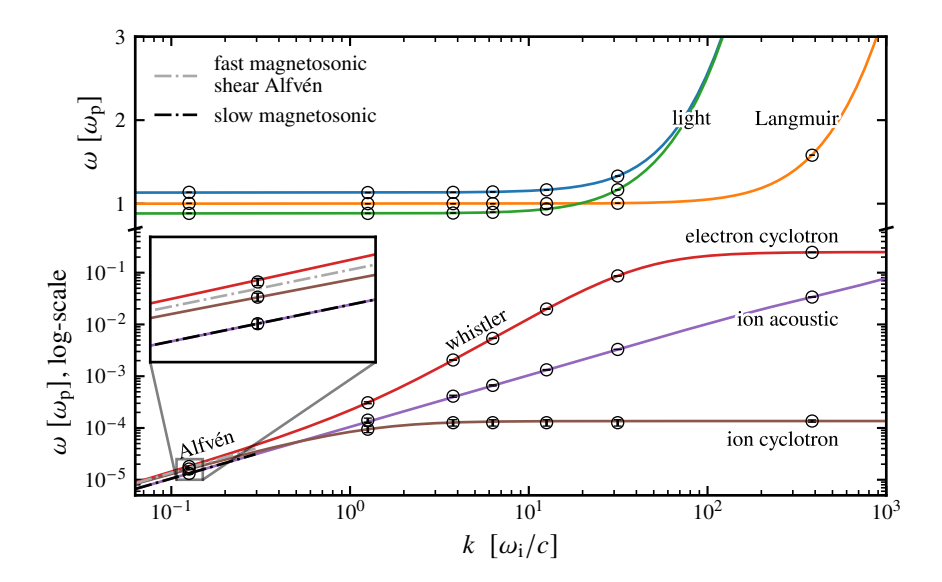


Figure 4.4. The six branches of the two-fluid dispersion relation are shown as lines, with two electrostatic wave branches (Langmuir and ion-acoustic) as well as four electromagnetic wave branches, of which two are left and two are right-hand circularly polarized (LCP and RCP). The lower RCP is referred to as the whistler or electron cyclotron branch and the lower LCP as ion cyclotron branch; for parallel propagation their phase velocities approach the Alfvén speed at small k. The upper RCP and LCP are modified light waves. We mark the six local extrema of the discrete Fourier-transformed fluid simulation outputs at each wavenumber with circles encapsulating the errorbars extending over the frequency bin. For comparison, we plot the dispersion relation of the three MHD waves at scales larger than the ion inertial length,  $1/k > c/\omega_i$ .

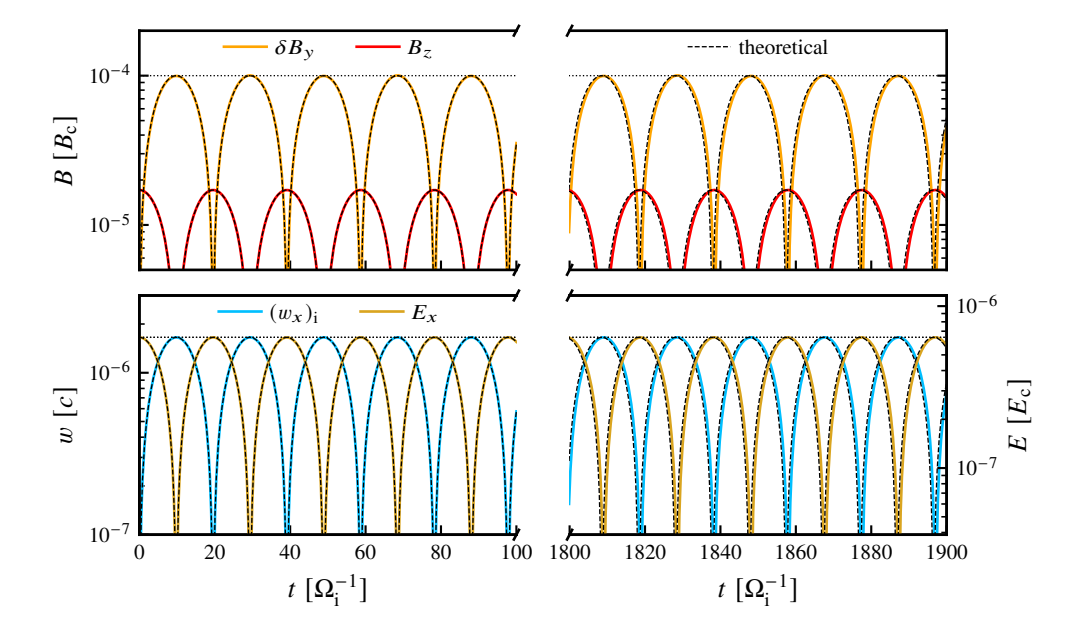


Figure 4.5. An oblique fast magnetosonic wave in the low  $\beta$  regime. We plot the absolute of the perturbations of the magnetic field strengths in the top panel, as well as the ion bulk velocity and electric field along the domain in the bottom panel. The theoretical predictions are shown as black-dashed lines while the black-dotted lines indicate the amplitude. Electric and magnetic field strengths are expressed in code units, denoted by the subscript c.

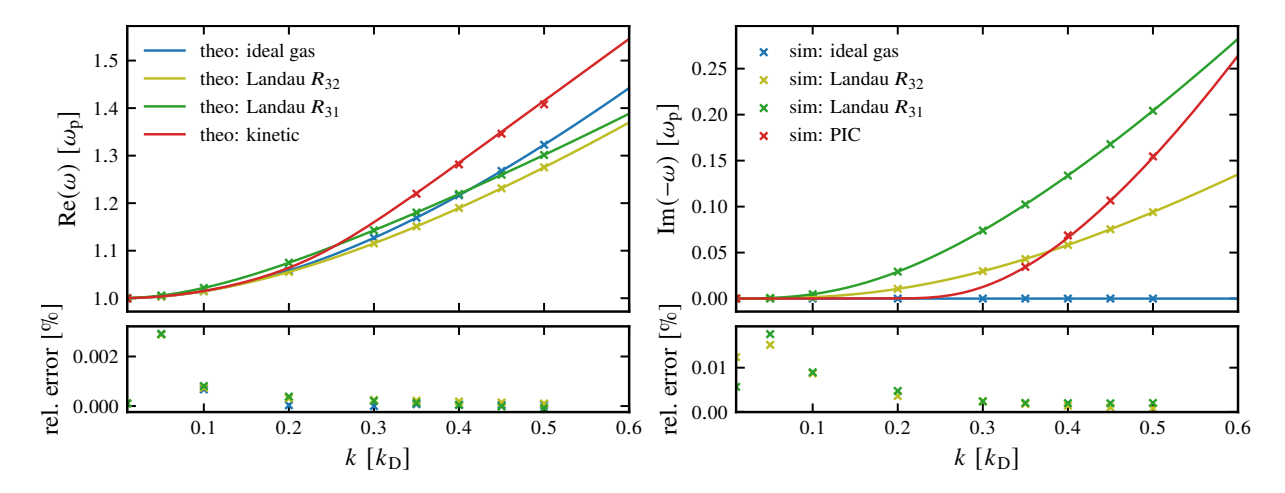


Figure 4.6. The linear dispersion relations of a Langmuir wave with immobile ions. Shown are, on the left-hand side, the real frequency components and, on the right-hand side, the negative imaginary frequency components (which are responsible for damping). The crosses present data points obtained from simulations with the respective closure while the theoretical result is shown with a solid line. The relative error between simulation and theoretical results  $(\omega^{\text{sim}} - \omega^{\text{theor}})/\omega^{\text{theor}}$  is shown in the lower panels. For reference, the red crosses display the data points as given in table 1 of Shalaby et al. (2017b).

conditions for all of our fluid simulations of waves are obtained as eigenvectors (in U, E, B) while theoretical predictions of  $\omega$  are obtained as eigenvalues using an extended algorithm based on the dispersion solver by Xie (2014), which can take into account the effects of both heat flux closures. We calculate the initial conditions to double precision, the machine precision of the simulation code. We normalise the amplitude of the eigenvectors by setting the maximum amplitude in any quantity to  $10^{-4}$  for each wave mode, to suppress non linear effects. The resolution is  $\Delta x = 0.1 \, c/\omega_e$  for all simulations. The box size for the intermediate scale is  $L_x = 214.2 \, c/\omega_e$ , covering waves with  $k = n_w k_0$  of  $n_w = 1, 3, 5, 10, 25$ , where  $k_0 = 2\pi/L_x$ . The largest and smallest scales use box sizes of  $L_x = 2142 \, c/\omega_e$  ( $n_w = 1$ ) and  $L_x = 21 \, c/\omega_e$  ( $n_w = 3$ ) respectively. A Fourier analysis in time has been performed and the six largest local extrema are shown as encircled bars extending over a Fourier bin in figure 4.4. It can be seen, that the simulation results are in excellent agreement with the analytical results. In the Fourier-analysis of the slowest two waves, the Fourier mode closest to the theoretical wave frequency is always observed. The largest error measured in this analysis occurs in the whistler branch for  $k \sim 31c/\omega_i$  with less than 0.5 per cent.

Because our Riemann solver is not explicitly informed about MHD wave speeds, for which the coupling between fluids and electromagnetic fields is especially strong, one could naively expect large errors or numerical instabilities in the MHD limit. In order to test the fidelity of the coupling, we set up a wave with a wave speed well separated from the propagation speeds of the uncoupled fluid Riemann and electromagnetic solvers, i.e.  $c_s \ll v_\varphi = \omega/k \ll c$ . We test a fast magnetosonic wave ( $v_\varphi = 0.03728c$  in two-fluid vs.  $v_{\rm fast} = 0.03703c$  in MHD) at very low  $\beta_{\parallel,i} = \beta_{\perp,i} = 0.02$  (corresponding to an oblique propagation angle of  $\theta = 45^{\circ}$  in the  $B_y - B_x$  plane). The parameters of k,  $\Delta x$ , etc., are the same as for the parallelly propagating waves in the MHD

limit in the previous test. While parallelly propagating electrostatic (electromagnetic) waves can be described using 1D1V (1D2V) models, oblique propagation requires the 1D3V model. In figure 4.5 the time evolution of two representative quantities along and perpendicular to the box size direction are shown. The time evolution of the different quantities are taken from the first cell in the simulation box. The fast magnetosonic wave is captured well, short and long term, without introducing numerical instabilities at low dissipation. The simulated wave velocity is 0.027 per cent slower than the theoretical prediction. In conclusion, the current-coupled fluid and electromagnetic solvers numerically approximate the analytical dispersion relation with high fidelity.

## 4.3.3. Langmuir wave damping

The electrostatic wave modes are directly subject to linear Landau damping, and thus present a good test for the heat flux closures. To test this, we initialize standing Langmuir waves in an electron plasma with immobile ions. We use the same grid layouts as in table 1 of Shalaby et al. (2017b), supplemented with fluid simulations run at  $k/k_{\rm D} \in \{0.1, 0.2, 0.3\}$  with a resolution of  $\lambda/\Delta x = 68$  cells per wavelength and a domain size of length  $L = 10\lambda$  wavelengths. The wavenumber associated with the Debye length is the ratio of plasma frequency to thermal velocity, i.e.  $k_{\rm D} = \omega_{\rm p}/\theta^{1/2}c$ . The amplitude of the wave is chosen, such that the density fluctuation to background ratio is fixed to  $\delta n/n_0 = 10^{-3}$ .

In order to find the numerical dispersion relation we perform curve fitting with the Powell algorithm on the time series for times up to  $80 \, \omega_{\rm p}^{-1}$ , while the simulations at  $k/k_{\rm D} = 0.01$  and 0.05 with small damping are analysed up to  $240 \, \omega_{\rm p}^{-1}$ . The computation of the heat fluxes for the  $R_{31}$  and  $R_{32}$  closures is performed using the FFT-based method. The results are shown in figure 4.6, where the ideal gas closure and the kinetic results are also depicted for reference (using  $\Gamma = 3$ ).

Generally, it can be seen, that at small scales the closures show larger deviations from each other, which is also where the fluid description starts breaking down naturally as the particle distribution is not in equilibrium. At larger scales, the various descriptions of Landau damping converge and approach zero. The numerical relative error of the fluid code is small and stays below 0.003 per cent for real frequencies and below 0.02 per cent for decay rates in this setup. The simulation at  $k/k_{\rm D}=0.05$  performs worse than the one at  $k/k_{\rm D}=0.1$  due to the significantly lower resolution. The error in  $\omega$  decreases at second-order with increasing spatial resolution, as shown in Appendix 4.B.

#### 4.3.4. Interacting Alfvén waves

A single Alfvén wave is purely transversal and not directly affected by Landau damping. However, two or more Alfvén waves drive a longitudinal electrostatic wave, which is susceptible to Landau damping, see figure 4.7. This leads to particle heating as a result of the collisionless damping of the Alfvén wave, also known as non-linear Landau damping (Lee and Völk, 1973).

Restricting ourselves to a setup of pairwise interacting waves, we can identify two distinct

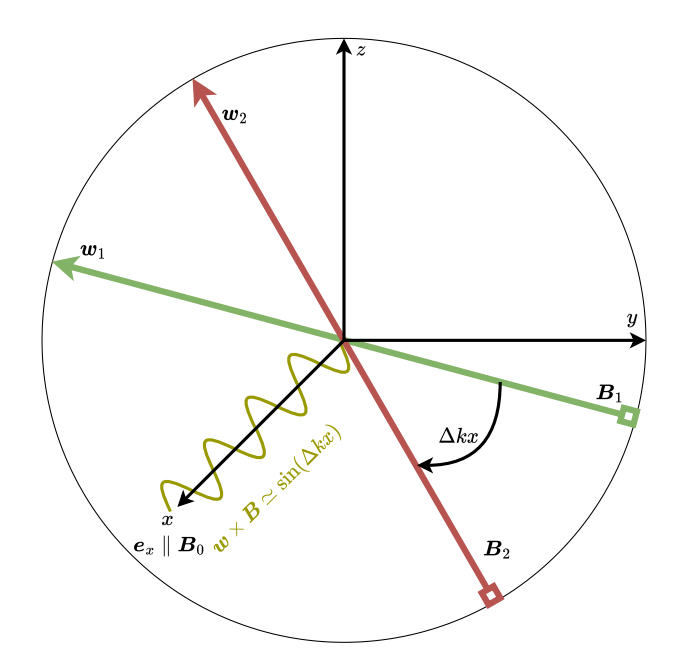


Figure 4.7. Two different Alfvén waves, with magnetic and velocity vectors  $\mathbf{B}_1$ ,  $\mathbf{B}_2$  and  $\mathbf{w}_1$ ,  $\mathbf{w}_2$ , propagate transversally along the x-axis, where the electromagnetic vectors rotate (counter)clockwise around it. Because of their phase difference  $\Delta kx$  the overall Lorentz force  $(\mathbf{w}_1 + \mathbf{w}_2) \times (\mathbf{B}_1 + \mathbf{B}_2)$  in x-direction is non-zero, thereby generating the longitudinal wave shown in dark yellow.

cases. In the first case counter-propagating waves are interacting. In consequence, both waves damp, lose energy to the longitudinal wave and subsequently heat the particles. In the second case the waves are co-propagating. Here the wave with the smaller wavelength will not only transfer energy to the particles, but also to the other Alfvén wave. Lee and Völk (1973) describe this mechanism in detail and formulate the following coupled set of differential equations while adopting a measure for the magnetic energy of a wave,  $I_j = |B_j|^2$ , where  $j \in \{1, 2\}$ :

$$\frac{\mathrm{d}}{\mathrm{dt}}I_j = 2\Gamma_j I_j. \tag{4.58}$$

The coupling between the differential equations is implicit because the damping coefficient has the dependency  $\Gamma_1 \propto I_2$ . For the counter-propagating case with an isothermal ion-electron-plasma in the high beta limit  $\beta_i = 2\mu_0 n_i k_B T_i/B_0^2 = 2 \gg 1$ , where  $B_0$  is the background magnetic field strength, the damping rate  $\Gamma_j$  is approximately equal for both wave polarizations with similar frequencies  $\omega_j$  and may be approximated by (Holcomb, 2019)

$$\Gamma_1 = -\frac{\sqrt{\pi}}{16} \frac{I_2}{B_0^2} \sqrt{\beta_i} \omega_1. \tag{4.59}$$

Note that  $\Gamma_2$  is found by substituting the subscripts  $1 \to 2$  and  $2 \to 1$ . This prediction is using kinetic physics and also includes damping effects due to modulation in  $B_{\perp}$  (see figure 4.5), which can electromagnetically heat or even trap particles analogous to Landau damping in the electrostatic case. This is not captured in the Landau fluid approximation. Therefore, we do not

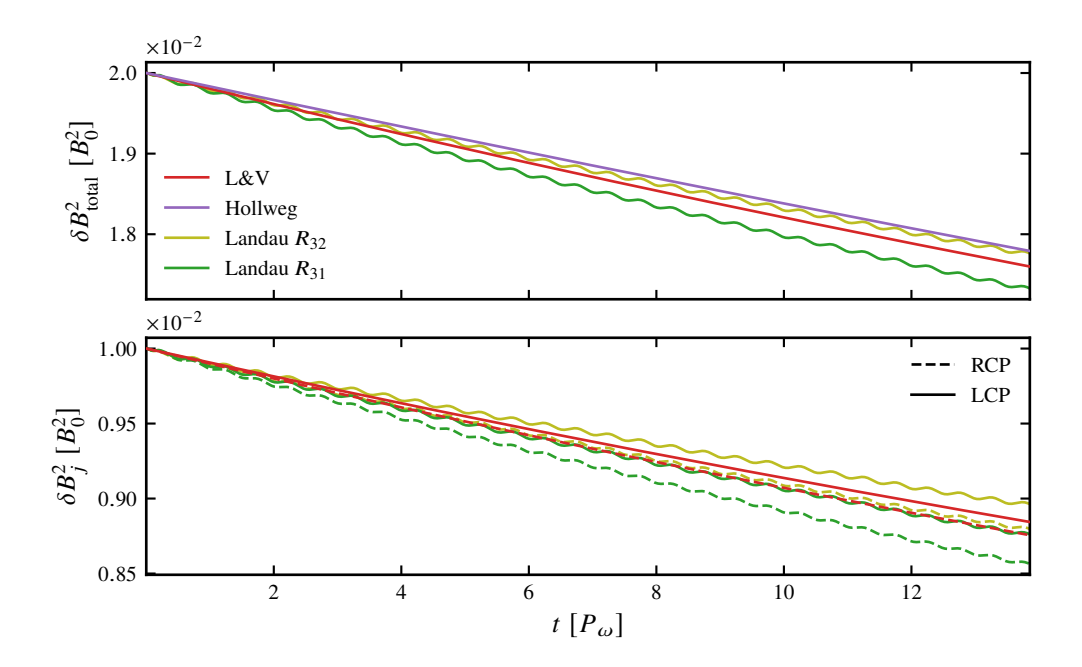


Figure 4.8. Time evolution of the magnetic energy of a linearly polarized Alfvén wave in our fluid simulations with Landau damping. Time is measured in units of the period of the mean wave frequencies  $P_{\omega} = 4\pi(\omega_1 + \omega_2)^{-1}$ . Analytical predictions for the damping rate are taken from Lee and Völk (1973, labelled L&V) and Hollweg (1971). The fluid simulations are presented with the different heat flux closures  $R_{31}$  and  $R_{32}$ . We compare the time evolution of the total magnetic wave energy (top panel) and the magnetic wave energy of the different polarization states (bottom panel). The RCP wave has a higher phase velocity and loses energy more quickly in comparison to the LCP wave.

expect our analytical and simulated damping rates to exactly match. However, they provide a good insight into whether wave modes are qualitatively correctly captured. Another prediction by Hollweg (1971) uses the fluid picture to derive the amplitude of the secondary, electrostatic wave, which is then damped according to kinetic prescriptions. This prediction agrees with our model. However, this analysis does not differentiate different wave types and therefore does not make individual predictions about interacting waves. In the case considered in the following, the damping rates are coincidentally similar.

In figure 4.8 we show simulations of a linearly polarized Alfvén wave, which consists of two counter-propagating waves of equal amplitude. The pure fluid simulations are shown with a box size of  $L = 252 \, c/\omega_{\rm i}$  and wavelengths  $\lambda = L/3$ . Right- and left-hand circularly polarized waves are initialized with phase velocities  $\omega_{\rm RCP}/k = 0.0342$  and  $\omega_{\rm LCP}/k = 0.0318$  with a perpendicular magnetic field amplitude of  $\delta B = 0.1 \, B_0$ . A reduced mass-ratio of  $m_{\rm i}/m_{\rm e} = 100$  is adapted here.

Our simulations are carried out with the different heat flux closures  $R_{32}$  and  $R_{31}$ , as shown in figure 4.8. Both closures reproduce the theoretical predictions quite well. A PIC simulation with similar parameters has been shown in figure 6.4 by Holcomb (2019), which reproduces half of the predicted damping rate until  $t \sim 2P_{\omega}$  and shows a quenching of the damping rate afterwards. In comparison to kinetic simulations, there is no saturation of the Landau-damping effect in fluids. This is because the distribution of the fluid particles is always assumed to be roughly

Maxwellian and resonant particles are not depleted as a function of time. Hence, Landau fluids are implicitly assumed to have small thermalization timescale in comparison to the damping timescale. On the other hand, PIC simulations are plagued by Poisson noise and an insufficient resolution of velocity space might lead to a reduced Landau damping rate.

## 4.3.5. Gyrotropic CR streaming instability

To test the entire code, we run CR streaming instability simulations, where electron and ion CRs are modelled with the PIC method and the background electron and ion plasmas are modelled as fluids. The initial CR momentum distribution for ions (electrons) is assumed to be a gyrotropic distribution with a non-vanishing (zero) pitch angle, while both CR electrons and ions are assumed to drift at the same velocity  $v_{\rm dr}$ . Namely, the phase space distributions for the electron and ion CR species  $s \in \{e, i\}$  are given by (Shalaby et al., 2021, 2023)

$$f_{\mathrm{cr},s}(\boldsymbol{x},\boldsymbol{u}) = \frac{n_{\mathrm{cr},s}}{2\pi u_{\perp}} \delta(u_{\parallel} - \gamma_s v_{\mathrm{dr}}) \delta(u_{\perp} - \gamma_s v_{\perp,s}), \tag{4.60}$$

where  $\gamma_s = (1 - v_{\rm dr}^2/c^2 - v_{\perp,s}^2/c^2)^{-1/2}$  is the Lorentz factor and  $v_{\perp,s}$  is the perpendicular component of the CR velocity. We choose  $v_{\perp,e} = 0$  and  $v_{\perp,i} = 13.1v_{\rm A}$ , where the ion Alfvén velocity is given by  $v_{\rm A} = B_0/(\mu_0 n_{\rm i} m_{\rm i})^{1/2} = 0.01c$  with the background magnetic field pointing along the spatial direction, and  $v_{\rm dr}$  of  $5v_{\rm A}$  resulting in a pitch angle for the ions of  $\tan^{-1}(v_{\perp,i}/v_{\rm dr}) = 69.1^{\circ}$ . The thermal background species are isothermal with the temperatures  $k_{\rm B}T/(mc^2) = 10^{-4}$  and a mass ratio  $m_{\rm i}/m_{\rm e} = 1836$ . We use a periodic box of length  $L_x = 10~971.5~c/\omega_{\rm p}$  and resolution  $\Delta x = 0.1~c/\omega_{\rm p}$ . The CR to background number density ratio  $\alpha = n_{\rm cr,i}/n_{\rm i} = 0.01$ .

We run two simulations where the background plasmas are modelled as fluids. The first one uses an ideal gas closure without accounting for Landau damping (FPIC ideal gas) while we include the heat flux source term in the second simulation to mimic the impact of linear Landau damping using the  $R_{31}$  closure of equation (4.46) (FPIC Landau  $R_{31}$ ). We compare these two fluid-PIC simulations against PIC simulations where both CRs and background plasmas are modelled as PIC species. The number of CR ions per cell is  $N_{\rm pc} = 25$  (75) and we call this simulation "PIC normal (high)  $N_{\rm pc}$ " (Shalaby et al., 2021). Like the "PIC normal  $N_{\rm pc}$ " simulation, the fluid-PIC simulations also use 25 particles per cell for modelling CRs.

Growth rates of the instability in the linear regime can be computed from the linear cold background plasma dispersion relation (Holcomb and Spitkovsky, 2019; Shalaby et al., 2022):

$$0 = 1 - \frac{k^{2}c^{2}}{\omega^{2}} + \frac{\omega_{i}^{2}}{\omega\left(-\omega \pm \Omega_{i,0}\right)} + \frac{\omega_{e}^{2}}{\omega\left(-\omega \pm \Omega_{e,0}\right)} + \frac{\alpha\omega_{e}^{2}}{\gamma_{e}\omega^{2}} \left(\frac{\omega - kv_{dr}}{kv_{dr} - \omega \pm \Omega_{e,0}}\right) + \frac{\alpha\omega_{i}^{2}}{\gamma_{i}\omega^{2}} \left(\frac{\omega - kv_{dr}}{kv_{dr} - \omega \pm \Omega_{i}} - \frac{v_{\perp}^{2}/c^{2}\left(k^{2}c^{2} - \omega^{2}\right)}{2\left(kv_{dr} - \omega \pm \Omega_{i}\right)^{2}}\right).$$

$$(4.61)$$

The non-relativistic and relativistic cyclotron frequencies of each species are given by  $\Omega_{\rm s,0} = q_s B_0/m_s$  and  $\Omega_{\rm s} = \Omega_{\rm s,0}/\gamma_{\rm s}$  respectively. The wavelength of the most unstable wave mode at the gyroscale is  $\lambda_{\rm g} = 2\pi (v_{\rm dr} - v_{\rm A})/\Omega_{\rm i}$ , which is properly captured in our setup using a box size of

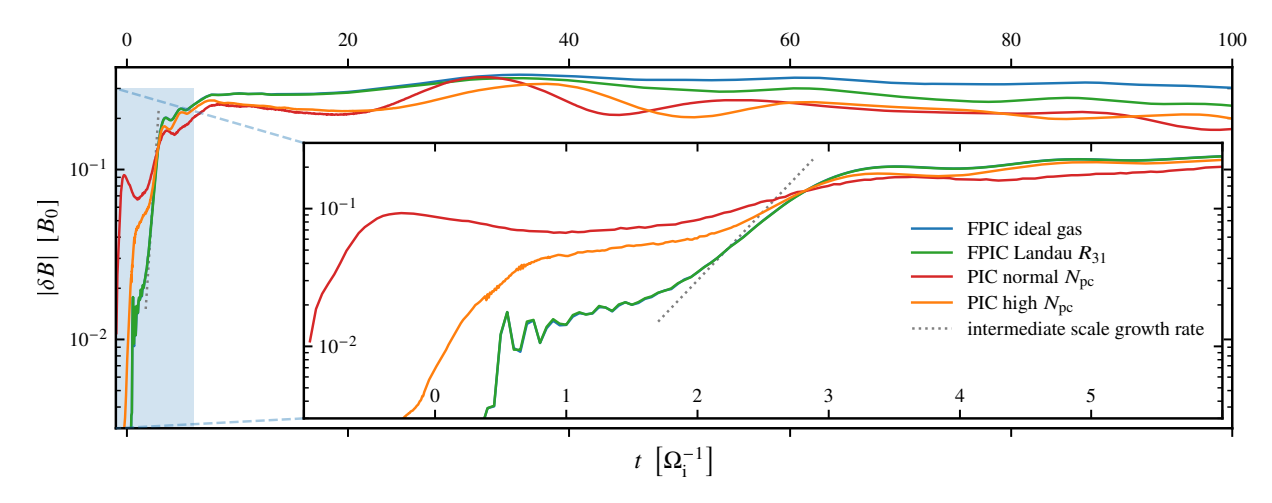


Figure 4.9. Growth of the perpendicular magnetic field as a function of time for a gyrotropic CR streaming setup. The maximum growth rate expected from the linear dispersion relation at intermediate scales is  $\Gamma_{\rm inter} = 2.299\Omega_{\rm i}$  and shown in dashed grey. because of the different initial seed populations for the particle species, the onset of the instabilities is not expected to happen at the same simulation time. Hence, we choose an arbitrary t=0 so that the different simulated growth phases roughly coincide.

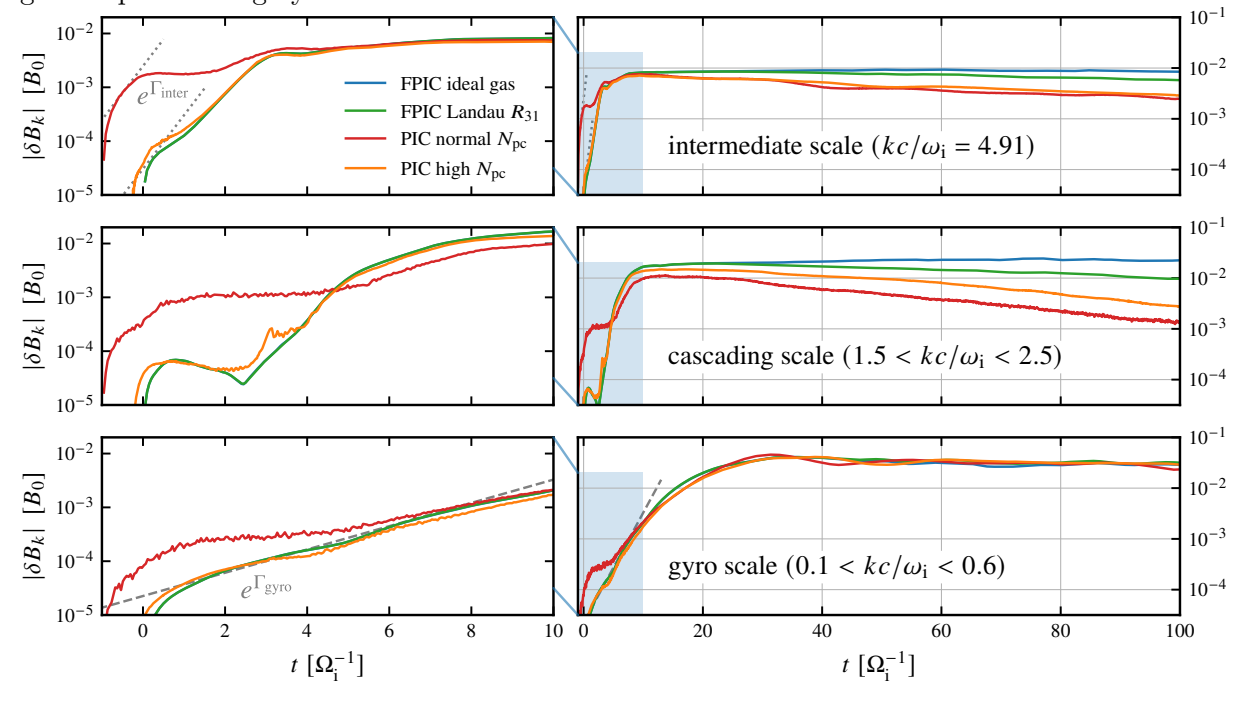


Figure 4.10. Growth of the perpendicular magnetic field as a function of time at different scales for a gyrotropic CR streaming setup. We show mean values of the fields that are averaged over a range of wave vectors k, as indicated in the legends. The maximum growth rates at the gyro scale and the intermediate scale are given by  $\Gamma_{\rm gyro} = 0.498\Omega_{\rm i}$  and  $\Gamma_{\rm inter} = 2.299\Omega_{\rm i}$ , and indicated by the grey dotted and dashed lines, respectively. At wavenumbers corresponding to cascading scales, there is no instability expected according to the linear dispersion relation, and wave growth solely arises as a result of cascading from other (unstable) scales.

 $L_x \sim 10.15 \lambda_g$ .

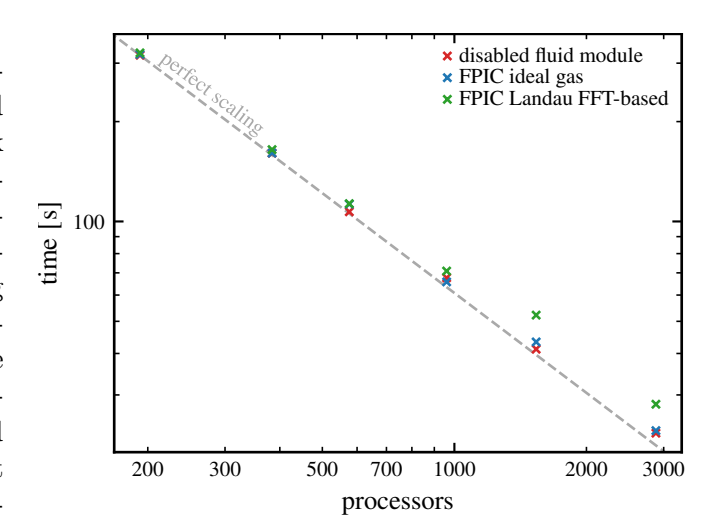
We show the amplification of the perpendicular magnetic field components as a function of time for this unstable setup in figure 4.9 for various simulations. It shows that the noise level of the fluid-PIC simulations is orders of magnitude lower in comparison to the "PIC normal  $N_{\rm pc}$ " resolution, even though the number of CR particles per cell is the same. Especially up to the saturation point  $(t\Omega_{\rm i}\sim 10)$  the fluid-PIC simulation compares more favourably to the PIC results with lower noise than to the PIC simulation with fewer  $N_{\rm pc}$ .

After saturation, i.e. when Alfvén waves at many scales have built up and their interaction has created an electrostatic field, these waves start to lose some energy to Landau damping of the electrostatic waves (see Section 4.3.4). At that point, the Landau closure becomes relevant. Qualitatively the ideal gas closure has no efficient mechanism for dissipating such electrostatic waves, resulting in a prolonged growth period leading to saturation at higher values at the cascading and intermediate scales. Utilization of a Landau closure leads to some damping, albeit it is quantitatively smaller than in the PIC simulations. While figure 4.6 indicates faster damping for the Landau closures in comparison to the kinetic results in the electron electrostatic branches, damping in the ion-acoustic branch might be underestimated in the Landau closures. We have compared the expected damping between kinetic and Landau fluid in the ion-acoustic branch for multiple wavenumbers, which confirmed that this is a likely scenario. The accuracy of this approximation is not the same at all scales, which can be seen in figure 4.10, where the magnetic field amplifications at various ranges of scales are compared. Especially in the highly Landau-damped scales, differences between fluid-PIC and PIC emerge. At ion gyro scales, where most of the magnetic energy is stored at saturation, there is a good agreement over the entire time period. Exponential growth at every scale is also in good agreement between PIC and fluid-PIC simulations at all scales. The initial exponential growth can also be compared to the expected growth rates from the linear dispersion relation. The growth rates of the two local maxima are plotted alongside the simulated data, one at the intermediate scales around  $ck = 4.91\omega_i$  and one at the gyro scale at  $ck = 0.38\omega_i$ . The intermediate scale starts an inverse cascade to larger scales almost immediately, which causes a reduced growth rate in comparison to the expectation from linear theory. By contrast, the gyro scale instability follows linear expectations to very good approximation.

While our fluid-PIC and PIC results are promisingly similar, differences after the saturation level might be attributed to multiple reasons. First, the Landau closures do not exactly reproduce the correct damping, and therefore will deviate quantitatively. Second, due to the high electron temperature chosen, relativistic effects might occur in PIC, but not in the non-relativistic fluid that we assumed for the background plasma. Third, the PIC method might exhibit more numerical dissipation at the given  $N_{\rm pc}$  in comparison to the fluid method. However, figure 4.10 seems to indicate numerical convergence at the intermediate and gyro scale.

Even though our simulations were run at unrealistically high  $\alpha$ , the background particles did not deviate significantly from the Maxwellian distribution at the end of the simulation time. The pressure anisotropy measured from the PIC thermal particles is below 2%. This indicates, that an isotropic fluid description for background species is a valid approach for this setup, especially

Figure 4.11 Strong scaling of the fluid-PIC code, with and without Fourier-based Landau closures. Shown is the wall-clock time needed to simulate 1250 time integration steps with 180000 cells at 1000 particles per cell at a varying number of processors. We show the perfect strong scaling that is proportional to the inverse number of processors as the grey dashed line for reference. For the disabled fluid module no background plasma was initialized and only CRs are initialized, showing that the bulk of the computational work is performed by the PIC routines.



for smaller, more realistic values of  $\alpha$ .

## 4.3.6. Computational scaling

We show the strong scaling properties of our fluid-PIC code in figure 4.11. The tests were run on Intel Cascade 9242 processors with 96 processors per node at the HLRN Emmy cluster. Simulations with 3000 processors or more typically cause severe bottlenecks due to the latency and/or the finite bandwidth of input/ouput operations. For this number of processors the Fourier-based closures are roughly 20 per cent more costly in comparison to the ideal gas closures. This is in stark contrast to pure PIC simulations, which scale with the inverse ratio of CR-to-background density  $\alpha^{-1}$ , consequently the fluid-PIC algorithm leads to a speed-up of a factor of 100 for the simulation performed in Section 4.3.5, which adopted unrealistically large  $\alpha$ .

The bottleneck in the communication procedure of our implementation is currently the "Iall-toally" MPI routine, which is not optimized for hierarchical architecture networks as of now. Further optimizations to this might provide fruitful in increasing the code's scalability further if necessary.

The fluid-PIC simulations in Section 4.3.5 used only  $N_{\rm pc}=25$  and seem to be sufficiently resolved. For such a low particle number, the FFT is the bottleneck for scalability because the overlap of communication and computation is small, i.e. we measure a 260 per cent increase in time with 2880 processors, while at 192 processors the increase is below 20 per cent. This indicates that scalability of fluid-only simulations is dominated quickly by the FFT, while the cost is almost negligible for fluid-PIC simulations. Still, simulations with only a few particles per cell are computationally inexpensive so that there is no reason for performing such a simulation on thousands of processors. Furthermore, the example of a mono-energetic cold CR beam is not very demanding regarding the phase-space resolution. More realistic scenarios include power law distributions for the CR population as well as larger spatial density inhomogeneities, both resulting in an increased requirement for the number of particles per cell in order to accurately resolve the velocity phase-space distribution along the entire spatial domain.

## 4.4. Conclusion

In this paper, we introduce a new technique termed fluid-PIC, which uses Maxwell's equations to self-consistently couple the PIC method to the fluid equations. This technique is particularly aimed at simulating energetic particles like CRs interacting with a thermal plasma. This enables us to resolve effects on electron time and length scales and to emulate Landau damping in the fluid by incorporating appropriate closures for the divergence of the heat flux. The underlying building blocks of our implementation are the SHARP 1D3V PIC-code extended by a newly developed fluid module and the overall algorithm is second-order accurate in space and time. While an ideal fluid does not exhibit Landau damping, we have implemented two different Landau fluid closures and studied their performance. Here we summarize our main findings:

- We developed a multi-species fluid code that is coupled to explicit PIC algorithm. In order to couple multi-fluid equations to Maxwell's equations, very often implicit and semi-implicit methods have been used for stability reasons. However, the resulting interdependency between all fluids complicates their coupling to explicit PIC methods. To ensure numerical stability, Riemann solvers that provide some numerical diffusion are used. However, we demonstrate that the level of numerical diffusivity needs to be small enough so that it does not numerically damp physical small-amplitude plasma waves or quench plasma instabilities. We confirm the numerical stability and small dissipation of our implementation by employing a diverse range of test setups that test the coupling between the fluid and electromagnetic modules. Most importantly, our new fluid-PIC code fully resolves the electron timescales, precluding the need to adopt any simplifying assumptions to the electrical field components or to Ohm's law. This enables the versatility of our implementation, allowing to instantiate an arbitrary number of species, which can be modelled individually either as a fluid or as particles.
- We compare various Landau fluid closures and demonstrate that local closures only produce reliable results close to a characteristic scale while they are prone to fail in multi-scale problems. By contrast, semi-local spatial filters or global (Fourier-based) methods to estimate Landau fluid closures produce reliable results for a large range of scales. Most importantly, we demonstrate that the inclusion of communication intensive (Fourier-based) fluid closures only have a minimal impact on our code performance (through the usage of non-blocking background communication) because the majority of the computational workload is taken up by the much more cost-intensive PIC module. This enables us to make use of the more accurate Fourier-based Landau closure for the fluid instead of relying on local approximations only.
- In numerical tests, our implementation of the multi-species fluid module showed excellent
  agreement with theoretical frequencies and damping rates of Langmuir waves, oscillation
  frequencies of various two fluid wave modes, as well as the non-linear Landau damping of
  Alfvén waves.

• First simulations of the CR streaming instability with our combined fluid-PIC code provide very good agreement with the results of pure PIC simulations, especially for the growth rates and saturation levels of the gyro-scale and intermediate-scale instabilities. This success is achieved at a substantially lower Poisson noise of the background plasma at the same number of computational CR particles per cell. Most importantly, the numerical cost of the fluid-PIC simulation is reduced by the CR-to-background number density ratio. However, we find that the late-time behaviour of the CR streaming instability differs for our fluid-PIC and PIC simulations. More work is needed to understand the reason for this, which could be either resulting from (i) numerical damping due to Poisson noise resulting from the finite number of PIC particles, (ii) missing relativistic (electron) effects in our non-relativistic fluid dynamics, or (iii) missing physics in our fluid closures that may be underestimating other relevant collisionless wave damping processes.

Three possible future extensions of the algorithm are left open here. (i) Extending the fluid formulation with a full pressure tensor, (ii) extending the code to two or three spatial dimensions, and (iii) the inclusion of direct interaction terms between the various fluids to explicitly incorporate scattering processes such as ion-neutral damping. The novel fluid-PIC framework greatly extends the computationally limited parameter space accessible to pure PIC methods whilst not compromising on some of the most important microphysical plasma effects. This opens up many possibilities for studying CR physics in physically relevant parameter regimes, such as the growth and saturation of the CR streaming instability in different environments, and including the effect of partial ionization, ion-neutral damping and inhomogeneities of the background plasma.

# **Appendix**

#### 4.A. C-WENO coefficients

We list all coefficients needed to implement the C-WENO reconstruction in this section. Because our reconstruction procedure is applied component-wise to each of the primitive variables, we assume for this appendix that we are reconstructing a single quantity u. The smoothness indicator for the low-order polynomials are given by (Jiang and Shu, 1996):

$$IS[P_{L}] = \frac{13}{12} (u_{i-2} - 2u_{i-1} + u_{i})^{2} + \frac{1}{4} (u_{i-2} - 4u_{i-1} + 3u_{i})^{2},$$
(4.62)

$$IS[P_{C}] = \frac{13}{12} (u_{i-1} - 2u_i + u_{i+1})^2 + \frac{1}{4} (u_{i+1} - u_{i-1})^2,$$
(4.63)

$$IS[P_{R}] = \frac{13}{12} (u_{i} - 2u_{i+1} + u_{i+2})^{2} + \frac{1}{4} (3u_{i} - 4u_{i+1} + u_{i+2})^{2},$$
(4.64)

while four auxiliary variables are defined

$$D_1 = \frac{(6w_0 - 1)(u_{i-2} + u_{i+2}) - 2(18w_0 - 1)(u_{i-1} - u_{i+1})}{48w_0},$$
(4.65)

$$D_2 = \frac{(2w_0 - 3)(u_{i-2} + u_{i+2}) - 2(2w_0 + 9)u_i + 12(u_{i-1} + u_{i+1})}{16w_0},$$
(4.66)

$$D_{3} = \frac{-u_{i-2} + 2(u_{i-1} - u_{i+1}) + u_{i+2}}{12w_{0}},$$

$$D_{4} = \frac{u_{i-2} - 4u_{i-1} + 6u_{i} - 4u_{i+1} + u_{i+2}}{24w_{0}},$$

$$(4.67)$$

$$D_4 = \frac{u_{i-2} - 4u_{i-1} + 6u_i - 4u_{i+1} + u_{i+2}}{24w_0},\tag{4.68}$$

to define the smoothness indicator for the  $P_0$  polynomial:

$$IS[P_0] = D_1^2 + \frac{13}{3}D_2^2 + \frac{3129}{80}D_3^2 + \frac{87617}{140}D_4^2 + \frac{1}{2}D_3D_1 + \frac{21}{5}D_2D_4.$$
 (4.69)

The overall smoothness indicator is given by (Cravero et al., 2018a):

$$\tau = |\operatorname{IS}[P_{\mathrm{L}}] - \operatorname{IS}[P_{\mathrm{R}}]|. \tag{4.70}$$

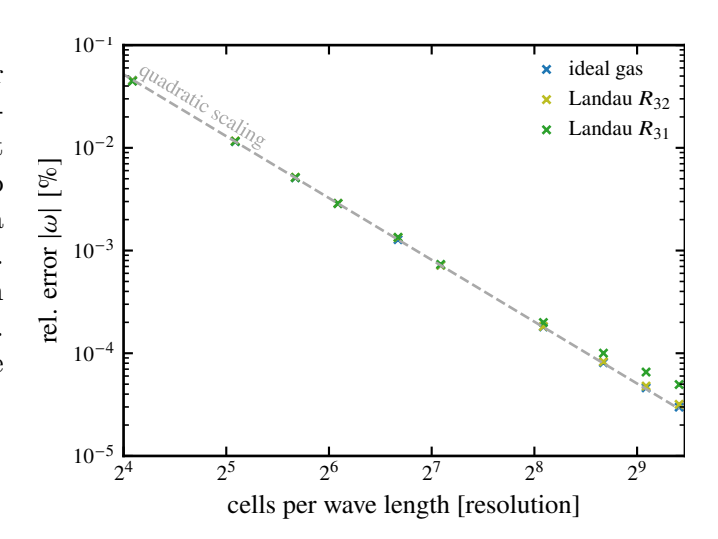
The low-order polynomials are evaluated at the left-hand interface of a given cell via:

$$P_{\mathcal{L}}\left(x_{i-\frac{1}{2}}\right) = \frac{1}{6}(-u_{i-2} + 5u_{i-1} + 2u_i),\tag{4.71}$$

$$P_{\mathcal{C}}\left(x_{i-\frac{1}{2}}\right) = \frac{1}{6}(2u_{i-1} + 5u_i - u_{i+1}),\tag{4.72}$$

$$P_{\mathcal{R}}\left(x_{i-\frac{1}{2}}\right) = \frac{1}{6}(11u_i - 7u_{i+1} + 2u_{i+2}),\tag{4.73}$$

Figure 4.12 Relative error  $|(\omega^{\text{sim}} - \omega^{\text{theor}})/\omega^{\text{theor}}|$  of the simulated frequency of a Langmuir wave at  $k = 0.05k_{\text{D}}$ . The same simulation setup is used in figure 4.6, where we use a resolution of 68 cells per wavelength. The resolution here is varied between 68/4 = 17 to  $68 \times 10$  cells per wavelength. The grey line is a reference line for the second-order scaling of the error.



while they evaluate to

$$P_{\mathcal{L}}\left(x_{i+\frac{1}{2}}\right) = \frac{1}{6}(2u_{i-2} - 7u_{i-1} + 11u_i),\tag{4.74}$$

$$P_{\mathcal{C}}\left(x_{i+\frac{1}{2}}\right) = \frac{1}{6}(-u_{i-1} + 5u_i + 2u_{i+1}),\tag{4.75}$$

$$P_{\rm R}\left(x_{i+\frac{1}{2}}\right) = \frac{1}{6}(2u_i + 5u_{i+1} - u_{i+2}),\tag{4.76}$$

at the right-hand interface. The optimal polynomial evaluates to

$$P_{\text{opt}}\left(x_{i-\frac{1}{2}}\right) = \frac{1}{60}\left(-3u_{i-2} + 27u_{i-1} + 47u_i - 13u_{i+1} + 7u_{i+2}\right)$$

$$= \frac{1}{10}\left[3P_{\text{L}}\left(x_{i-\frac{1}{2}}\right) + 6P_{\text{C}}\left(x_{i-\frac{1}{2}}\right) + P_{\text{R}}\left(x_{i-\frac{1}{2}}\right)\right],$$
(4.77)

$$P_{\text{opt}}\left(x_{i+\frac{1}{2}}\right) = \frac{1}{10} \left[ P_{\text{L}}\left(x_{i+\frac{1}{2}}\right) + 6P_{\text{C}}\left(x_{i+\frac{1}{2}}\right) + 3P_{\text{R}}\left(x_{i+\frac{1}{2}}\right) \right], \tag{4.78}$$

at both interfaces of the cell. The interface values of  $P_0$  can be derived from equation (4.24).

#### 4.B. Convergence order

In order to numerically prove a second order scaling of the plasma frequency for the different heat flux closures, the linear dispersion of the Langmuir wave setup described in Section 4.3.3 is simulated at different resolutions of  $\lambda/\Delta x$ . We concentrate here on the convergence of a wave with wavenumber  $k/k_{\rm D}=0.05$ . The results are shown in figure 4.12 and demonstrate a very good match with the predicted errors assuming a second order convergence. At first sight, the Landau closures do not seem to scale ideally for higher resolutions. However, this is the result of physical plasma heating due to wave damping in our setup leading to a non-linear increase in the expected plasma frequency. The accuracy of the spatial integration of our code is currently limited by the Yee grid to second order; the time integration of the code is also second order accurate, which is limited by the operator splitting of the fluid, the Yee grid as well as the leapfrog integration of the particles.

## 4.C. $R_{31}$ closure and adiabatic coefficients

While the  $R_{32}$  closure assumes a fixed adiabatic index  $\Gamma$  of 3, the  $R_{31}$  closure introduces a term proportional to  $\hat{w}$  which alters the pressure equation in such a way that it increases the effective adiabatic index. To show this, we simplify equation (4.46) by introducing the numerical coefficients  $a_w$  and  $a_T$  which are defined by comparing

$$\hat{Q} = a_w p_0 \hat{w} + i \operatorname{sign}(k) a_T \hat{T}. \tag{4.79}$$

to equation (4.46). Using this ansatz and perturbing the pressure equation (4.32) with  $p = p_0 + p_1$ , where  $p_1$  is the perturbation to the mean pressure  $p_0$ , in the absence of direct Landau damping ( $a_T = 0$ ), we have

$$\frac{\partial p_1}{\partial t} = (-\Gamma p - a_w p_0) \nabla \cdot \boldsymbol{w} - \boldsymbol{w} \cdot \nabla p = (-\Gamma_{\text{eff}} p_0 - \Gamma p_1) \nabla \cdot \boldsymbol{w} - \boldsymbol{w} \cdot \nabla p, \tag{4.80}$$

where  $\Gamma_{\rm eff} = a_w + \Gamma = 4/(4-\pi) \simeq 4.66$  can be interpreted as the effective adiabatic index of the fluid. The evolution of sound waves of a non-electromagnetic fluid in the linear regime is governed by the linear term  $\Gamma_{\rm eff} p_0 \nabla \cdot \boldsymbol{w}$  while the term  $\Gamma p_1 \nabla \cdot \boldsymbol{w}$  adds non-linearity to this equation. In the linear approximation, the speed of sound becomes  $c_s = (\Gamma_{\rm eff} p_0/n_0)^{1/2}$  which coincides with the typical expression for the sound speed  $c_s = (\Gamma p_0/n_0)^{1/2}$  in the limit of  $a_w = 0$ . This implies that the speed of sound is increased for the  $R_{31}$  closure even if direct Landau damping is not present  $(a_T = 0)$ . Interestingly, the effective adiabatic index and the speed of sound are independent of the choice of  $\Gamma$ . If direct Landau damping, as described by the  $R_{31}$  closure, is affecting the fluid (i.e.,  $a_T \neq 0$ ), then the effective adiabatic index attains somewhat smaller values in comparison to  $a_w + \Gamma$  while the wave frequency becomes complex because of the associated damping. Both are still independent of the choice of  $\Gamma$ .

This has consequences for simulations that model mildly relativistic fluids. If a simulation setup includes a fluid with an associated speed of sound near the speed of light  $c_{\rm s} \lesssim c$ , then a simulation that uses this setup with the  $R_{31}$  closure can become unstable because  $c_{\rm s}$  can now exceed the speed of light because of the aforementioned reason.

# 5. Quasilinear Theory of Cosmic Ray Streaming

The Vlasov equation (2.1) governs the evolution of a particle distribution function  $f = f(\mathbf{x}, \mathbf{v}, t)$  in phase space. For transparency, we suppress the subscript s labeling different species in this chapter, as all species-specific quantities refer to CRs unless explicitly stated otherwise. Quasilinear theory (QLT) provides a systematic approximation by decomposing the distribution function into  $f = f_0 + \delta f$ .  $f_0$  represents a slowly-varying background distribution and  $\delta f$  denotes a small perturbation ( $\delta f \ll f_0$ ) with vanishing mean  $\langle \delta f \rangle = 0$ , where the mean is obtained as an average over phase space. In distinction to linear theory, QLT allows the background distribution to evolve temporally at a slow pace, constrained by  $\partial/\partial t$   $f_0 \ll \partial/\partial t$   $\delta f$ .

With this approximation, the Vlasov equation is reformulated into the Fokker-Planck equation (Section 5.1), which describes statistical diffusion processes. Following the historical development, we first examine the diffusion rate of CRs interacting with Alfvén waves (Jokipii, 1966) in Section 5.2, and thereafter derive the growth rates of Alfvén waves for CR streaming (Wentzel, 1968) in Section 5.3. This chapter emphasizes the fundamental approximations in QLT and their implications for theoretical predictions.

We base the presentation in this chapter on the comprehensive treatments given by Schlickeiser (2002) and Kulsrud (2004), as well as the useful series of papers by Skilling (1975a,b,c) that provide a concise overview, and the more recent summaries found in the dissertations by Holcomb (2019) and Thomas (2022).

# 5.1. The Fokker-Planck Equation

We reformulate the Vlasov equation (2.1) using the relativistic momentum  $\mathbf{p} = \gamma m \mathbf{v}$  and the electromagnetic force  $\mathbf{F} = q(\mathbf{E} + \mathbf{v} \times \mathbf{B})$ . With  $\nabla_{\mathbf{p}} \cdot \mathbf{F} = 0$ , we obtain

$$\frac{\mathrm{d}f}{\mathrm{d}t} = \frac{\partial f}{\partial t} + \boldsymbol{v} \cdot \boldsymbol{\nabla} f + \boldsymbol{\nabla}_{\boldsymbol{p}} \cdot (\boldsymbol{F}f) = 0. \tag{5.1}$$

Analogous to the linearization of f, we also decompose the force into  $\mathbf{F} = \mathbf{F}_0 + \delta \mathbf{F}$ , likewise requiring a vanishing mean  $\langle \mathbf{F} \rangle = \mathbf{F}_0$ . Averaging (5.1) yields

$$\left\langle \frac{\mathrm{d}f}{\mathrm{d}t} \right\rangle = \frac{\partial f_0}{\partial t} + \boldsymbol{v} \cdot \boldsymbol{\nabla} f_0 + \boldsymbol{\nabla}_{\boldsymbol{p}} \cdot (\boldsymbol{F}_0 f_0 + \langle \delta \boldsymbol{F} \delta f \rangle) = 0. \tag{5.2}$$

The second-order fluctuation term  $\langle \delta F \delta f \rangle$  is the only second-order term we will keep in QLT,

as it is the dominant contribution to  $f_0$ . The evolution of  $\delta f$  is given by

$$\frac{\mathrm{d}}{\mathrm{d}t}\left(f - f_0\right) = \frac{\mathrm{d}\delta f}{\mathrm{d}t} = \underbrace{\frac{\partial\delta f}{\partial t} + \boldsymbol{v} \cdot \boldsymbol{\nabla}\delta f + \boldsymbol{\nabla_p} \cdot \boldsymbol{F}_0\delta f}_{=\frac{\mathrm{d}\delta f}{\mathrm{d}t}\Big|_{\mathrm{adv.}}} + \underbrace{\boldsymbol{\nabla_p} \cdot \delta \boldsymbol{F}_{f_0}}_{=-\frac{\mathrm{d}\delta f}{\mathrm{d}t}\Big|_{\mathrm{source}}} + \underbrace{\boldsymbol{\nabla_p} \left(\delta \boldsymbol{F}\delta f - \langle \delta \boldsymbol{F}\delta f \rangle\right)}_{\to 0} = 0, \quad (5.3)$$

where the second order fluctuations are negligible with respect to the first-order fluctuations, and we identify a term describing advection in phase space as well as a source term that does not explicitly depend on  $\delta f$ .

A formal solution of this equation requires expressing the advection through the use of a Green's function (Chavanis, 2008), but we are only interested in the ensemble average over phase space  $\langle \delta F \delta f \rangle$ . Thus, we follow a phase space element along its trajectory  $\tilde{x}(t)$  and  $\tilde{v}(t)$ , which changes according to the source term

$$\left| \frac{\mathrm{d}\delta f(\boldsymbol{x}, \boldsymbol{v}, t)}{\mathrm{d}t} \right|_{\mathrm{adv.}} = \left. \frac{\mathrm{d}\delta f}{\mathrm{d}t} \right|_{\mathrm{source}} = -\delta \boldsymbol{F} \cdot \boldsymbol{\nabla}_{\boldsymbol{p}} f_0 \tag{5.4}$$

$$\Rightarrow \delta f(\tilde{\boldsymbol{x}}(t), \tilde{\boldsymbol{v}}(t), t) = -\int_{-\infty}^{t} \delta \boldsymbol{F}(\tau) \cdot \boldsymbol{\nabla}_{\boldsymbol{p}} f_0(\tau) d\tau \approx -\left[\int_{-\infty}^{t} \delta \boldsymbol{F}(\tau) d\tau\right] \cdot \boldsymbol{\nabla}_{\boldsymbol{p}} f_0. \tag{5.5}$$

The slow variation of  $f_0$  relative to  $\delta f$  and its induced forces  $\delta F$  justifies extracting  $f_0$  from the integral. Substituting equation (5.5) into equation (5.2) yields the Fokker-Planck equation:

$$\frac{\partial f_0}{\partial t} + \boldsymbol{v} \cdot \nabla f_0 + \boldsymbol{F}_0 \cdot \nabla_{\boldsymbol{p}} f_0 = \nabla_{\boldsymbol{p}} \cdot \left[ \mathbf{D}(\boldsymbol{v}) \cdot \nabla_{\boldsymbol{p}} f_0 \right], \tag{5.6}$$

$$\mathbf{D}(\boldsymbol{p}) = \int_{-\infty}^{t} \langle \delta \boldsymbol{F}(\tau) \delta \boldsymbol{F}(t) \rangle \, d\tau = \int_{0}^{\infty} \langle \delta \boldsymbol{F}(\tau) \delta \boldsymbol{F}(0) \rangle \, d\tau.$$
 (5.7)

We adapted the integration bounds assuming invariance of time translation, such that the diffusion tensor  $\mathbf{D}$  visibly follows the Green–Kubo relation

$$\mathbf{D} = \int_0^\infty d\tau \left\langle \delta \dot{A}(\tau) \delta \dot{A}(0) \right\rangle \tag{5.8}$$

for the observable  $\mathbf{A} = \mathbf{p}$  with  $\dot{\mathbf{A}} = \mathrm{d}\mathbf{p}/\mathrm{d}t = \mathbf{F}$  (Green, 1952; Kubo, 1957). The Fokker-Planck equation describes diffusive particle transport arising from random force fluctuations. While these fluctuations preserve the mean particle trajectory, they lead to irreversible entropy production in the system. This irreversibility presents an apparent paradox, as our starting point was the time-reversible Vlasov equation (5.1).

To resolve this paradox, we note that we neglected the diffusion term  $\langle \delta F \delta f \rangle$  in equation (5.3) while it was included in equation (5.2). If we had kept the term in both equations, we could add them to find the original Vlasov equation  $d/dt(f_0 + \delta f) = 0$ . However, we deliberately discarded this expression in the evolution of  $\delta f$ . Without the knowledge about the evolution of the microstates of  $\delta f$ , we can not reconstruct previous macrostates of  $f_0$ , which is expressed by the increase in entropy. The irreversibility thus emerges not from any fundamental physical law, but from our practical choice to describe the system through its statistical properties that

depend entirely on the autocorrelation of stochastic force perturbations.

# 5.2. Pitch Angle Diffusion in the Presence of Random Alfvén Waves

The Fokker-Planck equation depends on the diffusion tensor **D**, which we will derive in the following. Initially, we assume that CRs are test particles, which scatter off of one preexisting Alfvén wave. This generalizes with ease to the case of a spectrum of Alfvén waves later on, as long as all waves have the same velocity.

Coordinates along the Magnetic Field. CRs primarily follow magnetic field lines when their gyroradius is small compared to the characteristic scale of magnetic field variations. This allows us to decompose the particle momentum into parallel and perpendicular components relative to the background magnetic field  $\hat{\boldsymbol{b}} = \boldsymbol{B}_0/B_0$ . We express the plane perpendicular to  $\hat{\boldsymbol{b}}$  using the orthogonal unit vectors  $\hat{\boldsymbol{c}}$  and  $\hat{\boldsymbol{d}}$ 

$$\boldsymbol{p} = p_{\parallel} \hat{\boldsymbol{b}} + p_{\perp} \left( \cos(\psi) \hat{\boldsymbol{c}} + \sin(\psi) \hat{\boldsymbol{d}} \right) \quad \text{where } p_{\parallel} = p\mu \quad \text{and} \quad p_{\perp} = p\sqrt{1 - \mu^2}, \tag{5.9}$$

where  $\psi$  represents the azimuthal angle, while the pitch angle cosine is  $\mu \in [-1,1]$ .

**Estimating Wave Forces in Ideal MHD.** In the ideal MHD framework, we focus on transverse Alfvén waves that can directly resonate with collisionless CRs, while the longitudinal waves in ideal MHD are acoustic waves that interact through collisions.

We already established an expression for  $\delta E$  in the linear case, see equation (2.70), which allowed us to determine the wave frequency  $\omega = \pm k \cdot v_A$ , where  $v_A$  and k are parallel to the magnetic field  $\hat{b}$ . We exclude oblique waves from the analysis, as these grow slower than the parallel waves excited by the streaming instability. Using Faraday's law (2.3) we find an expression for the perturbed force of a forward/backward ( $\pm v_A$ ) moving Alfvén wave that depends only on  $\delta B$ .

$$\delta \mathbf{E} = -(\pm \mathbf{v}_{\mathbf{A}}) \times \delta \mathbf{B},\tag{5.10}$$

$$\delta \mathbf{F} = q(\delta \mathbf{E} + \mathbf{v} \times \delta \mathbf{B}) = q(\mathbf{v} + \mathbf{v}_{\mathbf{A}}) \times \delta \mathbf{B}. \tag{5.11}$$

Restricting the Propagation Direction, Transformation into Wave Frame. For analytical tractability, we consider waves propagating in a single direction. We shift into the wave frame defining  $v'_{\parallel} = v_{\parallel} \mp v_{\text{A}}$ , while  $v'_{\perp} = v_{\perp}$ . Since  $v_{\text{A}} \ll c$ , we neglect relativistic corrections in this transformation, assuming  $\gamma \approx \gamma'$ . This choice of frame is advantageous because it conserves CR energy,  $dp'/dt = 0 = \delta F'_{p'}$  where p' = |p'|, causing momentum-related diffusion coefficients to vanish  $D_{p'p'} = D_{p'\mu'} = 0$ . The pitch angle cosine is given by

$$\mu' = (v\mu \mp v_{\rm A})/v' = p'_{\parallel}/p',$$
 (5.12)

and the force acting on the pitch angle is

$$\frac{\mathrm{d}\mu'}{\mathrm{d}t} = \delta F'_{\mu'} = \frac{q}{p'} \left[ \mathbf{v}' \times \delta \mathbf{B} \right]_{\mu'} = \frac{q}{p'} v'_{\perp} \times \delta B_{\perp} \sin(\varphi') = \frac{q}{\gamma' m} \sqrt{1 - {\mu'}^2} \delta B_{\perp} \sin(\varphi'), \tag{5.13}$$

where the gyrophase  $\varphi' = \Omega t - k \cdot x(t) + \psi' - \psi'_B = \Omega t - k \mu' v' t + \psi'$  denotes the angle between the magnetic field perturbation and the CR velocity vector in the plane perpendicular to  $\boldsymbol{B}_0$ . We calibrated the phase shift of the wave  $\psi'_B$  to 0 without loss of generality.  $\varphi'$  does not explicitly depend on the wave frequency, because the wave is static in the wave frame. However, the wave appears Doppler-shifted to the moving CRs, introducing a term that depends on  $k\mu'v't$ . For now, we restrict ourselves to a single k value, i.e., a single wave mode.

**Random Phase approximation.** Substituting the force into equation (5.7) gives

$$D_{\mu'\mu'} = \int_0^\infty \left\langle \left( \frac{q}{\gamma'm} \delta B(k) \sqrt{1 - {\mu'}^2} \right)^2 \sin(\Omega t - k\mu' v't + \psi') \sin(\psi') \right\rangle dt$$
$$= \Omega^2 \frac{\delta B^2}{B_0^2} (1 - {\mu'}^2) \int_0^\infty \frac{1}{2} \left[ \cos(\Omega t - k\mu' v't) - \langle \cos(2\psi' + \Omega t - k\mu' vt) \rangle \right] dt. \tag{5.14}$$

We utilize the random phase approximation that assumes uniformly distributed  $\psi'$ , which sets the ensemble average to 0 in the equation above. The motivation behind this approximation is, that only  $\mathbf{B}_0$  introduces an anisotropy in the physical system and the plane perpendicular to it should be fully symmetric (also called gyrotropic). However, this assumption becomes questionable in the presence of Alfvén waves, as the perpendicular magnetic field breaks the symmetry in this plane. We might estimate the deviation from a fixed phase approximation, such as  $\psi' = 0$ . In this case, the pitch-angle diffusion in Equation (5.14) trivially vanishes. This can be important for CR streaming, and we will return to this point at the end of this Chapter, and in Chapter 6.

The random phase approximation also prevents interactions between different wave modes, thereby excluding important nonlinear phenomena that naturally arise in the MHD fluid equations. For example, wave-wave coupling enables processes such as wave steepening and shock formation, which are essential features of plasma dynamics. Maron and Goldreich (2001) (Figures 18–21) illustrates the impact of the random phase approximation by artificially randomizing the phases of magnetic field fluctuations in a developed MHD turbulence simulation. Their visualization effectively demonstrates how the random phase approximation fundamentally alters the nature of plasma dynamics by eliminating the spatial correlations that give rise to organized structures. The random phase approximation represents a significant departure from realistic, nonlinear behavior in plasma systems, potentially limiting the applicability of QLT to linear rather than quasilinear systems.

**Infinitely Thin Resonance Width.** We continue with the QLT derivation, noticing that the remaining integral of equation (5.14) is the Fourier transform of 1

$$\int_{0}^{\infty} \frac{1}{2} \cos(\Omega t - k\mu' v') dt = \int_{-\infty}^{\infty} \frac{1}{4} \cos(\Omega t - k\mu' v') dt = \int_{-\infty}^{\infty} \frac{1}{8} \left( 1 \times e^{it(\Omega - k\mu' v')} + 1 \times e^{-it(\Omega - k\mu' v')} \right) dt$$
$$= \frac{\pi}{2} \delta(\Omega - k\mu' v'), \tag{5.15}$$

The resulting delta function implies an exact resonance condition where the Doppler-shifted wave frequency must precisely match the particle's gyrofrequency,

$$k\mu'v' = k(v_{\parallel} \mp v_{\rm A}) = \Omega. \tag{5.16}$$

If we limit ourselves to one propagation direction of CRs in the wave frame (without loss of generality), this equation can only be fulfilled if k>0. In the background frame, particles can resonate with both, forward and backward propagating waves (traveling at  $\pm v_{\rm A}$ ) with their respective conditions  $v_{\parallel} > \mp v_{\rm A}$ . These constraints emerge in ideal MHD and will be refined in Section 7.1.1.

The result in equation (5.15) is peculiar, as the particles have to exactly fulfill the resonance. As the pitch angle cosine approaches  $\mu' \to 0$  corresponding to a pitch angle of  $\theta' = 90^{\circ}$ , the resonance condition becomes impossible to satisfy. This creates an unphysical scenario where cosmic rays that scatter to 90° pitch angles become permanently trapped at this angle, unable to continue their diffusive evolution; thus, coining the term 90° problem. This artificial behavior arises from the  $\delta$ -shaped resonance in QLT. As shown by Shalchi et al. (2004), more sophisticated nonlinear theories predict a broadened resonance condition that better reflects physical reality.

We continue by incorporating equation (5.15) into equation (5.14), which gives the diffusion coefficient

$$D_{\mu'\mu'} = \frac{1 - {\mu'}^2}{2} \, \pi \Omega^2 \frac{\delta B^2(k)}{B_0^2} \delta(\Omega - k\mu'v') \,. \tag{5.17}$$

Here we identify  $d\nu'_{QLT}/dk$  as the scattering rate associated with a single wave according to QLT.

Spectrum of Waves Propagating in Identical Direction. Expanding this to a spectrum of waves with different modes k, the scattering rate is expressed as

$$\nu'_{\text{QLT}} = \int_{-\infty}^{\infty} \frac{\mathrm{d}\nu'_{\text{QLT}}}{\mathrm{d}k} \mathrm{d}k = \pi \Omega \underbrace{\frac{\Omega}{|\mu'v'|}}_{=k_{\text{res}}} \frac{\delta B^2(k_{\text{res}})}{B_0^2}, \tag{5.18}$$

where  $k_{\rm res}$  represents the wave number k fulfilling the resonance condition (5.16). The scattering rate thus is proportional to the intensity of waves  $\delta B^2(k_{\rm res})/B_0^2$  at resonance with the particle, but it is independent of all other magnetic fluctuations.

#### 5. Quasilinear Theory of Cosmic Ray Streaming

We will not derive the diffusion coefficient for  $\psi'$ , which we assumed to be uniformly distributed, implying  $\partial f/\partial \psi' = 0$  and therefore the absence of diffusion along this coordinate. The diffusion coefficients are often given in the background frame, which we derive using the coordinate transform

$$v^{2} = (v'_{\parallel} \pm v_{A})^{2} + v'_{\perp}^{2} = v'^{2} \pm 2\mu' v' v_{A} + v_{A}^{2}, \tag{5.19}$$

$$\Rightarrow 2v \frac{\mathrm{d}v}{\mathrm{d}t} = (2v' \pm 2\mu' v_{\mathrm{A}}) \underbrace{\frac{\mathrm{d}v'}{\mathrm{d}t}}_{2} \pm 2v_{\mathrm{A}}v' \frac{\mathrm{d}\mu'}{\mathrm{d}t}, \tag{5.20}$$

$$\Leftrightarrow \frac{\mathrm{d}p}{\mathrm{d}t} = \delta F_p = (\pm v_{\mathrm{A}}) \frac{p'}{v} \delta F'_{\mu'}. \tag{5.21}$$

This transformation generates non-zero momentum diffusion in the background frame. We have already computed  $D_{\mu'\mu'}$  from  $\delta F'_{\mu'}$  and thus can express the other diffusion coefficients using the appropriate prefactors

$$D_{\mu'\mu'} = \frac{1 - {\mu'}^2}{2} \pi \Omega k_{\rm res} \frac{\delta B^2(k_{\rm res})}{B_0^2}, \tag{5.22}$$

$$D_{\mu'p} = p' \frac{\pm v_{\rm A}}{v} D_{\mu'\mu'},\tag{5.23}$$

$$D_{pp} = \left(p' \frac{v_{\rm A}}{v}\right)^2 D_{\mu'\mu'}. \tag{5.24}$$

Up to leading order in these equations, we can approximate  $\mu' \approx \mu$  and  $p' \approx p$ , leading to the diffusion coefficients often quoted in the literature (more accurate transformations are given by Skilling, 1975a). The momentum diffusion in the background frame, while non-zero, remains small and arises purely from the frame transformation. In the wave frame, cosmic rays undergo pure pitch-angle diffusion and are constrained to move along surfaces of constant particle energy. This results in the cosmic ray population's mean velocity approaching the wave velocity  $\pm v_A$ . This outcome relies on dispersionless waves propagating at constant speeds in identical directions. It turns out that CRs can significantly influence the wave velocity, leading to nonlinear oscillations as we will explore in Section 6.5.3.

The presence of both forward- and backward-propagating waves substantially enhances momentum diffusion (compare Figures 7 and 11 of Schlickeiser, 1989; Shevchenko et al., 2002). This bidirectional wave field allows particles to scatter between two reference frames, thereby breaking the confinement to surfaces of constant particle energy in one wave frame, and leading to more complex steady-state distributions.

# 5.3. Linear Stability Analysis

Our previous analysis treated cosmic rays as test particles interacting with a pre-existing spectrum of Alfvén waves, explaining their tendency to approach the Alfvén velocity. However, these waves are not merely coincidental - they arise through the streaming instability. In this section, we are not primarily concerned with the growth rates themselves, but will derive them in order

to understand the physical basis of the instability.

The linear stability analysis parallels our earlier wave analysis from Chapter 2, but here we expect a complex valued wave frequency  $\omega = \omega_r + i\Gamma$ , where  $\Gamma$  represents the instability growth rate. We restrict ourselves to growth rates that are small compared to the wave frequency, i.e.,  $\Gamma \ll \omega_r$ , even though this assumption is not generally valid (Section 7.2.3). Building on the thermal species' transverse conductivity tensor from equation (2.70), we now incorporate CR contributions through the dispersion relation

$$\frac{k^2c^2}{\omega^2} = \chi_{\rm bg} + \chi_{\rm cr} = \frac{c^2}{v_{\rm A}^2} + \chi_{\rm cr}$$
 (5.25)

$$\Rightarrow k^2 c^2 - \frac{c^2}{v_{\rm A}^2} \left[ \omega_r^2 + 2i\Gamma \omega_r + \mathcal{V}^{\mathbb{Z}} \right] = \omega^2 \chi_{\rm cr}$$
 (5.26)

$$\Rightarrow \Gamma \approx -\frac{\omega}{2} \frac{v_{\rm A}^2}{c^2} \operatorname{Im}(\chi_{\rm cr}). \tag{5.27}$$

To determine the transverse CR susceptibility  $\chi_{\rm cr}$ , wed the linear relationship between current and electric field,  $\boldsymbol{J} = \mathrm{i}\omega\epsilon_0\chi_{\rm cr}\boldsymbol{E}$ . The perturbed current density in QLT is

$$\delta \mathbf{J} = \int d^3 p q \mathbf{v} \delta f = \int d^3 p q \mathbf{v} \int_{-\infty}^0 dt \delta \mathbf{F} \cdot \nabla_{\mathbf{p}} f_0(\mathbf{x}(t), \mathbf{p}(t), t).$$
 (5.28)

Working in the wave frame with the random phase approximation, such that  $F'_{p'} = F'_{\psi'} = 0$ , we obtain

$$\delta \mathbf{J}' = \int d^3 p' q \mathbf{v}' \int_{-\infty}^{0} dt \delta F' \frac{\partial f_0}{\partial \mu'} = \int d^3 p' q \mathbf{v}' \int_{-\infty}^{0} dt q \frac{v'}{p'} \sqrt{1 - {\mu'}^2} \sin(\varphi') \delta B_{\perp} \frac{\partial f_0}{\partial \mu'}. \tag{5.29}$$

The velocity vector  $\mathbf{v}'$  in Cartesian coordinates is given as  $\mathbf{v}' = \left(v'_{\parallel}, v'_{\perp}\sin(\psi'), v'_{\perp}\cos(\psi')\right)$  with  $v'_{\perp} = (1 - \mu'^2)^{1/2}v'$ . For analytical convenience, we introduce the complex perpendicular velocity vector  $\mathbf{v}'_{\perp} = (v'_{y} + \mathrm{i}v'_{z})\hat{e}_{\perp} = v'_{\perp}\exp(\mathrm{i}\psi')\hat{e}_{\perp}$ . Applying the random phase approximation and integrating over  $\psi'$  and t as in equations (5.14)–(5.15), we obtain

$$\int_{0}^{\infty} dt \int d\psi' \mathbf{v}'_{\perp} \sin(\varphi') \delta B_{\perp} = \int_{0}^{\infty} dt \int d\psi' \frac{i}{2} \left( -e^{i\varphi'} + e^{-i\varphi'} \right) \mathbf{v}'_{\perp} e^{i\psi'} \hat{\mathbf{e}}_{\perp} \delta B_{\perp}$$

$$= \int_{0}^{\infty} dt \frac{i}{2} \left( -\int d\psi' e^{i2\psi'} e^{i(\Omega t - k\mu'v't - \psi'_{\mathbf{B}})} + \int d\psi' e^{-i(\Omega t - k\mu'v't - \psi'_{\mathbf{B}})} \right) \mathbf{v}'_{\perp} \delta B_{\perp} \hat{\mathbf{e}}_{\perp}$$

$$= \int_{0}^{\infty} dt \int d\psi' \frac{1}{2} e^{-it(\Omega - k\mu'v')} \mathbf{v}'_{\perp} \left( i\delta B_{\perp} e^{i\psi'_{\mathbf{B}}} \hat{\mathbf{e}}_{\perp} \right) = \int d\psi' \frac{\pi}{2} \delta(\Omega - k\mu'v') \mathbf{v}'_{\perp} \left( i\delta B'_{\perp} \right). \quad (5.30)$$

We leave the last  $\psi'$  integral unevaluated to shorten the notation in the following, and introduce the complex perpendicular magnetic field perturbation  $\delta B'_{\perp}$  defined analogous to  $v'_{\perp}$ . The parallel component depends on  $v_{\parallel} \sin(\varphi')$ , which averages to 0 assuming random phases. Thus, we focus on the perpendicular component of the current perturbation  $\delta J$ , retrieved by substituting equation (5.30) into (equation 5.29)

$$\delta \mathbf{J}'_{\perp} = \left(i\delta \mathbf{B}'_{\perp}\right) \frac{\pi}{2} \int d^3 p' q^2 \frac{v'^2}{p'} \left(1 - \mu'^2\right) \delta(\Omega - k\mu' v') \frac{\partial f_0}{\partial \mu'}. \tag{5.31}$$

In ideal MHD the electric field  $\boldsymbol{E}$  is always perpendicular to  $\boldsymbol{B}$ . We express  $\mathrm{i}\delta\boldsymbol{B}'_{\perp} = -\delta\boldsymbol{E}_{\perp}/(\pm v_{\mathrm{A}})$  using Faraday's law in order to transform back to the background frame to stay consistent with equation (5.27). This allows us to readily identify the linear relationship between  $\boldsymbol{J}_{\perp}$  and  $\boldsymbol{E}_{\perp}$ . Using  $\boldsymbol{J}_{\perp} = \mathrm{i}\omega\epsilon_0\chi_{\mathrm{cr}}\boldsymbol{E}_{\perp}$ , we retrieve the growth rate of the transverse Alfvén waves:

$$\Gamma = q^2 \frac{\pi}{2\epsilon_0} \frac{\pm v_{\rm A}}{c} \int d^3 p' \frac{v'^2}{p'c} \frac{\left(1 - {\mu'}^2\right)}{2} \delta\left(\Omega - k\mu'v'\right) \frac{\partial f_0}{\partial \mu'},\tag{5.32}$$

which is the instability growth rate according to QLT, which depends primarily on the pitch angle gradient of f in the wave frame. A direct comparison to  $\chi_{\rm cr}$  derived without QLT (equation 2.22) reveals that the physical resonance is significantly broader, effectively replacing  $\delta(\Omega - k\mu'v')$  with  $1/(\Omega - k\mu'v')$ .

While further analytical simplification of equation (5.32) is possible, practical evaluation of growth rates is best accomplished through numerical tools, such as the Mathematica script provided by Holcomb (2019) or the more general dispersion relation solvers by Verscharen et al. (2018) and Xie (2019). Thus, instead of pursuing further analytical simplifications, let us examine the physical implications of these results.

**Physical Interpretation.** We find that pitch-angle diffusion (equation 5.7) and instability growth (equation 5.32) depend on  $\partial f_0/\partial \mu'$ . Thus both processes can occur unless the distribution has uniformly distributed pitch angles, which would correspond to a CR mean velocity of  $\pm v_A$ . Furthermore, the resonance conditions for diffusion and wave growth are identical, ensuring that instability growth is always accompanied by diffusion. As Alfvén waves at  $k_{\rm res}$  become large enough, the resulting diffusion flattens the distribution function at resonant pitch angles  $(\partial f_0/\partial \mu'|_{\mu'_{\rm res}} \to 0)$ , naturally limiting instability growth at that wave number in the nonlinear regime. However, we previously found that the pitch angle diffusion coefficient can vanish if we assume fixed phases with  $\psi = 0$  (all CRs align with the magnetic field) instead of random phases, see equation (5.14). An important question is thus, whether we obtain random or fixed phases in the nonlinear regime.

Equation (5.31) establishes that the instability grows as a result of the perpendicular CR current that is excited in response to the magnetic field perturbation. The physical origin of this effect is not at all obvious from the dispersion relation. We know, that  $\delta J_{\perp}$  has to form a wave-like structure that is coherent with the perturbation  $B_{\perp}$  introduced by the Alfvén waves (as it grows in response to the perturbation). Thus, we can infer that it must happen through a consolidation or bunching of the CRs' gyrophases  $\varphi$ , i.e. CRs have to align their (mean) perpendicular velocity with the magnetic perturbation up to a phase shift. This already answers whether such a bunching process must happen to grow the instability, but it does not specify the phase shift in the nonlinear regime. Notably, this bunching results from linear forces

acting on the CRs' pitch angle cosine  $\mu$ , not through a direct influence on the polar angle  $\psi$ . We will develop a physical intuition for this effect in the following Chapter 6, detailing the mechanism for driving gyroresonant instabilities and its implications for the nonlinear, saturated regime without the MHD and QLT approximations. We will conclude that the instability growth mechanism bunches CRs' gyrophases with a small phase shift relative to the wave perturbation, which thereby heavily reduces diffusion and enables other saturation mechanisms.

# 6. Growth and Saturation Mechanism of the Gyroresonant Instabilities

This chapter is based on the paper by Lemmerz, R.; Shalaby, M.; Thomas, T.; Pfrommer, C.: Accepted for publication in The Astrophysical Journal under doi:10.3847/1538-4357/ad8eb3.

Cosmic ray (CR) feedback is critical for galaxy formation as CRs drive galactic winds, regularize star formation in galaxies, and escape from active galactic nuclei to heat the cooling cores of galaxy clusters. The feedback strength of CRs depends on their coupling to the background plasma and, as such, on the effective CR transport speed. Traditionally, this has been hypothesized to depend on the balance between the wave growth of CR-driven instabilities and their damping. Here, we study the physics of CR-driven instabilities from first principles, starting from a gyrotropic distribution of CR ions that stream along a background magnetic field. We develop a theory of the underlying processes that organize the particles' orbits and in particular their gyrophases, which provides an intuitive physical picture of (i) wave growth as the CR gyrophases start to bunch up lopsidedly towards the local wave magnetic field, (ii) instability saturation as a result of CRs overtaking the wave and damping its amplitude without isotropizing CRs in the wave frame, and (iii) CR back-reaction onto the unstable plasma waves as the CR gyrophases follow a pendulum motion around the wave magnetic field. Using our new fluid-particle-in-cell code fluid-SHARP, we validate our theory on the evolution and excitation of individual unstable modes, such as forward and backward propagating Alfvén and whistler waves. We show that these kinetic simulations support our theoretical considerations, thus potentially foreshadowing a revision of the theory of CR transport in galaxies and galaxy clusters.

## 6.1. Introduction

## 6.1.1. Astrophysical motivation

Stellar feedback drives galactic winds, which is crucial for understanding the underpinnings of galaxy formation, most prominently the declining star conversion efficiency of gas from the scale of Milky Way-sized galaxies towards dwarf galaxies (Moster et al., 2013). Several physical processes have been suggested to drive those winds: energy and momentum deposition by exploding supernovae can self-regulate the interstellar medium and drive galactic fountains (Girichidis et al., 2016, 2018; Simpson et al., 2016, 2023; Kim and Ostriker, 2018). Ultraviolet radiation emitted by young stellar populations photoionizes the molecular environment and pushes on the gas via radiation pressure, which opens up channels in the optically thick, gas-enshrouding regions, enabling star formation. Radiation can then escape along those channels without providing much feedback (Rosdahl et al., 2015).

By contrast, cosmic rays (CRs) have long cooling times and dominate the pressure budget in the nearby interstellar medium (Boulares and Cox, 1990), making a strong case for efficient feedback (see Ruszkowski and Pfrommer, 2023, for a review). CRs stream and diffuse through the galaxy to build up an extended pressure distribution from the disk into the galactic halo. As they are advected by galactic outflows above the disk, CRs gradually deposit momentum and energy via wave-particle interactions far from their generation sites, thereby re-energizing and further accelerating galactic winds that can reach out to the virial radius of galactic halos (Uhlig et al., 2012; Booth et al., 2013; Salem and Bryan, 2014; Pakmor et al., 2016; Ruszkowski et al., 2017b; Thomas et al., 2023). This may even cause CRs to dominate the pressure budget in the inner circumgalactic medium, which promotes the formation of a colder and smoother thermal plasma while increasing the amount of mass and energy expelled from the galaxies into their circumgalactic medium (Rathjen et al., 2021; Thomas et al., 2024; Sike et al., 2024). This has dramatic consequences for the transport of angular momentum of the accreting gas onto the galactic disks and the spatial extents of stellar disks that form from the gaseous phase (Buck et al., 2020; Ji et al., 2020). In the cores of galaxy clusters, CRs escape the lobes of AGN jets, and can heat the surrounding cooling plasma to mitigate the cooling-induced collapse and star formation (Guo and Oh, 2008; Pfrommer, 2013; Ruszkowski et al., 2017a; Jacob and Pfrommer, 2017b,a).

#### 6.1.2. CR transport and CR-driven instabilities

To make progress, it is crucial to better understand the physics of CR transport in galaxies and clusters. The CR streaming instability (Rowlands et al., 1966; Lerche, 1967; Wentzel, 1968) plays a critical role in the interaction between CRs and their surrounding medium. In the classic picture of CR self-confinement in the galaxy set forth by Kulsrud and Pearce (1969), this instability hinges on the interplay between CRs driving resonant waves and scattering off of these self-induced waves. The framework of quasi-linear theory has been foundational in estimating the CR scattering frequency (Jokipii, 1966; Wentzel, 1969; Skilling, 1971; Schlickeiser and Miller,

1998). Quasi-linear theory of CR transport is a perturbation method concerned with updating a slowly evolving ground state (the gyrotropic CR distribution) around a first-order fluctuation (the perturbed CR distribution). In order to simplify statistical analysis, the random phase approximation is typically employed, which assumes that the rotational phases of the waves and particles are random and uncorrelated.

The scattering frequency of CRs is closely linked to the intensity of the saturated waves, and thus the saturation mechanism is of particular importance. The amplitude of the resonant waves can saturate as a result of the competition between wave growth and damping processes. Viable damping processes are thought to include wave damping through ion-neutral collisions (Kulsrud and Pearce, 1969; Zweibel and Shull, 1982; Ivlev et al., 2018), collisionless nonlinear Landau damping (Kulsrud and Pearce, 1969; Völk and Cesarsky, 1982) and turbulent damping (Eastman et al., 1981; Lazarian, 2016; Lazarian and Xu, 2022; Cerri, 2024). Provided there is sufficient wave energy available, CR scatter frequently and isotropize in the wave frame and, thus, stream at the wave velocity.

Alternatively, CRs are thought to align their gyrophases with the self-induced wave (Brice, 1963; Sudan and Ott, 1971). Observational evidence of gyrophase bunching has been documented for suprathermal ions upstream of the Earth's bow shock (Gurgiolo et al., 1981; Eastman et al., 1981; Thomsen et al., 1985). This phenomenon has been attributed to the gyroresonant instability inducing forward-moving Alfvén waves (Greenstadt et al., 1982; Winske and Leroy, 1984; Hoshino and Terasawa, 1985; Zachary et al., 1989). These observations have been successfully replicated using simplified models involving field-aligned ion beams. However, cosmic rays are more likely to interact with magnetic field lines at arbitrary angles, which can effectively initiate gyroresonant instabilities across various scales. In this paper we further explore the mechanism of gyrophase bunching and show, that it is an integral part of explaining the instability growth and saturation of the different CR gyroresonant instabilities for single-mode excitation.

Computational advances in recent years have allowed studying the gyroresonant CR streaming instability using particle-in-cell (PIC) simulations (Holcomb and Spitkovsky, 2019; Shalaby et al., 2021), which follow the orbits of macro particles representing individual particles of a plasma, which are subject to electromagnetic fields that obey Maxwell's equations. Alternatively, this can be done with hybrid-PIC (Weidl et al., 2019b; Haggerty et al., 2019; Schroer et al., 2022) methods, in which the electron timescale is integrated out, representing the electron population as an adiabatic fluid while treating the ions as macro particles within the kinetic PIC model. The large scale separation inherent to the streaming problem has also led to the development of new methods, such as improved hybrid-PIC methods (Burrows et al., 2014; Amano, 2018) and MHD-PIC (Zachary and Cohen, 1986; Lucek and Bell, 2000; Reville and Bell, 2012; Bai et al., 2015, 2019; Mignone et al., 2018; Lebiga et al., 2018; van Marle et al., 2018; Sun and Bai, 2023), which has been used to study ion-neutral damping (Plotnikov et al., 2021; Bai, 2022; Bambic et al., 2021). MHD-PIC describes the thermal plasma using the magnetohydrodynamic (MHD) approximation while capturing the kinetic physics of the CRs using the PIC method. This method has been commonly applied together with a scheme to randomize the CR gyrophases,

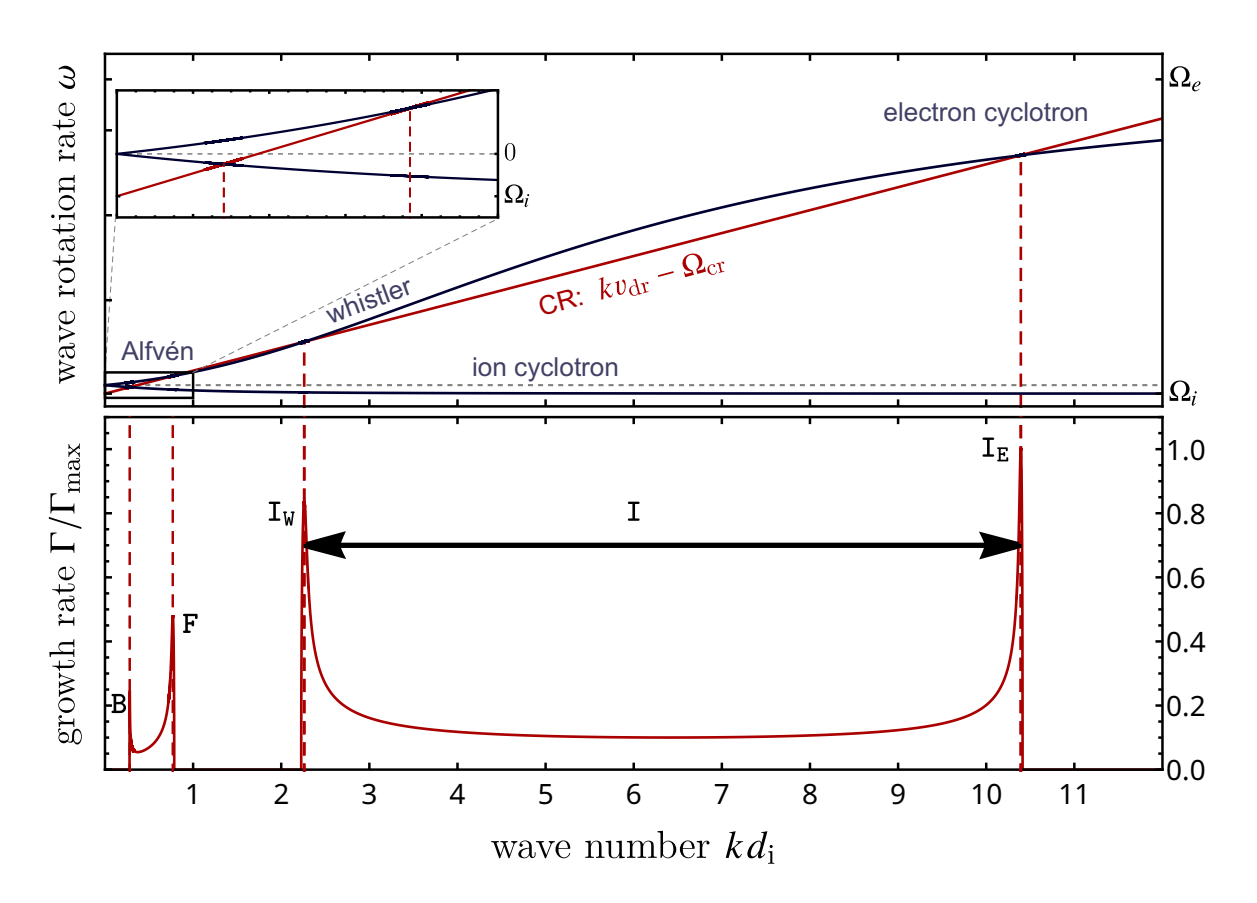


Figure 6.1. CRs drifting and gyrating along the magnetic field can resonantly excite unstable wave modes at different scales. The top panel shows the rotation rate of the CR ion cyclotron mode (red color) as well as the normal modes in the background (black), ranging from forward moving Alfvén waves to whistlers to electron cyclotron waves on the upper branch and on the bottom branch, they change character from backward moving Alfvén waves to ion cyclotron waves on small scales. The bottom panel shows the instability growth rate of the CR ion cyclotron wave that is maximized at the points of resonances with the background modes. We obtain the solutions by solving the dispersion relation of drifting CRs in a high-density background (equation 6.42) and evaluate them in the background rest frame. Solely for visualization purposes, we choose parameters that yield comparable grow rates and only a small scale separation:  $n_{\rm cr} = 10^{-6} n_{\rm bg}$ ,  $v_{\rm A} = 10^{-4} c$ ,  $m_r = 36$ ,  $v_{\perp} = v_{\rm A}$ , and  $v_{\rm dr} = 2.7 v_{\rm A} < v_{\rm A} \sqrt{m_r}/2$ . This choice fulfills the condition for exciting the intermediate-scale instability (Shalaby et al., 2023).

which enforces the random-phase approximation inherent to the theoretical framework of quasilinear theory, for details see (Bai et al., 2019).

More recently, the fluid-PIC method (Lemmerz et al., 2024b) has been devised, which treats the thermal plasma in the warm plasma approximation. This approach allows investigating physics at scales smaller than the ion skin-depth, where the MHD approximation breaks down, and in particular, it correctly captures gyroresonant streaming instabilities on these scales. Moreover, this method allows emulating nonlinear Landau damping.

## 6.1.3. Idea to elucidate the physics of CR-driven instabilities

In this work, we attempt to gain an intuitive picture of the growth and saturation of the resonant CR streaming instability by adopting an approach of isolating the physics of wave growth and wave interactions when studying the saturation behavior. To this end, we run three different simulations, each tailored to excite a single unstable mode at different spatial scales in the background with the goal to understand the essential physics of the instabilities. Specifically, CRs drifting at a mean velocity  $v_{\rm dr}$  along the mean magnetic field of strength  $B_0$  can excite forward propagating Alfvén waves (denoted by F), backward propagating Alfvén waves (denoted by B), both via the CR streaming instability (Kulsrud and Pearce, 1969), and whistler and electron cyclotron waves via the intermediate-scale instability (denoted by  $I_W$  and  $I_E$ , and collectively denoted by I, see Shalaby et al., 2021, 2023). This is visualized in Figure 6.1, which shows the wave rotation rates (top) and growth rates of unstable modes that result from the interaction of CR and background modes (bottom). CRs transfer energy fastest to the background modes at those wave numbers k at which the rotation rate of the CR ion cyclotron mode,  $\omega = k v_{\rm dr} - \Omega_{\rm cr}$ matches the rotation rate of the background modes, which get modified as a result of the CRwave interaction (as we will show later in this work). Here,  $\Omega_{\rm cr} = qB_0/(\gamma m)$  is the relativistic gyro frequency of a particle of charge q, mass m, and Lorentz factor  $\gamma$ . While this explains the possibility for instability growth in the linear regime, here we will specifically address the processes causing linear growth and nonlinear saturation of single wave modes.

In future work, we will study extensions of this picture arising from 1. interacting wave modes, 2. varying CR-to-background density ratios and Alfvén speeds, and 3. varying the CR energy and pitch angle distributions, where the pitch angle is measured between an individual CR momentum and the mean magnetic field. We acknowledge that our idealized approach of restricting ourselves to the growth of single wave modes does not necessarily capture the full physics of power-law distributed CRs. However, this enables us to grasp the underlying physics in this simple setup and to construct an analytic model for the feedback loop, which explains the wave growth, as well as the overall interplay of CRs with waves at the resonance.

The paper is structured as follows. We first introduce our numerical method and setup in Section 6.2, which is followed by theoretical considerations about CR particle orbits and derivation of the pendulum equation for CR-wave interactions in Section 6.3. We explain the microphysical mechanism for the linear wave growth in Section 6.4, while the nonlinear phase of the instabilities and wave saturation is discussed in Section 6.5. We conclude our paper in Section 6.6. We discuss our conventions and compare them to other popular choices in Appendix 6.A. To address the accuracy of our method, we compare a fluid-PIC and a PIC simulation of the intermediate-scale instability in Appendix 6.B and discuss the solution to the dispersion relation in the background frame in Appendix 6.D. Throughout this work, we use the SI system of units.

# 6.2. Numerical Method and Setup

In this section, we describe the numerical method and clarify our specific setups and choices for our parameters.

#### 6.2.1. Method

We use the fluid-PIC code fluid-SHARP (Shalaby et al., 2017b, 2021; Lemmerz et al., 2024b), which is an advantageous method for simulating energetic particle transport in a much denser background plasma in comparison to the pure PIC method. The fluid-PIC method combines a hydrodynamic solver, which allows us to treat background particles as a computationally cheap fluid, with a PIC solver that integrates the individual orbits of the energetic particles in the fully kinetic picture. Both components, the background and energetic particles are coupled via Maxwell's equations. Here, we give a brief overview of this method.

The CR particles are treated by the SHARP PIC code (Shalaby et al., 2017b, 2021), which advances macroparticles that represent CR ions and electrons in one spatial and three velocity dimensions. Moving charges generate currents that induce electromagnetic fields according to Maxwell's equations. These electromagnetic fluctuations create Lorentz forces that accelerate charged particles, altering the charge distribution and currents. The PIC method evolves this system by numerically iterating this loop on a fraction of the electron plasma timescale, thereby self-consistently taking micro-instabilities driven by these particles into account.

The more numerous background particles would result in a large computational cost if they were to be treated kinetically, but because they are not driving the instability, they can instead be approximated as a thermal fluid composed of electrons and protons. This corresponds to the "warm plasma" model, according to the definition found in many textbooks such as Stix (1992), which naturally captures Alfvén, whistler, electron cyclotron, ion cyclotron and Langmuir and ion acoustic waves. As such, CRs can resonate with the waves carried by the fluids and thus trigger resonant streaming instabilities. For convenience, we quote the fluid equations solved by the fluid-SHARP code (Lemmerz et al., 2024b), which are the fluid continuity, momentum, and energy conservation equations:

$$\frac{\partial n}{\partial t} + \nabla \cdot (n\boldsymbol{w}) = 0, \tag{6.1}$$

$$\frac{\partial n\boldsymbol{w}}{\partial t} + \nabla \cdot [p\mathbf{1} + n\boldsymbol{w}\boldsymbol{w}] = \frac{q}{m} \boldsymbol{S}_{w} (n, \boldsymbol{w}, \boldsymbol{B}, \boldsymbol{E}), \qquad (6.2)$$

$$\frac{\partial \epsilon}{\partial t} + \nabla \cdot [(p + \epsilon)w] + \frac{1}{\Gamma - 1} \nabla \cdot Q = \frac{q}{m} w \cdot S_w (n, w, B, E).$$
 (6.3)

The number density is denoted by n, the bulk velocity is  $\boldsymbol{w}$  and the energy and pressure are  $\epsilon$  and p, respectively. These are evolved for both ion and electron background species separately, which are each characterized by the charge q and particle mass m. The dyadic product of the two vectors is  $\boldsymbol{w}\boldsymbol{w}$  and the unit matrix is denoted by  $\boldsymbol{1}$ , indicating an isotropic pressure tensor of the background species. The energy density and pressure of thermal protons and electrons

are separably coupled via the adiabatic index  $\Gamma_{\rm ad} = 5/3$ :

$$\epsilon = \frac{p}{\Gamma_{\text{ad}} - 1} + \frac{1}{2} n \, \boldsymbol{w} \cdot \boldsymbol{w}. \tag{6.4}$$

Maxwell's equations are used to solve for the electric and magnetic fields E and B, which exert a force on the fluid that is captured by the source term,

$$S_w(n, \boldsymbol{w}, \boldsymbol{B}, \boldsymbol{E}) = n(\boldsymbol{E} + \boldsymbol{w} \times \boldsymbol{B}). \tag{6.5}$$

Even though collisionless physics is not modeled from first principles in this fluid model, it can still be approximated by using appropriate closures. We use a Landau closure, which models electrostatic Landau damping through a non-local approximation of the heat flux Q. For further details, we refer the reader to Lemmerz et al. (2024b) or the notes by Hunana et al. (2019b). As we will demonstrate below, in our setups we intentionally only excite individual wave modes, implying that the interference between different modes, and thus the impact of nonlinear Landau damping, is minimized.

#### 6.2.2. Setup

CRs are naturally distributed over space, velocity and time,  $f(\mathbf{x}, \mathbf{v}, t)$ . In the following, we work in a coordinate system where one of the coordinate axes is aligned with the direction of the static background magnetic field  $\mathbf{B}_0$ . Particles that are gyrating because of this magnetic field have rotating velocity components that lie in the plane perpendicular to  $\mathbf{B}_0$ . We denote the rotation phase of this gyration by  $\psi$ . The full particle velocity vector  $\mathbf{v}$  further depends on the velocity magnitude v and the pitch angle  $\theta$ . These definitions completely describe our phase space geometry, which we depicted in Figure 6.2. The presence of the background magnetic field naturally introduces a decomposition of the velocity vector into a parallel component  $v_{\parallel} = \mu v$  and a perpendicular component  $v_{\perp} = \sqrt{1 - \mu^2}v$ .

We investigate the interplay of charged particles with transverse waves, which have magnetic field components that also rotate in the plane perpendicular to the background magnetic field  $B_0$ . With no additional information about the distribution of particles in the perpendicular plane, it is customary to assume that all particles are distributed uniformly in rotation angle  $\psi$  because in the absence of any transverse magnetic fields there is no distinct direction in the perpendicular plane which could function as a reference direction. We will show that the presence of transverse magnetic fields introduce such a reference direction which ultimately break symmetry and cause anisotropic CR distributions in  $\psi$ .

Here, we perform three simulations, showcasing instabilities at different scales. We study the action of the gyroresonant instability (Kulsrud and Pearce, 1969), which excites Alfvén waves at scales larger than the ion skin depth. This instability is further separated into a forward (F) and backward (B) moving wave, as illustrated in Figure 6.1. In addition, we will study the intermediate-scale instability (I, Shalaby et al., 2021, 2023), which excites whistler waves ( $I_W$ ) and electron cyclotron waves ( $I_E$ ) below the scale of the ion skin depth (see Figure 6.1).

#### 6. Growth and Saturation Mechanism of the Gyroresonant Instabilities

Because we are interested in studying single-mode wave growth for these instabilities, it is convenient to use the simplifying setup of a cold, gyrotropic ring distribution of CRs, which is visualized in Figure 6.2, and given by

$$f_{\rm cr} = \frac{n_{\rm cr}}{2\pi u_{\perp}} \delta(u_{\parallel} - u_{\rm dr,0}) \delta(u_{\perp} - u_{\perp,0}). \tag{6.6}$$

Here,  $\mathbf{u} = \gamma \mathbf{v}$  is the relativistic particle velocity, where the Lorentz factor is  $\gamma = \left[1 - (\mathbf{v}/c)^2\right]^{-1/2}$  and  $\delta$  is the Dirac delta function. For this distribution, the pitch angle cosine  $\mu = v_{\parallel}/v$  is fixed, while all angles  $\psi$  around the parallel axis are equally likely. The advantage of this setup is, that it exhibits well-defined peaks in the linear dispersion relation while the physically and observationally motivated power-law distributions excite waves over a large spectrum of wave numbers k, making it more difficult to understand the underlying physics.

To enforce the quasi-neutrality assumption and to suppress initial parallel currents, we initialize a parallel electron beam with the same  $v_{\rm dr}$  as the CR ion beam. The existence of this electron beam is motivated numerically and not observationally, which is why we compare an alternative setup of drifting thermal electrons for the neutralizing electrons in Appendix 6.C. As expected, both methods lead to identical results (after the initial linear growth phase, where we observe a small difference in the noise properties of both setups).

This research has been triggered after observing a strong correlation between the rotational phases of the CR velocity and the wave magnetic field in the fluid-PIC and PIC streaming simulations presented in Lemmerz et al. (2024b), which also excite a broad spectrum of waves over time. In those simulations, the box is large enough so that CRs cannot travel across it before the instabilities saturate, suggesting that the finite box size has

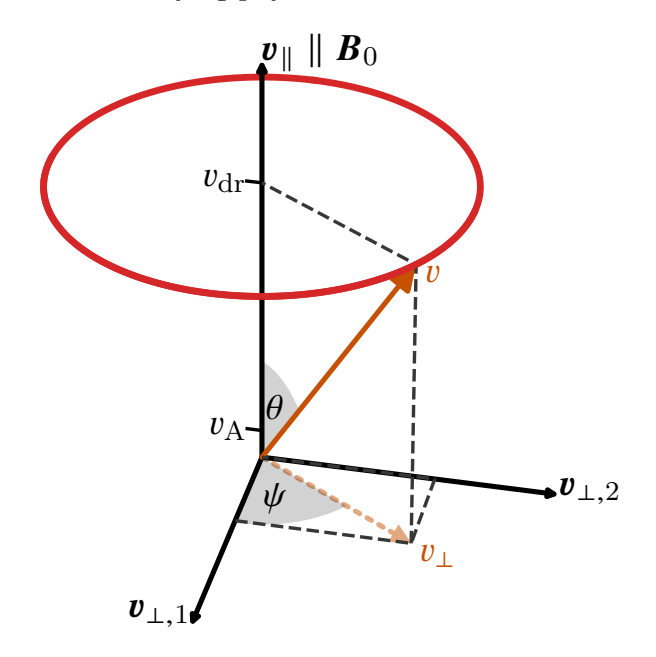


Figure 6.2. Visualization of the geometry of our initial CR distribution in velocity space. Two angles are defined, the pitch-angle  $\cos(\theta) = \mu = v_{\parallel}/v$  and the rotational angle  $\tan(\psi) = (v_{\perp}, 2/v_{\perp}, 1)$ . The CR ion initial conditions are shown as a red circle, with fixed  $\theta$  and uniformly distributed  $\psi$ . A neutralizing CR electron beam at the same  $v_{\rm dr}$  but with  $v_{\perp} = 0$  is initialized as well.

no influence on the simulated instability and is rooted in plasma physical processes. In the following, we design a simulation suite in which we limit the simulation box size and vary the simulation parameters so that the individual CR-driven instabilities are excited separately. This helps us to analyze the instabilities and their saturation in isolation and to understand the emerging phase correlation as it is observed in our previous simulation.

The numerical resolution samples the dispersion relation at discrete values in k-space (Shalaby

et al., 2017a). As such, a wave mode can only be resolved in simulations with periodic boxes if the absolute value of the wave vector k is an exact multiple of  $2\pi/L$ , where L is the length vector of the box. Typically, the goal is to reproduce the analytical dispersion relation by densely sampling the modes in k-space, i.e., using large box sizes L. In this paper, however, we concentrate our attention on the growth of only one resonant wave vector  $k_{\rm res}$  and try to prevent the growth of neighboring k, which would complicate the interpretation of the results because of possible mode-mode interactions masking the growth and saturation of an individual mode. In order to achieve this, we choose the one-dimensional box length to be only a few times the scale of interest. That is  $L_x = 2 \times 2\pi/k_{\rm res}$  for the B simulation, where  $k_{\rm res}$  is the scale of the largest growing wave mode of interest, while the simulation box is 3 times (F) and 6 (I) times the scale  $2\pi/k_{\rm res}$  in the other simulations. In the I simulation, this restriction also eliminates the growth of gyroscale instabilities, as Alfvén modes larger than the ion skin depth  $d_i = c/\omega_i$  remain unresolved. Here, the plasma frequency for a species s is given by  $\omega_s = (q_s^2 n_s/m_s \epsilon_0)^{1/2}$  and the overall plasma frequency is  $\omega_p = (\sum_s \omega_s^2)^{1/2}$ .

On the other hand, the intermediate-scale instability is eliminated from the F&B simulations by violating its growth condition,  $v_{\rm dr}/v_{\rm A} < \sqrt{m_r}/2$  (Shalaby et al., 2021), where the mass ratio is given by  $m_r \equiv m_i/m_e$  and the Alfvén velocity is  $v_{\rm A} = B_0/(\mu_0 n_{\rm i} m_{\rm i})^{1/2}$ . Thus, we performed this simulation with an unrealistic mass ratio of  $m_r = 100$  and  $v_{\rm dr}/v_{\rm A} = 10$ , such that the intermediate scale would only be triggered if the particles scatter below  $v_{\rm dr}/v_{\rm A} < \sqrt{100}/2 = 5$ , which is not seen in our setup. The I simulation uses a lower  $v_{\rm dr}/v_{\rm A} = 5$  and a realistic mass ratio for two reasons: First, together with an increase of the mass ratio, this ensures that the growth condition is satisfied. Second, this choice moves the unstable peak of  $I_{\rm E}$  to a smaller scale of  $kd_i = 362.32$ , increasing the scale separation and causing it to saturate at a smaller level, as demonstrated in Sec. 6.5.2. The I simulation is designed to best sample the peak of the whistler regime,  $I_{\rm W}$ , while suppressing the impact of  $I_{\rm E}$ .

As  $v_{\rm dr}$  is different between the F&B and I simulations, the remaining  $v_{\perp}$  parameter is chosen, such that the total velocity,  $v = |\mathbf{v}| \approx 0.14c$ , for CR ions is initially approximately the same in every simulation. In the following, we describe the common setup for all simulations while the different parameters are given in Table 6.2.2. All simulations use 75 particles per cell for CRs per species, at a density contrast of  $n_{\rm cr}/n_{\rm bg}=10^{-4}$ . In order to enforce charge density and current neutrality, we initialize and evolve an electron beam without a perpendicular velocity but with the same drift velocity as the CR proton beam. The background temperature for the isotropic fluid species is set to  $k_{\rm B}T_s/(m_ic^2)=10^{-4}$ , where  $k_{\rm B}$  is the Boltzmann constant and the different background species are denoted by the variable  $s \in (i, e)$ . All electromagnetic fields and fluid velocities are initialized as 0, except for the background magnetic field  $B_0$ , which is along the box direction, x. This implies, that the background is at rest and the CRs and waves move in the simulation frame. We set the (ion) Alfvén velocity  $v_A = B_0/\sqrt{\mu_0 m_i n_i} = 0.01c$ . Note that our three simulations differ in the assumed ion-to-electron mass ratio  $m_r = m_i/m_e$  and hence, also in the implicit ion cyclotron frequency of  $\Omega_i = qB_0/m_i$ , which serves as a physically motivated timescale. The cell size resolves the plasma skin depth,  $\Delta x = 0.1 c/\omega_p$ , and the time step size resolves the speed of light c = 1,  $\Delta t = 0.4\Delta x/c$ . We adopt periodic boundary conditions in our

Table 6.1.	Simulation parameters including the initial CR drift and perpendicular velocities,
as well	as the scale and growth rate of the associated dominant resonant wave mode.

Simulation	$\begin{bmatrix} L_x \\ [c/\omega_p] \end{bmatrix}$	$m_i/m_e$	$v_{ m dr} \ [v_{ m A}]$	$v_{\perp} \ [v_{ m A}]$	$\begin{bmatrix} k_{\rm res} \\ d_i^{-1} \end{bmatrix}$	$\Gamma_{ m res} \ [\Omega_i]$
В	1333.3	100	10	10	0.094	0.0579
F	1735.7	100	10	10	0.109	0.0640
I	346.8	1836	5	13.1	4.656	0.4880

simulation domain.

We compare our results for the standard PIC and fluid-PIC methods using the parameters of simulation I in Appendix 6.B. This shows that the fluid-PIC method provides similar results at a significantly reduced computational cost.

# 6.3. Particle motions and wave growth

The interaction of the CRs with the waves can be trivially broken down into two parts: the impact of the CRs on the wave and the impact of the wave on the CRs. In this section, we introduce the momentum equation to understand the former, as well as an evolution equation for the trajectories of individual CRs to understand the latter. Here, we will treat the CRs in isolation without accounting for the effect of waves on the CRs and discuss the resulting shortcomings. These equations serve then as a building block for later sections, which focus primarily on the wave-particle interaction.

#### 6.3.1. Momentum balance

The intensity of the growing waves is one of the most relevant quantity pertaining to CR streaming, and momentum conservation can be used to derive a useful equation relating it to changes in the CR velocity. The CR momentum of an individual particle along the background magnetic field is  $p_x = \gamma m_{\rm cr} v_x$ , thus the CR momentum density can be expressed as  $\mathcal{P}_{\rm cr} = n_{\rm cr} \bar{\gamma} m_i v_{\rm dr}$ , where  $\bar{\gamma}$  is a relativistic prefactor obtained from averaging the CR distribution (Bai et al., 2019). Because of momentum conservation, changes in the parallel momentum density of CRs correspond to changes in the parallel momentum density of the excited electromagnetic waves. The momentum density of the plasma waves is assumed to be stored predominantly in the movement of background particles, which needs to be taken into account. As the Poynting vector characterizes electromagnetic momentum without matter, which is negligible compared to the momentum carried by the background particles, it is appropriate to use the Minkowski momentum  $S_{\rm M} \equiv D \times B$  instead, which additionally accounts for the inertia in the wave-carrying background particles. The electric displacement field is  $D = \epsilon_{\rm bg} E$  and  $\epsilon_{\rm bg}$  denotes the electric permittivity of the background plasma (Chapter 2 of Groot and Suttorp 1972, Kemp 2011). Because  $v_{\rm wave} = (\epsilon_{\rm bg} \mu_{\rm bg})^{-1/2}$  and the magnetic susceptibility of the background plasma is almost

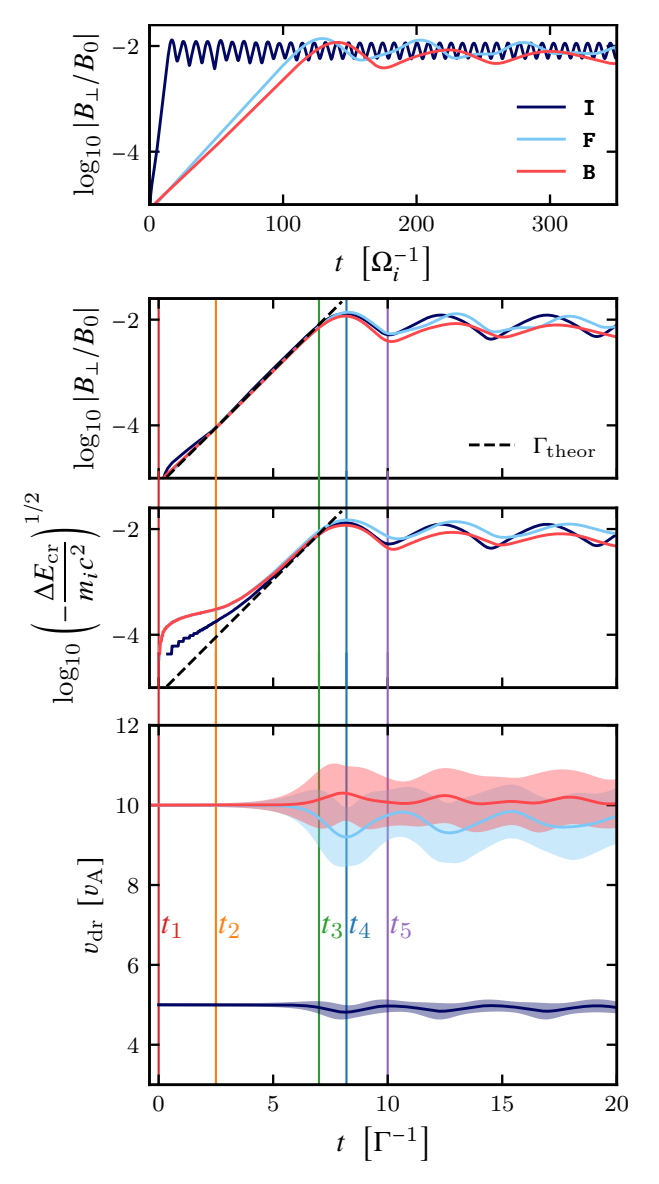


Figure 6.3 Top two panels: evolution of  $B_{\perp}$  over time for the different simulations in units of  $1/\Omega_i$  of the corresponding simulation and in units of the respective inverse growth rate  $1/\Gamma$ . The latter units are useful for comparing the simulations at specific times  $t_{1-5}$ . Third panel: energy lost by the CRs to the unstable modes as a function of time, which corresponds to the energy gain of the modes (see the second panel) up to numerical precision. Bottom panel: evolution of  $v_{\rm dr}$  over time, with one standard deviation of  $v_{\rm dr}$  indicating the spread around the mean value. Note that the mean velocity of CRs does not approach  $v_{\rm A}$  as it is usually assumed but saturates at a much larger value.

the same as in vacuum,  $\mu_{\rm bg} \approx \mu_0$ , the parallel momentum of the wave is

$$S_{\mathcal{M}} = \frac{\boldsymbol{E} \times \boldsymbol{B}}{\mu_0 v_{\text{wave}}^2} \bigg|_{\parallel} = \frac{B_{\perp}^2}{\mu_0 v_{\text{wave}}}.$$
 (6.7)

The last equality assumes a single, transverse wave mode traveling at a phase speed of  $v_{\text{wave}}$ , for which  $E_{\perp} = -iv_{\text{wave}}B_{\perp}$  follows according to Faraday's law. Evaluating the momentum balance of CR momentum lost by driving the unstable wave yields

$$\Delta S_{\rm M} + \Delta \mathcal{P}_{\rm cr} = 0 \quad \Rightarrow \quad \frac{\Delta B_{\perp}^2}{B_0^2} = -\frac{n_{\rm cr}}{n_{\rm bg}} \frac{v_{\rm wave} \Delta \left(\bar{\gamma} v_{\rm dr}\right)}{v_{\rm A}^2},\tag{6.8}$$

where  $\Delta x = x(b) - x(a)$  is the difference between the times a and b. This means, that the wave intensity mostly depends on the difference in drift velocity of the CR population.

<sup>&</sup>lt;sup>1</sup>For forward moving waves  $(v_{\text{wave}} > 0)$ , CRs slow down in the linear regime so that  $\Delta v_{\text{dr}} < 0$ .

The magnetic field growth for both simulations is shown in Figure 6.3. We note, that the saturation levels of the F&B and I simulations do not necessarily coincide if we were to use the same initial CR pitch angle. We postpone a systematic study of this topic to future work.

Although instability growth at the gyroscale takes significantly longer in physical time units, all simulations exhibit a similar behavior when the time is scaled to their maximum growth rates  $\Gamma$ . We mark 5 times of interest: first, the initialization, second, the phase of linear growth, third, the transition to the nonlinear regime, fourth, the time of saturation, and fifth, the rebound point, to which we will refer throughout the paper. The momentum equation (6.8) states that changes in the drift velocity affect the magnetic field strength as  $\Delta B_{\perp}^2 \propto -v_{\rm wave} \Delta v_{\rm dr}$ . The simulation B is qualitatively different from the other simulations as the CRs are accelerated rather than slowed down in the parallel direction. This is expected from the momentum equation because  $v_{\rm wave}$  is negative and as energy is transferred to these backward-propagating modes,  $v_{\rm dr}$  needs to increase over time. However, we can infer from the third panel of Figure 6.3 that CRs still lose energy, which stems from a decrease in perpendicular velocity  $v_{\perp}$ .

The wave velocity of the fastest driven modes of the intermediate-scale instability is faster than that driven by the gyroscale instabilities, i.e.,  $v_{\text{wave},I} \approx 6.52v_{\text{wave},F}$ . Thus, it generates a larger magnetic field with the same  $\Delta v_{\text{dr}}$  as can be inferred from equation (6.8). As a result, the pitch angle scattering of the intermediate-scale instability is significantly reduced because similar levels of magnetic field amplification are reached in all simulations. This effect is captured in the standard deviation around the drift velocity, which serves as a measure of this pitch angle scattering and can be compared between the simulations (see the bottom panel of Figure 6.3). After saturation, all simulations show oscillatory periods of wave growth and decay (corresponding to particle acceleration and deceleration) with a similar periodicity. This oscillatory behavior in the wave intensity is observed in most single wave mode instabilities, e.g., the electrostatic two-beam instability (Morse and Nielson, 1969; Shoucri, 1979), and beam-plasma instabilities (Shalaby et al., 2018, 2020).

# 6.3.2. Evolution of the instability without CR back-reaction: the pendulum equation

While the evolution of  $v_{\rm dr}$  plays a crucial role, it is instructive to study the angle  $\psi_{\rm cr} = \arg(\boldsymbol{v}_\perp)$  of the particles (cf. Figure 6.2). For all perpendicular vectors, we use the shorthand complex notation  $\boldsymbol{v}_\perp = (v_y + \mathrm{i}\,v_z)\boldsymbol{e}_\perp$ , where y and z span the plane perpendicular to  $\boldsymbol{B}_0$ , see also Appendix 6.A for our notation convention. It simply follows, that  $v_\perp = |\boldsymbol{v}_\perp|$ .

To motivate the following calculations, we first analyze the simulated structure of the distribution of rotation angles of CR ions,  $\psi_{\rm cr}$ , as well as  $\psi_B = \arg B_{\perp}$ . These are shown as CR distributions and lines, respectively, as a function of x position and rotation angles in Figure 6.4. The magnetic field is initially randomly aligned but the dominant wave mode is quickly excited and structures the perpendicular magnetic perturbation at  $t_2$ . The CR distribution is still mostly uniform, but changes significantly before entering the nonlinear stage at  $t_3$ . At every position x, the CRs have now bunched up to a narrow distribution in  $\psi_{\rm cr}$  so that we obtain a broader helical

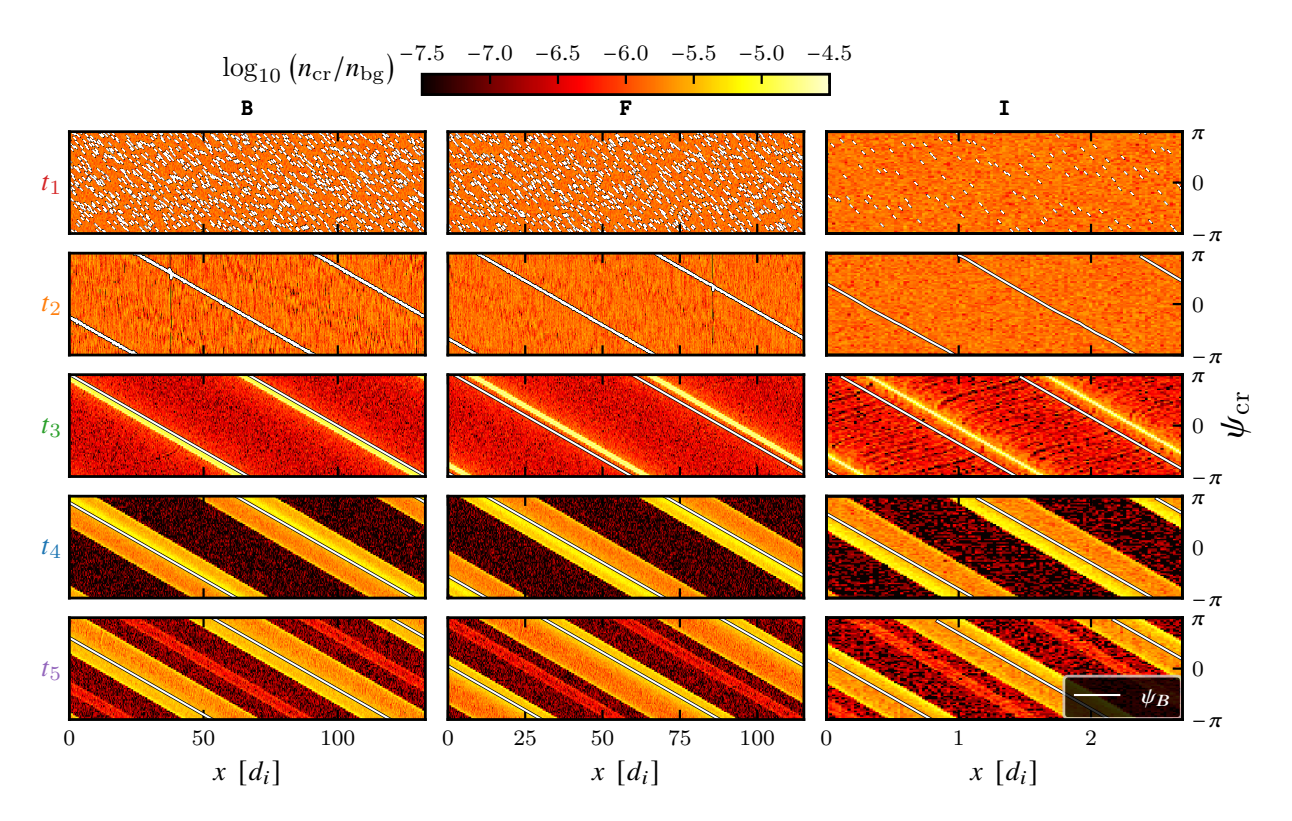


Figure 6.4. We show the CR distribution as a function of local rotational phase of CR ions,  $\psi_{\rm cr}$ , and the position along the initial magnetic field, x, at the five different times  $t_{1-5}$  as defined in Figure 6.3. These are overplotted with white lines, indicating the local rotation phase of the perturbed magnetic field vector,  $\psi_B$ . The angle  $\psi_B$  of the magnetic wave follows a straight, white line with slope of -k, according to  $\psi_B \propto \arg\{B_{\perp} \exp[\mathrm{i} (\omega t_i - kx)]\} = -kx$ , except at initialization where it is random. An illustration of the particle resonance is shown in Figure 6.5. The average CR density is  $n_{\rm cr}(x) = 10^{-4} n_{\rm bg}$ , which is retrieved when contracting the  $\psi$  dimension in this plot. We only show a part of the simulation boxes so that 2 cycles of the dominant wave mode are captured in all plots. Clearly, the action of the instability causes the CR phases to bunch up close to the local phase of the excited magnetic field.

structure that winds around the mean magnetic field  $B_0$ . This bunching has also been observed in other simulations (Hoshino and Terasawa, 1985; Zachary et al., 1989). The CR helix has exactly the same winding angle in comparison to the helix delineated by the unstable magnetic wave. However, the helical structures of the CRs and the magnetic wave are offset with respect to one another: we obtain  $\psi_{cr} > \psi_B$  for forward moving waves (Gary et al., 1986a) and  $\psi_{cr} < \psi_B$  for backward moving waves. At saturation, the spread in the  $\psi_{cr}$  angles is again larger so that they form a broader strip that extends over the magnetic field line. At  $t_5$  a "ghost" strip can be seen, which is the result of particles escaping from the main strip to the left and to the right, overlapping in between. Even though the spatial and temporal scales are very different, the F and I simulations share the same features.

When comparing the distributions of CRs and magnetic perturbations in Figure 6.4, it is obvious that  $\psi_{cr}$  and  $\psi_B$  are closely related. It is therefore useful to define the gyrophase

$$\varphi(x,t) = \psi_{\rm cr}(t) - \psi_B(x,t) = \arg(\mathbf{v}_\perp \mathbf{B}_\perp^\dagger)(x,t) \tag{6.9}$$

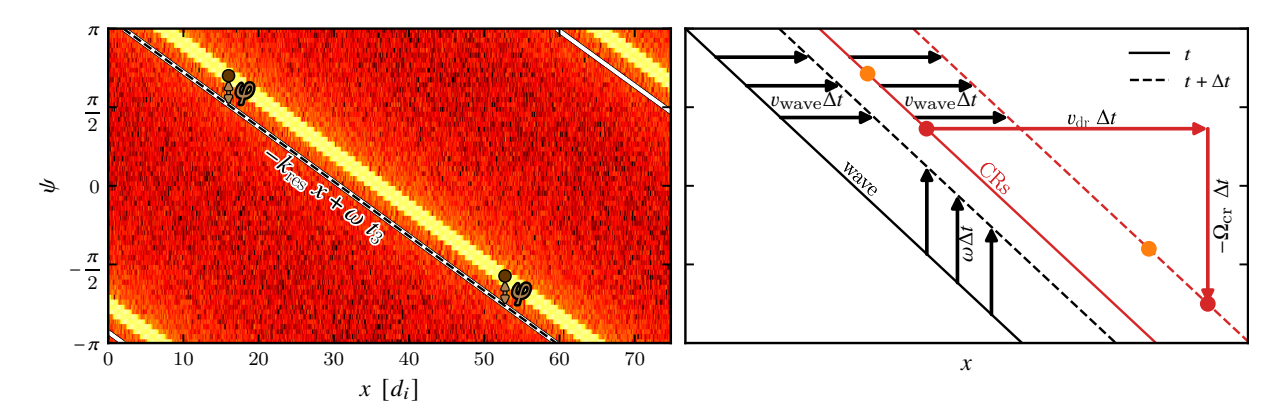


Figure 6.5. The left panel shows a zoom into the middle panel (F at  $t_3$ ) of Figure 6.4. The electromagnetic wave is shown to have a slope of  $-k_{\rm res}x$ , while two particles are indicated at a relative angle  $\varphi$ . The right panel shows an illustration of the left panel, which explains the conundrum that the CRs follow a helical structure that has the same winding angle as the magnetic field of the unstable wave, despite the fact that they are much faster than the wave. We show the wave and the dense, narrow CR band while we omit their periodic wrapping for clarity. According to the resonance condition, a CR particle (red) not only moves at  $v_{\rm dr}$  but also rotates at its gyrofrequency  $\Omega_{\rm cr}$ . Thus, the particles distributed along the helix at t (solid red) are mapped onto a somewhat displaced helix at  $t + \Delta t$  (dashed red). By contrast, the wave moves by  $v_{\rm wave}\Delta t$  along x, but its movement can alternatively be understood as a rotation of  $\omega \Delta t$  along  $\psi$ , thus mapping the wave from t (solid black) to  $t + \Delta t$  (dashed black). This explains how the CR helix maintains the same distance from that of the magnetic field vector of the wave.

for each particle. Here, † denotes the complex conjugate. Essentially, the particle angle  $\varphi$  is now defined in a helical coordinate system, where the helix is given by the electromagnetic wave. We can estimate the gyration period as  $\psi_{\rm cr}(t) \sim -\Omega_{\rm cr} t$  (where  $\Omega_{\rm cr} = \Omega_i/\gamma$ ) while the moving particles experience the magnetic field at  $\boldsymbol{B}(x_0 + v_{\rm dr} t, t)$ . Given that  $\arg(\boldsymbol{B}_{\perp})(x, t) = -kx + \omega t$  (for parallel waves with phase speed  $v_{\rm wave}$  and rotation rate  $\omega = kv_{\rm wave}$ ), it follows trivially that the gyrophase changes over time as

$$\varphi(x,t) = k(x_0 + v_{\rm dr}t) - \omega t - \Omega_{\rm cr}t$$

$$= \varphi_0 + [k(v_{\rm dr} - v_{\rm wave}) - \Omega_{\rm cr}]t, \tag{6.10}$$

where we chose  $\varphi_0 = kx_0$ . Enforcing  $\varphi(x,t)$  to be approximately constant over time, we recover the resonance condition (Kulsrud, 2004)

$$\mathcal{R}(\omega, k) \equiv k(v_{\rm dr} - v_{\rm wave}) - \Omega_{\rm cr}$$

$$= k v_{\rm dr} - \omega - \Omega_{\rm cr} = 0. \tag{6.11}$$

From this condition, one can find multiple waves with a given  $\omega(k)$  and k, which are resonant. Furthermore, equation (6.11) implies that resonant particles move in lockstep along the wave. This picture is geometrically illustrated in Figure 6.5. Interestingly, even though single particles move significantly faster than the wave, collectively they experience the wave as a static electromagnetic field. Thus, the CRs form a coherent, wave-like structure, which moves at velocity

 $v_{\rm dr} - \Omega_{\rm cr}/k$ . This excites waves, which move at the same velocity. Furthermore, if  $v_{\rm dr} < \Omega_{\rm cr}/k$ , then the CR band moves backwards and can excite backward moving waves.

We can expand on the previously described simplified picture, which only included the force exerted by  $B_0$  on a particle. In the following, we compute a single particle trajectory that results from the full Lorentz force introduced by the wave.

In the wave frame, we can neglect contributions to the electric field so that the CR particle energy and its relativistic Lorentz factor  $\gamma'$  remain constant. For this reason, we adopt this frame in order to derive the time evolution of the particle velocity with  $v'_{\parallel} = v_{\parallel} - v_{\text{wave}}$  and  $v'_{\perp} = v_{\perp}$  (Lutomirski and Sudan, 1966, see also the non-relativistic results by Roberts and Buchsbaum, 1964; Bell, 1965):

$$\frac{\partial [\gamma' v'_{\parallel}(t)]}{\partial t} = \frac{q}{m} [\mathbf{v}' \times \mathbf{B}]_{\parallel} = -\frac{q}{m} B_{\perp}(t) v'_{\perp}(t) \sin(\varphi(t)). \tag{6.12}$$

An equation for the perpendicular particle velocity can be easily derived by using the energy conservation in the wave frame, that is  $\partial_t \gamma' = 0$  implying that  $\partial_t (v_\perp'^2 + v_\parallel'^2) = 0$ . Thus,

$$\frac{\partial \left[\gamma' v_{\perp}'(t)\right]}{\partial t} = -\frac{\gamma' v_{\parallel}'}{v_{\perp}'} \frac{\partial v_{\parallel}'}{\partial t} = \frac{q}{m} B_{\perp}(t) v_{\parallel}'(t) \sin\left(\varphi(t)\right),\tag{6.13}$$

which is a projection of the Lorentz force term  $\mathbf{v}'_{\parallel} \times \mathbf{B}_{\perp} q/m$ . Specifically, if  $\mathbf{v}_{\perp}$  points along this Lorentz force term (i.e., for  $\varphi = \pi/2$ ) only the magnitude of  $\mathbf{v}_{\perp}$  is increased without changing its direction. In the case of  $\mathbf{v}_{\perp} \parallel \mathbf{B}_{\perp}$  (i.e., for  $\varphi = 0$ ), the length of  $\mathbf{v}_{\perp}$  remains invariant, but the Lorentz force on the particle causes it to change its rotational velocity. Assuming that both  $\psi_{\rm cr}$  and  $\psi_{B}$  are measured from the same starting point in the plane perpendicular to  $\mathbf{B}_{0}$ , the remaining part of the Lorentz force term  $\mathbf{v}'_{\parallel} \times \mathbf{B}_{\perp} q/m$  is projected onto  $\psi$ . Evaluating the angular velocity of the particle in the lab frame yields

$$\frac{\partial \psi_{\rm cr}}{\partial t} = -\Omega_{\rm cr} + \frac{q}{\gamma m} v_{\parallel}' B_{\perp}(t) \frac{\cos(\varphi(t))}{v_{\perp}(t)}. \tag{6.14}$$

In equation (6.10), we assumed  $v_{\parallel} = v_{\rm dr}$  at all times. However, the x-coordinate of an individual particle is correctly defined as  $x(t) = \int_0^t v_{\parallel}(\tau) d\tau$ . Taking the time derivative of  $\varphi$  (as defined in equation 6.9) and eliminating x(t) and  $\partial_t \psi_{\rm cr}$  (equation 6.14) yields

$$\frac{\partial \varphi}{\partial t} = -\Omega_{\rm cr} + k v'_{\parallel}(t) + \frac{q}{\gamma m} v'_{\parallel}(t) B_{\perp}(t) \frac{\cos(\varphi(t))}{v'_{\perp}(t)}. \tag{6.15}$$

Due to the different time dependent quantities, this equation is complicated to solve. As before,  $\partial \varphi/\partial t = 0$  can be interpreted as a resonance condition. However, we further make the approximation that  $qB_{\perp}/(\gamma mv_{\perp}) \ll k$ , which is equivalent to  $B_{\perp}/B_0 \ll kd_i \times v_{\perp}/v_A$ , and drop the last term of equation (6.15) from subsequent calculations. Thus, we retrieve the same resonance condition as before, but now in the comoving wave frame. With this simplification, the evolution

of  $\varphi$  can be further investigated, yielding

$$\varphi(t) = -\Omega_{\rm cr}t + k \int_0^t v'_{\parallel}(\tau) d\tau + \varphi_0, \tag{6.16}$$

$$\frac{\partial \varphi(t)}{\partial t} = -\Omega_{\rm cr} + k v'_{\parallel}(t), \tag{6.17}$$

$$\frac{\partial^2 \varphi(t)}{\partial t^2} = -k \frac{q B_{\perp}(t) v_{\perp}(t)}{\gamma' m} \sin \varphi(t). \tag{6.18}$$

This shows that in the limit of weak perturbations, the angle  $\varphi$  between  $\mathbf{v}_{\perp}$  and  $\mathbf{B}_{\perp}$  obeys a pendulum equation. We also see that the parallel Lorentz force from equation (6.12) multiplied with the wavenumber k can be interpreted as a pseudo torque on  $\varphi$ . This is because the gyrophase is defined in relation to a helical coordinate system spanned by  $\mathbf{B}_{\perp}$ . This pseudo torque is absent from the evolution of  $\psi_{\rm cr}$ , which is defined in an inertial frame.

While equation (6.17) shows that resonantly driven waves will not change the relative phase between the CR and the local wave magnetic field (i.e., up to zeroth order in  $B_{\perp}/B_0$ ) if the parallel velocity stays constant. Up to first order, these waves exert a parallel force given in equation (6.12) such that the particles accelerate towards locations where  $\varphi(t)$  is close to zero.

The set of equations (6.12)–(6.15) allows for two constants of motions (Bell, 1965): energy conservation in the waveframe, described by  $v'^2_{\parallel} + v'^2_{\perp} = \text{const.}$ , and an invariant connecting linear and angular momentum in the helical symmetry,

$$C|_{B_{\perp}=\text{const.}} = \frac{1}{2}v_{\perp}^2 + \frac{\Omega_{\text{cr}}}{k} \left[ v_{\parallel} + v_{\perp} \frac{B_{\perp}}{B_0} \cos(\varphi) \right]. \tag{6.19}$$

An extended derivation of the non-relativistic case by Otani (1988) shows that energy conservation in the wave frame holds only if the wave velocity and intensity are constant. Notably, changes in the wave velocity are not necessarily small in the non-linear regime, as will be discussed in Section 6.5.3, and the wave amplitude grows during the linear phase of the instability. On the other hand, changes to the CRs' Lorentz factor  $\gamma$  are small, extending the applicability of the results to the relativistic case. The complete constant of motion C is (Otani, 1988)

$$C = \frac{1}{2}v_{\perp}^2 + \frac{\Omega_{\rm cr}}{k} \left[ v_{\parallel} + v_{\perp} \frac{B_{\perp}}{B_0} \cos(\varphi) \right] + \frac{1}{2} \left( \frac{\Omega_{\rm cr}}{k} \frac{B_{\perp}}{B_0} \right)^2, \tag{6.20}$$

which includes one additional term in comparison to equation (6.19). For  $B_{\perp} \ll B_0$ , this can be simplified to

$$\frac{\partial v_{\perp}}{\partial t} \approx -\frac{\Omega_{\rm cr}/k}{v_{\perp}} \frac{\partial v_{\parallel}}{\partial t}.$$
 (6.21)

The presupposed energy conservation in a constant wave frame implies that,

$$\frac{\partial v_{\perp}}{\partial t} = -\frac{(v_{\parallel} - v_{\text{wave}})}{v_{\perp}} \frac{\partial v_{\parallel}}{\partial t}, \tag{6.22}$$

which is equivalent to equation (6.21) only when the resonance condition  $v_{\parallel} - v_{\text{wave}} = \Omega_{\text{cr}}/k$  is satisfied. Although we focus on the gyroresonant case with low wave intensity, where energy-

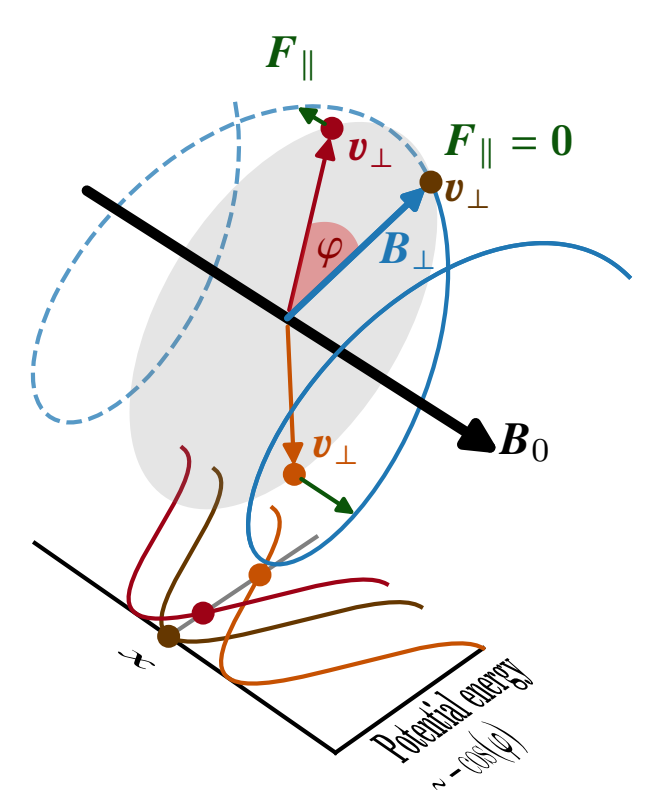


Figure 6.6 We show three CR particles at the same position x and perpendicular velocity  $v_{\perp}$ , which are in resonance with an electromagnetic wave (shown in blue), i.e., the angle  $\varphi$ changes only slowly over time. While the particles share a spatial position x, they experience different parallel forces, which depend on their gyrophases  $\varphi$ . The Lorentz forces on the particles act to minimize  $\varphi$ , meaning that the particles align themselves with the local orientation of the magnetic field vector. This is achieved by means of accelerating (decelerating) the particle in the parallel direction, which in turn increases (decreases) the Doppler-shifted gyration of the particles,  $kv_x - \Omega_{cr}$ , and thus acts as a pseudoforce in the  $\varphi$  direction. The particle's trajectory can be shown to follow a pendulum motion in a potential well that is centered on the local orientation of the perpendicular magnetic field.

conserving scattering is a reasonable approximation, caution is needed as particles move further away from resonance (Section 6.5.1).

### 6.3.3. Discussing the pendulum picture of CR motions

Figure 6.6 visualizes the parallel Lorentz force acting on three test particles at the same position x in the gray plane. Particles aligned with the perpendicular magnetic field do not experience a parallel Lorentz force while the unaligned particles are moving parallel to  $B_0$  towards the closest field line. As they move along x, their relative gyrophase  $\varphi = \psi_{\rm cr} - \psi_B$  is minimized – while this movement along x has no influence on the evolution of the angle  $\psi_{\rm cr}$  (equation 6.14) in the static coordinate system.

Interestingly, equation (6.18) is equivalent to the pendulum differential equations, and thus, the CRs are trapped in potential wells that are centered on the local direction of the magnetic perturbation, around which they oscillate. This potential well not only depends on the local magnetic field strength  $B_{\perp}$ , but also on the gyrophase of each particle. This differentiates it from a magnetic bottle, which is localized in space. Note that the adiabatic invariance of  $\gamma \mu_{\rm B}$ , where the magnetic moment is  $\mu_B = \gamma m v_{\perp}^2/(2B)$ , cannot be used to understand resonant CRs because there is no effective cyclotron motion with respect to the electromagnetic wave, which precludes the applicability of the adiabatic assumption.

If the wave amplitude saturated its growth and if changes in the CR velocities are small, the change in the pitch angle of a CR due to an interaction with a wave packet can be approximated (Chapter 12.2. of Kulsrud, 2004). Starting from a gyrotropic distribution of CRs, we are faced with another problem: the time average of the term  $\int_{-\pi}^{\pi} \sin(\varphi(t)) d\varphi \sim 0$  averages out, which

is equivalent to stating that  $\dot{\varphi}$  averages out for the CR population. This in turn means that  $\Delta v_{\rm dr}(t) \sim 0$ . Thus, no wave growth would occur according to the momentum equation (6.8), contrary to what our simulations and solutions of the dispersion relation show.

Using the linear dispersion relation, Gary et al. (1986b) show that the average  $\varphi$  angle of the resonant instabilities is non-vanishing, a necessity to transfer energy gyroresonantly from the CRs to the waves (Gary et al., 1986a). In the following we explore, how this misalignment between the CR perpendicular velocity  $v_{\perp}$  and their local magnetic field vector  $B_{\perp}$  arises and is sustained over the growth period of the instability.

One possible approach for explaining the surplus in transferred momentum assumes the interaction with individual wave packets of length d. The particles transit through the wave packet in time  $t_d = d/v_{\parallel}$ . Hence, particles that are accelerated in  $v_{\parallel}$  traverse the wave packet faster than decelerated particles. The change in momentum depends on the force times the time spent interacting with the wave packet,  $\Delta p_{\parallel} = F_{\parallel}t_d$ . Because  $t_d$  is smaller for fast particles, a stochastic imbalance between accelerated and decelerated particles occurs. If, for a forward moving wave, the faster CRs take momentum from the wave and the slower CRs give momentum to the wave, there would be a surplus of momentum given to the wave because of the longer interaction times of slower particles, which would amplify the wave. This mechanism is similar to second order Fermi acceleration, however particles are not reflected but pass through the wave packet and thus lose energy (Fermi, 1949; Tsytovich, 1985).

However, this argument would also predict a damping of backward moving waves, for which slower CRs take momentum from the wave and faster CRs give momentum to the wave, even though the unstable waves are still expected to grow. Because our simulations use a periodic box, d is effectively infinitely long and this effect is eliminated in our setup. Therefore, instability growth cannot be caused by differences in the transit time and motivates the search for another explanation. In Section 6.4 we investigate the underlying mechanism leading to a surplus of CRs giving momentum to the wave, creating the imbalance that is necessary for wave growth.

Before doing so, we point out two more intricacies, which differentiate the description of parallel CR motions from a traditional pendulum, complicating the application of this physical picture during the linear growth phase. A traditional pendulum oscillates at a frequency of  $(g/l)^{1/2}$ , where l is the length of the pendulum and g is the gravitational acceleration, both of which are approximately constant. Analogously, the CR pendulum frequency depends on the amplitude of  $B_{\perp}(t)$ . During wave growth,  $B_{\perp}(t)$  grows exponentially and is even closely related to  $\Delta v_{\parallel}$  through the momentum equation (6.8). Thus, the gyrophase of CRs in the linear growth phase resembles a pendulum whose length is shortened exponentially over time. Second, these equations are derived for the interaction of a single CR with a single wave mode and constant  $\Omega_{\rm cr}$ , while a realistic situation has many CRs interacting with multiple wave modes. A traditional analogue is a coupled pendulum, which further complicates an accurate analytical treatment.

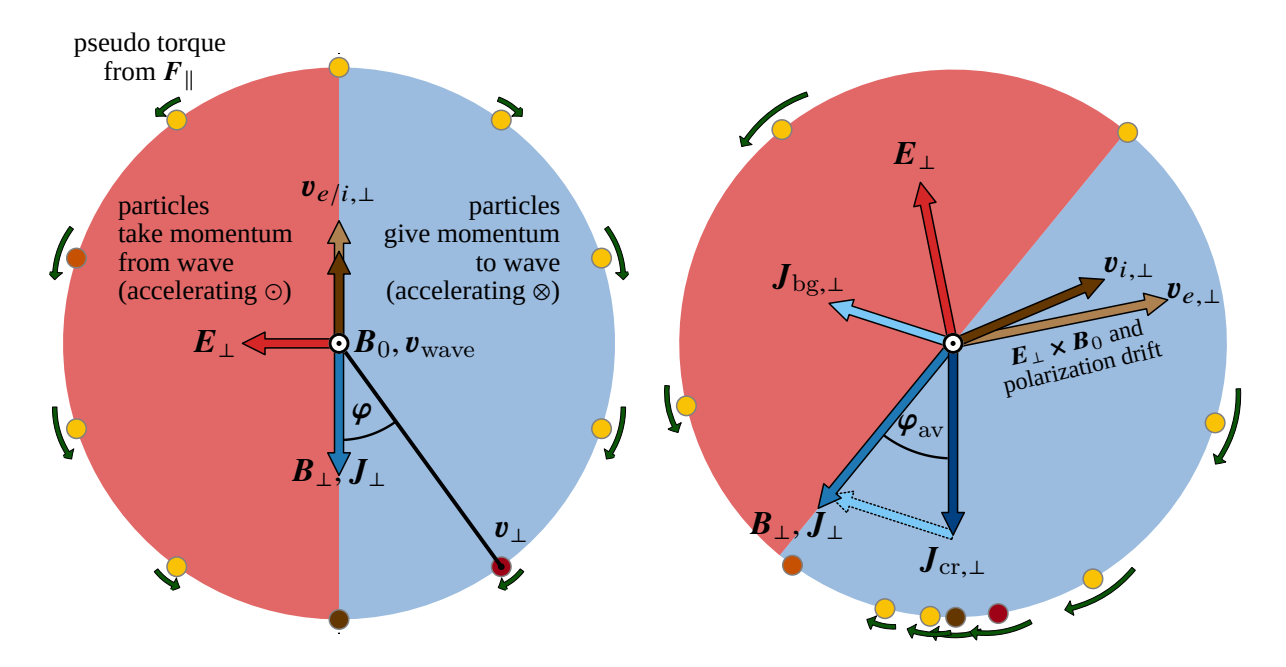


Figure 6.7. A drawing explaining the processes leading to instability. We show the  $\varphi$  angle of the streaming CRs in relation to their local direction of the perpendicular magnetic and electric fields,  $B_{\perp}$  and  $E_{\perp}$ , respectively. On the left-hand side, we show the initial seed wave with random particles at a given position x and use the same color coding of the three particles defined in Figure 6.6 (while we color code the additional particles with yellow). As explained in Figure 6.6, the parallel Lorentz force,  $q\mathbf{v}_{\perp} \times \mathbf{B}_{\perp}$ , causes all particles except for the brown one to move along  $B_0$  and x, implying a change in  $\varphi(t)$ , which we indicate by green arrows at each particle. Particles on the left (in the red semicircle) get accelerated out of the plane into the propagation direction of the wave, and hence take momentum from it to ensure momentum conservation while particles on the right (blue semicircle) are accelerated into the plane and transfer momentum to the wave. Thus, we would expect all particles to converge to the local magnetic field direction  $\boldsymbol{B}_{\perp}$  (albeit at different locations on the x axis). This situation is shown in the drawing on the right-hand side, which shows the particle distribution in  $\varphi$  at a later time. However, this bunching up of CRs implies a downwards pointing CR current,  $J_{cr,\perp}$ . After adding the background current,  $J_{\text{bg},\perp}$ , the total current, and hence the perturbed magnetic field  $B_{\perp}$ , is shifted to the left. Thus, the back-reaction of the CR current causes more CRs to be found in the blue region, in which there is a net transfer of CR momentum to the wave. This explains the inner workings of the resonant instability. The background velocities  $v_{i,\perp}$  and  $v_{e,\perp}$ determine the orientation of  $\boldsymbol{J}_{\mathrm{bg},\perp} = n_{\mathrm{bg}}(\boldsymbol{v}_{i,\perp} - \boldsymbol{v}_{e,\perp})$  while  $\varphi_{\mathrm{av}}$  denotes the averaged phase angle of the CRs.

# 6.4. The physics of wave growth and decay

As derived earlier, the gyro angles of CRs obey the pendulum equation with the force pointing in the direction of the local  $B_{\perp}$ . However, we do not observe the oscillating behavior of a pendulum during the linear growth phase but only after saturation. In this section, we concentrate on the linear phase and the physical mechanism behind wave growth. This section is structured in the following way: first, we provide an intuitive physical picture of the resonant wave growth and discuss its implications. To this end, the different equations and corresponding effects are discussed in succession. This model is then compared with the dispersion relation, which is an exact solution to the linearized wave equation and the CR Vlasov equation, capturing all effects simultaneously while making it difficult to extract a simple physical meaning underlying the equations. Finally, we connect these considerations through our simulation results.

## 6.4.1. Deconstructing the instability's feedback loop

Exponential growth processes often have an underlying feedback loop, which we will describe for the resonant CR-driven instabilities in the following. In essence, the CRs try to align their gyrophase with the perpendicular magnetic field, as pointed out in Figure 6.6. However, the resulting CR current does not only intensify the wave, but also modify its wave speed. Thus, the wave and the associated potential wells move constantly, but slowly away from the particles at resonance – leading to an asymmetry, which on average forces CRs to transfer momentum to the wave. In the following, we detail the individual physical processes leading to instability growth for a forward moving wave (defined by  $v_{\text{wave}} > 0$ ) with a wave vector k > 0 (cf. Figure 6.7).<sup>2</sup>

- A (seed) electromagnetic wave travelling at  $v_{\text{wave}}$  introduces an electromagnetic field perpendicular to its propagation direction. This is the starting point of the initial magnetic bunching provided by the magnetic perturbation  $\boldsymbol{B}_{\perp}$  of the seed wave.
- CRs are accelerated by the parallel Lorentz force, and hence experience a pseudo-torque by moving along the propagation direction of the rotating wave (cf. Figure 6.6). In result, the parallel motion of the CRs decreases  $\varphi$  and thus accelerates them toward  $\boldsymbol{B}_{\perp}$  with an amplitude depending on  $\boldsymbol{B}_{\perp}$  (magnetic bunching).
- As the CRs' perpendicular velocity vectors are bunching up in  $\varphi$ , this generates a perpendicular CR current density  $J_{\text{cr},\perp}$  (see Figure 6.7).
- The seed electric field  $\boldsymbol{E}_{\text{wave},\perp}$  is perpendicular to the magnetic field. Adding the CR current,  $\boldsymbol{J}_{\text{cr},\perp}$ , induces an additional electric field,  $\boldsymbol{E}_{\text{cr},\perp}$ , which opposes this current. As a result, the total electric field,  $\boldsymbol{E}_{\perp} = \boldsymbol{E}_{\text{cr},\perp} + \boldsymbol{E}_{\text{wave},\perp}$  is no longer perpendicular to  $\boldsymbol{B}_{\perp}$ .
- The electric field  $E_{\perp}$  leads to guiding center drifts of the background species s. This is the dominant effect for the background species because their perpendicular and drift velocities

<sup>&</sup>lt;sup>2</sup>In our convention, we have  $\boldsymbol{a}_{\parallel} \times \boldsymbol{b}_{\perp} = \mathrm{i}\,\boldsymbol{a}_{\parallel}\boldsymbol{b}_{\perp}$ ,  $\nabla \to -\mathrm{i}\,k$ ,  $\partial_{t} \to (\mathrm{i}\,\omega + \Gamma)$  so that  $\nabla \times \boldsymbol{b}_{\perp} = -\mathrm{i}^{2}\,\boldsymbol{b}_{\perp}$  (Appendix 6.A). A phase shift by i corresponds to a 90° counterclockwise rotation in Fig. 6.7.

are small and as such, their magnetic bunching due to the term  $v_{s,\perp} \times B_{\perp}$  is negligible. These guiding center drifts are the  $E \times B$  drift (Sturrock, 1994),

$$\mathbf{v}_{E \times B} = \mathbf{E}_{\perp} \times \mathbf{B}_0 / B_0^2 = -i \mathbf{E}_{\perp} / B_0, \tag{6.23}$$

and the polarization drift (Sturrock, 1994),

$$\mathbf{v}_{\text{pol}} = (\partial \mathbf{E}/\partial t)/(\Omega_s B_0) = (\mathrm{i}\,\omega + \Gamma)\mathbf{E}_{\perp}/(\Omega_s B_0),\tag{6.24}$$

where we assumed a single transverse, plane-parallel wave in the last step.<sup>3</sup> Combining both drifts introduces a perpendicular velocity component for the background ions and electrons:

$$\boldsymbol{v}_{\perp} = \boldsymbol{v}_{E \times B} + \boldsymbol{v}_{\text{pol}}.\tag{6.25}$$

This leads to a perpendicular current from the background ions and electrons,

$$\boldsymbol{J}_{\mathrm{bg},\perp} = n_{\mathrm{bg}}(q_{i}\boldsymbol{v}_{i,\perp} + q_{e}\boldsymbol{v}_{e,\perp}) = n_{\mathrm{bg}}(\boldsymbol{v}_{i,\perp} - \boldsymbol{v}_{e,\perp}). \tag{6.26}$$

• The induced magnetic field is well approximated using Ampère's law without the displacement current (see footnote 2),

$$\nabla \times \boldsymbol{B}_{\perp} = k_{\parallel} \boldsymbol{B}_{\perp} = \mu_0 \boldsymbol{J}_{\perp} = \mu_0 (\boldsymbol{J}_{\text{cr.}\perp} + \boldsymbol{J}_{\text{bg.}\perp}). \tag{6.27}$$

According to this equation,  $J_{\perp}$  and  $B_{\perp}$  are necessarily aligned for k > 0. Imagine a situation, where an initial  $B_{\perp}$  gives rise to the magnetic bunching of CRs and the background particle drifts described above. The resulting total perpendicular current is not aligned with this initial  $B_{\perp}$ . But the induced change of the magnetic field by the total current will realign  $B_{\perp}$  with  $J_{\perp}$  and hence rotates  $B_{\perp}$  in the perpendicular plane.

- Because the magnetically bunched CR current  $J_{\text{cr},\perp}$  is misaligned with  $J_{\text{bg},\perp}$ , so are  $J_{\text{cr},\perp}$  and  $B_{\perp}$ . As a result, the average Lorentz force on the CRs,  $J_{\text{cr},\perp} \times B_{\perp}$  leads to a parallel deceleration of the CRs on average (see Figure 6.7). This parallel momentum is transferred from the CRs to the background particles and the corresponding wave, as  $J_{\text{bg},\perp} \times B_{\perp} = -J_{\text{cr},\perp} \times B_{\perp}$  (which is obtained by taking the cross product of equation (6.27) with  $B_{\perp}$ ). These changes in momentum are directly coupled to the wave intensity, according to the momentum equation (6.8), and thus lead to wave growth.
- The graphical representation of this feedback loop in Figure 6.7 reveals that as the CRs try to align their perpendicular velocities with  $B_{\perp}$ ,  $B_{\perp}$  rotates away from them. CRs try to realign with the rotated  $B_{\perp}$ , which thus leads to a constant rotation of  $B_{\perp}$ . This is best

<sup>&</sup>lt;sup>3</sup>The drift for Alfvén waves is dominated by the polarization drift of the ions as the  $E \times B$  currents of ions and electrons exactly cancel each other. For whistlers, the guiding center approximation of the ions breaks down so that they can be considered to be immobile on this scale, leaving the electron  $E \times B$  drift.

#### 6. Growth and Saturation Mechanism of the Gyroresonant Instabilities

described as a frequency shift of the wave rotation rate by  $\omega \to \omega + \delta \omega$ , which represents a rotation in the resonance condition

$$\mathcal{R}(\omega + \delta\omega, k) = -\Omega_{\rm cr} + kv_{\rm dr} - (\omega + \delta\omega) = -\delta\omega, \tag{6.28}$$

as opposed to the expected resonance condition  $\mathcal{R}(\omega, k) = 0$  (see equation 6.11). For forward moving waves, we have  $\delta\omega < 0$ , which implies that the wave frequency is reduced and  $\omega + \delta\omega < \omega$ .

In Figure 6.7, we assumed that  $v_{\text{wave}}$  is aligned with the direction of  $B_0$ . Wave growth only occurs at k > 0 (according to our convention), but growth is not constrained by the direction of  $v_{\text{wave}}$ , which can be either positive or negative. Growth of backwards moving Alfvén waves is explained by simply mirroring the field vectors of Figure 6.7 about its vertical axis. When changing the sign of  $v_{\text{wave}}$ , the sign of  $\omega$  changes likewise. The direction of  $J_{\text{bg}}$ , which stems from the polarization drift (proportional to  $\omega$ ), thus changes sign as well. The drawing on the right-hand side of Figure 6.7 would then show the magnetic field  $B_{\perp}$  and  $J_{\text{bg}}$  preceding  $J_{\text{cr}}$ . This would lead to a parallel acceleration of CRs on average and (as the sign of the momentum equation switches likewise) wave growth of the backward moving wave. Similar to the forward moving wave, the wave rotation is counteracted as well, that is  $\delta\omega > 0$ . The growth of a backward moving wave can be observed in Figure 6.3, which shows that the particle drift velocity is growing over time, while the  $\varphi$  angle during growth is on average less than 0, as shown at  $t_3$  in the left panels of Figure 6.4. In the latter figure, it is instructive to directly compare the backwards moving wave of B with the forward moving wave of F, revealing the mirroring of the particles with respect to the field vector.

A corollary of these considerations is that the induced wave velocity,  $v_{\rm ind}$ , is always slower than the pristine wave velocity without CRs,  $v_{\rm prist}$ , irrespective of whether it propagates in the forward or backward direction. This can be seen by considering forward moving waves ( $\omega > 0$  and  $\delta\omega < 0$ ), which obey  $v_{\rm ind} = (\omega + \delta\omega)/k < \omega/k = v_{\rm prist}$ . For backward moving waves ( $\omega < 0$  and  $\delta\omega > 0$ ), we also have a slower moving induced wave as  $v_{\rm ind} = |\omega + \delta\omega|/k < |\omega/k| = v_{\rm prist}$ .

Wave damping, on the other hand, can occur in two ways in the picture presented here. First, if the particle rotation overtakes the perturbed wave rotation, and second, for wave modes at negative values of k. We will focus on the latter effect in this paragraph, while the former is discussed in Section 6.5.2. If there were a magnetic wave with k < 0, the CRs attempt to bunch up towards the perpendicular wave magnetic field at some initial time,  $B_{\text{init},\perp}$ . However, this bunching CR current will induce a magnetic field,  $k_{\parallel}B_{\text{ind},\perp} = \mu_0 J_{\text{cr},\perp}$ , which is oriented opposite to  $B_{\text{init},\perp}$ , thereby reducing the wave amplitude to approximately  $B_{\text{init},\perp} - B_{\text{ind},\perp}$ . Because the bunching efficiency depends on this field amplitude (which decreases over time), this describes a negative feedback loop and implies wave damping. Thus, only waves with k > 0 (according to the convention used here) can initially grow in our simulation, which includes forward and backward traveling waves ( $v_{\text{wave}} > 0$  and  $v_{\text{wave}} < 0$ ).

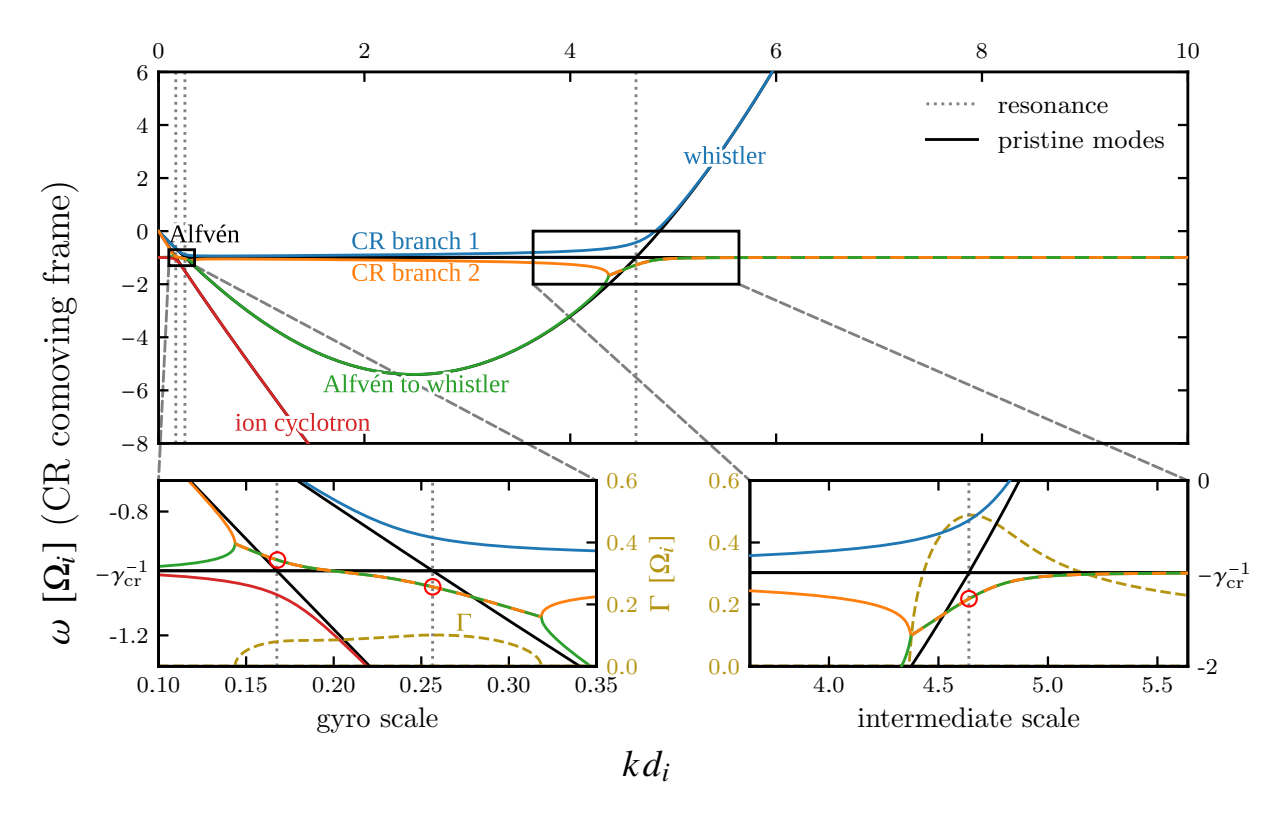


Figure 6.8. The solution of the dispersion relation (6.41) in the CR frame (see equation 6.29) using the parameters of the I simulation. Solid colored lines show the real frequency, while dashed colored lines show the growth rate of the wave modes. Solid black lines indicate the dispersion relation of the pristine background modes and CR ion-cyclotron waves without taking into account a mutual interaction. Black dotted vertical lines indicate the point of intersection of the black lines, i.e., the resonance condition  $\omega_{\text{wave}}/\Omega_i = -\gamma_{\text{cr}}^{-1}$ , at which we locally expect maximum growth. However, the interaction with CRs modifies the induced wave frequency by  $\delta\omega$ , as indicated by red circles, leading to a modification of the resonance condition ( $\omega_{\text{wave}} + \delta\omega$ )/ $\Omega_i = -\gamma_{\text{cr}}^{-1}$ . Please refer to Figure 6.15 for a representation of this solution in the background frame

### 6.4.2. Revisiting the dispersion relation

As argued in the preceding subsection, our model predicts that the induced wave velocity is slower than the pristine wave velocity without streaming CRs. In the following, we investigate whether this finding is also manifested in the dispersion relation. The dispersion relation is given in Appendix 6.D. We choose the parameters of the simulation I to visualize the solution of the dispersion relation, which includes the backward and forward moving Alfvén wave (which are not resolved in the simulation I) and the excited whistler wave from the intermediate-scale instability. This allows us to showcase all relevant instabilities, and the physical interpretations are transferable to the F&B simulations.

In Figure 6.8, we show the wave rotation rates as derived from the dispersion relation for a gyrotropic distribution of CRs, and evaluate them in the comoving CR frame where  $v_{\rm dr} = 0$  (i.e., not in the wave frame). Note that we show the same solution in the background frame in

Appendix 6.D for convenience. In the comoving frame, the resonance condition is given by

$$\mathcal{R}(\omega, k) = k v_{\rm dr} - \omega - \Omega_{\rm cr} = -\omega - \Omega_{\rm cr} = 0. \tag{6.29}$$

Indeed, this condition locates the waves with the maximum growth rate using the pristine rotation rate of the wave, i.e., without taking into account mutual interaction (see the vertical dotted lines in Figure 6.8).

However, there are more subtleties related to the interplay of the CRs with the background modes that go beyond this simplistic view. The color of an individual solution to the dispersion relation shown in Figure 6.8 describes a singly-connected branch that may or may not change character as it crosses a resonance. As we move from the left (small k values) to the right, we first see a degenerate branch (shown at small k values in red and green) which rotates at  $-\Omega_{\rm cr}$  in the frame comoving with CRs. These solutions can be interpreted as CR ion cyclotron wave modes (Shalaby et al., 2023). This solution splits up at  $kd_i \approx 0.1$  as a result of the interaction of CRs with the backward moving Alfvén wave. At  $kd_i \approx 0.14$  the upper CR ion cyclotron wave (green) interacts with the backward Alfvén wave (orange) so that the rotation rates exactly overlap, implying that their wave frequencies become degenerate. These degenerate waves complement each other, as their growth rates correspond to  $\pm\Gamma$  of which only the positive part is shown in gold in the zoom-in panels. This describes a transfer of energy from one degenerate wave mode to the other, which implies an instability. As this degenerate solution of CR-backward Alfvén waves approaches the scales of forward Alfvén wave (initially denoted in blue), there is again energy exchanged between CRs and the background that changes the character of this particular wave and causes it to turn into a faster-rotating CR ion-cyclotron wave (CR branch 1). At the same time, the degenerate solution splits up into a new forward moving Alfvén wave (green) and a slower rotating CR ion-cyclotron wave (orange, CR branch 2), which approaches the upper CR wave at even smaller scales (larger k values). We observe a similar behavior as we approach the resonance at the intermediate scale, where the interaction of CR ion cyclotron waves (blue and orange) with whistler waves (green) causes the rotation rates of the CR modes to deviate from each other so that the slower rotating CR mode (orange) overlaps with the modified whistler branch (green) and becomes degenerate, thus enabling the intermediate-scale instability. At smaller scales, the upper CR branch (blue) turns into a pure whistler wave.

Interestingly, a true degeneracy of a solution that either represents a CR ion cyclotron and a background branch or two CR branches only occurs provided the CR rotation rate is in between two (modified) background modes. This degeneracy gives rise to instability and is realized in between the forward and backward Alfvén modes for the CR streaming instability as well as in between the whistler and electron cyclotron modes for the intermediate-scale instability, see also Figure 6.1. Note that the growth rates are still maximized close to the resonances and significantly reduced in between the background modes, where the unstable solution represents two CR branches. This can also be seen in the lower left panel of Figure 6.8, where the pristine backward and forward moving Alfvén waves are shown in black, moving at  $-v_A$  and  $+v_A$ . Interactions with the CR branch modifies their rotation rates and causes unstable waves with speeds

in between this range,  $-v_A \lesssim v \lesssim +v_A$ . This enables wave growth at these smaller velocities, even at low CR densities. At scales larger than the ion skin depth, we often refer to these low-velocity CR-driven waves as Alfvén waves, which carries the connotation that they should propagate at  $\pm v_A$ , even though it would be more precise to characterize them as combined Alfvén-CR branch waves instead, as explained above.

We now focus on the fastest growing wave modes at resonance and its frequency shift  $\delta\omega$ . The resonances are marked by the vertical gray dotted lines, which intersect the dispersion relation at  $\delta\omega$ , as marked by a red circle. Indeed, we find that the frequency shift counteracts the wave speed, that is  $\delta\omega > 0$  for the backward moving wave (left-most resonance) while  $\delta\omega < 0$  for the two forward moving waves. This is in line with our model, which predicts that  $\delta\omega$  opposes the wave speed, and explains why the CRs bunch up on average at  $\varphi < 0$  for the backward moving wave and at  $\varphi > 0$  for the forward moving wave. Note that this has been found to be a necessary condition for instability. In conclusion, the unperturbed resonance condition can be used to estimate the wave number k with maximum growth. The actual observed resonance is perturbed by a small rotation rate, which is required for a positive feedback loop and, hence, for instability.

That is, for all unstable resonantly driven wave modes, the resonance is predicted by equating the isolated wave rotation and the Doppler-shifted CR ion-cyclotron wave mode  $\omega = kv_{\rm dr} - \Omega_{\rm cr}$  (Shalaby et al., 2023). However, the inclusion of CRs modifies the wave rotation rate  $\omega$  by  $\delta\omega$  at resonance. Therefore, the resonance condition is altered into  $\omega + \delta\omega = kv_{\rm dr} - \Omega_{\rm cr} = kv_{\parallel}(0) - \Omega_{\rm cr}$ , where the last equality only holds for the CR distribution we consider in this work and  $\delta\omega < 0$  (> 0) for forward (backward) propagating wave modes at resonance.  $\delta\omega$  is counteracting the propagation direction and therefore slowing the wave down, which changes the wave frame, as  $v_{\rm wave} = (\omega + \delta\omega)/k$ . That is, the CR velocity in the wave frame, which has been used in equation (6.17), can be transformed into the background frame via  $kv'_{\parallel}(t) = kv_{\parallel} - \omega - \delta\omega$ , and thus, equation (6.17) can be written as

$$\dot{\varphi}(t) = k\Delta v_{\parallel} - \delta \omega, \tag{6.30}$$

where we define  $\Delta v_{\parallel}(t) \equiv v_{\parallel}(t) - v_{\rm dr}(0)$ , and used the resonance condition to set  $kv_{\rm dr} - \omega - \Omega_{\rm cr} = 0$ .

#### 6.4.3. Simulated family of particle orbits

Figure 6.9 enables us to test our predictions for the linear growth regime. This figure compares various CR orbit parameters for the CR streaming instability, which excites forward moving Alfvén waves (top 4 panels), and the intermediate-scale instability at the whistler scale (bottom 4 panels). For each instability, we show (1) the gyrophases,  $\varphi(t)$ , of a representative sample of CRs in the wave frame, as well as the mean of a large random sample of CRs,  $\varphi_{\rm av}(t)$ , (2) the parallel CR velocity in the wave frame,  $v_{\parallel}(t)$ , as well as the mean of the large CR sample,  $v_{\parallel,\rm av}$ , (3) the time derivative of the CR gyrophase  $\dot{\varphi}(t)$ , and (4) the quantity  $\dot{\varphi} - k\Delta v_{\parallel}$ , which is a measure of the wave rotation rate relative to the CR frame. During linear growth (for  $t < t_3$ ), this analysis confirms our analytic predictions and supports the physics underlying the

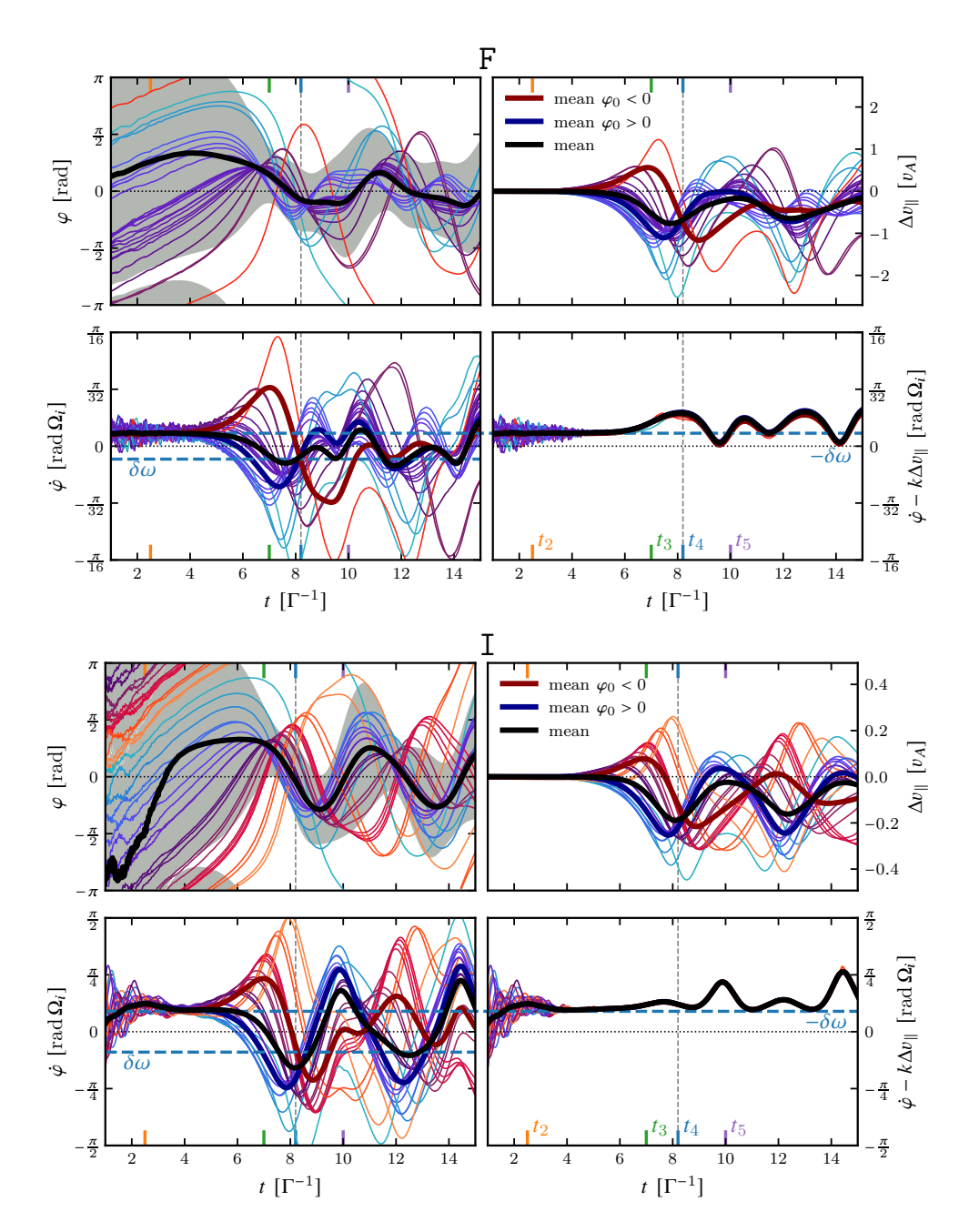


Figure 6.9. Simulated CR orbit parameters, which support our theoretical considerations regarding instability growth and the associated asymmetric bunching. We compare the cases of exciting forward propagating Alfvén waves (F, top 4 panels) and whistler waves via the intermediate-scale instability (I, bottom 4 panels). For each simulation, we show the evolution of  $\varphi(t)$ ,  $v_{\parallel}(t)$  in the wave frame, the time derivative  $\dot{\varphi}(t)$  and  $\dot{\varphi} - k\Delta v_{\parallel}$ , which is a measure of the wave rotation rate relative to the particle frame. Each panel shows multiple CR particles from a simulation with a single gyroresonant wave mode, mean values (thick black lines) and circular variance (gray band) are computed from 500 particles at random positions in the simulation box. The particle trajectories are colored from red to blue based on a gyrophase  $\varphi_0 = \varphi(t=6)$ , i.e., one e-fold before entering the nonlinear phase. Mean values for the different populations  $\varphi_0 > 0$  and  $\varphi_0 < 0$  are shown in corresponding colors. This analysis clearly demonstrates asymmetric CR bunching in  $\varphi > 0$  and confirms our theoretical picture that the CRs experience the unstable wave at relative rotation speed of  $\delta\omega \approx \omega_{\varphi} - kv_{\parallel}$  at resonance.

feedback loop described above. First, there is an anisotropy developing in the CR gyrophases with  $\varphi_{\rm av} > 0$ . Second, particles are accelerated along  $B_0$  such that there is a net momentum loss of CR ( $\Delta v_{\parallel,\rm av} < 0$ ). Third, the particles' angular velocity evolution is asymmetric for the subpopulations with  $\varphi_0 > 0$  and  $\varphi_0 < 0$ , respectively (where we select  $\varphi_0 = \varphi(t = 6\Gamma^{-1})$  towards the end of the linear growth phase for visualization purposes). Fourth, there is a universal, almost constant frequency shift  $\delta \omega$  observed due to the violation of the resonance condition.

We now detail the evolution of the CR gyrophases. The fact that the CRs' gyrophases are not randomly distributed but instead show a coherent bunching over time is due to the resonance between CRs and the wave. CRs with the same gyrophase  $\varphi_0$  develop similarly, and  $\varphi(t)$  of all particles shows a similar slope during the linear growth phase. To visualize the bunching of the CR gyrophases over time, we show the circular variance of  $\varphi(t)$  (multiplied by  $2\pi$ ) with a gray band that is centered on  $\varphi_{av}(t)$  (shown in black). The circular variance is also directly connected to the perpendicular CR current,  $J_{cr,\perp}$ , and the bunching in  $\varphi$  causes an increasing CR current. While the initial value of  $\varphi_{av}$  is noisy and physically irrelevant, it becomes decidedly positive for the forward moving waves as the particles bunch up towards  $\varphi_{av} > 0$ . After saturation, most particles oscillate around  $\varphi = 0$ , which indicates that these are trapped in the potential well. However, some CR trajectories observed in the plot swing over and take on more complicated trajectories.

In each of the two cases, the top right panels show that particles starting off at  $\varphi_0 < 0$  are accelerated in the parallel direction. Because this is aligned with the direction of the propagating wave, these CRs take momentum from the wave. The decelerating particles ( $\varphi_0 > 0$ ) are more numerous and thus, there is a net momentum gain by the wave at the expense of the CRs.

The bottom left panels show the time derivatives of the CR gyrophases, i.e., the instantaneous slopes of the CR trajectories shown in the top left panels. Once the wave mode starts to dominate the noise,  $\dot{\varphi}$  remains almost uniform in the linear phase, which corresponds to the similar slopes of  $\varphi(t)$  in the upper left panel. The similarity of the CR trajectories in the bottom left and top right panels shows that the particle acceleration term  $k\Delta v_{\parallel}$  dominates the evolution of  $\dot{\varphi}$  in equation (6.30).

We use equation (6.30) to estimate the resonance condition in the bottom right panel,

$$\mathcal{R}(\omega, k) = \dot{\varphi} - k\Delta v_{\parallel} = -\delta\omega$$
 at resonance. (6.31)

 $\delta\omega$  is the frequency shift introduced by the CRs, and the theoretically expected value obtained from the above dispersion relation is added as a dashed blue line in Figure 6.9. The theoretical expectations for  $\delta\omega$  are clearly very similar to the rotation rate in the resonance frame in the linear growth phase. In the nonlinear phase, the mean of  $\delta\omega$  also oscillates due to changes in wave velocity, that is,  $\delta\omega(t)$  is not constant in this phase. This is discussed further in Section 6.5.3. Deviations from the mean by individual particles are small, indicating that this is indeed a modification of the wave affecting all CRs at the same time. However, some individual deviations from the mean can be observed in F. These are due to the direct Lorentz-force term along  $v'_{\parallel} \times B_{\perp}$  acting on  $\psi_{\rm cr}$  which has been neglected initially, see equation (6.14). Due to the

		Satura	tion by scatte	Saturation by trapping (Eq. 6.36)									
Sim.	$v_{ m wave}$	$v_{ m lim}$	$\max(\Delta v_{ m dr})$	error	$\lim$ it	$\omega_{ m pend}$		$\omega_{ m pend}$		$\omega_{ m pend}$		error	limit
	$[v_{ m A}]$	$[v_{ m A}]$	$[v_{ m A}]$	[%]		$[\Omega_i]$		$[\Gamma]$		[%]			
						pred.	sim.	pred.	sim.				
В	-0.33	-0.611	0.303	50	X	0.079	0.076	1.364	1.312	3.8	$\checkmark$		
F	0.72	0.791	-0.798	0.9	$\checkmark$	0.100	0.083	1.562	1.297	17	X		
$I(I_W)$	4.73	4.783	-0.185	96	X	0.723	0.736	1.482	1.508	1.8	$\checkmark$		

Table 6.2. Mechanisms leading to saturation of resonant wave growth. To check whether wave growth is limited by CR scattering, we show wave velocities  $v_{\text{wave}}$  obtained by solving the dispersion relation, estimates for the scattering-limited velocity  $v_{\text{lim}} = v_{\text{dr}}(0) - \Omega_{\text{cr}}/k$ , and the maximum amplitude of  $\Delta v_{\text{dr}}$ . To check whether wave growth is limited by particle trapping, we show predicted (pred.) and simulated (sim.) pendulum frequencies. We compare the relative error of the theoretical saturation limits to the simulated quantities, which allows us to identify the exact saturation mechanism.

larger wave velocity and slower  $v_{\rm dr}$ ,  $v'_{\parallel}$  is significantly smaller in I compared to  $v'_{\parallel}$  in F, which is why these deviations from the mean are more visible in the latter simulation. Still, they are insignificant in comparison to the term  $k\Delta v'_{\parallel}$  and thus, the neglect of this effect is justified.

The nonlinear phase after  $t_3$  is discussed in the next section. Although the CR streaming and intermediate-scale instabilities in F and I act on very different spatial and temporal scales, the fundamental physical processes regulating wave growth are the same. While we omit a similar plot of B for brevity, the results are fundamentally similar, but qualitatively mirrored horizontally around 0.

# 6.5. Saturation of a single wave mode

During the linear growth phase, the CRs fall into the potential wells arising from the magnetic wave, see Figure 6.6. The nonlinear phase starts when an appreciable amount of CRs pass the minimum of the potential well and their acceleration direction reverses, that is roughly from  $t_3$  onward.

In this section, we discuss two wave saturation effects. First, we study wave damping as a result of CR scattering. Second, we scrutinize the effect of particle trapping by the waves on their growth. To this end, we determine the saturation time  $t_4$  of the instability when the majority of CRs has passed the potential minimum, which is defined as the reversal point of the growth of  $B_{\perp}$ , after which it starts to decline. This is followed by an analysis of the modification of the unstable waves as a result of CR feedback, and finally, we study the anisotropy introduced into the CR distribution function.

## 6.5.1. Saturation of wave growth due to CR scattering

We have previously established that, for CRs to impart momentum and energy to the waves, they must either accelerate (for backward-moving waves) or decelerate (for forward-moving waves) in the parallel direction. Here, we identify a limit on how much  $v_{\parallel}$  can change before the CRs

inadvertently begin to extract energy from the waves, thereby halting further wave growth. We built on the non-relativistic results from equation (6.21) (Otani, 1988) and assume that these results are transferable, as changes in the Lorentz factor  $\gamma$  are negligible within the scattering limit, which we will identify in the following. The rate of kinetic energy gain for a single CR along this constant of motion is given by

$$\frac{\partial E_{\rm cr}}{\partial t} = m_{\rm cr} \left( v_{\perp} \frac{\partial v_{\perp}}{\partial t} + v_{\parallel} \frac{\partial v_{\parallel}}{\partial t} \right) \approx \left( -\frac{\Omega_{\rm cr}}{k} + v_{\parallel} \right) \frac{\partial v_{\parallel}}{\partial t} 
\Longrightarrow \frac{\partial E_{\rm cr}}{\partial v_{\parallel}} \approx v_{\rm lim} + \Delta v_{\parallel}.$$
(6.32)

In the final step, we have adopted  $v_{\parallel}(t) = v_{\parallel}(0) + \Delta v_{\parallel}(t)$  and defined the limiting velocity  $v_{\text{lim}} = v_{\parallel}(0) - \Omega_{\text{cr}}/k \approx v_{\text{wave}}$ , which is approximately the wave velocity according to the resonance condition. Initially,  $\Delta v_{\parallel} \approx 0$  and equation (6.32) corresponds to  $\partial E_{\text{cr}}/\partial t \approx v_{\text{lim}}\partial v_{\parallel}/\partial t$ . This indicates that CRs can transfer energy to the waves if  $v_{\text{wave}} \approx v_{\text{lim}}$  and  $\partial v_{\parallel}/\partial t$  have opposite signs, such as when a CR decelerates in the presence of a forward-moving wave. However, once  $|\Delta v_{\parallel}|$  exceeds  $|v_{\text{lim}}|$ , the term  $v_{\text{lim}} + \Delta v_{\parallel}$  reverses sign, meaning that further deceleration of the CR would result in the extraction of energy from the forward-moving wave.

In essence, the maximum allowable change in  $v_{\parallel}$  for continued wave growth is constrained by the wave velocity, such that

$$|\Delta v_{\rm dr}| < |v_{\rm lim}| = |v_{\parallel}(0) - \Omega_{\rm cr}/k| \approx |v_{\rm wave}|.$$
 (6.33)

We examine this saturation mechanism in our simulations, and the results are presented in Table 6.2. This constraint is particularly stringent for Alfvén waves, when  $v_{\parallel} \gg v_{\rm wave}$ , and appears to be the reason for wave saturation in the simulation F. By contrast, this limit is essentially negligible for the intermediate-scale instability, where  $v_{\rm wave} \sim v_{\parallel}$ . The change in the total drift velocity should be bound by this scattering limit as well,  $\Delta v_{\rm dr} \leq v_{\rm lim}$ , which can be used to establish an upper bound for the maximum wave intensity through the momentum equation (6.8), assuming the wave speed remains constant:

$$\frac{\Delta B_{\perp}^2}{B_0^2} \le \frac{n_{\rm cr}}{n_{\rm bg}} \frac{\bar{y}v_{\rm wave}v_{\rm lim}}{v_{\Delta}^2} \approx \frac{n_{\rm cr}}{n_{\rm bg}},\tag{6.34}$$

where we adopted Alfvén waves in the last step,  $v_{\rm lim} \approx v_{\rm wave} = v_{\rm A}$ , and GeV CRs with  $\bar{\gamma} \approx 1$ . Clearly, this is an energetic limit for a single CR-wave interaction that may not impose a general limit for wave growth, provided the CR interacts with different waves on different scales after reaching this limit. In this case, the CR could be decelerated furthermore through a cascading process, and by virtue of energy conservation, cause corresponding wave growth of the interacting waves.

If CRs were scattered while exactly conserving their energy in the wave frame, this bound would not exist. However, our simulations suggest that CR scattering is better described by parabolic trajectories in the  $v_{\perp} - v_{\parallel}$  plane (Lemmerz in prep.), consistent with the constant of

motion C in equation (6.21) (Otani, 1988; Zachary et al., 1989), which leads to the emergence of this limit.

#### 6.5.2. Saturation of wave growth due to particle trapping

Here, we investigate Figure 6.9 with regard to the saturation time  $t_4$ , which is marked as a gray dashed line. At this time, the average  $\varphi$  reverses, switching from  $\varphi > 0$  to  $\varphi < 0$ , while  $\dot{\varphi}$  has reached a local minimum. As described beforehand, this reverses the overall acceleration direction and leads to more particles taking momentum from the wave, thus damping it according to the drawing of Figure 6.7. The perturbation of the wave frequency, which has been determined from the dispersion relationship beforehand, has been identified as the rate, with which the potential wells move in relation to the particles. Naturally, as the particles accelerate in parallel direction, they overtake the potential wells.

In the linear phase, the potential wells move away from the particles at a relative velocity of  $\delta\omega/k$ , as can be seen from the bottom-right panel in Figure 6.9. As a necessary condition, the particles need to move faster than the potential well to catch up. At  $t_4$  we observe that  $\dot{\varphi} \sim \delta\omega$ , and thus, using equation (6.30), the CRs move approximately twice as fast as the potential well with  $\Delta v_{\rm dr} \sim 2\delta\omega/k$ , where we adopted the mean over the particle distribution. Inserting this estimate for  $\Delta v_{\rm dr}$  into the momentum equation (6.8) yields a rough estimate for the saturation level of the magnetic wave field,

$$\frac{\Delta B_{\perp}^2}{B_0^2} \sim -\frac{n_{\rm cr}}{n_{\rm bg}} \frac{\bar{\gamma} v_{\rm wave}}{v_{\Delta}^2} \frac{2\delta\omega}{k}.$$
 (6.35)

This estimate is of the same order as the measured saturation level, e.g., for the I simulation we find that  $B_{\perp} = 0.0131B_0$  at saturation, while we predict  $B_{\perp} = 0.0076B_0$ .

Sudan and Ott (1971) proposed that the wave should saturate once the pendulum frequency, obtained from equation (6.18) for small angles of  $\varphi$ , is comparable to the growth rate:

$$\Gamma \sim \omega_{\rm pend} = \sqrt{\gamma k_{\rm res} d_i \frac{v_{\perp}}{v_{\rm A}} \frac{B_{\perp}}{B_0}} \Omega_{\rm cr}$$
 (6.36)

$$\Leftrightarrow \frac{B_{\perp}}{B_0} \sim (\gamma k_{\rm res} d_i)^{-1} \frac{v_{\rm A}}{v_{\perp}} \left(\frac{\Gamma}{\Omega_{\rm cr}}\right)^2. \tag{6.37}$$

Hence, the unstable wavelength at resonance as seen from a gyrating relativistic CR appears to be Lorentz contracted and – in tandem with the wave growth rate and  $v_{\perp}$  – determines the saturated magnetic wave field.

The pendulum frequency can be readily obtained from the oscillations of the magnetic field strength in Figure 6.3. We thus start by estimating the simulated pendulum frequency using a least-squares fit of the magnetic wave amplitude, while calculating the theoretical pendulum frequency using the mean  $v_{\perp}$  and  $B_{\perp}$  values from the simulation data after saturation  $(t > t_4)$ . The pendulum frequencies are given in Table 6.2. The excellent agreement of the simulated oscillations of the wave magnetic field and our theoretical estimates support our picture that

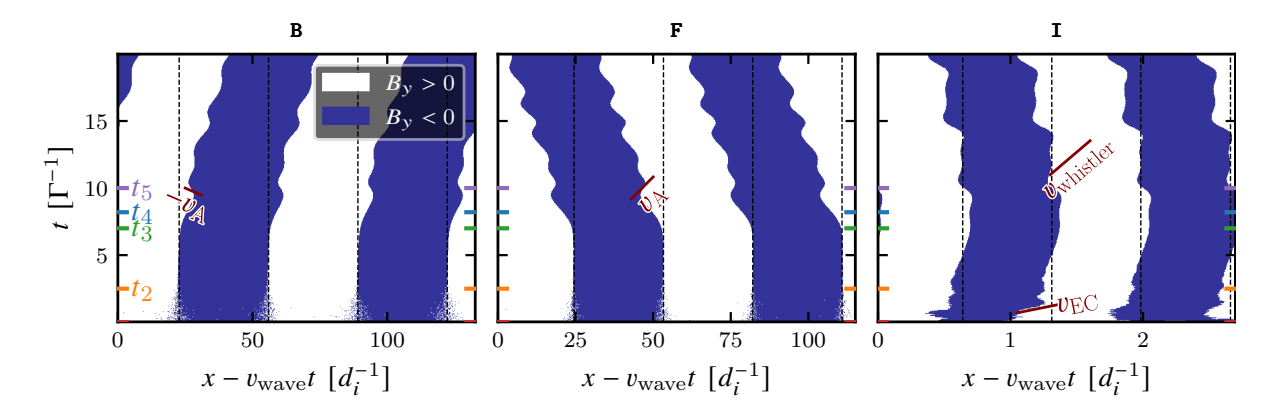


Figure 6.10. Visualization of the time evolution of the wave velocities of the resonant modes in the simulations B, F, and I. The x-axis of the plot is comoving with the wave at the speed  $v_{\text{wave}}$ , which is calculated from the dispersion relation at resonance while taking into account the CR perturbation:  $v_{\text{wave}}/v_{\text{A}} = [-0.33, 0.72, 4.73]$  from left to right (where we adopted the I<sub>W</sub> wave speed in the latter case). Dashed vertical lines indicate waves moving at this constant velocity. The slopes of the boundaries, where  $B_y$  changes sign, are a useful visual indication of the wave velocity. The wave velocity nearly approaches the pristine (unmodified) wave velocity in the nonlinear phase in the first two panels, i.e.,  $\mp v_{\text{A}}$ . The corresponding whistler and electron cyclotron velocities  $v_{\text{EC}}$  are indicated in the third panel. The times  $t_{1-5}$  are marked with their corresponding colors on the y-axis.

CRs collectively behave as a pendulum in the wave magnetic field. Upon closer inspection, the oscillation frequencies in the F&B simulations are not perfectly sinusoidal (Figure 6.3), as they have longer growth phases and shorter damping phases. In these simulations, a large number of particles approach the scattering limit described in Section 6.5.1, introducing further non-linearities. As a result, F saturates primarily through the scattering limit, although the pendulum effect remains clearly visible and the deviation from the pendulum limit is small. The relative influence of these saturation mechanisms depends on  $v_{\rm dr}, v_{\perp}$  and k and may vary with different parameters.

Next, we would like to scrutinize whether the growth rate  $\Gamma$  is comparable to  $\omega_{\rm pend}$  (equation 6.36). These ratios are given in the two rightmost columns of Table 6.2, and are similar enough to indicate that the oscillation frequencies of all gyroresonant instabilities at saturation are related to their growth rate, as predicted by equation (6.36). Parameter scans of different  $n_{\rm cr}/n_{\rm bg}$  for the forward moving Alfvén wave conducted by Zachary et al. (1989) and Holcomb and Spitkovsky (2019) also support our theory.

Although the growth rate of I is larger than that of F&B, this does not necessarily imply that the intermediate-scale instability also dominates at saturation. This is because it excites waves at a smaller scale (larger  $k_{\rm res}$ ) and thus saturates earlier, according to equation (6.37), leading to similar saturation levels between all of our simulations. Instabilities at even smaller scales, like the electron cyclotron wave  $I_{\rm E}$ , can have larger physical growth rates in comparison to the other instabilities, but the saturation level is still expected to be substantially lower. This is in particular the case for a large scale separation between the unstable scales of  $I_{\rm W}$  and  $I_{\rm E}$ , which is realized for small values of  $v_{\rm dr}/v_{\rm A}$  (Shalaby et al., 2021). If our simulations exactly resolved

the peak of  $I_E$ , we would expect a saturation rate of  $B_{\perp}/B_0 = 2.0 \times 10^{-4}$ , which is roughly 1/70 of the saturation level of  $I_W$ . However, because of our discrete sampling, we expect a reduced growth rate for  $I_E$  (as explained in Section 6.2.2) so that this instability does not significantly influence the I simulation.

## 6.5.3. Impact of CRs on the wave velocity

In this paragraph, we investigate the CR back-reaction on the unstable waves. In the linear phase, the unstable waves behave as predicted by the dispersion relation while the wave speeds in the nonlinear phase show a more complicated behavior. As the particles swing back and forth in the nonlinear wave magnetic field (see the bottom right panel of Figure 6.9), this oscillating CR current directly impacts wave propagation. These perturbations in  $\delta\omega$  over time indeed affect the wave velocity, which is shown in Figure 6.10. In all three cases after  $t_4$ , the absolute wave velocities slow down on average in comparison to their propagation speeds during linear growth.

The influence of CRs on the wave speed is substantially underestimated by adopting the formal definition of the Alfvén speed,  $v_{\rm A} = B_0/\sqrt{\mu_0 \sum_s m_s (n_s + n_{\rm cr})} \approx B_0/\sqrt{\mu_0 \sum_s m_s n_s}$  (for  $n_{\rm cr}/n_{\rm bg} \ll 1$ ), which weights CRs only by their comparably small mass density. This is because the equation for the Alfvén velocity assumes a plasma at rest. However, the current of CRs,  $J_{\rm cr,\perp}$ , is generated as a result of the magnetic bunching process, with an amplitude comparable to the background current,  $J_{\rm bg,\perp}$ . In consequence, the unstable waves in the F&B simulations propagate at  $-0.33v_{\rm A}$  and  $0.72v_{\rm A}$ , significantly slower than the unmodified Alfvén speed.

However, the unstable waves reach their corresponding (unmodified) Alfvén speeds at the rebound point  $t_5$  in the fully nonlinear phase. Hence, in order to estimate the saturation level of the instability, one would have to use the corresponding wave velocity in the momentum equation (6.8), i.e., the modified wave velocity. As the wave velocity is already varying before saturation, we would have to take into account those changes over time in the momentum equation, which is not trivial.

The case of the I simulation is even more complex. As the unstable  $I_E$  wave saturates shortly after  $t_2$ , there are several modes excited with wave velocities in between the  $I_W$  and the  $I_E$  modes (see Figure 6.10). After that time, there is a spectrum of waves close to the  $I_W$  resonance excited. The resulting combined wave field propagates at a velocity that is somewhat faster than expected for the purely growing  $I_W$  wave. In the saturated stage after  $t_4$ , this wave is considerably slowed down in response to the oscillating CR current.

#### 6.5.4. Evolving CR distribution

In the following, we examine changes to the CR distribution as a result of their wave-particle interactions. As the gyrophases of the CR ions generally follow the pendulum equation (6.18), their evolution mostly depends on the initial conditions  $\varphi_0$  and  $\dot{\varphi}_0$ . In Figure 6.9, we defined  $\varphi_0 = \varphi(t=6)$  shortly before the nonlinear phase, which is when  $\dot{\varphi}_0$  is still comparably small and thus negligible in the initial conditions. Because more particles have  $\varphi_0 > 0$  (which is the

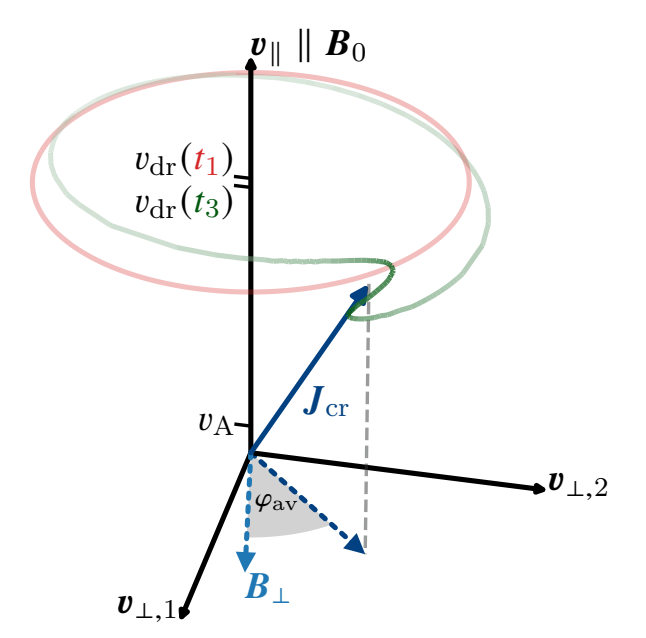


Figure 6.11 A visualization of the velocity space of simulation F. The CR ions have changed from their initial distribution at  $t_1$  (shown in red), to a bunched up, non-gyrotropic distribution at the onset of the nonlinear phase (at  $t_3$ , shown in green; denser areas are depicted by darker colors). All CR angles are measured in  $\varphi$  instead of  $\psi$ , which captures the natural anisotropy in the perpendicular plane introduced by the  $\boldsymbol{B}_{\perp}$ .

necessary condition for the instability to grow), these dominate the overall mean. A difference in the mean values of the  $\varphi_0 > 0$  and  $\varphi_0 < 0$  populations is indeed observed. Most notably, these swing out of phase with each other in the nonlinear regime, as expected from evolving pendulum with out-of-phase initial conditions.

Figure 6.11 shows the CR velocity distribution of F at the onset of the nonlinear phase  $t_3$ . At this time, most particles share a similar  $\varphi$  (as a result of the bunching), while the rotational velocity  $\dot{\varphi}$  is notably different. Particles with  $\varphi_0 < 0$  have been accelerated in parallel direction (i.e., their velocities depicted in green lie above their initial values, shown in red), while those with  $\varphi_0 > 0$  have a smaller  $v_{\parallel}$  in comparison to the initial gyrotropic ring distribution. Because particles are still accelerated by the magnetic field, this state is only quasi-stable – from  $t_3$  onwards, the particles oscillate around the wave magnetic field,  $\mathbf{B}_{\perp}$ . Therefore, they cyclically bunch up and spread out again, even though most particles stay roughly aligned with  $\mathbf{B}_{\perp}$ .

## 6.6. Conclusions

In this work, we studied the physics of streaming CRs in a background magnetic field and the associated excitation of plasma instabilities from first principles. We developed a theory of the underlying processes that organize the particles' orbits and in particular their gyrophases, which provides an intuitive physical picture of the growth, saturation, and back-reaction onto the plasma waves excited via CR-driven instabilities. However, for transparency, we restrict ourselves to single unstable modes. Starting from a gyrotropic setup of CRs, which embraces the symmetry of a magnetized plasma, we find that resonantly driven electromagnetic waves introduce an additional asymmetry perpendicular to the background magnetic field. As a result, a new stable equilibrium state emerges as the gyrophase of the CR ions follows this asymmetry to locally match the phase of the driven waves.

Based on our simulation results and theoretical considerations, our new theory for the growth

of individual unstable waves driven by CRs contains the following elements.

- Wave growth resulting from an instability necessitates k > 0, but occurs independent of the wave propagation direction. Fast moving CRs with  $v_{\parallel} > v_{\rm A}$  can excite forward and backward-propagating transverse waves, e.g., Alfvén waves (as measured in the background frame).
- The unstable waves cause the CRs to bunch up in gyrophase through parallel Lorentz forces. In result, the CR distribution develops a lopsided gyrophase with respect to the local wave magnetic field. In other words, the helical wave magnetic field is joined by a helical CR distribution (i.e., a CR ion cyclotron wave) that exhibits the exact same winding angle as the unstable wave. This lopsidedness is key for enabling momentum transfer from the CRs to the wave and thus, for instability.
- CRs are scattered asymmetrically parallel to the background magnetic field, preferentially but not exclusively in the direction opposite to that of the propagating waves. This is a secular scattering process dictated by the direction of the parallel Lorentz force and not a diffusive scattering process.
- CRs modify the wave velocity, which is always slower (in absolute terms) than the wave velocity without CRs. This effect is especially pronounced for induced Alfvén waves, which propagate at speeds significantly less in magnitude than  $v_A$ .
- The instability saturates once the majority of CRs become fast enough to overtake the unstable wave, which propagates at the CR-modified wave speed. In consequence, the wave is slowed down by the faster CRs, which implies wave damping and hence saturation of the instability. Additionally, we identified another possible saturation mechanism for the interaction of a CR with a single wave: if the CRs' parallel velocity is decelerated by approximately the velocity of the scattering (forward moving) wave, it reaches an energetic minimum. Further deceleration through scattering requires energy from the wave, and accordingly, the maximum wave intensity is limited by this energetic minimum. An analogous argument applies for backward moving waves, in which case further acceleration of CRs through scattering requires energy from the wave, and thus limits wave growth.
- The motion of the trapped CRs in the potential provided by the local wave magnetic field can be described by a pendulum equation. In this picture, linear wave growth of the instability results from the CR approaching the local wave magnetic field. As CRs overshoot the equilibrium position of an exact alignment of CRs and the local wave field, the instability saturates. The nonlinear behavior of the instability is then characterized by an oscillating CR distribution in the potential associated with the parallel Lorentz force, which is centered on the local wave field. This oscillating CR distribution generates perpendicular CR currents, which also cause the wave amplitude to oscillate and to further slow down.

Additionally, we find that the three main instabilities, which describe resonant interactions of streaming CRs with forward and backward traveling Alfvén waves, as well as with whistler waves via the intermediate-scale instability saturate via the exact same mechanism and to similar amplitudes in our setup.

In this work, we did not fully explore the relative importance of these three instabilities and instead concentrated on studying their underlying physics while adopting the simplest possible configuration for transparency. Thus, this paper is meant to provide a starting point for future research. Of prime importance will be the study of the differences of the CR-wave scattering for these various instabilities as this directly impacts the effective CR transport speed and momentum transferred by the CRs to the background plasma. Second, we need to extend the theory developed here for the growth of isolated wave modes to include wave-wave interactions of the unstable modes of the forward and backwards Alfvén and whistler branches, which could yield a modification of the criterion for instability saturation. Third, a necessary extension of this work would also be to generalize the initial gyrotropic ring distribution of CRs to a more natural power-law momentum distribution exhibiting all CR pitch angles.

While wave growth induced by a power-law momentum distribution of CRs is expected to be different from that of single wave modes, we believe that some of our main results such as CRs bunching up in gyrophase as a requirement for driving the instability by means of this anisotropy will carry over. Regardless, the results shown here indicate that some of the general assumptions commonly applied to CR transport based on quasi-linear theory could be violated. This includes the random phase approximation, as the gyrophase of CRs is potentially strongly correlated with the driven waves. Furthermore, our results indicate that the saturation level may not be estimated from the momentum equation (6.8) by assuming that  $v_{\rm dr}$  asymptotically converges to  $v_{\rm A}$  as it isotropizes in the frame of the forward moving Alfvén wave. Instead, the growth of different, potentially important wave modes with temporally changing wave velocities makes estimates using the momentum equation difficult and could identify the erroneous isotropization frame. Running physically motivated simulations requires great care, as the results can radically differ according to the box size or mass ratio, as shown by the simulations presented here, which are opening the door for a rich avenue of future research towards more complicated setups involving multiple wave modes, background inhomogeneities or power-law distributed CRs. While the analysis we performed here is only valid for the simplified case of a single CR pitch angle and energy, there is observational evidence of phase bunching in the solar wind ahead of the Earth's bowshock (Gurgiolo et al., 1981; Eastman et al., 1981; Thomsen et al., 1985). This suggests, that the main results discussed in this work may carry over to the more general case of CRs propagating in the galaxy.

# **Appendix**

#### 6.A. Conventions

It is convenient to use a definition of vectors, which naturally reproduces the symmetry of the problem. To this end, we align the x coordinate of our coordinate system with the background magnetic field  $\mathbf{B}_0$  and denote parallel vector components as  $\mathbf{b}_{\parallel} = b_x \mathbf{e}_x$ , where  $\hat{\mathbf{e}}_x$  denotes the unit vector. We express the perpendicular plane in complex notation: adopting  $\hat{\mathbf{e}}_{\perp} \equiv \hat{\mathbf{e}}_y$  and  $\mathrm{i}\,\hat{\mathbf{e}}_{\perp} \equiv \hat{\mathbf{e}}_z$  results in  $\mathbf{a}_{\perp} = (a_y + \mathrm{i}\,a_z)\hat{\mathbf{e}}_{\perp}$ . The following identity follows:

$$\boldsymbol{b}_{\parallel} \times \boldsymbol{a}_{\perp} = -b_{x} a_{z} \hat{\boldsymbol{e}}_{y} + b_{x} a_{y} \hat{\boldsymbol{e}}_{z} = b_{\parallel} \mathrm{i} \, \boldsymbol{a}_{\perp}. \tag{6.38}$$

Ions will experience a Lorentz force

$$\mathbf{F} = q\mathbf{v}_{\perp} \times \mathbf{B}_{\parallel} = -\mathrm{i}\,qB_0\mathbf{v}_{\perp} \tag{6.39}$$

around the mean field, which causes a gyration with  $\mathbf{v}_{\perp} = v_{\perp} \hat{\mathbf{e}}_{\perp} \exp(-\mathrm{i}\Omega_{i}t)$ .

Transverse waves evolve in the perpendicular plane like  $\exp\{i \left[(\omega - i\Gamma)t - k_{\parallel}x\right]\}\boldsymbol{e}_{\perp}$ , where  $\omega$  and  $\Gamma$  denote the wave rotation frequency and growth rate, respectively. According to this definition, waves with a positive  $k_{\parallel}$  have a left-handed helicity for increasing x. Furthermore, the sign of  $\omega$  indicates the polarization of the wave:  $\omega > 0$  corresponds to a right-handed wave while  $\omega < 0$  corresponds to a left-handed wave. The phase velocity of the wave,  $v_{\text{wave}} = \omega/k$ , must be invariant regardless of the convention and its sign indicates the direction of movement.

For reference, we compare our definition to another popular definition (Stix, 1992; Bai et al., 2019). In the following, we denote quantities defined in that convention with tilde symbols. In this definition,  $\tilde{\omega}$  is set to be always positive and our definition is recovered by setting  $\omega = \pm \tilde{\omega}$ , depending on the polarization of a wave. In their convection, the wave polarization cannot be inferred solely from  $\tilde{\omega}$  but needs to be explicitly specified, i.e., right-handed (left-handed) polarized waves are corotating with the electrons (ions) and are denoted by  $\exp\left[i\left(\pm \tilde{\omega}t - k_{\parallel}x\right)\right]e_{\perp}$ . Likewise, the definition of the wave velocity depends on the wave polarization:  $\tilde{v}_{\text{wave}} = \pm \tilde{\omega}/\tilde{k}$ , where the plus (minus) sign corresponds to a right-handed (left-handed) wave. Despite the difference in notation, both definitions for the wave velocity coincide,  $v_{\text{wave}} = \tilde{v}_{\text{wave}}$ , because it denotes the observable physical propagation direction of the wave.

### 6.B. Comparison of fluid-PIC and PIC methods

The simulations in this paper have been performed using the new fluid-PIC method (Lemmerz et al., 2024b). Here, we compare the I simulation obtained from this method with the traditional and well-tested PIC method using the SHARP code (Shalaby et al., 2017b, 2021). We use the same parameters as defined in Section 6.2.2, with the only exception that we use only 25 computational particles per cell for the CR species and  $2.5 \times 10^5$  particles per cell for the background species in the PIC simulations, in contrast to 75 particles per cell used in the fluid-PIC simulations. Because the fluid-PIC method does not have to follow particles of the

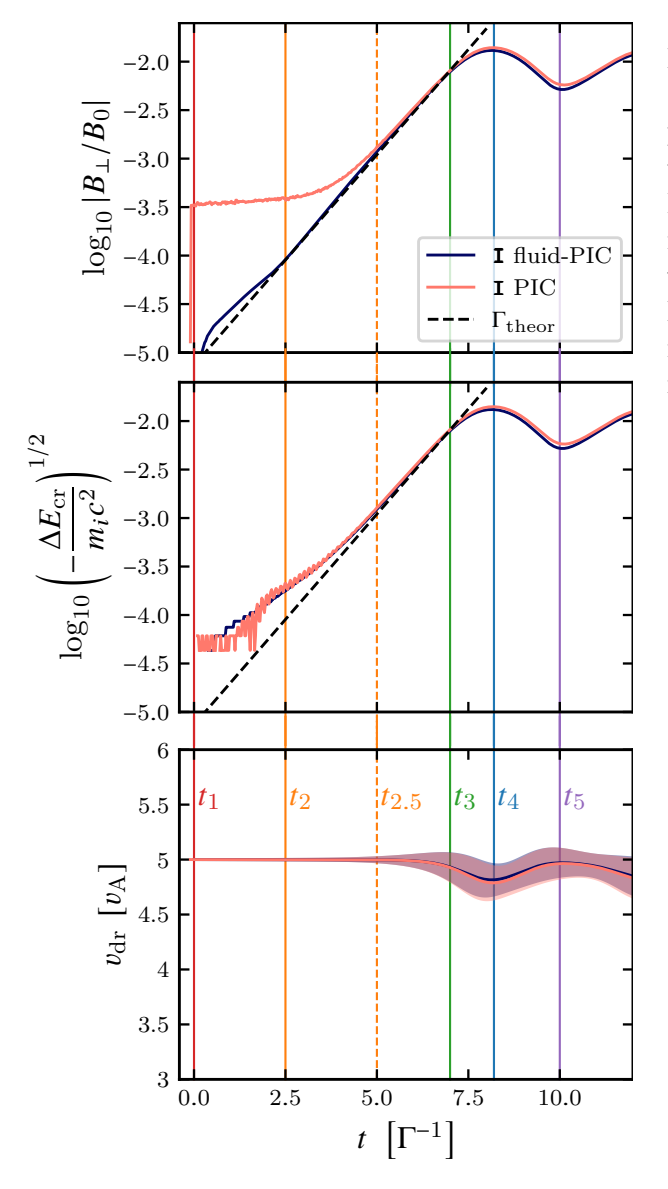


Figure 6.12 Same as Figure 6.3, but comparing I simulations performed using the fluid-PIC and pure PIC method. Both results are almost identical, except for the increased noise floor in the PIC simulation at early times. Due to the differences in the noise level, the time marker  $t_2$ , which initially denoted the linear growth phase, has been moved to a later time,  $t_{2.5}$ , to enable a fair comparison between the PIC and fluid-PIC methods in the linear growth regime.

background species, it is more computationally efficient.

The results for wave growth are shown in Figure 6.12, which compares the growth of the unstable wave magnetic field as a result of the intermediate-scale instability (top panel), the energy loss experienced by the CRs in exciting this modified whistler wave (middle panel), and the mean drift speed of the CR population (bottom panel). Overall, both simulations produce nearly identical results except for the perpendicular magnetic field at early times, which shows an obvious difference in the noise floor of the simulations. This could be lowered in the PIC simulation by increasing the computational particles per cell, at the expense of becoming more computationally expensive.

In Figure 6.13, we compare the CR phases  $\psi_{\rm cr}$  and magnetic field angles  $\psi_B$  for both simulations. We can identify all important characteristics in both simulations: wave growth and the emergence of a helical magnetic field structure at  $t_{2.5}$ , asymmetric bunching of particles at  $t_3$ , saturation through particles oscillating at around  $B_{\perp}$  at  $t_4$ , and the back-swing as well as the "ghost" strip at  $t_5$ . Because waves in both boxes grow from different realizations, the

#### 6. Growth and Saturation Mechanism of the Gyroresonant Instabilities

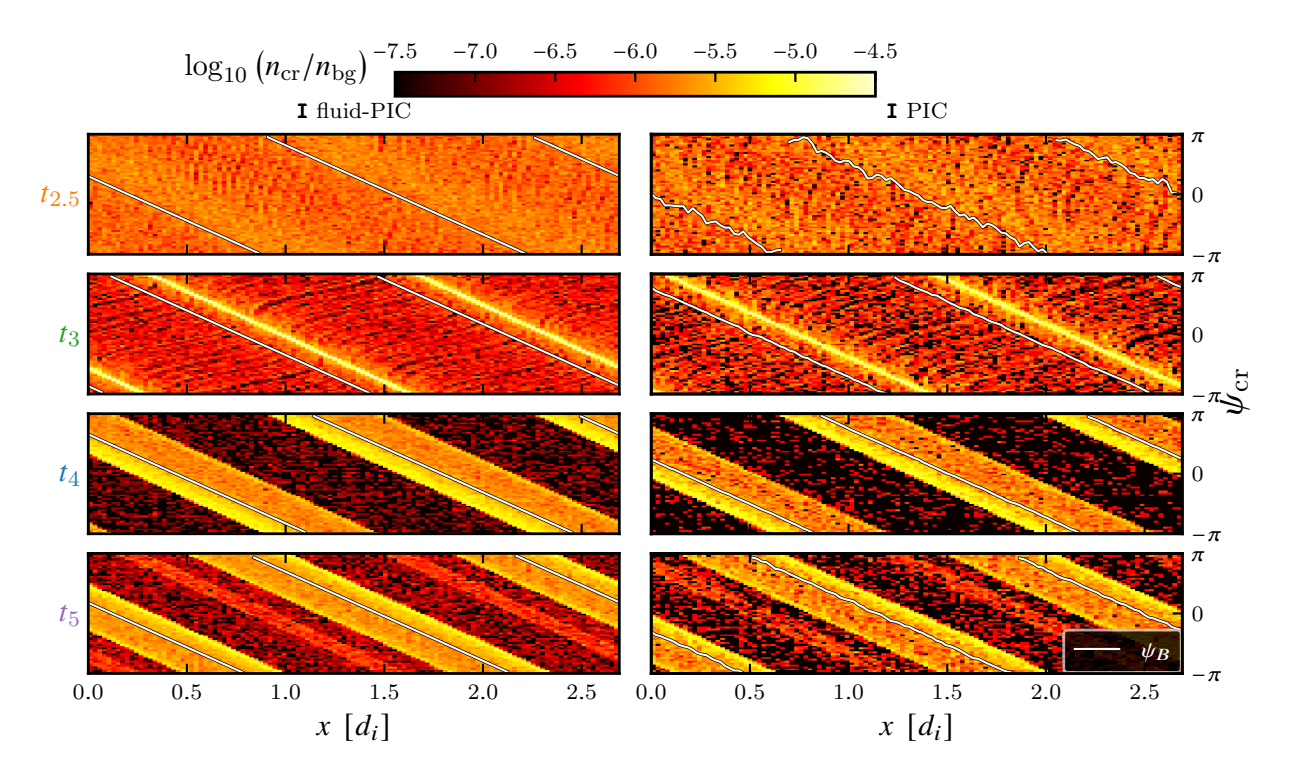


Figure 6.13. Same as Figure 6.4, but comparing I simulations performed using the fluid-PIC (left panels) and pure PIC (right panels) methods.  $t_{2.5}$  is used instead of  $t_2$  to ensure a fair comparison between the two methods because of the increased electromagnetic noise floor in the PIC simulation at earlier times, see Figure 6.12. The CRs at time  $t_{2.5}$  show more structure compared to  $t_2$  used in Figure 6.4 as a result of the larger magnetic wave intensity.

specific  $\psi$  values are not expected to match in between different simulations, i.e., an offset in the phases of the waves is expected. As discussed before, the PIC results are noisier due to the smaller number of CR particles per cell. This also influences the wave magnetic field in the PIC simulation, which does not appear as straight white lines but instead shows wiggles as a consequence of small-scale noise generated by the shot noise of the finite CR and background particle number. Notwithstanding this minor difference, the physical effects described in this paper agree to high precision between both simulations and are thus independent of the choice of the numerical methods used.

#### 6.C. Robustness of initial setup

To enforce the quasi-neutrality assumption and to suppress initial parallel currents, we initialize a parallel electron beam with the same  $v_{\rm dr}$  as the CR ion beam. To check whether this particular setup for the neutralizing electrons impacts our results, we also tested alternative initial conditions. Instead of using a CR electron beam, the background electrons are adjusted to cancel the current from the CR ions. We set the background electron density to  $n_{\rm e} = n_{\rm i} + n_{\rm cr}$  and their bulk flow velocity to  $(nw)_{\rm e} = (nv_{\rm dr})_{\rm cr}$ . In Fig. 6.14 we compare both setups for all of the simulations carried out in this paper, where we use the same initial seed of CR ions. The method for enforcing neutrality does not have any noticeable impact on our results; indeed, the growth and

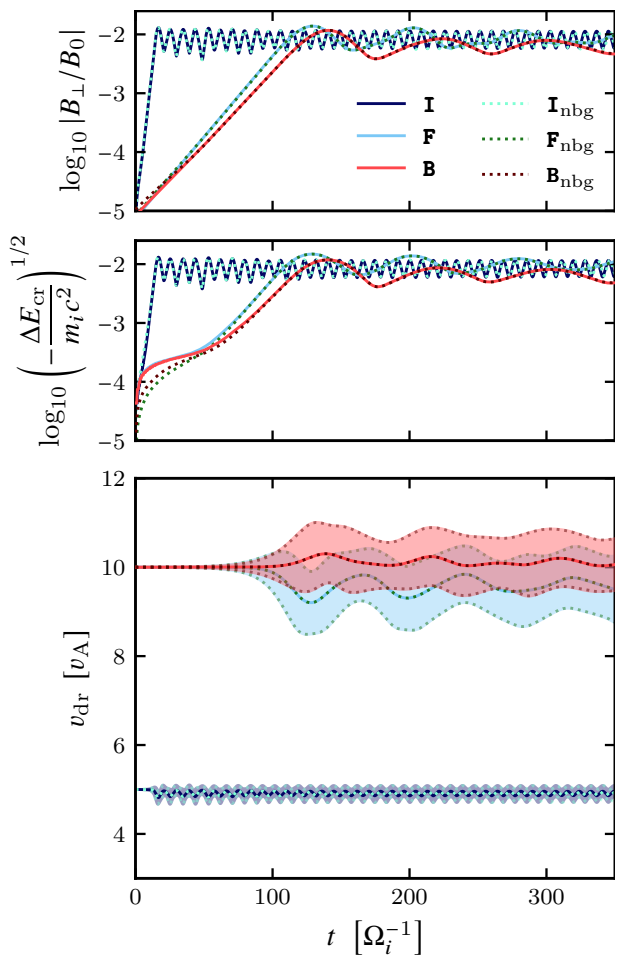


Figure 6.14 Comparison between two methods of neutralizing the CR ion beam. The first method uses a CR electron beam (simulation identifiers without subscript) while the second uses a slowly moving background electron distribution (simulation identifiers with subscript nbg). We show the evolution of the same quantities as shown in Fig. 6.3, demonstrating excellent agreement between both setups. Conclusively, both neutralizing methods may be used interchangeably for the CR streaming setup.

non-linear phase are practically indistinguishable in the simulations. Intuitively, the excellent agreement between both setups can be understood by comparing the relevance of the electron and ion beams. Even in simulations F&B with a reduced mass ratio of  $m_i/m_e = 100$ , the energy density of the electron beam is less than 1% of the CR ion beam's and is roughly equivalent to the magnetic wave energy density at saturation. Given that only a small fraction of the electron beam's kinetic energy is likely converted to wave energy — similar to the CR ion beam — it has negligible impact on the instability's evolution. Instead, its primary function is to compensate the current, a role fulfilled equally by the moving background electrons. Only during very early times a minor difference between the setups is noticeable, here the neutralizing background electrons introduce less noise in the CR ion population. There is another, more tangible advantage of using the neutralizing background setup: The amount of computational particles is halved, as no electron beam particles are included in the simulation. This decreases the computational cost substantially when using the fluid-PIC method, since increasing the density of the background electrons does not add any computational cost.

#### 6. Growth and Saturation Mechanism of the Gyroresonant Instabilities

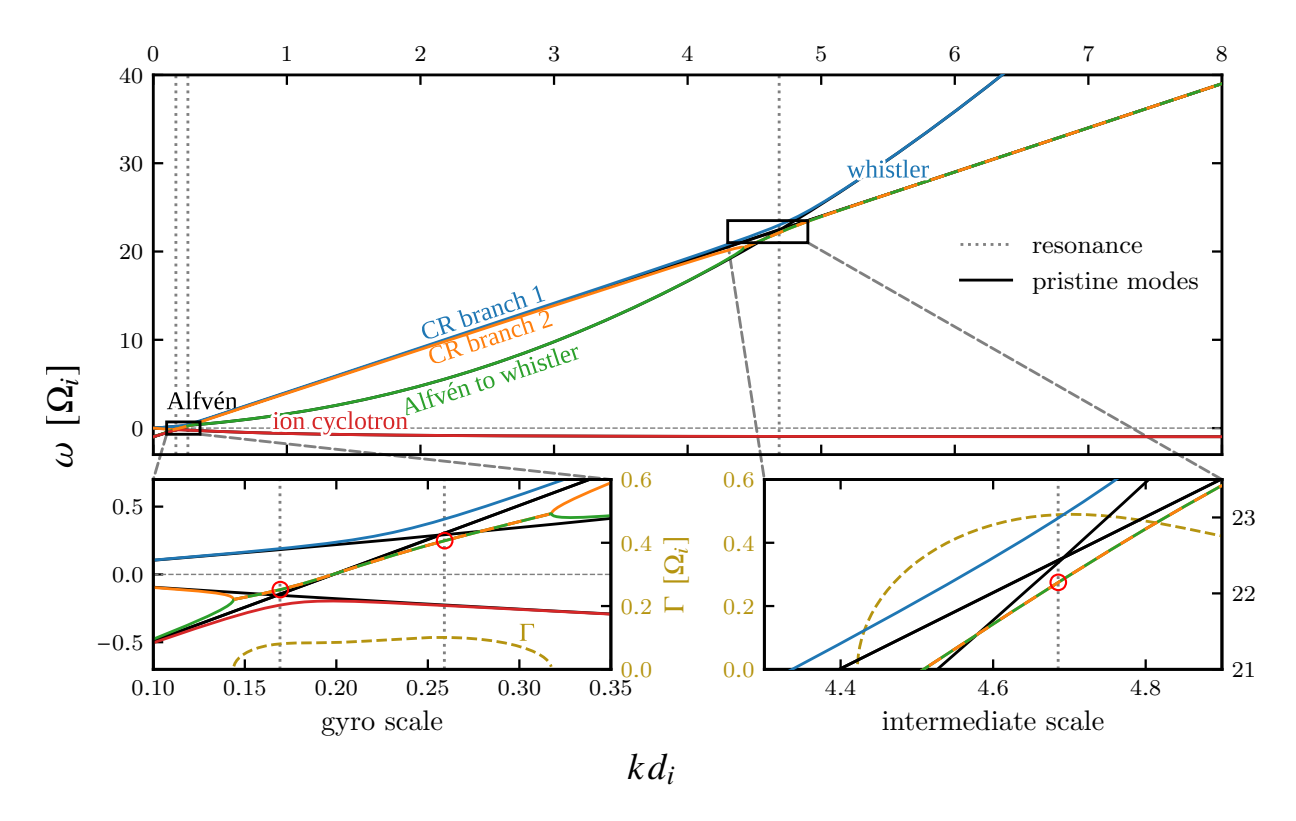


Figure 6.15. The solution of the dispersion relation (6.42) in the background frame using the parameters of the I simulation. Solid colored lines show the real frequency, while dashed colored lines show the growth rate of the wave modes. Solid black lines indicate the dispersion relation of the pristine background modes and CR ion-cyclotron waves without taking into account a mutual interaction. Black dotted vertical lines indicate the point of intersection of the black lines, i.e., the resonance condition  $\omega_{\text{wave}} = k v_{\text{dr}} - \Omega_{\text{cr}}$ , at which we locally expect maximum growth. However, the interaction with CRs modifies the induced wave frequency by  $\delta \omega$ , as indicated by red circles, leading to a modification of the resonance condition  $\omega_{\text{wave}} + \delta \omega = k v_{\text{dr}} - \Omega_{\text{cr}}$ . Please refer to Figure 6.8 for a representation of this solution in the comoving CR frame.

#### 6.D. Dispersion Relation

#### **Equations**

We use the plasma dispersion function for transverse waves with a gyrotropic ring distribution (e.g. Wu and Davidson, 1972; Shalaby et al., 2023)

$$\zeta_{s}(v_{\mathrm{dr},s}, v_{\perp,s}, n_{s}) = \frac{\omega_{s}^{2}}{\gamma_{s}} \left[ \frac{\omega - k v_{\mathrm{dr},s}}{k v_{\mathrm{dr},s} - \omega - \Omega_{s}} - \frac{v_{\perp,s} c^{-2} \left(k^{2} c^{2} - \omega^{2}\right)}{2 \left(k v_{\mathrm{dr},s} - \omega - \Omega_{s}\right)^{2}} \right].$$
(6.40)

Here,  $\omega_s = \omega_s(n_s) = \sqrt{n_s q_s^2/(m_s \epsilon_0)}$  is the plasma frequency of a species s and  $\Omega_s$  is the relativistic cyclotron frequency for a particle of that species in the corresponding frame. To obtain  $\omega(k)$  in the frame comoving with the CRs, the following equation is solved numerically, and we account

for the background species, CR ions and the neutralizing CR electron beam:

$$\omega_{\text{comoving}}^{2} - k^{2}c^{2} + \zeta_{e}(-v_{\text{dr}}, 0, n_{\text{bg}}) + \zeta_{i}(-v_{\text{dr}}, 0, n_{\text{bg}}) + \zeta_{e,\text{cr}}(0, 0, n_{\text{cr}}) + \zeta_{i,\text{cr}}(0, v_{\perp,\text{cr}}, n_{\text{cr}}) = 0.$$
(6.41)

Wave speed estimates in the background frame are retrieved from the following equation:

$$\omega_{\text{bg}}^{2} - k^{2}c^{2} + \zeta_{\text{e}}(0, 0, n_{\text{bg}}) + \zeta_{\text{i}}(0, 0, n_{\text{bg}}) + \zeta_{\text{e,cr}}(v_{\text{dr}}, 0, n_{\text{cr}}) + \zeta_{\text{i,cr}}(v_{\text{dr}}, v_{\perp, \text{cr}}, n_{\text{cr}}) = 0.$$
(6.42)

The pristine modes are recovered by solving these equations in the limit of  $n_{\rm cr}/n_{\rm bg} \to 0$ .

#### Dispersion relation in the background frame

In Figure 6.15, we show the solution of the dispersion relation (6.42) in the background frame using the parameters of the I simulation. This solution in the background frame shows the familiar behavior of the dispersion relation of the background modes, i.e., the backward and forward moving Alfvén wave ( $\omega \approx \pm kv_A$ ) and the parallel whistler wave ( $\omega \approx k^2 d_e^2 \Omega_e$ , where the electron skin depth is  $d_e = c/\omega_e$  and the electron cyclotron frequency is  $\Omega_e = qB_0/m_e$ ). In this frame, the changes of the character of a wave from pure background modes to degenerate CR-background modes due to CR-wave interactions are less obvious in comparison to the presentation in the comoving CR frame (Figure 6.8).

Chapter 6 examined the fundamental commonalities between the gyroresonant streaming instabilities. This Chapter focuses on their differences, with a particular emphasis on refining the criteria for resonance and comparing their growth rates to evaluate their relative significance in CR interactions.

Our analysis employs the gyrotropic ring distribution to isolate CR populations with specific pitch angles, allowing us to identify fundamental mechanisms that may extend to more complex distributions. The transverse dispersion relation for CRs distributed as a gyrotropic ring, with background ions and current-compensating background electrons is (Wu and Davidson, 1972; Shalaby et al., 2023, and Section 6.D)

$$1 - \frac{k^2 c^2}{\omega^2} + P_{e,\text{bg}}^{\pm}(v_{\text{dr}} n_{\text{cr}} / n_{\text{bg}}, 0, n_{\text{bg}}) + P_{i,\text{bg}}^{\pm}(0, 0, n_{\text{bg}}) + P_{i,\text{cr}}^{\pm}(v_{\text{dr}}, v_{\perp,\text{cr}}, n_{\text{cr}}) = 0,$$

$$(7.1)$$

where

$$P_s^{\pm}(v_{\text{dr},s}, v_{\perp,s}, n_s) = \frac{\omega_s^2}{\omega^2 \gamma_s} \left[ \frac{\omega - k v_{\text{dr},s}}{k v_{\text{dr},s} - \omega \pm \Omega_s} - \frac{v_{\perp,s} c^{-2} \left( k^2 c^2 - \omega^2 \right)}{2 \left( k v_{\text{dr},s} - \omega \pm \Omega_s \right)^2} \right]. \tag{7.2}$$

We employ the equation with "-", where  $\omega > 0$  corresponds to right-hand polarized waves and  $\omega < 0$  corresponds to left-hand polarized waves. This maintains generality, as we allow for positive and negative values of  $\omega$  and k (Weidl et al., 2019a). Analytical solutions to equation (7.1) are challenging to obtain in their complete form. However, we can derive accurate approximations by exploiting the scale separation of the relevant instabilities and focusing on the dominant species interactions at each scale.

We denote  $\Omega_{\rm cr} = \Omega_i/\gamma = qB_0/(\gamma m_i)$ , where  $\gamma$  is the Lorentz factor of CR ions. For our analytical derivations, we assume that  $v_{\rm dr} n_{\rm cr}/n_{\rm bg} \approx 0$  in equation (7.1).

## 7.1. Constraints on Resonance with Forward Moving Waves

#### 7.1.1. Electron-scale Effects

In the ideal MHD limit, forward-propagating Alfvén waves possess a phase velocity equal to the Alfvén speed  $v_A$ . This sets a minimal threshold for CR resonance, requiring parallel velocities  $v_{\parallel} > v_A$ . However, this criterion becomes insufficient when considering plasma dynamics beyond

MHD. As illustrated in Fig. 6.1, resonances arise from the intersection the Doppler-shifted CR gyration frequency with the wave dispersion curves, which are not linear in k in the multi-fluid description. The forward wave mode exhibits a continuous transition from the Alfvénic into the whistler regime, accompanied by an increase in phase velocity. Therefore, the resonance condition necessitates a modified lower bound for  $v_{\parallel}$  that accounts for this dispersive behavior.

In the transition region between forward-moving Alfvén and whistler waves, we reduce the dispersion relation of the background distribution in the limit of  $|\omega| \ll |\Omega_e|$  and thereby also drop the constant of unity that describes the displacement current (which is only important at high frequencies)

$$0 = 1 - \frac{c^2 k^2}{\omega^2} + \frac{\omega_e^2}{\omega (-\omega - \Omega_e)} + \frac{\omega_i^2}{\omega (-\omega - \Omega_i)}$$

$$\approx -\frac{c^2 k^2}{\omega^2} - \frac{\omega_e^2}{\omega \Omega_e} - \frac{\omega_i^2}{\omega (\omega + \Omega_i)}$$
(7.3)

$$\Leftrightarrow 0 = d_i^2 k^2 + \omega \frac{\omega_e^2}{\omega_i^2 \Omega_e} + \frac{\omega}{(\omega + \Omega_i)}$$

$$(7.4)$$

$$\Leftrightarrow 0 = (\omega + \Omega_i)\Omega_i d_i^2 k^2 - \omega^2, \tag{7.5}$$

where we multiplied by  $\Omega_i(\omega - \Omega_i)$  to arrive at the last equation. Using the identity  $\Omega_i d_i = v_A$  yields the dispersion relation

$$\omega = kv_{\mathcal{A}} \frac{kd_i \pm \sqrt{(kd_i)^2 + 4}}{2},\tag{7.6}$$

where the "+" sign corresponds to the forward and the "-" sign to the backward moving waves. The expression for forward moving waves captures both Alfvén waves  $(kd_i \ll 1)$ , and the characteristic  $k^2$ -dependence of whistler waves  $(kd_i \gg 1)$ .

Therefore, the resonance condition (equation 2.21) with the forward moving waves is

$$kv_{\parallel} - \Omega_{\rm cr} = \omega = kv_{\rm A} \frac{kd_i \pm \sqrt{(kd_i)^2 + 4}}{2}$$

$$\frac{v_{\parallel}}{v_{\rm A}} - \frac{1}{\gamma kd_i} = \frac{kd_i + \sqrt{(kd_i)^2 + 4}}{2}.$$
(7.7)

In the following, we aim to identify the smallest value of  $v_{\parallel}$  that allows gyroresonance with the waves. We denote  $\hat{k} = (kd_i)_{\min}$  as the spatial scale resonant with this value of  $v_{\parallel}$ . In order to find  $\hat{k}$ , we differentiate  $v_{\parallel}$  as given by equation (7.7) with respect to  $kd_i$  and set it to 0 to arrive at the following expression:

$$\frac{1}{\gamma \hat{k}^2} = \frac{1}{2} \left( 1 + \frac{\hat{k}}{\sqrt{\hat{k}^2 + 4}} \right). \tag{7.8}$$

This condition can be rearranged to a polynomial of second order,

$$4\gamma^{-2} + (-4\gamma^{-1} + \gamma^{-2})\hat{k}^2 + (1 - \gamma^{-1})\hat{k}^4 = 0,$$

$$\Leftrightarrow 4\gamma^{-2}x^2 + (-4\gamma^{-1} + \gamma^{-2})x + (1 - \gamma^{-1}) = 0, \text{ where } x = \hat{k}^{-2}.$$
(7.9)

The physically relevant solution describing the transition between Alfvénic and whistler scales is

$$\hat{k}(\gamma) = +\sqrt{\frac{8}{-1 + 4\gamma + \sqrt{1 + 8\gamma}}}. (7.10)$$

Substituting back into equation (7.7) provides the lower bound for resonant parallel velocity

$$\frac{v_{\parallel}}{v_{\rm A}} \ge \frac{\hat{k}(\gamma) + \sqrt{\hat{k}^2(\gamma) + 4}}{2} + \frac{\gamma^{-1}}{\hat{k}(\gamma)}.$$
 (7.11)

Non-relativistic CRs ( $\gamma = 1$ ) require  $v_{\parallel} \geq 2.60v_{\text{A}}$  to achieve resonance at  $kd_i = 1.15$ , mildly relativistic particles ( $\gamma = 2$ ) can resonate at lower velocities ( $v_{\parallel} \geq 2.10v_{\text{A}}$ ) and larger scales ( $kd_i = 0.85$ ).

#### 7.1.2. Grid-Scale Limitations on Resonant CRs in MHD Simulations

In ideal MHD, Alfvén waves exhibit a strictly linear dispersion relation with  $\omega = \pm k v_{\rm A}$ , and the whistler branch is absent from this relation. The resonance condition  $k(v_{\parallel} \mp v_{\rm A}) = \Omega_{\rm cr}$  admits solutions for backward-propagating waves at all velocities, while resonance with forward-propagating waves requires  $v_{\parallel} > v_{\rm A}$ . A fundamental limitation emerges when considering parallel velocities approaching the Alfvén speed. The resonant wavelength  $l_{\rm res} = 2\pi/k_{\rm res}$  diminishes rapidly as  $v_{\parallel}$  approaches  $v_{\rm A}$  for forward-propagating waves, violating the assumption  $l \gg d_i$  fundamental to MHD.

This scale separation constraint manifests differently in analytical theory and numerical implementations of MHD. Numerical simulations truncate scale through spatial discretization. For a numerical grid with spacing  $\Delta x$ , the shortest resolvable wavelength corresponds to  $k_{\rm grid} = 2\pi/(2\Delta x)$ . At this scale, the resonance condition for CRs yields

$$\frac{v_{\parallel}}{v_{\rm A}} = \frac{\Omega_{\rm cr}}{k_{\rm grid}v_{\rm A}} + 1 = \frac{1}{\gamma} \frac{\Delta x}{d_i \pi} + 1. \tag{7.12}$$

Grid scale waves are not well resolved and damped by numerical dissipation. This may require adopting an effective  $\Delta x$  that is larger than the actual step size. While the ion inertial length  $d_i$  lacks explicit representation in the ideal MHD equations, we retain it through the relation  $v_A/\Omega_i = d_i$ . To give an example, non-relativistic CRs ( $\gamma = 1$ ) in simulations with grid spacing  $\Delta x = 10d_i$  require  $v_{\parallel} \geq 3.18v_A$  to achieve resonance with forward-propagating waves, substantially exceeding the analytical MHD threshold. As CRs with larger Lorentz factors resonate with waves at longer scales, they may still resonate at a lower threshold of  $v_{\parallel}$ .

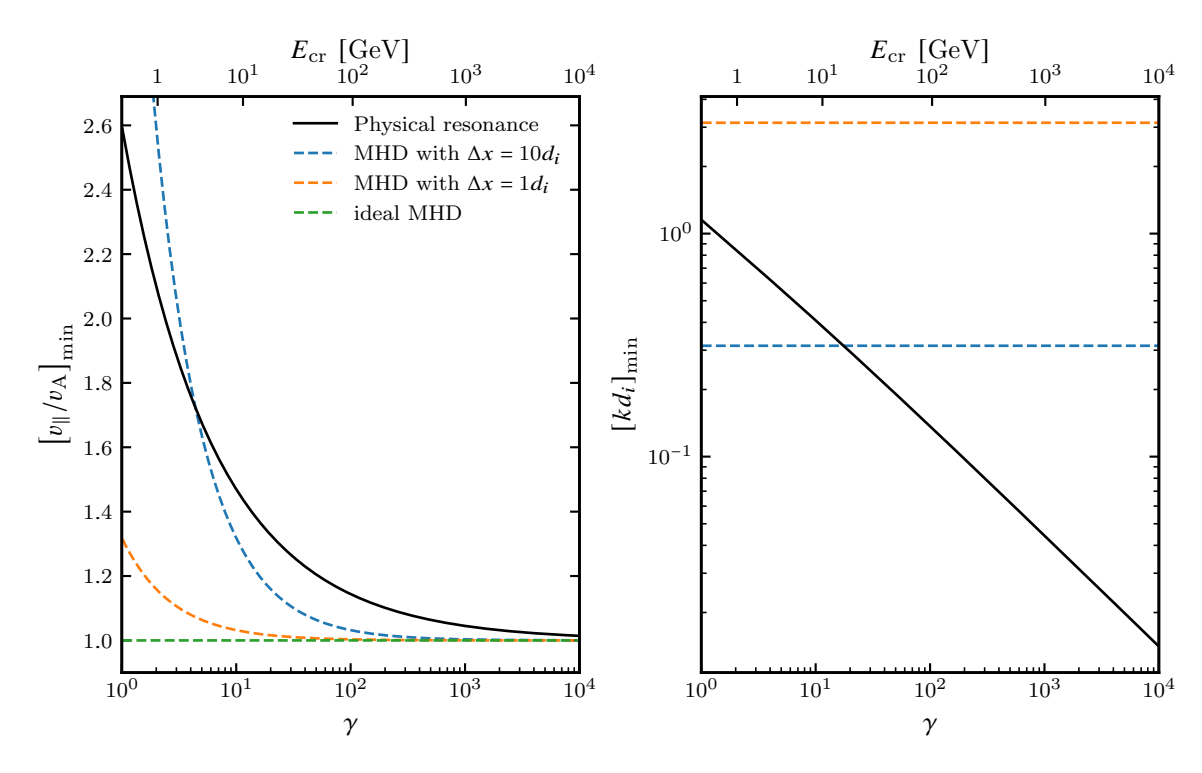


Figure 7.1. Left panel: Minimum  $v_{\parallel}$  of a CR that allows gyroresonance with the forward Alfvén and whistler waves as a function of the CR Lorentz factor  $\gamma$  (equation 7.11). Right panel: The associated scale of a wave that resonates with a CR propagating at the minimum  $v_{\parallel}$ , where  $\hat{k} = [kd_i]_{\min}$ . We show the physical resonance taking electron effects into account (equation 7.11), as well as the resonances in ideal MHD simulations that resolve the spatial size of  $\Delta x$  (equation 7.12).

#### 7.1.3. Comparison and Implications of Resonance Bounds

We summarize our findings in Fig. 7.1, contrasting the minimum parallel wave velocities needed to achieve resonance at different  $\gamma$ . The results demonstrate a resonance gap predominantly affecting CRs with low Lorentz factors. This gap is of importance for CRs as their parallel velocity approaches the Alfvén velocity through scattering,  $v_{\parallel} \rightarrow v_{\rm A}$ , where resonant CR interactions with forward-propagating Alfvén and whistler waves get diminished. This suggests a transport barrier, where CRs will not further scatter in pitch angle once their parallel velocity reaches  $v_{\parallel} \leq 2.60v_{\rm A}$  (at Lorentz factors of  $\gamma = 1$ ), keeping them confined to positive pitch angle cosines  $\mu$ . This phenomenon shows parallels to the established 90° problem in QLT in the MHD approximation, which predicts a narrow resonance gap at  $v_{\parallel} = v_{\rm A}$ . While both gaps impede particle transport, their underlying physics differs fundamentally. The QLT gap emerges from the mathematical idealization of infinitesimally narrow resonance widths whereas our multi-fluid treatment reveals a broader gap arising from the physical dispersion properties of plasma waves. Despite their different origin, these phenomena generate analogous constraints on particle transport processes.

The practical significance of this resonance gap requires careful consideration given several mitigating mechanisms. Our analysis in Section 6.5.3 demonstrates that CR-driven Alfvén waves can propagate at velocities substantially below  $v_A$ . This nonlinear modification of wave prop-

erties combined with resonance broadening and non-resonant scattering mechanisms provides additional ways for CRs to cross the gap.

Particles with  $v_{\parallel} < v_{\rm A}$  maintain resonant coupling with backward-propagating Alfvén waves. Though these waves scatter, on average, CRs toward increasing parallel velocities, they diffuse the CR momentum. This diffusive process enables CRs to cross the resonance gap. Thus, the backward-propagating waves may play an important role in achieving full isotropization.

### 7.2. Instability Growth Rates

#### 7.2.1. Derivation of the Intermediate-scale Instability Growth Rate

Shalaby et al. (2021) obtained a numerical fit for the growth rate of the intermediate scale instability driven by a gyrotropic ring distribution

$$\frac{\Gamma_{\rm IS,n}}{\Omega_i} \approx \alpha^{3/4} + \left(\frac{\alpha}{3}\right)^{1/3} \left(\frac{v_{\rm dr}v_{\perp}}{v_{\rm A}^2}\right)^{2/3}.\tag{7.13}$$

Our analytical derivation extends this result by incorporating relativistic effects through an additional factor of  $\gamma^{-1/3}$  (see equation 7.27). Unlike in the previous section, we are now concerned with distributions of CRs instead of single particles. We make this change more clear by using the parallel drift velocity  $v_{\rm dr}$  instead of  $v_{\parallel}$ , even though these are initially of identical values.

We analyze the dispersion relation by incorporating electromagnetic waves, background electron dynamics, and perpendicular CR ion rotation. While parallel drift terms exhibit a first-order pole at the gyroresonance condition  $(kv_{\rm dr} - \omega - \Omega_{\rm cr})$ , the perpendicular velocity components generate a second-order pole, making them the dominant contribution. Furthermore, taking the limit  $m_{i,\text{bg}} \to \infty$  eliminates background ion contributions and Alfvén waves, focusing our analysis on whistler and electron cyclotron modes. The resulting dispersion relation takes the form

$$0 = 1 - \frac{c^2 k^2}{\omega^2} - \frac{\omega_e^2}{\omega (\omega + \Omega_e)} - \frac{\alpha \omega_i^2 v_\perp^2 / c^2 (k^2 c^2 - \omega^2)}{2\omega^2 \gamma (k v_{\rm dr} - \omega - \Omega_{\rm cr})^2},$$

$$\Leftrightarrow 0 \approx -c^2 k^2 - \omega \frac{\omega_e^2}{\omega + \Omega_e} - \frac{\alpha (\omega_i k c v_\perp / c)^2}{2\gamma (k v_{\rm dr} - \omega - \Omega_{\rm cr})^2},$$

$$(7.14)$$

$$\Leftrightarrow 0 \approx -c^2 k^2 - \omega \frac{\omega_e^2}{\omega + \Omega_e} - \frac{\alpha \left(\omega_i k c v_{\perp} / c\right)^2}{2\gamma \left(k v_{\rm dr} - \omega - \Omega_{\rm cr}\right)^2},\tag{7.15}$$

where we drop the constant of order unity that describes the displacement current. Multiplying by  $-(\omega - \Omega_e)$  yields

$$0 = -c^2 k^2 \Omega_e - \omega(\omega_e^2 + c^2 k^2) - (\omega + \Omega_e) \frac{\alpha (\omega_i k c v_\perp / c)^2}{2\gamma (k v_{\rm dr} - \Omega_{\rm cr} - \omega)^2},$$
(7.16)

$$\Leftrightarrow 0 = \underbrace{\frac{-c^2 k^2 \Omega_e}{\omega_e^2 + c^2 k^2}}_{=\omega_{\rm bg}} - \omega + \left(1 + \frac{\omega}{\Omega_e}\right) \underbrace{\frac{-c^2 k^2 \Omega_e}{\omega_e^2 + c^2 k^2}}_{=\omega_{\rm bg}} \underbrace{\frac{\alpha \left(\omega_i v_{\perp}/c\right)^2}{2\gamma}}_{=\omega_{\rm crp}} \underbrace{\frac{1}{\left(\underline{k} v_{\rm dr} - \Omega_{\rm cr}}_{-\omega} - \omega\right)^2}_{=\omega_g}, \tag{7.17}$$

$$\Leftrightarrow 0 = (\omega_{\rm bg} - \omega)(\omega_g - \omega)^2 + \omega_{\rm bg}\omega_{\rm crp}^2 \left(1 + \frac{\omega}{\Omega_e}\right). \tag{7.18}$$

Here,  $\omega_{\rm bg}$  represents the background wave frequency (cf. equation 2.56 in the limit  $d_i \to \infty$ , whereas we find the  $P_-$  solution of equation 2.52 here).  $\omega_{\rm bg}$  approaches the frequency of parallel propagating whistlers in the regime of  $k \ll \omega_e/c = d_e^{-1}$ , that is  $\omega_{\rm whistler} = -\Omega_e k^2 d_e^2$ . Equivalently, the background wave frequency asymptotically approaches the electron cyclotron frequency,  $\omega_{\rm bg} \to -\Omega_e$ , for  $k \to \infty$ . We define the Doppler-shifted CR gyrofrequency  $\omega_g = k v_{\rm dr} - \Omega_{\rm cr}$  and a modulated CR plasma frequency  $\omega_{\rm crp}$  as well.

At the resonant scale, where the frequency of the background mode is equivalent to the Doppler-shifted CR gyration,  $\omega(k_{\rm res}) \sim \omega_{\rm bg}(k_{\rm res}) = \omega_g(k_{\rm res})$ , this yields the simplified dispersion relation

$$0 = (\omega_{\rm bg} - \omega)^3 + \omega_{\rm bg} \omega_{\rm crp}^2 \left( 1 - \frac{\omega_{\rm bg}}{\Omega_e} \right). \tag{7.19}$$

The last term,  $(1 + \omega_{\rm bg}/\Omega_e)$ , takes on values between 0 and 1. This dispersion relation has three solutions: a purely real one,  $\omega = \omega_{\rm bg} + 2\delta\omega_{\rm I}$ , and the complex conjugate pair  $\omega = \omega_{\rm bg} - \delta\omega_{\rm I}(1 \pm i\sqrt{3})$ , where at resonance we obtain

$$\delta\omega_{\rm I} = \frac{1}{2} \left[ \omega_{\rm crp}^2 \omega_{\rm bg} (1 + \omega_{\rm bg}/\Omega_e) \right]^{1/3} = \frac{1}{2} \left[ \omega_{\rm crp}^2 (-\Omega_e) \frac{k_{\rm res}^2 d_e^2}{\left(1 + k_{\rm res}^2 d_e^2\right)^2} \right]^{1/3},\tag{7.20}$$

$$\Gamma_{\rm I} = \sqrt{3} \times \delta \omega_{\rm I}. \tag{7.21}$$

The term  $\omega_{\rm bg}(1 + \omega_{\rm bg}/\Omega_e)$  manifests as a parabola bounded by roots at  $\omega_{\rm bg} = 0$  and  $\omega_{\rm bg} = -\Omega_e$  with symmetry about its maximum at  $\omega_{\rm bg} = -\Omega_e/2$ . This maximum coincides with the peak wave velocity,  $v_{\rm wave}$ , that occurs in the transition region at  $kd_e = 1$  between the whistler regime characterized by  $v_{\rm wave} \sim -\Omega_e k$  and the electron cyclotron regime, where  $v_{\rm wave} \sim -\Omega_e/k$ .

The wave velocity maximum,  $v_{\text{wave}} \leq -\Omega_e/(2k)$  at  $k = d_e^{-1}$ , establishes an upper bound for the drift velocity  $v_{\text{dr}}$  that is compatible with the intermediate-scale instability through the resonance condition

$$kv_{\rm dr} \le -\Omega_e/2 + \Omega_{\rm cr} \tag{7.22}$$

$$\Rightarrow v_{\rm dr} \le v_{\rm A,e}/2 + \Omega_{\rm cr} d_e \tag{7.23}$$

where  $v_{A,e} = |\Omega_e| d_e = B_0/\sqrt{\mu_0 m_e n_e}$  denotes the electron Alfvén speed. For the assumptions of quasi-neutrality and  $|\Omega_{cr}| \ll |\Omega_e|$ , equation (7.23) reduces to  $v_{dr}/v_A \leq \sqrt{m_r}/2$ , which is consistent with Shalaby et al. (2021).

We caution, that the summand 1 of equation (7.14), which corresponds to the displacement current and which we initially neglected, becomes relevant for relativistic phase velocities  $v_{\text{wave}} = \omega/k$ . This happens at Alfvén speeds of  $v_{\text{A}} \approx 10^{-2}c$ , which translates into whistler and electron-cyclotron phase velocities of up to  $v_{\text{A}} \times \sqrt{m_r}/2 \approx 0.2c$  for the driven whistler and electron cyclotron waves. Equation (7.23) slightly overestimates the maximal drift velocity in this regime.

In the following, we express equation (7.20) by substituting  $k_{\rm res}$  in terms of the CR velocity

components. Given that  $\Omega_{\rm cr} \ll \Omega_e$ ,  $k_{\rm res}$  follows from the resonance condition

$$kv_{\rm dr} - \omega_{\rm bg}(k) \approx 0 \tag{7.24}$$

$$\Rightarrow k_{\rm res} d_e = \frac{v_{\rm A,e}}{2v_{\rm dr}} \left[ 1 \pm \sqrt{1 - \left(\frac{2v_{\rm dr}}{v_{\rm A,e}}\right)^2} \right]$$
 (7.25)

The negative branch corresponds to the whistler resonance at  $k_{\rm res} < d_e^{-1}$  while the positive branch indicates electron cyclotron resonance at  $k_{\rm res} > d_e^{-1}$ . Substituting  $k_{\rm res} d_e$  into equation (7.20) with  $k_{\rm res}^2 d_e^2 / (1 + k_{\rm res}^2 d_e^2)^2 = (v_{\rm dr}/v_{\rm A,e})^2$  produces the growth rate

$$\delta\omega_{\rm I} = \frac{1}{2} \left[ \alpha \frac{v_{\perp}^2}{2d_i^2} \frac{v_{\rm dr}^2}{v_{\rm A,e}^2} (-\Omega_e) \right]^{1/3} = \frac{\Omega_i}{2^{4/3}} \left( \frac{\alpha}{\gamma} \right)^{1/3} \left( \frac{v_{\perp}v_{\rm dr}}{v_{\rm A}^2} \right)^{2/3}, \tag{7.26}$$

$$\frac{\Gamma_{\rm I}}{\Omega_i} = \frac{\sqrt{3}}{2^{4/3}} \left(\frac{\alpha}{\gamma}\right)^{1/3} \left(\frac{v_\perp v_{\rm dr}}{v_{\rm A}^2}\right)^{2/3} \approx 0.687 \left(\frac{\alpha}{\gamma}\right)^{1/3} \left(\frac{v_\perp v_{\rm dr}}{v_{\rm A}^2}\right)^{2/3}.$$
 (7.27)

Our analytical derivation differs from the numerical result in equation (7.13) by a factor of approximately  $0.991\gamma^{-1/3} \approx \gamma^{-1/3}$ , but agrees with the scaling of the other parameters. The  $\gamma^{-1/3}$  factor emerges from relativistic length contraction modifying the effective CR density ratio  $\alpha/\gamma = (n_{\rm cr}/\gamma)/n_{\rm bg}$ . The numerically derived  $\alpha^{3/4}$  term remains absent in our analysis, which considers only perpendicular velocity contributions to the dispersion relation. This term is negligible unless  $v_{\perp} \to 0$ .

The omission of  $\Omega_{\rm cr}$  in the resonance condition (7.24) leads to the prediction of equal growth rates for whistler and electron cyclotron waves. Including  $\Omega_{\rm cr}$  decreases the resulting resonant wave frequency in comparison to our previous estimate. This modifies the growth rate estimate equation (7.20) that depends on the term  $\omega_{\rm bg}(1-\omega_{\rm bg}/\Omega_e)$ , which is enhanced for the electron cyclotron waves and decreased for the whistler waves. Nevertheless, these corrections on the growth rates are in the percentile range, and we may assume equal growth rates for both wave modes.

#### 7.2.2. Alfvén Wave Growth Rates

We analyze the growth rates of forward and backward propagating Alfvén waves within the MHD approximation for the background plasma. The dispersion relation in equation (7.1) without parallel CR drift terms simplifies to (cf. equation 2.70)

$$\left(\frac{\omega c}{v_{\rm A}}\right)^2 - k^2 c^2 - \left(\frac{kc\omega_{\rm crp}}{\omega_g - \omega}\right)^2 = 0,\tag{7.28}$$

$$\iff (\omega + v_{A}k) (\omega - v_{A}k) (\omega - \omega_{g})^{2} - (kv_{A}\omega_{crp})^{2} = 0.$$
 (7.29)

The wave frequency can be decomposed into the resonant contribution and a perturbation  $\omega(k) = \omega_g(k) + \delta\omega = \pm k_{\rm res,A} v_{\rm A} + \delta\omega$ , where the resonant wave number for forward and backward

propagating Alfvén waves is given by

$$k_{\rm res,A} = \frac{\Omega_{\rm cr}}{v_{\rm dr} \mp v_{\rm A}}.$$
 (7.30)

This decomposition transforms equation (7.29) into

$$\delta\omega \left(\pm 2v_{\rm A}k_{\rm res,A} + \delta\omega\right) \left(\delta\omega\right)^2 - \left(k_{\rm res,A}v_{\rm A}\omega_{\rm crp}\right)^2 = 0. \tag{7.31}$$

The analysis proceeds through two limiting cases which approximate the term  $(\pm 2v_A k_{\rm res,A} + \delta\omega)$  differently. The commonly employed weak growth limit assumes  $\delta\omega \ll v_A k$  (e.g. Lerche 1967, a derivation for the gyrotropic ring is given by Shevchenko et al. 2002), while the strong growth limit posits  $\delta\omega \gg v_A k$ .

**Weak Growth Limit.** In the weak growth regime, equation (7.31) yields a third-order polynomial given by

$$(\delta\omega)^3 = \pm \frac{k_{\rm res,A} v_{\rm A}}{2} \left(\omega_{\rm crp}\right)^2. \tag{7.32}$$

Analogous to the intermediate-scale instability growth rate of equation (7.20), the solutions comprise one purely real mode  $\omega = \pm k_{\rm res,A} v_{\rm A} \pm 2\delta \omega$  and a complex conjugate pair  $\omega = \pm k_{\rm res,A} v_{\rm A} \mp \delta \omega_{\rm A} (1 \pm {\rm i}\sqrt{3})$  with

$$\delta\omega_{\rm A} = \frac{1}{2} \left[ \omega_{\rm crp}^2 \frac{k_{\rm res,A} v_{\rm A}}{2} \right]^{1/3} = \Omega_i \frac{1}{2^{4/3}} \left[ \alpha \left( \frac{v_{\perp}}{\gamma v_{\rm A}} \right)^2 \frac{1}{2(v_{\rm dr}/v_{\rm A} \mp 1)} \right]^{1/3}, \tag{7.33}$$

$$\Gamma_{\rm A} = \sqrt{3} \times \delta \omega_{\rm A}. \tag{7.34}$$

The ratio of intermediate-to-gyroscale instability of growth rates in this limit becomes

$$\frac{\Gamma_{\rm I}}{\Gamma_{\rm A}} = \left[\frac{2\omega_{\rm bg}(1 - \omega_{\rm bg}/\Omega_e)}{k_{\rm res,A}v_{\rm A}}\right]^{1/3} \approx \left[2\gamma \left(\frac{v_{\rm dr}}{v_{\rm A}}\right)^2 \left(\frac{v_{\rm dr}}{v_{\rm A}} \mp 1\right)\right]^{1/3} > 1,\tag{7.35}$$

establishing the dominance of intermediate-scale instability growth given that its criterion of instability is fulfilled,  $\sqrt{m_r}/2 > v_{\rm dr}/v_{\rm A} > 1$ . The additional factor of  $\gamma^{1/3}$  appears, because the resonant scale of the Alfvén instability is mainly determined by the CR gyration  $(k_{\rm res,A}v_{\rm dr} \approx \Omega_{\rm cr} = \Omega_i/\gamma)$ , while the intermediate-scale instability is determined by matching the corresponding wave frequencies  $(k_{\rm res,I}v_{\rm dr} \approx \omega(k_{\rm res,I}))$ . High-energy CRs therefore interact with Alfvén waves at larger spatial scales compared to low-energy CRs, resulting in slower growth rates. By contrast, the scale of intermediate-scale waves is (approximately) independent of  $\gamma$ .

For the weak growth limit to be applicable, it has to be at least self-consistent. We compare

the predicted growth rate (equation 7.34) with the unperturbed wave frequency  $\omega \approx k_{\rm res,A} v_{\rm A}$ :

$$k_{\rm res,A}v_{\rm A} \gg \Gamma_{\rm A}$$
 (7.36)

$$\Leftrightarrow k_{\rm res,A} v_{\rm A} \gg \left(\frac{\sqrt{3}}{2^{4/3}}\right)^{3/2} \omega_{\rm crp}$$
 (7.37)

$$\Rightarrow k_{\rm res,A} v_{\rm A} \approx \frac{\Omega_{\rm cr}}{v_{\rm dr}} v_{\rm A} \gg \frac{3^{3/4}}{4} \sqrt{\frac{\alpha}{2\gamma}} \frac{v_{\perp}}{d_i}$$
 (7.38)

$$\Rightarrow 2.5 \gg \sqrt{\gamma \alpha} \frac{v_{\rm dr}}{v_{\rm A}} \frac{v_{\perp}}{v_{\rm A}}.\tag{7.39}$$

Even though we have neglected perturbations of the wave frequency by  $\delta\omega$  – which results in an even stronger constraint as the perturbed wave velocity is always smaller than the unperturbed wave velocity – this condition is not fulfilled for, e.g., values of  $\alpha \approx 10^{-9}$  and non-relativistic CR velocities  $v_{\perp} = v_{\rm dr} = 10^3 v_{\rm A}$ . This motivates the search for an alternative growth limit.

**Strong Growth Limit.** The strong growth analysis assumes the growth rate decouples from the real frequency with  $\delta\omega \approx i\Gamma$  and  $\Gamma \gg kv_A$ . For these assumptions, equation (7.31) yields

$$\Gamma_{\rm A}^4 = \left(k_{\rm res,A} v_{\rm A} \omega_{\rm crp}^2\right)^2 \qquad \Rightarrow \qquad \frac{\Gamma_{\rm A}}{\Omega_i} = \left(\frac{\alpha}{2\gamma^3}\right)^{1/4} \sqrt{\frac{v_{\perp}}{|v_{\rm dr} \mp v_{\rm A}|}}.$$
(7.40)

The relative growth rate between intermediate-scale and Alfvén waves in this regime becomes

$$\frac{\Gamma_{\rm I}}{\Gamma_{\rm A}} = \frac{\sqrt{3}}{2} \left(\frac{\alpha}{2} \gamma^5\right)^{1/12} \left(\frac{v_{\rm dr}^4 (v_{\rm dr} \mp v_{\rm A})^3 v_{\perp}}{v_{\rm A}^8}\right)^{1/6}.$$
 (7.41)

In both limits (i.e., the regimes of weak and strong growth), the Alfvén growth rate is attenuated in comparison to the growth on intermediate scales at large values of  $\gamma$ , which may have implications for the transport of high-energy CRs.

The strong growth approximation introduces a distinctive scaling behavior that differs from the weak growth regime. Peculiarly, the strong growth rate prediction does not necessarily exceed the weak growth rate predictions, as both limits may produce results that are not self-consistent. While deriving the intermediate-scale instability growth rates we assumed the weak growth limit, see equation (7.18), which is also an assumption that should be tested. For this reason, we will compare the analytically obtained scaling laws with numerically derived solutions of the growth rate in the following.

#### 7.2.3. Comparison of Pitch Angle-dependent Growth Rates

Figure 7.2 illustrates the pitch angle dependence of the instability growth rates for CRs with an energy of 1 GeV. We derived the scaling formulas for  $v_{\parallel}$  and  $v_{\perp}$ , but these are easily reformulated using the definitions  $\mu = v_{\parallel}/v$  and  $v_{\perp} = (1 - \mu^2)^{1/2}v$ . For example, the intermediate-scale instability scales with  $(v_{\perp}^2 v_{\parallel}^2)^{1/3} = \left[ (1 - \mu^2) \mu^2 v^4 \right]^{1/3}$ .

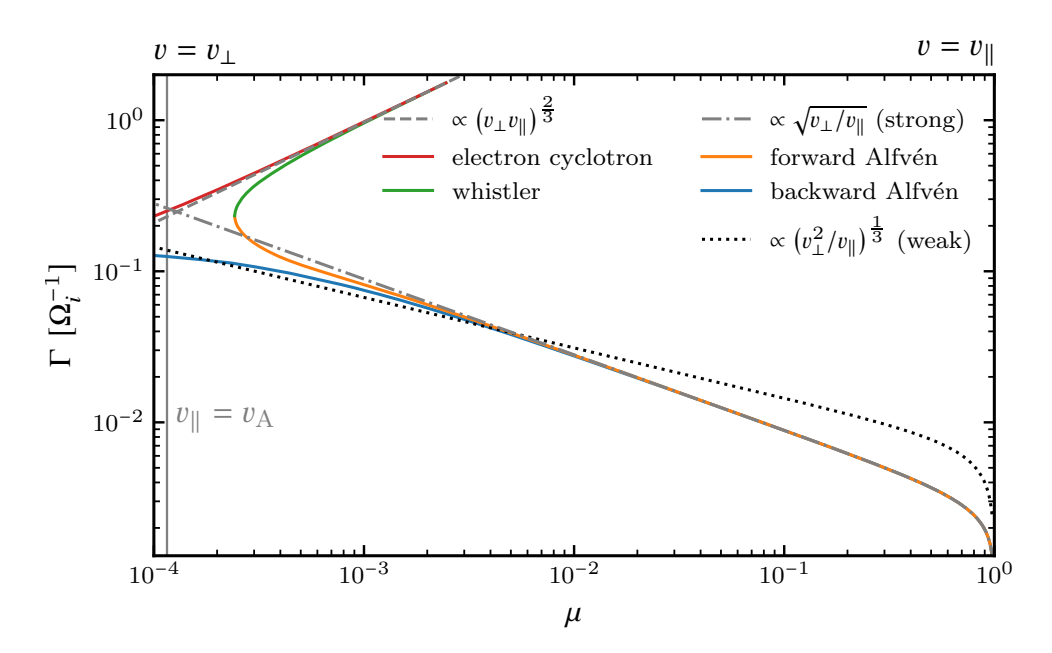


Figure 7.2. Instability growth rates for a population of CRs with 1 GeV ( $\gamma=2$ ) at different pitch angle cosines  $\mu=v_{\parallel}/v$ , presuming a gyrotropic ring distribution of CRs. The colored growth rates are obtained numerically using the parameters  $v_{\rm A}/c=10^{-4}$ ,  $n_{\rm cr}/n_{\rm bg}=10^{-9}$ . We contrast these growth rates with our analytical formulas for the intermediate-scale instability growth (equation 7.27), and the weak (equation 7.29) and strong (equation 7.40) growth limit for the Alfvén waves. These are indicated in the legend by their scaling laws, where the formulas for the Alfvén waves approximate  $v_{\rm dr} \pm v_{\rm A} \approx v_{\rm dr}$ .

For parameters representative of interstellar medium conditions, our analysis reveals significant limitations in the weak growth approximation conventionally presented in standard references (e.g., Kulsrud, 2004) and employed in QLT derivations (cf. equation 5.27). The observed pitch angle dependence deviates substantially from weak growth predictions, demonstrating the importance of validating the weak growth approximation when analyzing growth rates for different CR distributions.

By contrast, the strong growth limit shows excellent agreement with the numerical growth rates across a broad range of  $\mu$  values, and the intermediate-scale instability also aligns well with our theoretical estimates. Forward-propagating Alfvén and whistler modes emerge exclusively when parallel velocities exceed the threshold  $v_{\parallel} \geq 2.1v_{\rm A}$  (at  $\gamma = 2$ ) established in Section 7.1.1, where the dispersion branches converge.

The gyrotropic ring distribution represents the time-averaged configuration of individual gyrating CRs. It describes how a CR (back)reacts to the different waves, giving us insights into the fundamental mechanics of the streaming instability. While these insights may not directly translate to more complex scenarios like power-law distributions, they serve as a foundation for developing physical intuition. In the following, we interpret a gyrotropic ring as a subsample of a full distribution, which is only in resonance with specific modes of the full wave spectrum.

The significantly slower growth of large-scale modes driven by CRs moving nearly parallel to the magnetic field enables the escape of CRs with large pitch angle cosines, resulting in a losscone with decreased scattering probability. This loss cone may be broadened by wave damping mechanisms. For instance, assuming uniform damping from ion-neutral collisions across all wavelengths with a rate of  $\Gamma_d = -10^{-2} \Omega_i^{-1}$  would prevent excitation of resonant waves that are necessary for scattering CRs with  $\mu \geq 0.1$ , allowing CRs with these pitch angle cosines to escape. Thus, the loss-cone may depend on the damping rate. Nevertheless, ion-neutral damping does not generally provide flat damping and is less effective at very large scales. Moreover, ion-neutral damping of Alfvén waves generally does not occur faster than the wave frequency  $\Gamma_{\rm IN} < \omega$  (though exceptions to this exist, such as in the evanescent band, as pointed out by Plotnikov et al. 2021). Thus, in the strong growth limit where  $\Gamma_{\rm IN} < \omega \ll \Gamma$ , Alfvén waves are not efficiently damped by ion-neutral damping, even in regions dominated by neutrals. This is in contrast with the weak growth limit, applicable for CR distributions sufficiently close to isotropization, for which strong ion-neutral damping can limit wave growth.

Furthermore, ion-neutral damping does not impede electron cyclotron waves, and is less effective for whistler waves as these are mainly mediated by electrons (Pandey and Wardle, 2008). Electron cyclotron waves are subject to thermal electron cyclotron damping, likely leading to their saturation at low levels (Amano and Hoshino, 2010). In contrast, whistler waves not only exhibit rapid growth but can achieve saturation amplitudes comparable to those of Alfvén waves, as we demonstrate in Chapter 6.

Wave-wave interactions introduce additional complexity to the picture laid out so far, particularly through the ability of whistler waves to drive an inverse cascade that transfers energy to modes at longer wavelengths. However, numerical investigations of these interactions face significant challenges, requiring multi-dimensional simulations that simultaneously resolve electron dynamics (Cho, 2011) and CR evolution timescales. Building upon these insights into waveparticle interactions, wave coupling mechanisms, and their numerical challenges, we will explore future research directions in Chapter 8.

## 8. Conclusions

In this work I made three principal contributions, namely the development of a novel numerical method specifically designed to study low-density beams interacting with a denser background plasma, applicable to the CR streaming problem. I applied this numerical method to develop a physical picture of the CR streaming instability growth through lopsided gyrophase bunching, and provided insights into possible saturation mechanisms. I demonstrated the existence of a resonance gap of CRs propagating quasi-perpendicular to the magnetic field lines and compare the relative importance of the different streaming instabilities at different pitch-angles.

The discovery that whistler waves are driven unstable by CRs propagating almost perpendicular to the magnetic fields dates back at least to Ginzburg et al. (1973), but were deemed unimportant in achieving full CR isotropization due to their rather narrow instability criteria. The commonly applied MHD approximation eradicates this effect completely from theoretical considerations. The rapid growth of these whistlers to appreciable wave amplitudes was recently discovered by Shalaby et al. (2021) in the context of CR streaming, and thereafter this intermediate scale instability was found to play an important role in overcoming the injection problem for shock-acceleration of electrons (Shalaby et al., 2022). Given these initial discoveries, a necessity for numerical codes that support investigations into its non-linear behavior emerged.

The development of the fluid-PIC numerical method in this thesis represents a significant methodological contribution, providing an alternative to the MHD-PIC method (Zachary and Cohen, 1986; Bai et al., 2015) by not only including electron scales and therefore the intermediate scale instability, but also by modeling Landau damping and enabling arbitrary CR distributions without limitations set by the  $\delta f$ -method. The fluid-PIC method bridges the substantial computational challenges inherent in simulating the multi-scale nature of CR streaming instabilities by treating the dense thermal background plasma as a multi-species fluid while maintaining a fully kinetic description of the sparse CR population. The method successfully captures essential kinetic effects associated with CRs and emulates Landau damping in the thermal plasma through appropriate fluid closures. The only assumption underlying the fluid-PIC method is, that thermal populations are modeled as a fluid. It solves Maxwell's equations without simplifications, and conserves key constraints like divergence-free magnetic fields and Poisson's equation. The fluid-PIC method enables investigating the CR streaming problem accurately at a fraction of the computational cost that would incur for a similar PIC simulation.

My numerical and theoretical analysis reveals that the growth mechanism of gyroresonant CR-driven instabilities fundamentally relies on the bunching of CR gyrophases with respect to the wave magnetic field. The CR's parallel velocity is influenced by the Lorentz-force, which changes its Doppler-shifted rotational frequency and leads to an alignment of its rotational

#### 8. Conclusions

phase with the rotational phase of the wave's magnetic field. This gyrophase bunching creates a coherent perpendicular CR current that drives wave growth through a positive feedback loop. The feedback mechanism involves modification of the wave velocity by the CR current which maintains a lopsided distribution of CR gyrophases necessary for sustained momentum transfer from CRs to waves. This physical picture provides a unified explanation for the growth of all gyroresonant streaming instabilities including forward and backward-moving Alfvén waves, whistler waves and electron cyclotron waves.

The saturation of these instabilities occurs through two distinct mechanisms in our simulations. First, CRs can become trapped in the magnetic potential wells of the waves executing pendulum-like oscillations that manifest as periodic variations in the wave amplitude. The frequency of these oscillations scales with the growth rate of the instability indicating the fundamental connection between wave growth and particle trapping. Second, wave growth saturates when the mean change in CR parallel velocity approaches the wave velocity at which point further scattering would extract energy from rather than amplify the wave. Damping processes are excluded from the analysis so far, which are believed to result in additional saturation mechanisms.

I have shown, that CRs can significantly modify the wave velocity, specifically for Alfvén waves. The induced wave velocity in the linear regime is always slower in magnitude than the unmodified wave speed, and changes periodically in the saturated, non-linear regime, which has important implications for CR transport models that assume scattering occurs in a fixed wave frame. My findings contrast with assumptions conventionally made in QLT, calling into question the pitch-angle diffusion coefficients derived by assuming a single wave frame and especially the random phase approximation.

I advanced understanding of the recently discovered intermediate-scale instability by revealing its similarities and differences to the larger-scale Alfvén waves. Unstable whistler waves exhibit faster growth rates while saturating at comparable wave amplitudes as Alfvén waves in our setup. I pointed out that instability growth rates strongly depend on the pitch angle of CRs (at a fixed CR energy), where wave growth is most efficient at small scales, corresponding to CRs with a parallel velocity few times larger than the Alfvén velocity. Moreover, I showed the physical existence of a resonance gap at pitch angles close to 90°(quasi-perpendicular propagation) that arises from the wave dispersion properties in the transition region between Alfvén and whistler waves. This behavior only occurs in the more accurate two-fluid background description and is absent in MHD. This resonance gap shares the same implications – but not the same origin – as the 90° problem resulting from the mathematical idealization in QLT under the MHD approximation. While often only forward-moving Alfvén waves are regarded in CR streaming, I emphasize the role backward-moving Alfvén waves have in bridging the resonance gaps. I further show, that the weak-growth limit typically applied in deriving growth rates is invalid under ISM conditions for a gyrotropic ring distribution of CRs.

#### **Outlook**

The analysis in this work focused on the gyrotropic ring distribution, which excites distinct wave modes and allows for careful examination of some fundamental effects present in CR streaming absent of further complications. The clarity gained by investigating CR streaming using the gyrotropic ring distribution may have not been possible with more complex distributions, but the concepts found in this thesis must be extended to more complex scenarios, which include, among others, power-law distributions of CRs, broader wave spectra, and inhomogeneities in the background magnetic fields. These effects allow for a rich variety of non-linear effects, such as wave-wave coupling and energy cascades. We might interpret wave-wave interactions more loosely, because it was pointed out in this thesis and by Shalaby et al. (2023) that the CRs appear as a wave-like structure as they resonate with the background, as such wave-wave interactions also influence CRs directly. It is of particular interest how such non-linear interactions can change CR observables.

Recently, Kempski and Quataert (2022) have demonstrated that neither CR confinement by external turbulence nor self-confinement theories of CR transport provide accurate predictions of observational data by themselves. One potential avenue of research attempts unifying both models (Aloisio and Blasi, 2013; Aloisio et al., 2015), where specific interest lies in finding efficient interactions between both paradigms. While Chandran (2000) established that anisotropic MHD turbulence suppresses many resonant wave-particle interactions for high-energy cosmic rays (CRs), the resonant interactions at intermediate scales remain unexplored. A fundamental constraint of the intermediate-scale instability lies in its stringent resonance requirement, specifically that CRs must propagate nearly perpendicular to the local magnetic field. This constraint may be lifted within turbulent environments, the reasoning given for this is as follows: Notwithstanding resonant interactions, CRs gyrate around magnetic field lines without changing their pitch angles if the background magnetic field changes on scales that are large compared with the gyroradius, which is important for the growth of Alfvén waves. However, when CRs traverse magnetic structures smaller than their gyroradii, they follow approximately linear trajectories, resulting in effective randomization of their pitch angles relative to smallscale fluctuations. This randomization process potentially facilitates resonant interactions with whistler waves. The investigation of these effects requires two-dimensional numerical implementations. While the primary components of the fluid-PIC method naturally extend to two dimensions, the treatment of global Landau closures in this geometry presents significant computational challenges, potentially necessitating the implementation of less precise local Landau closure schemes.

Further research directions include refinement of the self-confinement theory, which has been fundamentally linked to QLT since its inception. This work identifies several questionable assumptions underlying QLT, that provide starting points for further theoretical investigation. Additionally, the interactions between forward and backward-propagating Alfvén waves and intermediate scale waves warrant examination, particularly regarding energy cascades and wave-wave coupling mechanisms. These phenomena might enable efficient energy injection at whistler

#### 8. Conclusions

scales, facilitating energy transport to larger-scale wave modes or vice versa, thereby generating multiple scattering frames that modify macroscopic transport behavior.

A related objective involves incorporating CR physics into galactic simulation frameworks. Recent progress has been achieved by, e.g., Jiang and Oh (2018) and Thomas and Pfrommer (2019). However, systematic comparisons between these coarse-grained models and simulations capturing kinetic plasma physics remain outstanding. Such comparisons should focus on calibrating scattering coefficients to better represent underlying microphysical processes, but may also reveal previously unrecognized physical effects significant for macroscopic transport. Methodologically, the framework of information field theory (Enßlin, 2019; Steininger et al., 2019; Edenhofer et al., 2024) provides a promising approach. This framework employs forward models with uncertain parameters, such as CR hydrodynamic models with undetermined scattering coefficients, and derives these parameters through variational inference from data, which may be produced by fluid-PIC simulations. This yields both optimal parameter estimates and associated uncertainties. This approach is particularly promising as it not only calibrates existing theories and indicates missing effects, but also reveals unnecessary terms that exhibit large parameter uncertainties. Elimination of these terms reduces model complexity, facilitating implementation in galactic simulation codes.

This work demonstrates the necessity of re-examining CR transport processes through detailed plasma physical analysis and exploring the parameter space where traditional MHD and QLT approaches prove insufficient. The theoretical frameworks and numerical tools developed here establish a foundation for future investigations that potentially bridge the gap between microscopic plasma and galactic scales.

## **Commented Publication List**

For publications that are part of this thesis, I state the contributions by myself and by my co-authors. I summarize the contents of publications that are not part of this thesis.

#### **Publications Presented in this Thesis**

- Lemmerz, Rouven, Mohamad Shalaby, Timon Thomas, and Christoph Pfrommer (2024).
   "Coupling Multi-Fluid Dynamics Equipped with Landau Closures to the Particle-in-Cell Method". In: *Journal of Plasma Physics* 90.1, p. 905900104. ISSN: 0022-3778, 1469-7807.
   DOI: 10.1017/S0022377823001113
  - I developed the code, conceptualized and conducted the simulations, created the figures, and prepared the manuscript. An early, unstable prototype of the code without Landau closures was provided to me by MS and TT, which was reworked in large parts during this thesis. MS proposed the general idea. TT lead the part on the CWENO scheme. All authors contributed to the discussions and interpretation of the paper.
- Lemmerz, Rouven, Mohamad Shalaby, Christoph Pfrommer, and Timon Thomas (2024). The Theory of Resonant Cosmic Ray-Driven Instabilities Growth and Saturation of Single Modes. DOI: 10.3847/1538-4357/ad8eb3. arXiv: 2406.04400 [astro-ph, physics:physics]. Pre-published, accepted for publication in The Astrophysical Journal. I proposed the general idea, conducted the simulations, created the figures, and prepared the manuscript. CP contributed by clarifying the presentation. All authors contributed to the discussion and the interpretation of the paper.

# Publications Outside this Work Conducted during my Doctoral Studies

Shalaby, Mohamad, Rouven Lemmerz, Timon Thomas, and Christoph Pfrommer (2022).
 "The Mechanism of Efficient Electron Acceleration at Parallel Nonrelativistic Shocks". In: The Astrophysical Journal 932.2, p. 86. ISSN: 0004-637X, 1538-4357. DOI: 10.3847/1538-4357/ac6ce7

In this publication, we show that the injection problem of electron shock acceleration can be overcome through excitation of the intermediate scale instability within and adjacent to the shock transition region. We provide PIC simulations of parallel non-relativistic shocks, at varying mass ratio and Mach numbers, where only those simulations that excite the

#### 8. Conclusions

intermediate scale instability efficiently accelerate electrons and allow them to reach high energies.

Shalaby, Mohamad, Timon Thomas, Christoph Pfrommer, Rouven Lemmerz, and Virginia Bresci (2023). "Deciphering the Physical Basis of the Intermediate-Scale Instability".
 In: Journal of Plasma Physics 89.6, p. 175890603. ISSN: 0022-3778, 1469-7807. DOI: 10.1017/S0022377823001289

Here, we provide a simple, graphical interpretation of the gyroresonant condition that proves that the intermediate scale instability is a gyroresonant instability. We compare MHD, Hall-MHD and two-fluid backgrounds, where only the latter is able to capture the intermediate scale instability correctly.

## **Acknowledgments**

I would like to express my gratitude to my supervisor Christoph Pfrommer, whose guidance, enthusiasm, and unwavering support have shaped not only this thesis but also my development as a scientist. His broad knowledge of astrophysics and outstanding ability to convey complex concepts have been instrumental in shaping this work.

I am particularly indebted to Mohamad Shalaby, whose expertise in plasma physics and scientific meticulousness have led to countless enlightening discussions. His relentless pursuit of fundamental understanding and high standards of scientific rigor have profoundly influenced my approach to research. Special thanks go to Timon Thomas for his insightful feedback and valuable contributions, and to Philipp Girichidis for sharing his numerical expertise and providing encouragement during the challenging times of the COVID-lockdowns. I extend my gratitude to all other members of the AIP group, who created such a vibrant and enjoyable working environment.

This research would not have been possible without funding provided by the European Research Council under ERC-CoG grant CRAGSMAN-646955 and ERC-AdG grant PICOGAL-101019746 and the computational resources provided by AIP and HLRN (projects bbp00046 and bbp00072). I gratefully acknowledge the support of the National Science Foundation (grant PHY-2210452) for my enriching stay at the Aspen Center for Physics.

On a personal note, I want to express my heartfelt appreciation to my wife Janneke, whose love, patience and support helped me whose love, patience, and unwavering support helped me tremendously throughout these years. You have brought balance to my academic life and filled it with countless moments of joy. I am deeply grateful to my parents for their lifelong support and encouragement throughout my studies. Finally, I am grateful to the dear friends I made in Potsdam, whose companionship has enriched my life beyond physics and whose presence has made this journey all the more meaningful.

## **Bibliography**

- Abbasi, R. et al. (2012). "Observation of Anisotropy in the Galactic Cosmic-Ray Arrival Directions at 400 TeV with IceCube". In: *The Astrophysical Journal* 746, p. 33. ISSN: 0004-637X. DOI: 10.1088/0004-637X/746/1/33.
- Adriani, O. et al. (2011). "PAMELA Measurements of Cosmic-Ray Proton and Helium Spectra". In: Science 332.6025, pp. 69–72. ISSN: 0036-8075, 1095-9203. DOI: 10.1126/science.1199172.
- Aguilar, M. et al. (2013). "First Result from the Alpha Magnetic Spectrometer on the International Space Station: Precision Measurement of the Positron Fraction in Primary Cosmic Rays of 0.5–350 GeV". In: *Physical Review Letters* 110.14, p. 141102. ISSN: 0031-9007, 1079-7114. DOI: 10.1103/PhysRevLett.110.141102.
- Allmann-Rahn, F., S. Lautenbach, and R. Grauer (2022). "An Energy Conserving Vlasov Solver That Tolerates Coarse Velocity Space Resolutions: Simulation of MMS Reconnection Events".
  In: Journal of Geophysical Research: Space Physics 127.2, e2021JA029976. ISSN: 2169-9402.
  DOI: 10.1029/2021JA029976.
- Allmann-Rahn, F., T. Trost, and R. Grauer (2018). "Temperature Gradient Driven Heat Flux Closure in Fluid Simulations of Collisionless Reconnection". In: *Journal of Plasma Physics* 84.3. ISSN: 0022-3778, 1469-7807. DOI: 10.1017/S002237781800048X.
- Aloisio, R., V. Berezinsky, and A. Gazizov (2012). "Transition from Galactic to Extragalactic Cosmic Rays". In: *Astroparticle Physics* 39, pp. 129–143. ISSN: 0927-6505. DOI: 10.1016/j.astropartphys.2012.09.007.
- Aloisio, R., P. Blasi, and P. D. Serpico (2015). "Nonlinear Cosmic Ray Galactic Transport in the Light of AMS-02 and Voyager Data". In: *Astronomy and Astrophysics* 583, A95. ISSN: 0004-6361. DOI: 10.1051/0004-6361/201526877.
- Aloisio, Roberto and Pasquale Blasi (2013). "Propagation of Galactic Cosmic Rays in the Presence of Self-Generated Turbulence". In: *Journal of Cosmology and Astroparticle Physics* 2013, p. 001. ISSN: 1475-7516. DOI: 10.1088/1475-7516/2013/07/001.
- Amano, Takanobu (2015). "Divergence-Free Approximate Riemann Solver for the Quasi-Neutral Two-Fluid Plasma Model". In: *Journal of Computational Physics* 299, pp. 863–886. ISSN: 00219991. DOI: 10.1016/j.jcp.2015.07.035.
- (2018). "A Generalized Quasi-Neutral Fluid-Particle Hybrid Plasma Model and Its Application to Energetic-Particle-Magnetohydrodynamics Hybrid Simulation". In: *Journal of Computational Physics* 366, pp. 366–385. ISSN: 0021-9991. DOI: 10.1016/j.jcp.2018.04.020.
- Amano, Takanobu and Masahiro Hoshino (2010). "A Critical Mach Number for Electron Injection in Collisionless Shocks". In: *Physical Review Letters* 104.18, p. 181102. DOI: 10.1103/PhysRevLett.104.181102.

- Amenomori, M. et al. (2008). "The All-Particle Spectrum of Primary Cosmic Rays in the Wide Energy Range from 1014 to 1017 eV Observed with the Tibet-III Air-Shower Array". In: *The Astrophysical Journal* 678.2, p. 1165. ISSN: 0004-637X. DOI: 10.1086/529514.
- Anchordoqui, Luis A. (2019). "Ultra-High-Energy Cosmic Rays". In: *Ultra-high-energy cosmic rays* 801, pp. 1–93. ISSN: 0370-1573. DOI: 10.1016/j.physrep.2019.01.002.
- Anderson, Carl D. (1933). "The Positive Electron". In: *Physical Review* 43.6, pp. 491–494. DOI: 10.1103/PhysRev.43.491.
- Anderson, E. C., W. F. Libby, S. Weinhouse, A. F. Reid, A. D. Kirshenbaum, and A. V. Grosse (1947). "Radiocarbon From Cosmic Radiation". In: *Science* 105.2735, pp. 576–577. ISSN: 0036-8075, 1095-9203. DOI: 10.1126/science.105.2735.576.
- Arber, T D et al. (2015). "Contemporary Particle-in-Cell Approach to Laser-Plasma Modelling". In: *Plasma Physics and Controlled Fusion* 57.11, p. 113001. ISSN: 0741-3335, 1361-6587. DOI: 10.1088/0741-3335/57/11/113001.
- Auger, Pierre, P. Ehrenfest, R. Maze, J. Daudin, and Robley A. Fréon (1939). "Extensive Cosmic-Ray Showers". In: *Reviews of Modern Physics* 11.3-4, pp. 288–291. ISSN: 0034-6861. DOI: 10.1103/RevModPhys.11.288.
- Axford, W. I., E. Leer, and G. Skadron (1977). "The Acceleration of Cosmic Rays by Shock Waves". In: *Proceedings International Cosmic Ray Conference* 11, p. 132.
- Baade, W. and F. Zwicky (1934). "Cosmic Rays from Super-Novae". In: *Proceedings of the National Academy of Sciences* 20.5, pp. 259–263. DOI: 10.1073/pnas.20.5.259.
- Bai, Xue-Ning (2022). "Towards First-principle Characterization of Cosmic-ray Transport Coefficients from Multi-scale Kinetic Simulations". In: *The Astrophysical Journal* 928.2, p. 112. ISSN: 0004-637X, 1538-4357. DOI: 10.3847/1538-4357/ac56e1. arXiv: 2112.14782 [astro-ph].
- Bai, Xue-Ning, Damiano Caprioli, Lorenzo Sironi, and Anatoly Spitkovsky (2015). "Magnetohydrodynamic-Particle-in-Cell Method for Coupling Cosmic Rays with a Thermal Plasma: Application to Non-relativistic Shocks". In: *The Astrophysical Journal* 809.1, p. 55. ISSN: 0004-637X. DOI: 10.1088/0004-637X/809/1/55.
- Bai, Xue-Ning, Eve C. Ostriker, Illya Plotnikov, and James M. Stone (2019). "Magnetohydrodynamic Particle-in-cell Simulations of the Cosmic-Ray Streaming Instability: Linear Growth and Quasi-linear Evolution". In: *The Astrophysical Journal* 876.1, p. 60. ISSN: 0004-637X. DOI: 10.3847/1538-4357/ab1648.
- Bailey, David H. (1990). "FFTs in External or Hierarchical Memory". In: *The Journal of Supercomputing* 4.1, pp. 23–35. ISSN: 1573-0484. DOI: 10.1007/BF00162341.
- Bambic, Christopher J., Xue-Ning Bai, and Eve C. Ostriker (2021). "MHD-PIC Simulations of Cosmic-Ray Scattering and Transport in Inhomogeneously Ionized Plasma". In: *The Astrophysical Journal* 920, p. 141. ISSN: 0004-637X. DOI: 10.3847/1538-4357/ac0ce7.
- Bell, A. R. (1978). "The Acceleration of Cosmic Rays in Shock Fronts I." In: *Monthly Notices of the Royal Astronomical Society* 182, pp. 147–156. ISSN: 0035-8711. DOI: 10.1093/mnras/182.2.147.

- (1978). "The Acceleration of Cosmic Rays in Shock Fronts II." In: Monthly Notices of the Royal Astronomical Society 182, pp. 443–455. ISSN: 0035-8711. DOI: 10.1093/mnras/182.3.443.
- (2004). "Turbulent Amplification of Magnetic Field and Diffusive Shock Acceleration of Cosmic Rays". In: Monthly Notices of the Royal Astronomical Society 353.2, pp. 550–558. ISSN: 00358711, 13652966. DOI: 10.1111/j.1365-2966.2004.08097.x.
- Bell, A. R., K. M. Schure, B. Reville, and G. Giacinti (2013). "Cosmic-Ray Acceleration and Escape from Supernova Remnants". In: *Monthly Notices of the Royal Astronomical Society* 431, pp. 415–429. ISSN: 0035-8711. DOI: 10.1093/mnras/stt179.
- Bell, T. F. (1965). "Nonlinear Alfvén Waves in a Vlasov Plasma". In: *The Physics of Fluids* 8.10, pp. 1829–1839. ISSN: 0031-9171. DOI: 10.1063/1.1761115.
- Birdsall, Charles K. and A. Bruce Langdon (1991). *Plasma Physics via Computer Simulation*. The Adams Hilger Series on Plasma Physics. Bristol, Philadelphia: Adam Hilger; IOP. 479 pp. ISBN: 978-0-07-005371-7.
- Blackett, P. M. S. and G. P. S. Occhialini (1933). "Some Photographs of the Tracks of Penetrating Radiation". In: *Proceedings of the Royal Society of London. Series A, Containing Papers of a Mathematical and Physical Character* 139.839, pp. 699–720+722+724+726. JSTOR: 96057.
- Blandford, R. D. and J. P. Ostriker (1978). "Particle Acceleration by Astrophysical Shocks." In: *The Astrophysical Journal* 221, pp. L29–L32. ISSN: 0004-637X. DOI: 10.1086/182658.
- Blandford, Roger and David Eichler (1987). "Particle Acceleration at Astrophysical Shocks: A Theory of Cosmic Ray Origin". In: *Physics Reports* 154.1, pp. 1–75. ISSN: 03701573. DOI: 10.1016/0370-1573(87)90134-7.
- Blasi, Pasquale, Elena Amato, and Pasquale D. Serpico (2012). "Spectral Breaks as a Signature of Cosmic Ray Induced Turbulence in the Galaxy". In: *Physical Review Letters* 109.6, p. 061101. DOI: 10.1103/PhysRevLett.109.061101.
- Booth, C. M., Oscar Agertz, Andrey V. Kravtsov, and Nickolay Y. Gnedin (2013). "Simulations of Disk Galaxies with Cosmic Ray Driven Galactic Winds". In: 777.L16 (1), p. L16. DOI: 10.1088/2041-8205/777/1/L16.
- Boris, Jay P et al. (1970). "Relativistic Plasma Simulation-Optimization of a Hybrid Code". In: *Proc. Fourth Conf. Num. Sim. Plasmas*. Naval Research Laboratory, Washington, D.C., pp. 3–67.
- Bothe, W. and W. Kolhörster (1929). "Das Wesen der Höhenstrahlung". In: Zeitschrift für Physik 56.11-12, pp. 751–777. ISSN: 1434-6001, 1434-601X. DOI: 10.1007/BF01340137.
- Boulares, Ahmed and Donald P. Cox (1990). "Galactic Hydrostatic Equilibrium with Magnetic Tension and Cosmic-Ray Diffusion". In: *The Astrophysical Journal* 365, p. 544. ISSN: 0004-637X. DOI: 10.1086/169509.
- Boyd, J.P. (2013). Chebyshev and Fourier Spectral Methods: Second Revised Edition. Dover Books on Mathematics. Dover Publications. ISBN: 978-0-486-14192-3.
- Boyd, T. J. M. and J. J. Sanderson (2003). *The Physics of Plasmas*. Cambridge: Cambridge University Press. ISBN: 978-0-521-45912-9. DOI: 10.1017/CB09780511755750.

- Braginskii, S. I. (1965). "Transport Processes in a Plasma". In: Reviews of Plasma Physics 1, p. 205.
- Breitschwerdt, D., J. F. McKenzie, and H. J. Voelk (1991). "Galactic Winds. I. Cosmic Ray and Wave-Driven Winds from the Galaxy." In: *Astronomy and Astrophysics* 245, p. 79. ISSN: 0004-6361.
- Bret, A. (2009). "Weibel, Two-Stream, Filamentation, Oblique, Bell, Buneman... Which One Grows Faster?" In: *The Astrophysical Journal* 699.2, p. 990. ISSN: 0004-637X. DOI: 10.1088/0004-637X/699/2/990.
- Bret, A. and M. E. Dieckmann (2010). "How Large Can the Electron to Proton Mass Ratio Be in Particle-in-Cell Simulations of Unstable Systems?" In: *Physics of Plasmas* 17.032109 (3), p. 032109. DOI: 10.1063/1.3357336.
- Bret, A., L. Gremillet, and M. E. Dieckmann (2010). "Multidimensional Electron Beam-Plasma Instabilities in the Relativistic Regime". In: *Physics of Plasmas* 17.120501 (12), p. 120501. DOI: 10.1063/1.3514586.
- Brice, Neil (1963). "An Explanation of Triggered Very-Low-Frequency Emissions". In: *Journal of Geophysical Research* 68.15, pp. 4626–4628. ISSN: 01480227. DOI: 10.1029/JZ068i015p04626.
- Brio, M. and C. C. Wu (1988). "An Upwind Differencing Scheme for the Equations of Ideal Magnetohydrodynamics". In: *Journal of Computational Physics* 75, pp. 400–422. ISSN: 0021-9991. DOI: 10.1016/0021-9991(88)90120-9.
- Buck, Tobias, Christoph Pfrommer, Rüdiger Pakmor, Robert J. J. Grand, and Volker Springel (2020). "The Effects of Cosmic Rays on the Formation of Milky Way-mass Galaxies in a Cosmological Context". In: *Monthly Notices of the Royal Astronomical Society* 497.2, pp. 1712–1737. ISSN: 0035-8711, 1365-2966. DOI: 10.1093/mnras/staa1960. arXiv: 1911.00019 [astro-ph].
- Burrows, R. H., X. Ao, and G. P. Zank (2014). "A New Hybrid Method". In: *Outstanding Problems in Heliophysics: From Coronal Heating to the Edge of the Heliosphere*. Ed. by Q. Hu and G. P. Zank. Vol. 484. Astronomical Society of the Pacific Conference Series. Astronomical society of the pacific, p. 8.
- Butcher, J. C. (2016). Numerical Methods for Ordinary Differential Equations. 3rd ed. Wiley. ISBN: 978-1-119-12150-3 978-1-119-12153-4. DOI: 10.1002/9781119121534.
- Capdeville, G. (2008). "A Central WENO Scheme for Solving Hyperbolic Conservation Laws on Non-Uniform Meshes". In: *Journal of Computational Physics* 227.5, pp. 2977–3014. ISSN: 0021-9991. DOI: 10.1016/j.jcp.2007.11.029.
- Caprioli, D. and A. Spitkovsky (2014). "Simulations of Ion Acceleration at Non-relativistic Shocks. I. Acceleration Efficiency". In: *The Astrophysical Journal* 783, p. 91. ISSN: 0004-637X. DOI: 10.1088/0004-637X/783/2/91.
- (2014). "Simulations of Ion Acceleration at Non-relativistic Shocks. II. Magnetic Field Amplification". In: The Astrophysical Journal 794, p. 46. ISSN: 0004-637X. DOI: 10.1088/0004-637X/794/1/46.
- (2014). "Simulations of Ion Acceleration at Non-relativistic Shocks. III. Particle Diffusion". In: The Astrophysical Journal 794, p. 47. ISSN: 0004-637X. DOI: 10.1088/0004-637X/794/1/47.

- Cerri, Silvio Sergio (2024). "Revisiting the Role of Cosmic-Ray Driven Alfvén Waves in Pre-Existing Magnetohydrodynamic Turbulence: I. Turbulent Damping Rates and Feedback on Background Fluctuations". In: *Astronomy & Astrophysics* 688, A182. ISSN: 0004-6361, 1432-0746. DOI: 10.1051/0004-6361/202449492.
- Chandran, Benjamin D. G. (2000). "Scattering of Energetic Particles by Anisotropic Magnetohydrodynamic Turbulence with a Goldreich-Sridhar Power Spectrum". In: *Physical Review Letters* 85.22, pp. 4656–4659. ISSN: 0031-9007, 1079-7114. DOI: 10.1103/PhysRevLett.85.4656. arXiv: astro-ph/0008498.
- Chavanis, Pierre-Henri (2008). "Hamiltonian and Brownian Systems with Long-Range Interactions: IV. General Kinetic Equations from the Quasilinear Theory". In: *Physica A: Statistical Mechanics and its Applications* 387.7, pp. 1504–1528. ISSN: 03784371. DOI: 10.1016/j.physa. 2007.10.034. arXiv: 0705.4579 [cond-mat].
- Chen, Francis F. (2016). *Introduction to Plasma Physics and Controlled Fusion*. Cham: Springer International Publishing. ISBN: 978-3-319-22308-7 978-3-319-22309-4. DOI: 10.1007/978-3-319-22309-4.
- Chen, Gui-Qiang and Tai-Ping Liu (1993). "Zero Relaxation and Dissipation Limits for Hyperbolic Conservation Laws". In: Communications on Pure and Applied Mathematics 46.5, pp. 755–781. ISSN: 1097-0312. DOI: 10.1002/cpa.3160460504.
- Cheng, C. Z. and G. Knorr (1975). "Integration of the Vlasov Equation in Configuration Space". In: DOI: 10.2172/4200114.
- Cho, Jungyeon (2011). "Magnetic Helicity Conservation and Inverse Energy Cascade in Electron Magnetohydrodynamic Wave Packets". In: *Physical Review Letters* 106.19, p. 191104. DOI: 10.1103/PhysRevLett.106.191104.
- Clay, Jacob (1927). "Penetrating Radiation". In: Proceedings of the Royal Academy of Sciences Amsterdam. Vol. 30, pp. 1115–1127.
- Cooley, James W. and John W. Tukey (1965). "An Algorithm for the Machine Calculation of Complex Fourier Series". In: *Mathematics of Computation* 19.90, pp. 297–301. ISSN: 0025-5718, 1088-6842. DOI: 10.1090/S0025-5718-1965-0178586-1.
- Cravero, I., G. Puppo, M. Semplice, and G. Visconti (2018). "Cool WENO Schemes". In: *Computers & Fluids*. Recent Progress in Nonlinear Numerical Methods for Time-Dependent Flow & Transport Problems 169, pp. 71–86. ISSN: 0045-7930. DOI: 10.1016/j.compfluid.2017.07.022.
- (2018). "CWENO: Uniformly Accurate Reconstructions for Balance Laws". In: Mathematics of Computation 87.312, pp. 1689–1719. ISSN: 0025-5718, 1088-6842. DOI: 10.1090/mcom/3273.
- Dalgarno, A. (2006). "Interstellar Chemistry Special Feature: The Galactic Cosmic Ray Ionization Rate". In: *Proceedings of the National Academy of Science* 103, pp. 12269–12273. ISSN: 0027-8424. DOI: 10.1073/pnas.0602117103.
- (2006). "The Galactic Cosmic Ray Ionization Rate". In: Proceedings of the National Academy of Sciences 103.33, pp. 12269–12273. DOI: 10.1073/pnas.0602117103.

- Daughton, W., V. Roytershteyn, H. Karimabadi, L. Yin, B. J. Albright, B. Bergen, and K. J. Bowers (2011). "Role of Electron Physics in the Development of Turbulent Magnetic Reconnection in Collisionless Plasmas". In: *Nature Physics* 7.7, pp. 539–542. DOI: 10.1038/nphys1965.
- Daughton, William, Jack Scudder, and Homa Karimabadi (2006). "Fully Kinetic Simulations of Undriven Magnetic Reconnection with Open Boundary Conditions". In: *Physics of Plasmas* 13.072101 (7), p. 072101. DOI: 10.1063/1.2218817.
- Davis Jr, Leverett (1960). "On the Diffusion of Cosmic Rays in the Galaxy". In: *International Cosmic Ray Conference*. Vol. 3, p. 220.
- Dawson, John (1962). "One-Dimensional Plasma Model". In: *Physics of Fluids* 5.4, p. 445. ISSN: 00319171. DOI: 10.1063/1.1706638.
- Dedner, A., F. Kemm, D. Kröner, C.-D. Munz, T. Schnitzer, and M. Wesenberg (2002). "Hyperbolic Divergence Cleaning for the MHD Equations". In: *Journal of Computational Physics* 175.2, pp. 645–673. ISSN: 00219991. DOI: 10.1006/jcph.2001.6961.
- Dellacherie, Stéphane (2010). "Analysis of Godunov Type Schemes Applied to the Compressible Euler System at Low Mach Number". In: *Journal of Computational Physics* 229.4, pp. 978–1016. ISSN: 00219991. DOI: 10.1016/j.jcp.2009.09.044.
- Dimits, A. M., I. Joseph, and M. V. Umansky (2014). "A Fast Non-Fourier Method for Landau-fluid Operators". In: *Physics of Plasmas* 21.5, p. 055907. ISSN: 1070-664X, 1089-7674. DOI: 10.1063/1.4876617.
- Dimits, A. M. and W. W. Lee (1993). "Partially Linearized Algorithms in Gyrokinetic Particle Simulation". In: *Journal of Computational Physics* 107.2, pp. 309–323. ISSN: 0021-9991. DOI: 10.1006/jcph.1993.1146.
- Ding, Hengfei, Changpin Li, and YangQuan Chen (2015). "High-Order Algorithms for Riesz Derivative and Their Applications (II)". In: *Journal of Computational Physics* 293, pp. 218–237. ISSN: 00219991. DOI: 10.1016/j.jcp.2014.06.007.
- Draine, Bruce T. (2011). Physics of the Interstellar and Intergalactic Medium. Princeton Series in Astrophysics. Princeton, N.J.: Princeton University Press. 540 pp. ISBN: 978-0-691-12213-7 978-0-691-12214-4.
- Eastman, T. E., R. R. Anderson, L. A. Frank, and G. K. Parks (1981). "Upstream Particles Observed in the Earth's Foreshock Region". In: *Journal of Geophysical Research* 86, pp. 4379–4396. ISSN: 0148-0227. DOI: 10.1029/JA086iA06p04379.
- Edenhofer, Gordian et al. (2024). "Re-Envisioning Numerical Information Field Theory(NIFTy.Re): A Library for Gaussian Processes and VariationalInference". In: *Journal of Open Source Software* 9.98, p. 6593. ISSN: 2475-9066. DOI: 10.21105/joss.06593.
- Einfeldt, B, C. D Munz, P. L Roe, and B Sjögreen (1991). "On Godunov-type Methods near Low Densities". In: *Journal of Computational Physics* 92.2, pp. 273–295. ISSN: 0021-9991. DOI: 10.1016/0021-9991(91)90211-3.
- Engelbrecht, N. Eugene, F. Effenberger, V. Florinski, M. S. Potgieter, D. Ruffolo, R. Chhiber, A. V. Usmanov, J. S. Rankin, and P. L. Els (2022). "Theory of Cosmic Ray Transport in the Heliosphere". In: *Space Science Reviews* 218.4, p. 33. ISSN: 1572-9672. DOI: 10.1007/s11214-022-00896-1.

- Enßlin, Torsten A. (2019). "Information Theory for Fields". In: *Annalen der Physik* 531.3, p. 1800127. ISSN: 0003-3804, 1521-3889. DOI: 10.1002/andp.201800127. arXiv: 1804.03350 [astro-ph].
- Esirkepov, T.Zh. (2001). "Exact Charge Conservation Scheme for Particle-in-Cell Simulation with an Arbitrary Form-Factor". In: *Computer Physics Communications* 135.2, pp. 144–153. ISSN: 00104655. DOI: 10.1016/S0010-4655(00)00228-9.
- Evans, Charles R. and John F. Hawley (1988). "Simulation of Magnetohydrodynamic Flows: A Constrained Transport Model". In: *The Astrophysical Journal* 332, p. 659. ISSN: 0004-637X. DOI: 10.1086/166684.
- Evoli, Carmelo, Tim Linden, and Giovanni Morlino (2018). "Self-Generated Cosmic-Ray Confinement in TeV Halos: Implications for TeV Gamma -Ray Emission and the Positron Excess". In: *Physical Review D* 98, p. 063017. ISSN: 1550-79980556-2821. DOI: 10.1103/PhysRevD.98.063017.
- Evoli, Carmelo, Giovanni Morlino, Pasquale Blasi, and Roberto Aloisio (2020). "AMS-02 Beryllium Data and Its Implication for Cosmic Ray Transport". In: *Physical Review D* 101.2, p. 023013. DOI: 10.1103/PhysRevD.101.023013.
- Farber, R., M. Ruszkowski, H.-Y. K. Yang, and E. G. Zweibel (2018). "Impact of Cosmic Ray Transport on Galactic Winds". In: *The Astrophysical Journal* 856.2, p. 112. ISSN: 1538-4357. DOI: 10.3847/1538-4357/aab26d. arXiv: 1707.04579 [astro-ph].
- Farmer, Alison J. and Peter Goldreich (2004). "Wave Damping by Magnetohydrodynamic Turbulence and Its Effect on Cosmic-Ray Propagation in the Interstellar Medium". In: *The Astrophysical Journal* 604.2, pp. 671–674. ISSN: 0004-637X, 1538-4357. DOI: 10.1086/382040.
- Fehske, H., R. Schneider, and A. Weiße, eds. (2008). Computational Many-Particle Physics. SpringerLink Bücher. Berlin, Heidelberg: Springer Berlin Heidelberg. ISBN: 978-3-540-74685-0 978-3-540-74686-7. DOI: 10.1007/978-3-540-74686-7.
- Fermi, Enrico (1949). "On the Origin of the Cosmic Radiation". In: *Physical Review* 75.8, pp. 1169–1174. ISSN: 0031-899X. DOI: 10.1103/PhysRev.75.1169.
- Finelli, F., S. S. Cerri, F. Califano, F. Pucci, D. Laveder, G. Lapenta, and T. Passot (2021). "Bridging Hybrid- and Full-Kinetic Models with Landau-fluid Electrons. I. 2D Magnetic Reconnection". In: antike und abendland 653.A156, A156. DOI: 10.1051/0004-6361/202140279. arXiv: 2101.00040 [physics.plasm-ph].
- Fonseca, R. A. et al. (2002). "OSIRIS: A Three-Dimensional, Fully Relativistic Particle in Cell Code for Modeling Plasma Based Accelerators". In: *Computational Science ICCS 2002*. Ed. by Peter M. A. Sloot, Alfons G. Hoekstra, C. J. Kenneth Tan, and Jack J. Dongarra. Berlin, Heidelberg: Springer, pp. 342–351. ISBN: 978-3-540-47789-1. DOI: 10.1007/3-540-47789-6\_36.
- Freier, Phyllis, E. J. Lofgren, E. P. Ney, F. Oppenheimer, H. L. Bradt, and B. Peters (1948). "Evidence for Heavy Nuclei in the Primary Cosmic Radiation". In: *Physical Review* 74.2, pp. 213–217. ISSN: 0031-899X. DOI: 10.1103/PhysRev.74.213.
- Fried, Burton D. and Samuel D. Conte (1961). The Plasma Dispersion Function. DOI: 10.1016/C2013-0-12176-9.

- Gabici, Stefano (2022). "Low-Energy Cosmic Rays: Regulators of the Dense Interstellar Medium". In: *The Astronomy and Astrophysics Review* 30.1, p. 4. ISSN: 1432-0754. DOI: 10.1007/s00159-022-00141-2.
- Gardiner, Thomas A. and James M. Stone (2005). "An Unsplit Godunov Method for Ideal MHD via Constrained Transport". In: *Journal of Computational Physics* 205, pp. 509–539. ISSN: 0021-9991. DOI: 10.1016/j.jcp.2004.11.016.
- Gargaté, L., R. Bingham, R. A. Fonseca, and L. O. Silva (2007). "dHybrid: A Massively Parallel Code for Hybrid Simulations of Space Plasmas". In: *Computer Physics Communications* 176.6, pp. 419–425. ISSN: 0010-4655. DOI: 10.1016/j.cpc.2006.11.013.
- Gary, S. Peter, Lan K. Jian, Thomas W. Broiles, Michael L. Stevens, John J. Podesta, and Justin C. Kasper (2016). "Ion-Driven Instabilities in the Solar Wind: Wind Observations of 19 March 2005". In: *Journal of Geophysical Research: Space Physics* 121.1, pp. 30–41. ISSN: 2169-9402. DOI: 10.1002/2015JA021935.
- Gary, S. Peter, Christian D. Madland, David Schriver, and Dan Winske (1986). "Computer Simulations of Electromagnetic Cool Ion Beam Instabilities". In: *Journal of Geophysical Research:* Space Physics 91.A4, pp. 4188–4200. ISSN: 0148-0227. DOI: 10.1029/JA091iA04p04188.
- Gary, S. Peter, Michelle F. Thomsen, and Stephen A. Fuselier (1986). "Electromagnetic Instabilities and Gyrophase-Bunched Particles". In: *The Physics of Fluids* 29.2, pp. 531–535. ISSN: 0031-9171. DOI: 10.1063/1.865441.
- Giacalone, J. and J. R. Jokipii (1999). "The Transport of Cosmic Rays across a Turbulent Magnetic Field". In: *The Astrophysical Journal* 520, pp. 204–214. ISSN: 0004-637X. DOI: 10.1086/307452.
- Ginzburg, V. L., V. S. Ptuskin, and V. N. Tsytovich (1973). "On the Role of Plasma Effects in the Cosmic Ray Propagation and Isotropization in the Galaxy". In: *Astrophysics and Space Science* 21.1, pp. 13–38. ISSN: 1572-946X. DOI: 10.1007/BF00642191.
- Ginzburg, V. L. and S. I. Syrovatskii (1964). The Origin of Cosmic Rays.
- Girichidis, Philipp, Thorsten Naab, Michał Hanasz, and Stefanie Walch (2018). "Cooler and Smoother the Impact of Cosmic Rays on the Phase Structure of Galactic Outflows". In: Monthly Notices of the Royal Astronomical Society 479, pp. 3042–3067. ISSN: 0035-8711. DOI: 10.1093/mnras/sty1653.
- Girichidis, Philipp et al. (2016). "The SILCC (SImulating the LifeCycle of Molecular Clouds) Project II. Dynamical Evolution of the Supernova-Driven ISM and the Launching of Outflows". In: 456.4, pp. 3432–3455. DOI: 10.1093/mnras/stv2742.
- Green, Melville S. (1952). "Markoff Random Processes and the Statistical Mechanics of Time-Dependent Phenomena". In: *The Journal of Chemical Physics* 20.8, pp. 1281–1295. ISSN: 0021-9606, 1089-7690. DOI: 10.1063/1.1700722.
- Greenstadt, E. W., M. M. Hoppe, and C. T. Russell (1982). "Large-Amplitude Magnetic Variations in Quasi-Parallel Shocks: Correlation Lengths Measured by ISEE 1 and 2". In: *Geophysical Research Letters* 9.7, pp. 781–784. ISSN: 1944-8007. DOI: 10.1029/GL009i007p00781.

- Grenier, Isabelle A., John H. Black, and Andrew W. Strong (2015). "The Nine Lives of Cosmic Rays in Galaxies". In: *Annual Review of Astronomy and Astrophysics* 53.1, pp. 199–246. ISSN: 0066-4146, 1545-4282. DOI: 10.1146/annurev-astro-082214-122457.
- Groot, Sybren Ruurds de and Leendert Gerrit Suttorp (1972). Foundations of Electrodynamics. Amsterdam: Noord-Hollandsche U.M.
- Guo, Fulai and S. Peng Oh (2008). "Feedback Heating by Cosmic Rays in Clusters of Galaxies". In: 384.1, pp. 251–266. DOI: 10.1111/j.1365-2966.2007.12692.x.
- Gupta, Siddhartha, Damiano Caprioli, and Anatoly Spitkovsky (2024). "Electron Acceleration at Quasi-parallel Nonrelativistic Shocks: A 1D Kinetic Survey". In: *The Astrophysical Journal* 976, p. 10. ISSN: 0004-637X. DOI: 10.3847/1538-4357/ad7c4c.
- Gurgiolo, C., G. K. Parks, B. H. Mauk, C. S. Lin, K. A. Anderson, R. P. Lin, and H. Reme (1981). "Non-E×B Ordered Ion Beams Upstream of the Earth's Bow Shock". In: *Journal of Geophysical Research* 86, pp. 4415–4424. ISSN: 0148-0227. DOI: 10.1029/JA086iA06p04415.
- Haggerty, Colby, Damiano Caprioli, and Ellen Zweibel (2019). "Hybrid Simulations of the Resonant and Non-Resonant Cosmic Ray Streaming Instability". In: *Proceedings of 36th International Cosmic Ray Conference PoS(ICRC2019)*. 36th International Cosmic Ray Conference. Madison, WI, U.S.A.: Sissa Medialab, p. 279. DOI: 10.22323/1.358.0279.
- Hakim, A., J. Loverich, and U. Shumlak (2006). "A High Resolution Wave Propagation Scheme for Ideal Two-Fluid Plasma Equations". In: *Journal of Computational Physics* 219.1, pp. 418–442. ISSN: 00219991. DOI: 10.1016/j.jcp.2006.03.036.
- Hammett, Gregory W. and Francis W. Perkins (1990). "Fluid Moment Models for Landau Damping with Application to the Ion-Temperature-Gradient Instability". In: *Physical Review Letters* 64.25, pp. 3019–3022. DOI: 10.1103/PhysRevLett.64.3019.
- Hanasz, M., H. Lesch, T. Naab, A. Gawryszczak, K. Kowalik, and D. Wóltański (2013). "Cosmic Rays Can Drive Strong Outflows from Gas-Rich High-Redshift Disk Galaxies". In: *ApJL* 777.L38 (2), p. L38. DOI: 10.1088/2041-8205/777/2/L38.
- Hanasz, Michał, Dominik Wóltański, and Kacper Kowalik (2009). "Global Galactic Dynamo Driven by Cosmic Rays and Exploding Magnetized Stars". In: *The Astrophysical Journal* 706, pp. L155–L159. ISSN: 0004-637X. DOI: 10.1088/0004-637X/706/1/L155.
- Harten, Ami and James M Hyman (1983). "Self Adjusting Grid Methods for One-Dimensional Hyperbolic Conservation Laws". In: *Journal of Computational Physics* 50.2, pp. 235–269. ISSN: 0021-9991. DOI: 10.1016/0021-9991(83)90066-9.
- Hess, V F (1912). "Über Beobachtungen Der Durchdringenden Strahlung Bei Sieben Freiballonfahrten". In: Z. Phys. 13, p. 1084.
- Hesthaven, Jan S. and Tim Warburton (2008). Nodal Discontinuous Galerkin Methods. Red. by J. E. Marsden, L. Sirovich, and S. S. Antman. Vol. 54. Texts in Applied Mathematics. New York, NY: Springer New York. ISBN: 978-0-387-72065-4 978-0-387-72067-8. DOI: 10.1007/978-0-387-72067-8.
- Hewett, Dennis W and A Bruce Langdon (1987). "Electromagnetic Direct Implicit Plasma Simulation". In: *Journal of Computational Physics* 72.1, pp. 121–155. ISSN: 0021-9991. DOI: 10.1016/0021-9991(87)90075-1.

- Higuera, A. V. and J. R. Cary (2017). "Structure-Preserving Second-Order Integration of Relativistic Charged Particle Trajectories in Electromagnetic Fields". In: *Physics of Plasmas* 24.5, p. 052104. ISSN: 1070-664X, 1089-7674. DOI: 10.1063/1.4979989.
- Hockney, R.W (1971). "Measurements of Collision and Heating Times in a Two-Dimensional Thermal Computer Plasma". In: *Journal of Computational Physics* 8.1, pp. 19–44. ISSN: 00219991. DOI: 10.1016/0021-9991(71)90032-5.
- Hockney, Roger W. (1988). Computer Simulation Using Particles. CRC Press. 1 p. ISBN: 978-0-367-80693-4.
- Holcomb, Cole and Anatoly Spitkovsky (2019). "On the Growth and Saturation of the Gyroresonant Streaming Instabilities". In: *The Astrophysical Journal* 882.1, p. 3. ISSN: 0004-637X. DOI: 10.3847/1538-4357/ab328a.
- Holcomb, Cole James (2019). "The Microphysics of Gyroresonant Streaming Instabilities and Cosmic Ray Self-Confinement". Princeton University.
- Hollweg, Joseph V. (1971). "Nonlinear Landau Damping of Alfvén Waves". In: *Physical Review Letters* 27.20, pp. 1349–1352. ISSN: 0031-9007. DOI: 10.1103/PhysRevLett.27.1349.
- Hong, Jinhy, Ensang Lee, Kyoungwook Min, and George K. Parks (2012). "Effect of Ion-to-Electron Mass Ratio on the Evolution of Ion Beam Driven Instability in Particle-in-Cell Simulations". In: *Physics of Plasmas* 19.092111 (9), p. 092111. DOI: 10.1063/1.4754002.
- Hoshino, M. and T. Terasawa (1985). "Numerical Study of the Upstream Wave Excitation Mechanism. I Nonlinear Phase Bunching of Beam Ions". In: *Journal of Geophysical Research* 90, pp. 57–64. ISSN: 0148-0227. DOI: 10.1029/JA090iA01p00057.
- Hsiao, Ling (1997). Quasilinear Hyperbolic Systems and Dissipative Mechanisms. Singapore: World Scientific. 223 pp. ISBN: 978-981-02-3205-4.
- Hunana, P., G. P. Zank, M. Laurenza, A. Tenerani, G. M. Webb, M. L. Goldstein, M. Velli, and L. Adhikari (2018). "New Closures for More Precise Modeling of Landau Damping in the Fluid Framework". In: *Physical Review Letters* 121.13, p. 135101. DOI: 10.1103/PhysRevLett.121. 135101.
- Hunana, P. et al. (2019). "An Introductory Guide to Fluid Models with Anisotropic Temperatures. Part 1. CGL Description and Collisionless Fluid Hierarchy". In: *Journal of Plasma Physics* 85.6, p. 205850602. ISSN: 0022-3778, 1469-7807. DOI: 10.1017/S0022377819000801.
- Hunana, P. et al. (2019). "An Introductory Guide to Fluid Models with Anisotropic Temperatures. Part 2. Kinetic Theory, Padé Approximants and Landau Fluid Closures". In: *Journal of Plasma Physics* 85.6. ISSN: 0022-3778, 1469-7807. DOI: 10.1017/S0022377819000850.
- IceCube Collaboration\* (2013). "Evidence for High-Energy Extraterrestrial Neutrinos at the IceCube Detector". In: *Science* 342.6161, p. 1242856. ISSN: 0036-8075, 1095-9203. DOI: 10.1126/science.1242856.
- Ipavich, F. M. (1975). "Galactic Winds Driven by Cosmic Rays." In: *The Astrophysical Journal* 196, pp. 107–120. ISSN: 0004-637X. DOI: 10.1086/153397.
- Ivlev, A. V., V. A. Dogiel, D. O. Chernyshov, P. Caselli, C.-M. Ko, and K. S. Cheng (2018). "Penetration of Cosmic Rays into Dense Molecular Clouds: Role of Diffuse Envelopes \*". In:

- The Astrophysical Journal 855.1, p. 23. ISSN: 0004-637X, 1538-4357. DOI: 10.3847/1538-4357/aaadb9.
- Jackson 1925-2016, John David (1999). Classical Electrodynamics. Third edition. New York: Wiley, [1999] © 1999.
- Jacob, Svenja and Christoph Pfrommer (2017). "Cosmic Ray Heating in Cool Core Clusters II. Self-regulation Cycle and Non-Thermal Emission". In: 467.2, pp. 1478–1495. DOI: 10.1093/mnras/stx132.
- (2017). "Cosmic Ray Heating in Cool Core Clusters I. Diversity of Steady State Solutions".
   In: Monthly Notices of the Royal Astronomical Society 467.2, pp. 1449–1477. ISSN: 0035-8711.
   DOI: 10.1093/mnras/stx131.
- Ji, Suoqing, T K Chan, Cameron B Hummels, Philip F Hopkins, Jonathan Stern, Dušan Kereš, Eliot Quataert, Claude-André Faucher-Giguère, and Norman Murray (2020). "Properties of the Circumgalactic Medium in Cosmic Ray-Dominated Galaxy Haloes". In: *Monthly Notices of the Royal Astronomical Society* 496.4, pp. 4221–4238. ISSN: 0035-8711. DOI: 10.1093/mnras/staa1849.
- Jiang, Guang-Shan and Chi-Wang Shu (1996). "Efficient Implementation of Weighted ENO Schemes". In: *Journal of Computational Physics* 126.1, pp. 202–228. ISSN: 0021-9991. DOI: 10.1006/jcph.1996.0130.
- Jiang, Yan-Fei and Peng Oh (2018). "A New Numerical Scheme for Cosmic Ray Transport". In: *The Astrophysical Journal* 854.1, p. 5. ISSN: 0004-637X, 1538-4357. DOI: 10.3847/1538-4357/aaa6ce. arXiv: 1712.07117 [astro-ph].
- Jikei, Taiki and Takanobu Amano (2021). "A Non-Local Fluid Closure for Modeling Cyclotron Resonance in Collisionless Magnetized Plasmas". In: *Physics of Plasmas* 28.4, p. 042105. ISSN: 1070-664X, 1089-7674. DOI: 10.1063/5.0045335.
- Jokipii, J. R. (1966). "Cosmic-Ray Propagation. I. Charged Particles in a Random Magnetic Field". In: *The Astrophysical Journal* 146, p. 480. ISSN: 0004-637X, 1538-4357. DOI: 10.1086/148912.
- Jokipii, J. R. and E. N. Parker (1969). "Stochastic Aspects of Magnetic Lines of Force with Application to Cosmic-Ray Propagation". In: *The Astrophysical Journal* 155, p. 777. ISSN: 0004-637X, 1538-4357. DOI: 10.1086/149909.
- Kemp, B. A. (2011). "Resolution of the Abraham-Minkowski Debate: Implications for the Electromagnetic Wave Theory of Light in Matter". In: *Journal of Applied Physics* 109.11, p. 111101. ISSN: 0021-8979, 1089-7550. DOI: 10.1063/1.3582151.
- Kempski, Philipp, Drummond B. Fielding, Eliot Quataert, Alisa K. Galishnikova, Matthew W. Kunz, Alexander A. Philippov, and Bart Ripperda (2023). "Cosmic Ray Transport in Large-Amplitude Turbulence with Small-Scale Field Reversals". In: *Monthly Notices of the Royal Astronomical Society* 525.4, pp. 4985–4998. ISSN: 0035-8711, 1365-2966. DOI: 10.1093/mnras/stad2609. arXiv: 2304.12335 [astro-ph, physics:physics].
- Kempski, Philipp and Eliot Quataert (2022). "Reconciling Cosmic Ray Transport Theory with Phenomenological Models Motivated by Milky-Way Data". In: *Monthly Notices of the Royal Astronomical Society* 514.1, pp. 657–674. ISSN: 0035-8711. DOI: 10.1093/mnras/stac1240.

- Kim, Chang-Goo and Eve C. Ostriker (2018). "Numerical Simulations of Multiphase Winds and Fountains from Star-Forming Galactic Disks. I. Solar Neighborhood TIGRESS Model". In: 853.173 (2), p. 173. DOI: 10.3847/1538-4357/aaa5ff.
- Kolobov, V. I. and R. R. Arslanbekov (2012). "Towards Adaptive Kinetic-Fluid Simulations of Weakly Ionized Plasmas". In: *Journal of Computational Physics*. Special Issue: Computational Plasma Physics 231.3, pp. 839–869. ISSN: 0021-9991. DOI: 10.1016/j.jcp.2011.05.036.
- Kubo, Ryogo (1957). "Statistical-Mechanical Theory of Irreversible Processes. I. General Theory and Simple Applications to Magnetic and Conduction Problems". In: *Journal of the Physical Society of Japan* 12.6, pp. 570–586. ISSN: 0031-9015. DOI: 10.1143/JPSJ.12.570.
- Kulikov, GV and GB Khristiansen (1959). "On the Size Spectrum of Extensive Air Showers". In: Soviet Physics–JETP [translation of Zhurnal Eksperimentalnoi i Teoreticheskoi Fiziki] 35.8, pp. 441–444.
- Kulsrud, Russell (2004). *Plasma Physics for Astrophysics*. Princeton University Press. ISBN: 978-0-691-12073-7.
- Kulsrud, Russell and William P. Pearce (1969). "The Effect of Wave-Particle Interactions on the Propagation of Cosmic Rays". In: *The Astrophysical Journal* 156, p. 445. ISSN: 0004-637X, 1538-4357. DOI: 10.1086/149981.
- Kunz, Matthew W., James M. Stone, and Xue-Ning Bai (2014). "Pegasus: A New Hybrid-Kinetic Particle-in-Cell Code for Astrophysical Plasma Dynamics". In: *Journal of Computational Physics* 259, pp. 154–174. ISSN: 0021-9991. DOI: 10.1016/j.jcp.2013.11.035.
- Lagage, P. O. and C. J. Cesarsky (1983). "The Maximum Energy of Cosmic Rays Accelerated by Supernova Shocks." In: *Astronomy and Astrophysics* 125, pp. 249–257. ISSN: 0004-6361.
- Lammer, H. et al. (2009). "What Makes a Planet Habitable?" In: *The Astronomy and Astrophysics Review* 17.2, pp. 181–249. ISSN: 1432-0754. DOI: 10.1007/s00159-009-0019-z.
- Landau, Lev Davidovič, Evgenij M. Lifšic, Lev Davidovič Landau, and Lev Davidovič Landau (1990). Elektrodynamik der Kontinua: 2 Tabellen. 5., von E. M. Lifschitz u. L. P. Pitajewski erg. u. berichtigte Aufl. Lehrbuch der theoretischen Physik / von L. D. Landau; E. M. Lifschitz 8. Berlin: Akademie-Verlag. 565 pp. ISBN: 978-3-05-500072-0 978-3-8171-1333-0 978-3-8085-5500-2
- Langdon, A. Bruce and Charles K. Birdsall (1970). "Theory of Plasma Simulation Using Finite-Size Particles". In: *The Physics of Fluids* 13.8, pp. 2115–2122. ISSN: 0031-9171. DOI: 10.1063/1.1693209.
- Langdon, A.Bruce (1970). "Effects of the Spatial Grid in Simulation Plasmas". In: *Journal of Computational Physics* 6.2, pp. 247–267. ISSN: 00219991. DOI: 10.1016/0021-9991(70)90024-0.
- Lazarian, A. (2016). "Damping of Alfvén Waves by Turbulence and Its Consequences: From Cosmic-Ray Streaming to Launching Winds". DOI: 10.3847/1538-4357/833/2/131. arXiv: 1607.02042 [astro-ph.HE].
- Lazarian, Alex and Siyao Xu (2022). "Damping of Alfvén Waves in MHD Turbulence and Implications for Cosmic Ray Streaming Instability and Galactic Winds". In: Frontiers in Physics 10.702799, p. 702799. DOI: 10.3389/fphy.2022.702799. arXiv: 2201.05168 [astro-ph.GA].

- Lebiga, O, R Santos-Lima, and H Yan (2018). "Kinetic-MHD Simulations of Gyroresonance Instability Driven by CR Pressure Anisotropy". In: *Monthly Notices of the Royal Astronomical Society* 476.2, pp. 2779–2791. ISSN: 0035-8711, 1365-2966. DOI: 10.1093/mnras/sty309.
- Lee, Martin A. and Heinrich J. Völk (1973). "Damping and Nonlinear Wave-Particle Interactions of Alfvén-waves in the Solar Wind". In: *Astrophysics and Space Science* 24.1, pp. 31–49. ISSN: 1572-946X. DOI: 10.1007/BF00648673.
- Lemmerz, Rouven, Mohamad Shalaby, Christoph Pfrommer, and Timon Thomas (2024). *The Theory of Resonant Cosmic Ray-Driven Instabilities Growth and Saturation of Single Modes*. DOI: 10.3847/1538-4357/ad8eb3. arXiv: 2406.04400 [astro-ph, physics:physics]. Prepublished.
- Lemmerz, Rouven, Mohamad Shalaby, Timon Thomas, and Christoph Pfrommer (2024). "Coupling Multi-Fluid Dynamics Equipped with Landau Closures to the Particle-in-Cell Method". In: *Journal of Plasma Physics* 90.1, p. 905900104. ISSN: 0022-3778, 1469-7807. DOI: 10.1017/S0022377823001113.
- Lemoine, Martin (2019). "Generalized Fermi Acceleration". In: *Physical Review D* 99.8, p. 083006. ISSN: 2470-0010, 2470-0029. DOI: 10.1103/PhysRevD.99.083006.
- (2023). "Particle Transport through Localized Interactions with Sharp Magnetic Field Bends in MHD Turbulence". In: *Journal of Plasma Physics* 89.5, p. 175890501. ISSN: 0022-3778, 1469-7807. DOI: 10.1017/S0022377823000946. arXiv: 2304.03023 [astro-ph, physics:physics].
- Lemoine, Martin, Kumiko Kotera, and Jérôme Pétri (2015). "On Ultra-High Energy Cosmic Ray Acceleration at the Termination Shock of Young Pulsar Winds". In: *Journal of Cosmology and Astroparticle Physics* 2015.07, pp. 016–016. ISSN: 1475-7516. DOI: 10.1088/1475-7516/2015/07/016. arXiv: 1409.0159 [astro-ph].
- Lerche, I. (1967). "Unstable Magnetosonic Waves in a Relativistic Plasma". In: *The Astrophysical Journal* 147, p. 689. ISSN: 0004-637X, 1538-4357. DOI: 10.1086/149045.
- LeVeque, Randall J and Marica Pelanti (2001). "A Class of Approximate Riemann Solvers and Their Relation to Relaxation Schemes". In: *Journal of Computational Physics* 172.2, pp. 572–591. ISSN: 0021-9991. DOI: 10.1006/jcph.2001.6838.
- LeVeque, Randall J. (2002). Finite Volume Methods for Hyperbolic Problems. Cambridge Texts in Applied Mathematics. Cambridge: Cambridge University Press. DOI: 10.1017/CB09780511791253.
- Lewis, H. Ralph (1970). "Energy-Conserving Numerical Approximations for Vlasov Plasmas". In: Journal of Computational Physics 6.1, pp. 136–141. DOI: 10.1016/0021-9991(70)90012-4.
- Lipatov, Alexander S. (2002). *The Hybrid Multiscale Simulation Technology*. Scientific Computation. Berlin, Heidelberg: Springer Berlin Heidelberg. ISBN: 978-3-642-07508-7 978-3-662-05012-5. DOI: 10.1007/978-3-662-05012-5.
- Lucek, S. G. and A. R. Bell (2000). "Non-Linear Amplification of a Magnetic Field Driven by Cosmic Ray Streaming". In: *Monthly Notices of the Royal Astronomical Society* 314.1, pp. 65–74. ISSN: 0035-8711, 1365-2966. DOI: 10.1046/j.1365-8711.2000.03363.x.
- Lutomirski, R. F. and R. N. Sudan (1966). "Exact Nonlinear Electromagnetic Whistler Modes". In: *Physical Review* 147, pp. 156–165. ISSN: 1536-6065. DOI: 10.1103/PhysRev.147.156.

- Marcowith, A., A. J. van Marle, and I. Plotnikov (2021). "The Cosmic Ray-Driven Streaming Instability in Astrophysical and Space Plasmas". In: *Physics of Plasmas* 28, p. 080601. ISSN: 1070-664X. DOI: 10.1063/5.0013662.
- Marcowith, A. et al. (2016). "The Microphysics of Collisionless Shock Waves". In: *Reports on Progress in Physics* 79.4, p. 046901. ISSN: 0034-4885. DOI: 10.1088/0034-4885/79/4/046901.
- Marcowith, Alexandre, Gilles Ferrand, Mickael Grech, Zakaria Meliani, Illya Plotnikov, and Rolf Walder (2020). "Multi-Scale Simulations of Particle Acceleration in Astrophysical Systems". In: Living Reviews in Computational Astrophysics 6.1, p. 1. ISSN: 2365-0524. DOI: 10.1007/s41115-020-0007-6.
- Markidis, Stefano and Giovanni Lapenta (2011). "The Energy Conserving Particle-in-Cell Method". In: *Journal of Computational Physics* 230.18, pp. 7037–7052. ISSN: 0021-9991. DOI: 10.1016/j.jcp.2011.05.033.
- Maron, Jason and Peter Goldreich (2001). "Simulations of Incompressible Magnetohydrodynamic Turbulence". In: *The Astrophysical Journal* 554, pp. 1175–1196. ISSN: 0004-637X. DOI: 10.1086/321413.
- McMillan, B. F. (2020). "Is It Necessary to Resolve the Debye Length in Standard or Delta-f PIC Codes?" In: *Physics of Plasmas* 27.5, p. 052106. ISSN: 1070-664X, 1089-7674. DOI: 10.1063/1.5139957.
- Mignone, A., G. Bodo, B. Vaidya, and G. Mattia (2018). "A Particle Module for the PLUTO Code. I. An Implementation of the MHD-PIC Equations". In: *The Astrophysical Journal* 859.1, p. 13. ISSN: 0004-637X. DOI: 10.3847/1538-4357/aabccd.
- Millikan, Robert Andrews (1925). "High Frequency Rays of Cosmic Origin". In: *Science* 62.1612, pp. 445–448. ISSN: 0036-8075. JSTOR: 1648786.
- Moreno, Q., M. E. Dieckmann, X. Ribeyre, S. Jequier, V. T. Tikhonchuk, and E. d'Humières (2018). "Impact of the Electron to Ion Mass Ratio on Unstable Systems in Particle-in-Cell Simulations". In: *Physics of Plasmas* 25.062125 (6), p. 062125. DOI: 10.1063/1.5027913.
- Morse, R. L. and C. W. Nielson (1969). "One-, Two-, and Three-Dimensional Numerical Simulation of Two-Beam Plasmas". In: *Physical Review Letters* 23.19, pp. 1087–1090. ISSN: 0031-9007. DOI: 10.1103/PhysRevLett.23.1087.
- Moschüring, Nils (2020). "Effects and Adaptation of Particle Noise in Large-Scale PIC Simulations". Ludwig-Maximilians-Universität München.
- Moster, Benjamin P., Thorsten Naab, and Simon D. M. White (2013). "Galactic Star Formation and Accretion Histories from Matching Galaxies to Dark Matter Haloes". In: 428.4, pp. 3121–3138. DOI: 10.1093/mnras/sts261.
- Muñoz, P. A., N. Jain, P. Kilian, and J. Büchner (2018). "A New Hybrid Code (CHIEF) Implementing the Inertial Electron Fluid Equation without Approximation". In: *Computer Physics Communications* 224, pp. 245–264. ISSN: 0010-4655. DOI: 10.1016/j.cpc.2017.10.012.
- Nakamura, Kenzo (2010). "Review of Particle Physics". In: Journal of Physics G: Nuclear and Particle Physics 37 (7 A).

- Ng, Jonathan, A. Hakim, L. Wang, and A. Bhattacharjee (2020). "An Improved Ten-Moment Closure for Reconnection and Instabilities". In: *Physics of Plasmas* 27.8, p. 082106. ISSN: 1070-664X. DOI: 10.1063/5.0012067.
- Niemiec, Jacek, Martin Pohl, Thomas Stroman, and Ken-Ichi Nishikawa (2008). "Production of Magnetic Turbulence by Cosmic Rays Drifting Upstream of Supernova Remnant Shocks". In: *The Astrophysical Journal* 684.2, p. 1174. ISSN: 0004-637X. DOI: 10.1086/590054.
- Oraevskii, V, R Chodura, and W Feneberg (1968). "Hydrodynamic Equations for Plasmas in Strong Magnetic Fields I: Collisionless Approximation". In: *Plasma Physics* 10.9, pp. 819–828. ISSN: 0032-1028. DOI: 10.1088/0032-1028/10/9/302.
- Otani, Niels F. (1988). "Application of Nonlinear Dynamical Invariants in a Single Electromagnetic Wave to the Study of the Alfvén-ion-cyclotron Instability". In: *The Physics of Fluids* 31.6, pp. 1456–1464. ISSN: 0031-9171. DOI: 10.1063/1.866736.
- Pacini, Domenico, translated, commented by Michela De Maria, and Alessandro De Angelis (1910). *Penetrating Radiation on the Sea.* arXiv: 1101.3015 [physics]. Pre-published.
- Padovani, Marco et al. (2020). "Impact of Low-Energy Cosmic Rays on Star Formation". In: Space Science Reviews 216, p. 29. ISSN: 0038-6308. DOI: 10.1007/s11214-020-00654-1.
- Pakmor, R., C. Pfrommer, C. M. Simpson, and V. Springel (2016). "Galactic Winds Driven by Isotropic and Anisotropic Cosmic-Ray Diffusion in Disk Galaxies". In: *The Astrophysical Journal* 824, p. L30. ISSN: 0004-637X. DOI: 10.3847/2041-8205/824/2/L30.
- Palmroth, Minna et al. (2018). "Vlasov Methods in Space Physics and Astrophysics". In: Living Reviews in Computational Astrophysics 4.1, p. 1. ISSN: 2367-3621, 2365-0524. DOI: 10.1007/s41115-018-0003-2. arXiv: 1808.05885 [physics].
- Pandey, B. P. and Mark Wardle (2008). "Hall Magnetohydrodynamics of Partially Ionized Plasmas". In: *Monthly Notices of the Royal Astronomical Society* 385, pp. 2269–2278. ISSN: 0035-8711. DOI: 10.1111/j.1365-2966.2008.12998.x.
- Park, W. et al. (1992). "Three-Dimensional Hybrid Gyrokinetic-Magnetohydrodynamics Simulation". In: *Physics of Fluids B* 4.7, pp. 2033–2037. DOI: 10.1063/1.860011.
- Parker, E. N. (1992). "Fast Dynamos, Cosmic Rays, and the Galactic Magnetic Field". In: 401, p. 137. DOI: 10.1086/172046.
- Parker, S. E. and W. W. Lee (1993). "A Fully Nonlinear Characteristic Method for Gyrokinetic Simulation". In: *Physics of Fluids B: Plasma Physics* 5.1, pp. 77–86. ISSN: 0899-8221. DOI: 10.1063/1.860870.
- Passot, T. and P. L. Sulem (2004). "A Landau Fluid Model for Dispersive Magnetohydrodynamics". In: *Physics of Plasmas* 11.11, pp. 5173–5189. ISSN: 1070-664X, 1089-7674. DOI: 10.1063/1.1780533.
- (2007). "Collisionless Magnetohydrodynamics with Gyrokinetic Effects". In: *Physics of Plasmas* 14.8, p. 082502. ISSN: 1070-664X. DOI: 10.1063/1.2751601.
- Passot, Thierry, Pierre Henri, Dimitri Laveder, and Pierre-Louis Sulem (2014). "Fluid Simulations of Ion Scale Plasmas with Weakly Distorted Magnetic Fields". In: *The European Physical Journal D* 68.7, p. 207. ISSN: 1434-6079. DOI: 10.1140/epjd/e2014-50160-1.

- Peery, K. and S. Imlay (1988). "Blunt-Body Flow Simulations". In: 24th Joint Propulsion Conference. 24th Joint Propulsion Conference. Boston, MA, U.S.A.: American Institute of Aeronautics and Astronautics. DOI: 10.2514/6.1988-2904.
- Pfrommer, C., R. Pakmor, K. Schaal, C. M. Simpson, and V. Springel (2017). "Simulating Cosmic Ray Physics on a Moving Mesh". DOI: 10.1093/mnras/stw2941. arXiv: 1604.07399 [astro-ph.GA].
- Pfrommer, Christoph (2013). "Toward a Comprehensive Model for Feedback by Active Galactic Nuclei: New Insights from M87 Observations by LOFAR, Fermi, and HESS". In: *The Astrophysical Journal* 779.1, p. 10. ISSN: 0004-637X. DOI: 10.1088/0004-637X/779/1/10.
- Pierre Auger Collaboration et al. (2007). "Correlation of the Highest-Energy Cosmic Rays with Nearby Extragalactic Objects". In: *Science* 318, p. 938. ISSN: 0036-8075. DOI: 10.1126/science.1151124.
- Pirozzoli, Sergio (2011). "Numerical Methods for High-Speed Flows". In: *Annual Review of Fluid Mechanics* 43.1, pp. 163–194. ISSN: 0066-4189, 1545-4479. DOI: 10.1146/annurev-fluid-122109-160718.
- Plotnikov, Illya, Eve C. Ostriker, and Xue-Ning Bai (2021). "Influence of Ion-Neutral Damping on the Cosmic-Ray Streaming Instability: Magnetohydrodynamic Particle-in-cell Simulations". In: *The Astrophysical Journal* 914, p. 3. ISSN: 0004-637X. DOI: 10.3847/1538-4357/abf7b3.
- Pohl, Martin, Masahiro Hoshino, and Jacek Niemiec (2020). "PIC Simulation Methods for Cosmic Radiation and Plasma Instabilities". In: *Progress in Particle and Nuclear Physics* 111, p. 103751. ISSN: 01466410. DOI: 10.1016/j.ppnp.2019.103751. arXiv: 1912.02673 [astro-ph].
- Powell, Kenneth G., Philip L. Roe, Timur J. Linde, Tamas I. Gombosi, and Darren L. De Zeeuw (1999). "A Solution-Adaptive Upwind Scheme for Ideal Magnetohydrodynamics". In: *Journal of Computational Physics* 154.2, pp. 284–309. ISSN: 00219991. DOI: 10.1006/jcph.1999.6299.
- Protheroe, R. J. and A. P. Szabo (1992). "High Energy Cosmic Rays from Active Galactic Nuclei". In: *Physical Review Letters* 69, pp. 2885–2888. ISSN: 0031-9007. DOI: 10.1103/PhysRevLett.69.2885.
- Ptuskin, V. S., S. I. Rogovaya, V. N. Zirakashvili, L. G. Chuvilgin, G. B. Khristiansen, E. G. Klepach, and G. V. Kulikov (1993). "Diffusion and Drift of Very High Energy Cosmic Rays in Galactic Magnetic Fields". In: 268.2, pp. 726–735.
- Ptuskin, V. S., V. N. Zirakashvili, and A. A. Plesser (2008). "Non-Linear Diffusion of Cosmic Rays". In: *Advances in Space Research* 42.3, pp. 486–490. ISSN: 0273-1177. DOI: 10.1016/j.asr.2007.12.007.
- Qin, Hong, Shuangxi Zhang, Jianyuan Xiao, Jian Liu, Yajuan Sun, and William M. Tang (2013). "Why Is Boris Algorithm so Good?" In: *Physics of Plasmas* 20, p. 084503. ISSN: 1070-664X. DOI: 10.1063/1.4818428.
- Qiu, Jing-Mei and Chi-Wang Shu (2011). "Conservative High Order Semi-Lagrangian Finite Difference WENO Methods for Advection in Incompressible Flow". In: *Journal of Computational Physics* 230.4, pp. 863–889. ISSN: 0021-9991. DOI: 10.1016/j.jcp.2010.04.037.

- Rathjen, Tim-Eric, Thorsten Naab, Philipp Girichidis, Stefanie Walch, Richard Wünsch, Frantisek Dinnbier, Daniel Seifried, Ralf S. Klessen, and Simon C. O. Glover (2021). "SILCC VI-Multiphase ISM Structure, Stellar Clustering, and Outflows with Supernovae, Stellar Winds, Ionizing Radiation, and Cosmic Rays". DOI: 10.1093/mnras/stab900. arXiv: 2103.14128 [astro-ph.GA].
- Recchia, Sarah (2020). "Cosmic Ray Driven Galactic Winds". In: *International Journal of Modern Physics D* 29.07, p. 2030006. ISSN: 0218-2718, 1793-6594. DOI: 10.1142/S0218271820300062. arXiv: 2101.02052 [astro-ph].
- Recchia, Sarah and Stefano Gabici (2024). "On the Origin of the Spectral Features Observed in the Cosmic Ray Spectrum". In: *Astronomy & Astrophysics* 692, A20. ISSN: 0004-6361, 1432-0746. DOI: 10.1051/0004-6361/202349005. arXiv: 2312.11397 [astro-ph].
- Reichherzer, P, J Becker Tjus, E G Zweibel, L Merten, and M J Pueschel (2020). "Turbulence-Level Dependence of Cosmic Ray Parallel Diffusion". In: *Monthly Notices of the Royal Astronomical Society* 498.4, pp. 5051–5064. ISSN: 0035-8711. DOI: 10.1093/mnras/staa2533.
- Reville, B. and A. R. Bell (2012). "A Filamentation Instability for Streaming Cosmic Rays: Cosmic Ray Filamentation Instability". In: *Monthly Notices of the Royal Astronomical Society* 419.3, pp. 2433–2440. ISSN: 00358711. DOI: 10.1111/j.1365-2966.2011.19892.x.
- Rieger, Frank M. (2022). "Active Galactic Nuclei as Potential Sources of Ultra-High Energy Cosmic Rays". In: *Universe* 8, p. 607. DOI: 10.3390/universe8110607.
- Riquelme, Mario A. and Anatoly Spitkovsky (2009). "Nonlinear Study of Bell's Cosmic Ray Current-Driven Instability". In: *The Astrophysical Journal* 694, pp. 626–642. ISSN: 0004-637X. DOI: 10.1088/0004-637X/694/1/626.
- Roberts, Charles S. and S. J. Buchsbaum (1964). "Motion of a Charged Particle in a Constant Magnetic Field and a Transverse Electromagnetic Wave Propagating along the Field". In: *Physical Review* 135, pp. 381–389. ISSN: 1536-6065. DOI: 10.1103/PhysRev.135.A381.
- Rochester, G. D. and C. C. Butler (1947). "Evidence for the Existence of New Unstable Elementary Particles". In: *Nature* 160, pp. 855–857. ISSN: 0028-0836. DOI: 10.1038/160855a0.
- Roe, P. L (1981). "Approximate Riemann Solvers, Parameter Vectors, and Difference Schemes". In: *Journal of Computational Physics* 43.2, pp. 357–372. ISSN: 0021-9991. DOI: 10.1016/0021-9991(81)90128-5.
- Roennmark, K. (1982). "Waves in Homogeneous, Anisotropic Multicomponent Plasmas (WHAMP)". In: *Unknown*.
- Rosdahl, Joakim, Joop Schaye, Romain Teyssier, and Oscar Agertz (2015). "Galaxies That Shine: Radiation-Hydrodynamical Simulations of Disc Galaxies". In: 451.1, pp. 34–58. DOI: 10.1093/mnras/stv937.
- Rowlands, J., V. D. Shapiro, and V. I. Shevchenko (1966). "Quasilinear Theory of Plasma Cyclotron Instability". In: *Soviet Journal of Experimental and Theoretical Physics* 23, p. 651. ISSN: 1063-7761.
- Ruszkowski, Mateusz and Christoph Pfrommer (2023). "Cosmic Ray Feedback in Galaxies and Galaxy Clusters: A Pedagogical Introduction and a Topical Review of the Acceleration, Trans-

- port, Observables, and Dynamical Impact of Cosmic Rays". In: The Astronomy and Astrophysics Review 31.1, p. 4. ISSN: 0935-4956, 1432-0754. DOI: 10.1007/s00159-023-00149-2.
- Ruszkowski, Mateusz, H.-Y. Karen Yang, and Christopher S. Reynolds (2017). "Cosmic-Ray Feedback Heating of the Intracluster Medium". In: *The Astrophysical Journal* 844.1, p. 13. ISSN: 0004-637X. DOI: 10.3847/1538-4357/aa79f8.
- Ruszkowski, Mateusz, H.-Y. Karen Yang, and Ellen Zweibel (2017). "Global Simulations of Galactic Winds Including Cosmic-ray Streaming". In: *The Astrophysical Journal* 834.2, p. 208. ISSN: 0004-637X, 1538-4357. DOI: 10.3847/1538-4357/834/2/208.
- Salem, Munier and Greg L. Bryan (2014). "Cosmic Ray Driven Outflows in Global Galaxy Disc Models". In: 437.4, pp. 3312–3330. DOI: 10.1093/mnras/stt2121.
- Sangeeth, Simon and J. C. Mandal (2019). "A Simple Cure for Numerical Shock Instability in the HLLC Riemann Solver". In: *Journal of Computational Physics* 378, pp. 477–496. ISSN: 0021-9991. DOI: 10.1016/j.jcp.2018.11.022.
- Schlickeiser, Reinhard (1989). "Cosmic-Ray Transport and Acceleration I. Derivation of the Kinetic Equation and Application to Cosmic Rays in Static Cold Media". In: ApJ. . . 336.1.
- (2002). Cosmic Ray Astrophysics. Red. by I. Appenzeller, G. Börner, M. A. Dopita, M. Harwit,
   R. Kippenhahn, J. Lequeux, A. Maeder, and V. Trimble. Astronomy and Astrophysics Library.
   Berlin, Heidelberg: Springer Berlin Heidelberg. ISBN: 978-3-642-08573-4 978-3-662-04814-6.
   DOI: 10.1007/978-3-662-04814-6.
- Schlickeiser, Reinhard and James A. Miller (1998). "Quasi-linear Theory of Cosmic Ray Transport and Acceleration: The Role of Oblique Magnetohydrodynamic Waves and Transit-Time Damping". In: *The Astrophysical Journal* 492.1, pp. 352–378. ISSN: 0004-637X, 1538-4357. DOI: 10.1086/305023.
- Schroer, B, O Pezzi, D Caprioli, C C Haggerty, and P Blasi (2022). "Cosmic-Ray Generated Bubbles around Their Sources". In: *Monthly Notices of the Royal Astronomical Society* 512.1, pp. 233–244. ISSN: 0035-8711, 1365-2966. DOI: 10.1093/mnras/stac466.
- Schroer, Benedikt, Damiano Caprioli, and Pasquale Blasi (2024). The Role of Non-Linear Landau Damping for Cosmic-Ray Transport. arXiv e-prints. DOI: 10.48550/arXiv.2409.02230. Prepublished.
- Schween, Nils Walter, Florian Schulze, and Brian Reville (2024). Sapphire++: A Particle Transport Code Combining a Spherical Harmonic Expansion and the Discontinuous Galerkin Method. DOI: 10.2139/ssrn.4808843. Social Science Research Network: 4808843. Pre-published.
- Shalaby, Mohamad, Avery E. Broderick, Philip Chang, Christoph Pfrommer, Astrid Lamberts, and Ewald Puchwein (2017). "Importance of Resolving the Spectral Support of Beam-plasma Instabilities in Simulations". In: *The Astrophysical Journal* 848.2, p. 81. ISSN: 0004-637X. DOI: 10.3847/1538-4357/aa8b17.
- (2017). "SHARP: A Spatially Higher-order, Relativistic Particle-in-cell Code". In: *The Astro-physical Journal* 841.1, p. 52. ISSN: 0004-637X. DOI: 10.3847/1538-4357/aa6d13.
- (2018). "Growth of Beam-Plasma Instabilities in the Presence of Background Inhomogeneity".
   In: The Astrophysical Journal 859.1, p. 45. ISSN: 1538-4357. DOI: 10.3847/1538-4357/aabe92.
   arXiv: 1804.05071 [astro-ph, physics:physics].

- Shalaby, Mohamad, Avery E. Broderick, Philip Chang, Christoph Pfrommer, Ewald Puchwein, and Astrid Lamberts (2020). "The Growth of the Longitudinal Beam–Plasma Instability in the Presence of an Inhomogeneous Background". In: *Journal of Plasma Physics* 86.2. ISSN: 0022-3778, 1469-7807. DOI: 10.1017/S0022377820000215.
- Shalaby, Mohamad, Rouven Lemmerz, Timon Thomas, and Christoph Pfrommer (2022). "The Mechanism of Efficient Electron Acceleration at Parallel Nonrelativistic Shocks". In: *The Astrophysical Journal* 932.2, p. 86. ISSN: 0004-637X, 1538-4357. DOI: 10.3847/1538-4357/ac6ce7.
- Shalaby, Mohamad, Timon Thomas, and Christoph Pfrommer (2021). "A New Cosmic-Raydriven Instability". In: *The Astrophysical Journal* 908.2, p. 206. ISSN: 1538-4357. DOI: 10.3847/1538-4357/abd02d.
- Shalaby, Mohamad, Timon Thomas, Christoph Pfrommer, Rouven Lemmerz, and Virginia Bresci (2023). "Deciphering the Physical Basis of the Intermediate-Scale Instability". In: *Journal of Plasma Physics* 89.6, p. 175890603. ISSN: 0022-3778, 1469-7807. DOI: 10.1017/S0022377823001289.
- Shalchi, A., J. W. Bieber, W. H. Matthaeus, and G. Qin (2004). "Nonlinear Parallel and Perpendicular Diffusion of Charged Cosmic Rays in Weak Turbulence". In: *The Astrophysical Journal* 616.1, pp. 617–629. ISSN: 0004-637X, 1538-4357. DOI: 10.1086/424839.
- Shapiro, VD and VI Shevchenko (1964). "Quasilinear Theory of Instability of a Plasma with an Anisotropic Ion Velocity Distribution". In: Soviet Physics–JETP [translation of Zhurnal Eksperimentalnoi i Teoreticheskoi Fiziki] 18, pp. 1109–1116.
- Shevchenko, V. I., V. L. Galinsky, and S. K. Ride (2002). "Excitation of Left-Hand-Polarized Nonlinear Alfvén Waves by an Ion Beam in a Plasma". In: *Journal of Geophysical Research:* Space Physics 107.A11, SSH 10-1-SSH 10-12. ISSN: 2156-2202. DOI: 10.1029/2001JA009208.
- Shoucri, Magdi M. (1979). "Nonlinear Evolution of the Bump-on-tail Instability". In: The Physics of Fluids 22.10, pp. 2038–2039. ISSN: 0031-9171. DOI: 10.1063/1.862470.
- Shumlak, U., R. Lilly, N. Reddell, E. Sousa, and B. Srinivasan (2011). "Advanced Physics Calculations Using a Multi-Fluid Plasma Model". In: *Computer Physics Communications* 182.9, pp. 1767–1770. ISSN: 00104655. DOI: 10.1016/j.cpc.2010.12.048.
- Shumlak, U. and J. Loverich (2003). "Approximate Riemann Solver for the Two-Fluid Plasma Model". In: *Journal of Computational Physics* 187.2, pp. 620–638. ISSN: 0021-9991. DOI: 10.1016/S0021-9991(03)00151-7.
- Sike, Brandon, Timon Thomas, Mateusz Ruszkowski, Christoph Pfrommer, and Matthias Weber (2024). "Cosmic Ray-Driven Galactic Winds with Resolved ISM and Ion-Neutral Damping". In: arXiv e-prints, arXiv:2410.06988. DOI: 10.48550/arXiv.2410.06988. arXiv: 2410.06988 [astro-ph.GA].
- Simpson, Christine M., Rüdiger Pakmor, Federico Marinacci, Christoph Pfrommer, Volker Springel, Simon C. O. Glover, Paul C. Clark, and Rowan J. Smith (2016). "The Role of Cosmic-Ray Pressure in Accelerating Galactic Outflows". In: *The Astrophysical Journal* 827, p. L29. ISSN: 0004-637X. DOI: 10.3847/2041-8205/827/2/L29.

- Simpson, Christine M., Rüdiger Pakmor, Christoph Pfrommer, Simon C. O. Glover, and Rowan Smith (2023). "How Cosmic Rays Mediate the Evolution of the Interstellar Medium". DOI: 10.1093/mnras/stac3601. arXiv: 2204.02410 [astro-ph.GA].
- Simpson, J. A. and M. Garcia-Munoz (1988). "Cosmic-Ray Lifetime in the Galaxy Experimental Results and Models". In: 46.3-4, pp. 205–224. DOI: 10.1007/BF00212240.
- Sironi, Lorenzo and Anatoly Spitkovsky (2011). "Particle Acceleration in Relativistic Magnetized Collisionless Electron-Ion Shocks". In: *The Astrophysical Journal* 726, p. 75. ISSN: 0004-637X. DOI: 10.1088/0004-637X/726/2/75.
- (2014). "Relativistic Reconnection: An Efficient Source of Non-Thermal Particles". In: The Astrophysical Journal 783.1, p. L21. ISSN: 2041-8205, 2041-8213. DOI: 10.1088/2041-8205/783/1/L21. arXiv: 1401.5471.
- Sironi, Lorenzo, Anatoly Spitkovsky, and Jonathan Arons (2013). "The Maximum Energy of Accelerated Particles in Relativistic Collisionless Shocks". In: *The Astrophysical Journal* 771.1, p. 54. ISSN: 0004-637X. DOI: 10.1088/0004-637X/771/1/54.
- Skilling, J. (1975). "Cosmic Ray Streaming–I Effect of Alfven Waves on Particles". In: *Monthly Notices of the Royal Astronomical Society* 172.3, pp. 557–566. ISSN: 0035-8711, 1365-2966. DOI: 10.1093/mnras/172.3.557.
- (1975). "Cosmic Ray Streaming-II Effect of Particles on Alfven Waves". In: Monthly Notices of the Royal Astronomical Society 173.2, pp. 245-254. ISSN: 0035-8711, 1365-2966. DOI: 10.1093/mnras/173.2.245.
- (1975). "Cosmic Ray Streaming-III Self-consistent Solutions". In: Monthly Notices of the Royal Astronomical Society 173.2, pp. 255–269. ISSN: 0035-8711, 1365-2966. DOI: 10.1093/mnras/173.2.255.
- Skilling, John (1971). "Cosmic Rays in the Galaxy: Convection or Diffusion?" In: *The Astro-*physical Journal 170, p. 265. ISSN: 0004-637X. DOI: 10.1086/151210.
- Snyder, P. B., G. W. Hammett, and W. Dorland (1997). "Landau Fluid Models of Collisionless Magnetohydrodynamics". In: *Physics of Plasmas* 4.11, pp. 3974–3985. ISSN: 1070-664X. DOI: 10.1063/1.872517.
- Soares Frazao, Sandra and Yves Zech (2002). "Undular Bores and Secondary Waves Experiments and Hybrid Finite-Volume Modelling". In: *Journal of Hydraulic Research* 40.1, pp. 33–43. ISSN: 0022-1686, 1814-2079. DOI: 10.1080/00221680209499871.
- Sonnendrücker, Eric, Jean Roche, Pierre Bertrand, and Alain Ghizzo (1999). "The Semi-Lagrangian Method for the Numerical Resolution of the Vlasov Equation". In: *Journal of Computational Physics* 149.2, pp. 201–220. ISSN: 00219991. DOI: 10.1006/jcph.1998.6148.
- Spitkovsky, Anatoly (2008). "Particle Acceleration in Relativistic Collisionless Shocks: Fermi Process at Last?" In: *The Astrophysical Journal* 682.1, p. L5. ISSN: 0004-637X. DOI: 10.1086/590248.
- Steininger, Theo et al. (2019). "NIFT y 3 Numerical Information Field Theory: A Python Framework for Multicomponent Signal Inference on HPC Clusters". In: *Annalen der Physik* 531.3, p. 1800290. ISSN: 0003-3804, 1521-3889. DOI: 10.1002/andp.201800290.

- Stix, Thomas Howard (1992). Waves in Plasmas. New York: AIP. 566 pp. ISBN: 978-0-88318-859-0.
- Strang, Gilbert (1968). "On the Construction and Comparison of Difference Schemes". In: SIAM Journal on Numerical Analysis 5.3, pp. 506–517. ISSN: 0036-1429. DOI: 10.1137/0705041.
- Strong, A. W. and I. V. Moskalenko (1998). "Propagation of Cosmic-Ray Nucleons in the Galaxy". In: *The Astrophysical Journal* 509.1, pp. 212–228. ISSN: 0004-637X, 1538-4357. DOI: 10.1086/306470. arXiv: astro-ph/9807150.
- Strong, Andrew W., Igor V. Moskalenko, and Vladimir S. Ptuskin (2007). "Cosmic-Ray Propagation and Interactions in the Galaxy". In: *Annual Review of Nuclear and Particle Science* 57, pp. 285–327. ISSN: 0163-8998. DOI: 10.1146/annurev.nucl.57.090506.123011.
- Sturrock, Peter Andrew (1994). Plasma Physics, an Introduction to the Theory of Astrophysical, Geophysical and Laboratory Plasmas. Cambridge University Press. DOI: 10.1017/CB09781139170598.
- Sudan, R. N. and E. Ott (1971). "Theory of Triggered VLF Emissions". In: *Journal of Geophysical Research* 76.19, pp. 4463–4476. ISSN: 01480227. DOI: 10.1029/JA076i019p04463.
- Sun, Xiaochen and Xue-Ning Bai (2023). "The Magnetohydrodynamic-Particle-in-Cell Module in Athena++: Implementation and Code Tests". In: *Monthly Notices of the Royal Astronomical Society* 523.3, pp. 3328–3347. ISSN: 0035-8711, 1365-2966. DOI: 10.1093/mnras/stad1548.
- Takahashi, Daisuke and Yasumasa Kanada (2000). "High-Performance Radix-2, 3 and 5 Parallel 1-D Complex FFT Algorithms for Distributed-Memory Parallel Computers". In: *The Journal of Supercomputing* 15.2, pp. 207–228. ISSN: 1573-0484. DOI: 10.1023/A:1008160021085.
- Tautz, R. C., A. Shalchi, and R. Schlickeiser (2008). "Solving the 90° Scattering Problem in Isotropic Turbulence". In: *The Astrophysical Journal* 685.2, p. L165. DOI: 10.1086/592498.
- The LHAASO Collaboration et al. (2021). "Peta-Electron Volt Gamma-Ray Emission from the Crab Nebula". In: *Science* 373.6553, pp. 425–430. DOI: 10.1126/science.abg5137.
- Thomas, T. and C. Pfrommer (2019). "Cosmic-Ray Hydrodynamics: Alfvén-wave Regulated Transport of Cosmic Rays". In: *Monthly Notices of the Royal Astronomical Society* 485.3, pp. 2977–3008. ISSN: 0035-8711. DOI: 10.1093/mnras/stz263.
- Thomas, T., C. Pfrommer, and R. Pakmor (2023). "Cosmic-Ray-Driven Galactic Winds: Transport Modes of Cosmic Rays and Alfvén-wave Dark Regions". In: *Monthly Notices of the Royal Astronomical Society* 521, pp. 3023–3042. ISSN: 0035-8711. DOI: 10.1093/mnras/stad472.
- Thomas, Timon (2022). "Hydrodynamik der kosmischen Strahlung: Theorie, Numerik, Anwendungen Cosmic-ray hydrodynamics: theory, numerics, applications". Universität Potsdam, 10980 KB, 334 pages. DOI: 10.25932/PUBLISHUP-56384.
- Thomas, Timon, Christoph Pfrommer, and Torsten A. Enßlin (2020). "Probing Cosmic Ray Transport with Radio Synchrotron Harps in the Galactic Center". In: *The Astrophysical Journal* 890.2, p. L18. ISSN: 2041-8213. DOI: 10.3847/2041-8213/ab7237. arXiv: 1912.08491 [astro-ph].
- Thomas, Timon, Christoph Pfrommer, and Rüdiger Pakmor (2024). Why Are Thermally- and Cosmic Ray-Driven Galactic Winds Fundamentally Different? arXiv: 2405.13121 [astro-ph]. Pre-published.

- Thomsen, M. F., J. T. Gosling, S. J. Bame, and C. T. Russell (1985). "Gyrating Ions and Large-amplitude Monochromatic MHD Waves Upstream of the Earth's Bow Shock". In: *Journal of Geophysical Research: Space Physics* 90.A1, pp. 267–273. ISSN: 0148-0227. DOI: 10.1029/JA090iA01p00267.
- Toro, E. F. (2009). Riemann Solvers and Numerical Methods for Fluid Dynamics: A Practical Introduction. 3rd ed. Dordrecht; New York: Springer. 724 pp. ISBN: 978-3-540-25202-3 978-3-540-49834-6.
- Toro, E. F., M. Spruce, and W. Speares (1994). "Restoration of the Contact Surface in the HLL-Riemann Solver". In: *Shock Waves* 4.1, pp. 25–34. ISSN: 1432-2153. DOI: 10.1007/BF01414629.
- Treumann, R A and W Baumjohann (1997). *Advanced Space Plasma Physics*. Imperial College Press. ISBN: 978-1-86094-026-2 978-1-86094-307-2. DOI: 10.1142/p020.
- Tsytovich, V. N. (1985). "Mechanism for Wave Absorption or Amplification in Stochastic Acceleration of Particles". In: *Soviet Journal of Experimental and Theoretical Physics* 62, p. 483. ISSN: 1063-7761.
- Uhlig, M., C. Pfrommer, M. Sharma, B. B. Nath, T. A. Enßlin, and V. Springel (2012). "Galactic Winds Driven by Cosmic Ray Streaming". In: *Monthly Notices of the Royal Astronomical Society* 423, pp. 2374–2396. ISSN: 0035-8711. DOI: 10.1111/j.1365-2966.2012.21045.x.
- Umansky, M. V., A. M. Dimits, I. Joseph, J. T. Omotani, and T. D. Rognlien (2015). "Modeling of Tokamak Divertor Plasma for Weakly Collisional Parallel Electron Transport". In: *Journal of Nuclear Materials*. Plasma-Surface Interactions 21 463, pp. 506–509. ISSN: 0022-3115. DOI: 10.1016/j.jnucmat.2014.10.015.
- Valentini, F., P. Trávníček, F. Califano, P. Hellinger, and A. Mangeney (2007). "A Hybrid-Vlasov Model Based on the Current Advance Method for the Simulation of Collisionless Magnetized Plasma". In: *Journal of Computational Physics* 225.1, pp. 753–770. ISSN: 0021-9991. DOI: 10.1016/j.jcp.2007.01.001.
- Van Marle, Allard Jan, Fabien Casse, and Alexandre Marcowith (2018). "On Magnetic Field Amplification and Particle Acceleration near Non-Relativistic Astrophysical Shocks: Particles in MHD Cells Simulations". In: *Monthly Notices of the Royal Astronomical Society* 473.3, pp. 3394–3409. ISSN: 0035-8711. DOI: 10.1093/mnras/stx2509.
- Vay, J.-L. (2008). "Simulation of Beams or Plasmas Crossing at Relativistic Velocity". In: *Physics of Plasmas* 15.5, p. 056701. ISSN: 1070-664X, 1089-7674. DOI: 10.1063/1.2837054.
- Verscharen, D., K. G. Klein, B. D. G. Chandran, M. L. Stevens, C. S. Salem, and S. D. Bale (2018). "ALPS: The Arbitrary Linear Plasma Solver". In: *Journal of Plasma Physics* 84.4. ISSN: 0022-3778, 1469-7807. DOI: 10.1017/S0022377818000739.
- Villasenor, John and Oscar Buneman (1992). "Rigorous Charge Conservation for Local Electromagnetic Field Solvers". In: *Computer Physics Communications* 69.2-3, pp. 306–316. ISSN: 00104655. DOI: 10.1016/0010-4655(92)90169-Y.
- Völk, Heinrich J. (1975). "Cosmic Ray Propagation in Interplanetary Space". In: *Reviews of Geophysics* 13.4, pp. 547–566. ISSN: 8755-1209, 1944-9208. DOI: 10.1029/RG013i004p00547.

- Völk, Heinrich J. and Catherine J. Cesarsky (1982). "Nonlinear Landau Damping of Alfvén Waves in a High Beta Plasma". In: *Zeitschrift für Naturforschung A* 37.8, pp. 809–815. ISSN: 1865-7109. DOI: 10.1515/zna-1982-0814.
- Wang, Liang, Ammar H. Hakim, A. Bhattacharjee, and K. Germaschewski (2015). "Comparison of Multi-Fluid Moment Models with Particle-in-Cell Simulations of Collisionless Magnetic Reconnection". In: *Physics of Plasmas* 22.1, p. 012108. ISSN: 1070-664X. DOI: 10.1063/1.4906063.
- Wang, Liang, Ammar H. Hakim, Jonathan Ng, Chuanfei Dong, and Kai Germaschewski (2020). "Exact and Locally Implicit Source Term Solvers for Multifluid-Maxwell Systems". In: *Journal of Computational Physics* 415, p. 109510. ISSN: 0021-9991. DOI: 10.1016/j.jcp.2020.109510.
- Wang, Libo, Ben Zhu, Xue-qiao Xu, and Bo Li (2019). "A Landau-fluid Closure for Arbitrary Frequency Response". In: *AIP Advances* 9.1, p. 015217. DOI: 10.1063/1.5063916.
- Waxman, Eli (1995). "Cosmological Gamma-Ray Bursts and the Highest Energy Cosmic Rays". In: *Physical Review Letters* 75.3, pp. 386–389. DOI: 10.1103/PhysRevLett.75.386.
- Weidl, Martin S., Dan Winske, and Christoph Niemann (2019). "On the Background-gyroresonant Character of Bell's Instability in the Large-current Regime". In: *The Astrophysical Journal* 872, p. 48. ISSN: 0004-637X. DOI: 10.3847/1538-4357/aafad0.
- (2019). "Three Regimes and Four Modes for the Resonant Saturation of Parallel Ion-beam Instabilities". In: The Astrophysical Journal 873, p. 57. ISSN: 0004-637X. DOI: 10.3847/1538-4357/ab0462.
- Wentzel, Donat G. (1968). "Hydromagnetic Waves Excited by Slowly Streaming Cosmic Rays". In: *The Astrophysical Journal* 152, p. 987. ISSN: 0004-637X, 1538-4357. DOI: 10.1086/149611.
- (1969). "The Propagation and Anisotropy of Cosmic Rays. I. Theory for Steady Streaming".
   In: The Astrophysical Journal 156, p. 303. ISSN: 0004-637X. DOI: 10.1086/149965.
- Whitham, G. B. (1974). *Linear and Nonlinear Waves*. John Wiley & Sons. 661 pp. ISBN: 978-1-118-03120-9.
- Wiener, Joshua, Christoph Pfrommer, and S. Peng Oh (2017). "Cosmic Ray-Driven Galactic Winds: Streaming or Diffusion?" In: *Monthly Notices of the Royal Astronomical Society*, stx127. ISSN: 0035-8711, 1365-2966. DOI: 10.1093/mnras/stx127. arXiv: 1608.02585 [astro-ph].
- Winske, D. and M. M. Leroy (1984). "Diffuse Ions Produced by Electromagnetic Ion Beam Instabilities". In: *Journal of Geophysical Research: Space Physics* 89.A5, pp. 2673–2688. ISSN: 0148-0227. DOI: 10.1029/JA089iA05p02673.
- Wolfgang Baumjohann, Rudolf A Treumann (2012). Basic Space Plasma Physics (Revised Edition). Revised ed. Imperial College Press. ISBN: 1-84816-894-2 978-1-84816-894-7.
- Wu, C. S. and R. C. Davidson (1972). "Electromagnetic Instabilities Produced by Neutral-Particle Ionization in Interplanetary Space". In: Journal of Geophysical Research (1896-1977) 77.28, pp. 5399–5406. ISSN: 2156-2202. DOI: 10.1029/JA077i028p05399.
- Xie, Hua-sheng (2014). "PDRF: A General Dispersion Relation Solver for Magnetized Multi-Fluid Plasma". In: *Computer Physics Communications* 185.2, pp. 670–675. ISSN: 0010-4655. DOI: 10.1016/j.cpc.2013.10.012.

- Xie, Hua-sheng (2019). "BO: A Unified Tool for Plasma Waves and Instabilities Analysis". In: Computer Physics Communications 244, pp. 343–371. ISSN: 0010-4655. DOI: 10.1016/j.cpc. 2019.06.014.
- Yan, Huirong and A. Lazarian (2002). "Scattering of Cosmic Rays by Magnetohydrodynamic Interstellar Turbulence". In: *Physical Review Letters* 89, p. 281102. ISSN: 0031-9007. DOI: 10.1103/PhysRevLett.89.281102.
- (2004). "Cosmic-Ray Scattering and Streaming in Compressible Magnetohydrodynamic Turbulence". In: The Astrophysical Journal 614, pp. 757–769. ISSN: 0004-637X. DOI: 10.1086/423733.
- Yee, Kane (1966). "Numerical Solution of Initial Boundary Value Problems Involving Maxwell's Equations in Isotropic Media". In: *IEEE Transactions on Antennas and Propagation* 14.3, pp. 302–307. ISSN: 1558-2221. DOI: 10.1109/TAP.1966.1138693.
- Yoon, Y. S. et al. (2011). "Cosmic-Ray Proton and Helium Spectra from the First CREAM Flight". In: *The Astrophysical Journal* 728.2, p. 122. ISSN: 0004-637X, 1538-4357. DOI: 10.1088/0004-637X/728/2/122.
- Yoshida, Haruo (1990). "Construction of Higher Order Symplectic Integrators". In: *Physics Letters A* 150.5, pp. 262–268. ISSN: 0375-9601. DOI: 10.1016/0375-9601(90)90092-3.
- Zachary, Andrew L and Bruce I Cohen (1986). "An Orbit-Averaged Darwin Quasi-Neutral Hybrid Code". In: *Journal of Computational Physics* 66.2, pp. 469–480. ISSN: 0021-9991. DOI: 10.1016/0021-9991(86)90076-8.
- Zachary, Andrew L., Bruce I. Cohen, Claire E. Max, and Jonathan Arons (1989). "The Long-Time Evolution of a Low-Density Ion Beam". In: *Journal of Geophysical Research: Space Physics* 94.A3, pp. 2443–2458. ISSN: 2156-2202. DOI: 10.1029/JA094iA03p02443.
- Zhang, Hao, Lorenzo Sironi, and Dimitrios Giannios (2021). "Fast Particle Acceleration in Three-dimensional Relativistic Reconnection". In: *The Astrophysical Journal* 922, p. 261. ISSN: 0004-637X. DOI: 10.3847/1538-4357/ac2e08.
- Zirakashvili, V. N., V. S. Ptuskin, and H. J. Voelk (2008). "Modeling Bell's Non-resonant Cosmic Ray Instability". In: *The Astrophysical Journal* 678.1, pp. 255–261. ISSN: 0004-637X, 1538-4357. DOI: 10.1086/529579. arXiv: 0801.4486 [astro-ph].
- Zweibel, E. G. and J. M. Shull (1982). "Confinement of Cosmic Rays in Molecular Clouds". In: *The Astrophysical Journal* 259, p. 859. ISSN: 0004-637X, 1538-4357. DOI: 10.1086/160220.
- Zweibel, Ellen G. (2013). "The Microphysics and Macrophysics of Cosmic Rays". In: *Physics of Plasmas* 20.5, p. 055501. ISSN: 1070-664X. DOI: 10.1063/1.4807033.
- (2017). "The Basis for Cosmic Ray Feedback: Written on the Wind". In: *Physics of Plasmas* 24.5, p. 055402. ISSN: 1070-664X. DOI: 10.1063/1.4984017.